MAX PLANCK INSTITUTE
FOR POLYMER RESEARCH

JOHANNES GUTENBERG
UNIVERSITÄT MAINZ

DEVICE PHYSICS OF PEROVSKITE SOLAR CELLS

DISSERTATION

submitted for the award of the title

"Doctor of Natural Sciences"

to the Faculty of Physics, Mathematics, and Computer Science

MAX-PLANCK INSTITUTE FOR POLYMER RESEARCH

AND

JOHANNES GUTENBERG UNIVERSITY OF MAINZ

Mohammad Sajedi Alvar

Mainz, September 2020

Summary

Lead halide perovskite solar cells (PSCs) emerged as a highly promising photovoltaic technology for converting solar radiation into electricity. Over the past decade, a remarkable progress has been achieved in improving the performance of PSCs and the power conversion efficiency of PSCs has significantly increased from 3.9% to 25.2%. Despite such a rapid and significant progress, the physics of PSCs is not fully understood. In this thesis, the device physics of perovskite solar cells has been comprehensively studied to provide an improved understanding of the operation of PSCs as the most promising photovoltaic technology among the emerging technologies.

In this thesis, a combined experimental and simulation approach is used to study the physics of methylammonium lead iodide ($MAPbI_3$) devices, as is the most commonly used perovskite composition. Experimentally, $MAPbI_3$ devices with different configurations, such as parallel-plate capacitors, electron-only devices, hole-only devices, and PSCs were fabricated and a variety of characterizations were performed on the devices. Theoretically, a device model was developed for simulating the operation of $MAPbI_3$ devices as mixed electronic-ionic semiconductor devices. By combining the numerical simulations with the experimental results, various physical properties of $MAPbI_3$ thin films were evaluated and a desirable understanding of the operation of $MAPbI_3$ devices is provided.

In the first chapter of this thesis, an introduction to solar energy, various photovoltaic technologies, and different aspects crystalline perovskite materials and PSCs is provided. In the second chapter, the accomplished experimental processing steps for producing high quality $MAPbI_3$ thin films are presented. Additionally, the route toward the fabrication and optimization of $MAPbI_3$ optoelectronic devices such as parallel-plate capacitors, electron-only devices, hole-only devices, and solar cells is provided.

For modelling the operation of $MAPbI_3$ optoelectronic devices, an electronic-ionic drift-diffusion device model is developed and provided in the third chapter. The device model is capable of simulating electronic and ionic charge transport in mixed electronic-ionic devices and can provide the time and position dependence of various electrical properties of the device, including the density and transportation of electronic and ionic charges as well as the distribution of electric potential.

Experimentally, ferroelectric properties of $MAPbI_3$ thin films were examined by measuring the electric displacement-voltage (*D*-*V*) and current-voltage (*I*-*V*) of $MAPbI_3$ parallel-plate capacitors and PSCs at different frequencies. No ferroelectric switching was observed in the *I*-*V* curves and it was demonstrated that the strong frequency dependence of hysteretic *D*-*V* characteristics originates from the migration of ions, rather than ferroelectricity.

As the next step, impedance spectroscopy (IS) was introduced as a novel approach to quantify the ionic properties of $MAPbI_3$ thin films in $MAPbI_3$ capacitor configuration. From the characteristic

frequencies of impedance spectrum, the density and diffusivity of mobile ions in $MAPbI_3$ thin films were extracted. Additionally, the frequency-dependent permittivity of $MAPbI_3$ thin films showed a significant enhancement at low frequency regime. As a complimentary method for validation of the measured ionic properties, *D-V* measurements were performed on $MAPbI_3$ capacitors to obtain the ion density and diffusivity in $MAPbI_3$ thin films. The frequency dependent *D-V* loops were reproduced by numerical simulations by assuming mobile positive ions and uniformly distributed stationary negative ions. From the magnitude and the frequency dependence of the electric displacement, respectively the ion density and the ion diffusion coefficient were obtained, which were in excellent agreement with values obtained from IS.

With the knowledge of the ion dynamics, electron- and hole-transport properties of $MAPbI_3$ thin films were independently explored. For this purpose, electron-only and hole-only devices were fabricated and optimized for efficient charge injection. Electron and hole currents were measured at different voltage scan rates and temperatures. Both the electron and hole currents as well as the hysteresis therein depend on temperature and frequency of the applied voltage signal. The temperature-dependent ion diffusion and apparent permittivity were quantified by IS and were used as input parameters for simulating the frequency and temperature dependence of electron and hole currents. It is demonstrated that for the space-charge-limited current (SCLC) analysis of the electron and hole currents in $MAPbI_3$ thin films, the frequency dependence of the permittivity and ion dynamics have to be taken into account. The mobility of electrons and holes in $MAPbI_3$ thin films were obtained from the SCLC analysis and showed no considerable temperature dependence. Additionally, from the direction of the hysteresis in electron and hole currents the sign of mobile ions was inferred to be positive.

As the final step, efficient $MAPbI_3$ PSCs with power conversion efficiency of 17.2% were fabricated and characterized, to elucidate their operational mechanism. IS and *D-V* measurements, as well as temperature- and scan-rate dependent *I-V* measurements were employed to study the physics of $MAPbI_3$ PSCs in dark conditions and under illumination. The permittivity showed a frequency-dependent behavior in dark and under illumination. The low frequency permittivity under illumination is 2 to 3 orders of magnitude greater than in dark. Comparing the *D-V* loops in dark and under illumination showed that a hysteresis loop appears at high frequencies due to illumination. By combining the IS and *D-V* measurements with the numerical simulations, it is demonstrated that the illumination activates the stationary negative ions, giving rise to the enhanced low-frequency permittivity and a high-frequency *D-V* loop due to high negative ion diffusivity. In addition, despite the hysteresis-free *I-V* characteristics of $MAPbI_3$ PSC under illumination at low scan rates at room temperature, the *I-V* characteristics showed temperature and scan-rate dependent hysteresis for lower temperatures and higher scan rates. These characteristics were consistently reproduced by simulations using the experimentally measured values for the frequency-dependent permittivity, positive and negative ion density, positive and negative ion diffusion coefficient, electron mobility, and hole mobility.

Contents

List of Figures

Chapter 1

Chapter 2

Chapter 1

Introduction to Hybrid Organic-Inorganic Perovskite Solar Cells

1.1. Solar energy

The global energy demand is annually increasing due to the rapid growth of the world's population and it is predicted to approximately double by the middle of the current century[1, 2]. In addition, due to the environmental drawbacks of the extraction of fossil fuels, pollutions caused by their consumption, and non-renewable nature of fossil energy resources, alternative clean sources of energy are highly demanded. During the recent decades, several clean sources of energy have been introduced, such as wind power, water power, and solar energy. The aforementioned sources are known as "renewable source of energy".

Today, electricity generation from renewable energy sources shows a rapid development. The share of renewable resources in global power generation is expected to increase from 25% in 2017 to 85% in 2050[3, 4]. Among the available renewable energy resources, solar energy is the most

abundant, globally accessible, and clean source of energy to supply the globally growing energy demand for future generations. Promisingly, during recent years the electricity production from solar energy shows a significant enhancement[4]. The share of power production from solar energy is predicted to increase from almost 1% in 2018 to 22% in 2050[4]. Therefore, improvement and optimization of the existing technologies and development of novel technologies are critical subjects for the scientific and economic communities.

There are several possibilities to convert solar energy to other forms of energy for different applications, such as solar thermal and photovoltaic technology. The process of direct conversion of solar radiation using electronic devices, called solar cells, to electricity is termed "photovoltaics". In this concept, the sunlight is absorbed by a solar cell and generates mobile electric charges, which produces electric power. Historically, numerous scientists from all over the world attempted to generate electricity from sunlight using the concept of photovoltaics. Photovoltaic technology was born at Bell Labs[5], where Daryl Chapin, Calvin Fuller, and Gerald Pearson developed the first silicon-based photovoltaic (PV) cell with an efficiency of 6%. They presented a classical model based on a typical semiconductor p-n junction for single junction solar cells. Theoretically, the Shockley-Queisser (SQ) model[6] has predicted a maximum power conversion efficiency of 31% for a single p-n junction based on a semiconductor with an energy gap of $E_g = 1.3\ eV$. The limited efficiency originates from two major facts: First, the photons with an energy of $E_{ph} < E_g$ cannot be absorbed. Second, the electrons excited by photons with $E_g < E_{ph}$ can only deliver the energy of $E_g$to the circuit. The rest of the energy of the electrons ($E_{ph} - E_g$) will be thermally lost.

During the last decades, enormous experimental and theoretical studies have been performed to achieve novel technologies and materials for producing PV devices to efficiently convert solar

energy to electricity. However, silicon solar cells are still the dominant photovoltaic technology among all the available technologies. Along with the remarkable progress in the development of silicon solar cells, there has been rapid advancement in developing alternative light absorbing semiconducting materials and technologies for solar cell applications. In the following, different PV technologies will be briefly reviewed.

1.2. Photovoltaic technologies

Photovoltaic is a scientific term for describing the process of generating electricity (voltage and electrical current) from solar radiation or light (*photo*) in general. Accordingly, a "Solar Cell" is an electronic device, which is designed to absorb the sunlight and convert it to electricity based on the photovoltaic concept. Typically, a solar cell consists of one or more electronic junctions between a semiconductor with other semiconductors or conductors. In such a device, the incident photons of solar radiation are absorbed by a semiconducting material, exciting an electron and leaving behind a hole. In some semiconductors, these electrons and holes are Coulombically bound, forming electron-hole pairs, called excitons. Under certain conditions, the generated excitons can be dissociated into individual electrons and holes and collected at the electrodes to produce electric power.

Over the last decades, variety of PV technologies and numerous materials have been developed and studied[7, 8]. Depending on the device architecture and the material characteristics, PV technologies can be categorized into different classes[7, 8], which are briefly discussed in the following.

1.2.1. First generation of PV technologies: crystalline silicon solar cells

The first generation of PV technologies consist of crystalline materials with maximum purity and minimum structural defects[2, 7, 9-13]. The first emerged PV modules were fabricated using crystalline silicon (c-Si) by Sharp Corporation of Japan in 1963[7, 14]. c-Si solar cells are continuously being developed to improve the power conversion efficiency and lower the production cost[2, 7, 9-13]. Si PV technologies can be classified in three groups, *viz.* monocrystalline (mc-Si), polycrystalline (pc-Si), and amorphous (a-Si) solar cells. Among them, a-Si cells are classified in the category of thin-film technologies (the second generation of solar cells)[7, 9, 11, 12]. Although Si is one of the most abundant elements on our planet and many research and development has been performed on Si PV technology, c-Si is not an ideal material for solar applications[7]. This is due to the fact that Si is a semiconductor with an indirect band gap of 1.1 eV in its crystalline form and therefore c-Si has a low optical absorption coefficient. Thus, appropriate light absorption requires above 100 μm thick Si-wafers. Moreover, the purification and crystallization costs of c-Si increases the production cost of Si solar modules[15]. This technology has been the dominating technology in the PV industry for more than three decades, with improvements such as increased cell size and reduced cell thickness from 300 µm to 180 µm[7, 10-12, 16]. However, over the last decade due to continuous improvement of the production process, the production cost of the c-Si modules has decreased by ten times[11] (as presented in Figure 1.1.) and the efficiency of c-Si solar cells has improved to 27.6%[8, 11-13] (Figure 1.2). Due to the great progress of Si PV technology over recent years, in 2018 silicon wafer-based technology has consolidated its role as the dominant solar technology accounting for over 95% of the PV market[11, 12].

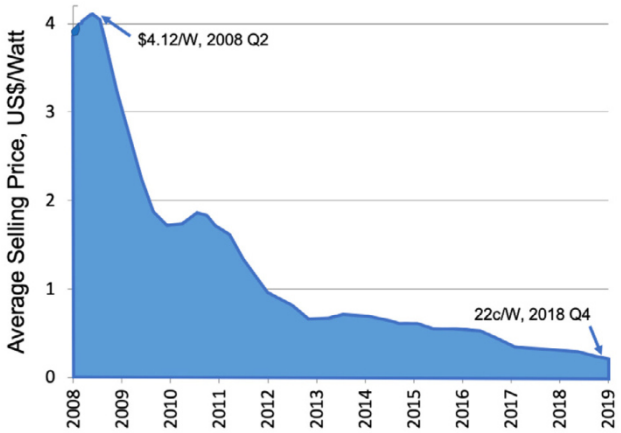

Figure 1.1. Average Quarterly Wholesale Selling Price of Multicrystalline Silicon Photovoltaic Modules.[11]

In addition to c-Si, inorganic semiconductors with a direct band gap such as GaAs, GaAlAs, GaInAsP, InSb, and InP are also used in solar cells[7]. GaAs is commonly used in concentrator PV modules and for space-industry application due its high heat resistance, high cell efficiency (> 30%), and lighter weight compare to poly-Si and mc-Si (which makes GaAs suitable for space power systems)[7, 8, 12, 13, 17, 18]. Although due to the direct band gap GaAs based materials, these materials are ideal for solar cells, the material cost and the manufacturing process can be expensive in comparison with Si-based solar cells[7, 17]. One of the solutions for reducing the production cost of PV modules has been developing the solar cells based on thin film technology[9], which will be discussed in the following.

1.2.2. Second generation of PV technologies: thin-film solar cells

The second category of solar cells is based on thin-film technology. Practically, utilizing thin layers results in a lower quantity of PV material used for absorbing the incident solar radiation[7]. Similar to the first generation of PV technologies, thin-film solar cells are also based on a single junction and therefore they obey the SQ limit. The main motivation for developing thin-film solar

cells was their potential for reducing the production costs of modules by lowering material and manufacturing costs without affecting the lifetime of the cells[7]. Hydrogenated amorphous silicon (a-Si:H) and microcrystalline silicon (μc-Si), Cadmium Telluride (CdTe), copper indium selenide (CIS), and Copper Indium Gallium Diselenide (CIGS) based solar cells are known as the main thin-film technologies[7, 8, 10, 12]. a-Si is one of the primary thin film PV technologies. Clearly, the difference between c-Si and a-Si arises from their crystallinity or the order in which the Si atoms are assembled. In contrast to c-Si that has a diamond lattice structure, in a-Si the atoms are randomly distributed in the solid. As the optoelectronic properties of a solid highly depend on atomic structure, the randomness in the atomic structure of a-Si has a major effect on its optoelectronic properties. Compared to c-Si, a-Si has a bandgap of 1.7 eV and an absorption coefficient of 40 times higher than c-Si[7]. The major disadvantage of a-Si cells is the degradation under illumination, which causes a significant reduction in their performance over time (15–35%)[7, 19].

CdTe and CIGS are semiconductors with near-ideal band gaps of 1.45 eV and 1.4 eV for absorbing solar radiation[7, 9, 20]. Due to their direct bandgap and high absorption coefficient, for full absorption of the solar radiation a few micron thin film is sufficient, compared to crystalline Si wafers that required to be several hundred microns thick[7, 9, 20]. In addition, semiconductor thin films can be deposited on large areas, which is a great advantage for mass production of solar modules. Whereas, c-Si solar modules are an assembly of numerous individual cells[7, 9]. Considering the aforementioned advantages, the highest achieved power conversion efficiency is improved to 23.4% for CIGS cells and 22.1% for CdTe cells[8, 11-13] (Figure 1.2), which is still far below the SQ limit. Despite the considerable progress of thin films technologies[12], the major

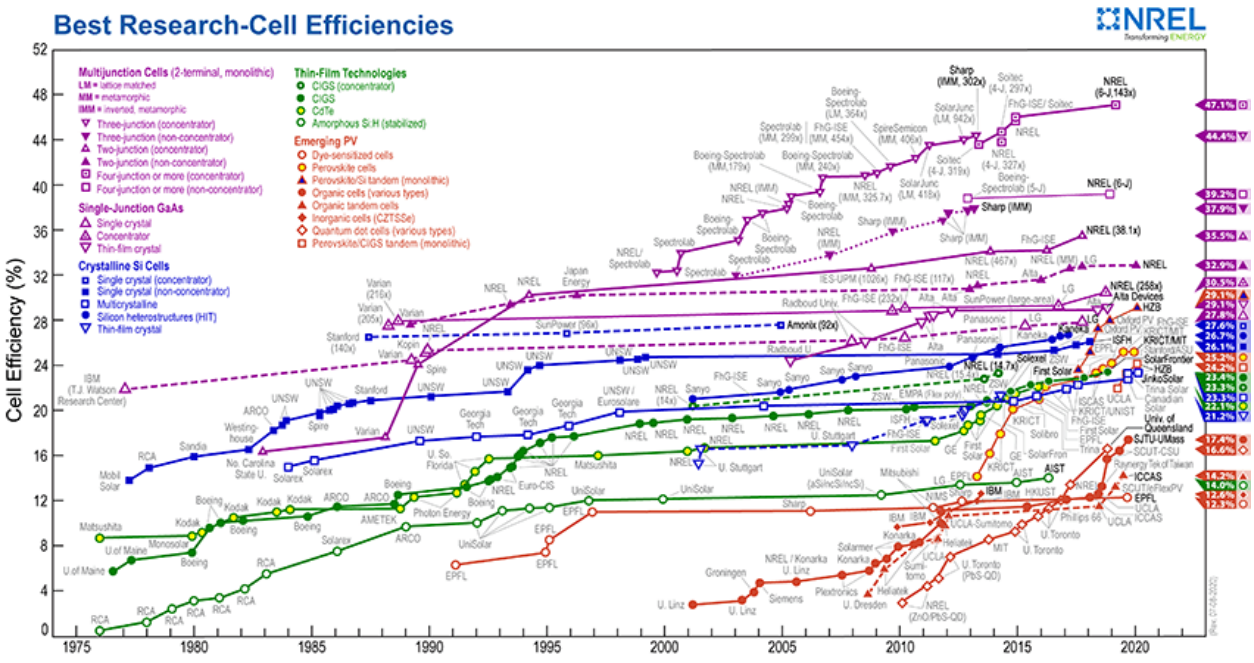

Figure 1.2. The best research-cell efficiencies of various PV technologies published by National Renewable Energy Laboratory (NREL)[8]

drawbacks of these technologies are that the applied elements are either scarce (such as indium and telluride) or toxic (such as cadmium)[9, 12, 21-23].

1.2.3. Third generation of PV technologies: emerging technologies

The term “third generation solar cells” is referring to PV technologies that are at the precommercial stage and, in part, are aiming to overcome the SQ limit. Third generation technology is covering a range from technologies under demonstration (such as multi-junction concentrating PV (CPV)) to novel emerging PV technologies that still require basic research and development investigations[7, 9]. The novel technologies are often benefiting from nanotechnology and they provide innovative techniques and materials to achieve PV materials with tunable band gap and other optoelectronic properties[7, 9, 24, 25].

In 1990, novel concepts such as nanostructured and organic based solar cells were developed as a new approach to achieve efficient and cheap photovoltaic devices[26]. The objective of these emerging PV technologies is to produce low-cost clean electricity in large scale. Some of the emerging technologies are: organic dye-sensitized cells[9, 26], inorganic semiconducting quantum-dot cells[8, 27-29], organic cells[8, 30, 31], inorganic cells (CZTSSe)[8, 32], organic–inorganic hybrid perovskite cells[8, 33-36], and different types of tandem (multijunction) cells[9, 10, 12, 13, 36, 37].

Organic solar cells or organic photovoltaic (OPV): OPVs are a class of solar cells that are mainly made of organic semiconductors including conjugated polymers and small molecules[7, 30, 31]. OPV technology significantly attracted the attention of PV community due to the unique features of organic materials such as possibility of low temperature processing, disposability, and bendability. Typically, an OPV cell consists of an electron donor-acceptor pair, for example P3HT-PCBM, where the incident photons of light generate electron-hole pairs (excitons) in the donor and/or acceptor. Such a donor-acceptor heterojunction is required to split up the tightly bound excitons generated in organic materials. The electrons are transferred to the acceptor, leaving holes in the donor[7, 30, 31, 38]. The separated electrons and holes move to electrodes and thereby the electricity is generated. The efficiency of OPVs has recently reached 17.4% (Figure 1.2)[8, 13]. Despite their lower efficiency compared to other technologies, OPVs are still popular due to the mechanical flexibility and possibility of solution processing of organic materials. OPVs can be produced on bendable substrates using low-cost and simple techniques such as roll to roll printing. The aforementioned characteristics make OPV a suitable candidate for portable electronic devices as an alternative candidate for portable energy supply that is foldable or can be rolled up[7, 30, 31].

Dye-sensitized solar cells (DSSCs): DSSCs consist of a mesoporous layer of inorganic semiconductor (typically TiO_2 or ZnO) covered by organic dye molecules and surrounded by

liquid electrolyte (a conductive solution made of a salt dissolved in a solvent liquid)[26]. The photons of solar radiation are absorbed by the dye molecules and generate an electron-hole pair. The electron is transferred to the inorganic semiconductor and subsequently the liquid electrolyte reduces the oxidized dye molecule and thereby the cycle is completed. The main drawbacks of the DSSCs are that the performance can degrade over time upon exposure to ultraviolet (UV) radiation and the liquid electrolyte can be problematic under very high and low operating temperatures[7, 9]. After almost three decades of research and development, laboratory power conversion efficiencies of ~12% have been achieved (Figure 1.2)[7, 8, 13].

Quantum-dot Sensitized Solar Cells: Many studies have been done to explore alternative absorbers for replacing the organic dye molecules and to replace the liquid electrolyte by a solid hole transport material in DSSCs[9, 27-29]. Replacing the organic dye by inorganic semiconductor quantum-dots together with substituting the liquid electrolyte by solid HTLs were performed to improve the stability and performance of the DSSCs[27, 29]. This resulted in a new class of cells known as quantum dot-sensitized solar cells (QDSSCs)[27]. The power conversion efficiency of QDSSCs has exceeded the efficiency of DSSCs and recently reached 16.6% (Figure 1.2)[8].

Perovskite solar cells: A novel and highly promising class of emerging PV technologies are "perovskite solar cells", born from DSSCs and QDSSCs[33, 35, 36, 39, 40]. The device configuration of a typical perovskite device is depicted in Figure 1.3. The device configuration consists of a perovskite layer sandwiched between an electron transport layer (ETL) and a hole transport layer (HTL). In this configuration, the incident photon is absorbed by the perovskite layer and an electron-hole pair is generated. The electron and hole move toward the selective electron and hole contacts (namely ETL and HTL). Finally, the electrons and holes will be collected at the corresponding contacts and deliver their energy to an external circuit.

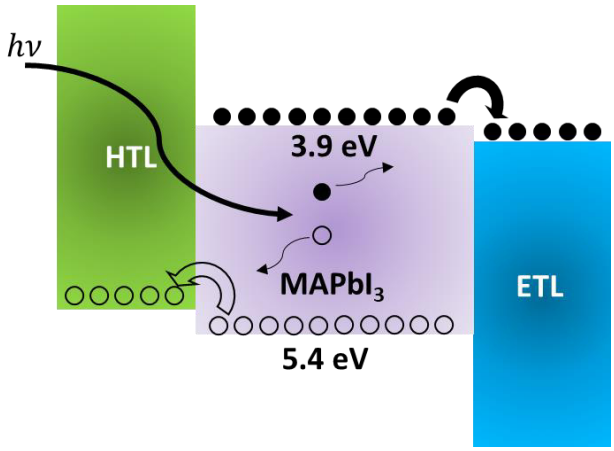

Figure 1.3. Typical device configuration of a perovskite solar cell. The incident photon is absorbed by the perovskite layer and generates an electron-hole pair. The electron and hole move toward and are collected at the electron transport and hole transport layer, respectively.

The first report on application of perovskite compounds in solar cells was in 2006[37, 40, 41], where lead halide quantum dots were introduced as a candidate for replacement of the dye molecules in DSSCs. Miyasaka et al. sensitized the mesoporous electrodes with lead halide perovskite compounds in a photoelectrochemical cell configuration with a liquid electrolyte and produced a cell with a PCE of 2.2%[37, 41, 42]. Two years later, using the same system and replacing the liquid electrolyte by a solid-state hole transport material (HTM), Myasaka et al. produced a cell with a lower efficiency of 0.4%[37, 42]. In 2009, the same group published the first journal paper on application of organometal halide perovskites as visible-light sensitizer in solar cells, where they reported a PCE of 3.9%[33, 37, 42]. Two years later, Im et al. reported a perovskite quantum dot sensitized solar cell using a liquid iodide/iodine based redox electrolyte with a PCE of 6.5%[43]. They showed that the methylammonium lead iodide ($CH_3NH_3PbI_3$ or $MAPbI_3$) perovskite quantum dots exhibit an absorption coefficient ten times higher than the conventional organic N719 dye, which was one of the best dye molecules. Such a high absorption coefficient make $MAPbI_3$ nanocrystals attractive for application in solid state sensitized solar cells, where a much

thinner TiO_2 layer is required compared to liquid junction devices. However, due to the dissolving of the $MAPbI_3$ quantum dots in the liquid electrolyte, the performance of the device rapidly degraded in time[35, 43]. In August 2012, Grätzel et al.[44] employed spiro-MeOTAD as a solid state HTM in a solid-state mesoscopic heterojunction solar cell based on $MAPbI_3$ nanoparticles as light harvesters, which resulted in an improved stability and enhanced efficiency of the cell to 9.7%. Three months later, further advancement of lead halide perovskite based devices were discovered by Snaith and Myasaka[35, 45]. They reported on a solar cell based on an extremely thin absorber layer of lead halide perovskite that overcomes the fundamental losses of organic absorbers and disordered metal oxides. The cell was made of an extremely thin absorber layer of $MAPbI_{3-x}Cl_x$ formed on a mesoscopic layer of metal oxides in junction with spiro-OMeTAD as HTM. By replacing the mesoporous semiconducting TiO_2 layer by a scaffold layer of insulating Al_2O_3 the efficiency of the cell was improved to 10.9% due to the superior electron transport properties of $CH_3NH_3PbI_{3-x}Cl_x$ compared to TiO_2. Moreover, the ambipolar charge transport property of the lead halide perovskites was demonstrated by fabricating simple planar cells with configuration of FTO/Compact TiO_2/ $CH_3NH_3PbI_{3-x}Cl_x$ (150 nm)/spiro-OMeTAD/Ag.

By introducing a solid $MAPbI_3$ perovskite capping layer overlying the scaffolding layer and using a poly-triarylamine (PTAA) HTM the efficiency was boosted to 12%[46]. An efficiency of 15% was achieved for planar perovskite cells using a layer of vapor deposited $MAPbI_3$ as the absorber, spiro-OMeTAD as HTM, and compact TiO_2 as ETL[47]. Since then, numerous research and development projects have been conducted and thousands of publications have been published, in which researchers from all over the world continuously have been trying to improve the performance and stability of the perovskite solar cells[8, 13, 36, 37, 40, 48]. By implementing numerous modifications such as improving perovskite film processing, utilizing mixed perovskite

compounds, novel HTMs and ETMs, and device optimization techniques, the performance of PSCs has vastly improved[37]. In fact, after a decade the PCE of PSCs has considerably increased from 3.9% in 2009 to 25.2% in 2020 (Figure 1.2)[8, 33]. Such a magnificently rapid progress in PCE is unique among all the PV technologies and made PSCs an attractive and promising PV technology.

All the aforementioned emerging PV technologies have been experiencing a continuous improvement in power conversion efficiencies (PCEs), along with low cost solution-based fabrication processes[8, 36, 37]. Among them, organic–inorganic hybrid perovskite PV technology as the newest entry has shown remarkable potential as one of the emerging PV technologies that can compete with the well-established silicon solar cells in terms of ease of production, PCE, and costs[36, 37]. Hence, the great potential and astonishing progress of PSCs vastly attracted the attention of the scientific communities over the last decade[36, 37, 48]. This thesis is focused on "device physics of perovskite solar cells" with the intention of providing a better understanding of the operation of PSCs to facilitate further improvement of the PSC technology. Therefore, in the following sections different aspects of PSCs will be discussed in more detail.

1.3. Performance characterization of solar cells

The main method for measuring the performance of a solar cell is the measurement of the current (density) as a function of voltage, providing I (J)-V characteristics. In this method, a time varying bias voltage is applied to the device and at the time the current is recorded. Typically, the time varying voltage is swept from a negative value or zero to a positive value. The output J-V characteristics can be measured while the device under test is in dark conditions or under illumination. In the case of illumination, the device is illuminated by a light source, which is

usually a solar simulator. Such a light source is designed to generate the solar radiation spectrum. Figure 1.4a shows a typical *J-V* of a solar cell in dark condition and under illumination. The dark *J-V* characteristic of a solar cell equals the *J-V* characteristic of a diode, which, for a classical p-n junction[49], can be described by

$$J_D = J_0\left(e^{\left(\frac{qV}{k_\beta T}\right)} - 1\right) \tag{1.1}$$

Where J, J_0, V and T are the current density, the reverse saturation current density, the applied voltage, and the temperature, respectively.

Under illumination, in steady state the photocurrent density (J_{Ph}) is created by a constant flow of photogenerated charge carriers in the opposite direction of the dark current (J_D). Therefore to obtain the current under illumination, the contribution of the photocurrent has to be subtracted from the previously described dark current (equation (1)), giving:

$$J_L = J_0\left(e^{\left(\frac{qV}{k_\beta T}\right)} - 1\right) - J_{Ph} = J_D - J_{Ph} \tag{1.2}$$

In order to calculate the power conversion efficiency (*PCE*) of a solar cell, the *J-V* characteristics under illumination are analyzed. One of the main features for evaluating the performance of a solar cell is the short circuit current density J_{SC} (see Figure 1.4a). By definition, J_{SC} is the current density under illumination at zero bias voltage

$$J_{SC} = J(V = 0) = -J_{Ph} \tag{1.3}$$

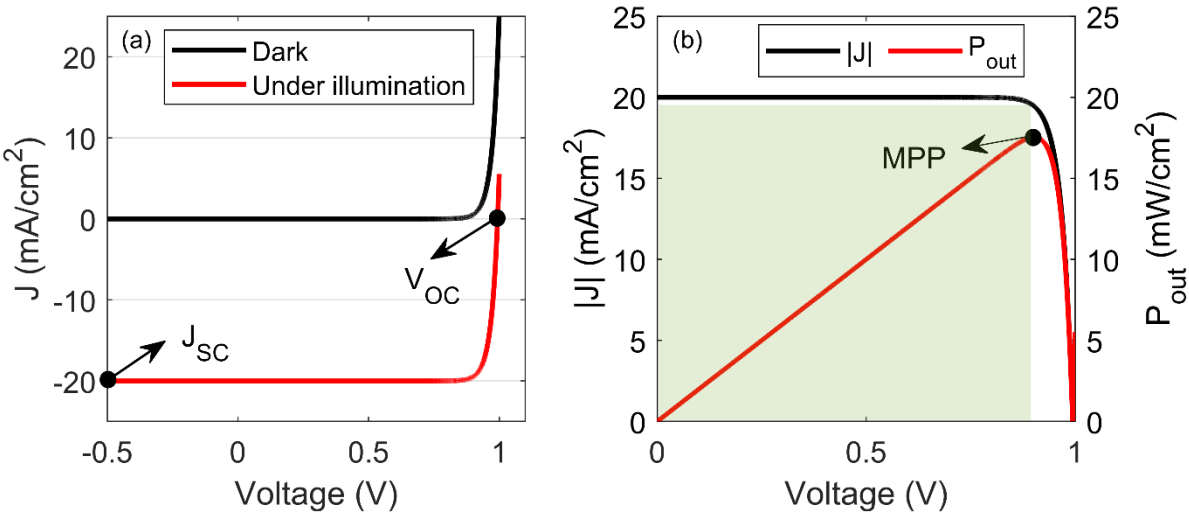

Figure 1.4. (**a**) Typical *J-V* characteristics of a solar cell, in dark (black line) and under illumination (red line). The corresponding V_{OC} and J_{SC} are presented in the figure. (**b**) The output power of the cell (red line) as function of voltage. The *MPP* of the device is presented by a black dot in the figure.

J_{SC} shows how many electrons and holes are generated, separated and transported toward the electrodes, and collected. The second crucial parameter for analyzing the performance of solar cells is the open-circuit voltage V_{OC} (see Figure 1.4a). Clearly, V_{OC} is the voltage over the device when the net current flowing through the device is zero. In fact, $V = V_{OC}$ is the voltage at which the photocurrent exactly equals the dark current as indicated in the following equation and in the Figure 1.4 a.

$$J\,(V = V_{OC}) = J_0\left(e^{\left(\frac{qV_{OC}}{k_\beta T}\right)} - 1\right) - J_{Ph} = 0 \qquad (1.4)$$

The third important parameter for evaluating the performance of solar cells is the fill factor *FF*. The fill factor is defined as the ratio of the maximum of the product of *J* and *V* (green shaded area in Figure 1.4b) and $J_{SC}V_{OC}$

$$FF = \frac{|J_{MPP}V_{MPP}|}{J_{SC}V_{OC}} \quad (1.5)$$

Where J_{MPP} and VMPP are the current density and the voltage at the maximum output power point (MPP) (see Figure 1.4b). In fact, the maximum output power of a solar cell is the point at where $|I \times V|$ reaches its maximum

$$P_{out} = JV \quad (1.6)$$

$$P_{out.max} = P_{out}(V_{MPP}) = |JV|_{max} = J_{SC}V_{SC}FF \quad (1.7)$$

In Figure 1.4 b the output power of the device is presented as a function of voltage, which shows a maximum in the range of $0<V<V_{OC}$.

The *PCE* of a solar cells is the efficiency of the conversion of incident radiation energy into electrical energy and equals the ratio of maximum output power and the input power

$$PCE = \frac{P_{out.max}}{P_{in}} = \frac{|IV|_{max}}{P_{in} \times Area_{cell}} = \frac{|JV|_{max}}{P_{in}} = \frac{J_{SC}V_{OC}FF}{P_{in}} \quad (1.8)$$

Here P_{in} is the input power, which is the power per unit area of the incident light on the device. $Area_{cell}$ is the active area of the device or the area that is exposed to the incident light.

Generally, the *J-V* characteristics and therefore the *PCE* of a solar cell are highly dependent on the intensity and the spectral distribution of the light as well as the temperature of the device. Thus, certain criteria for standard characterization of solar cells have been defined to facilitate the comparability of the reported results from different labs[48, 50, 51]. The main conditions are a light intensity of 100 mW/cm^2 (known as 1 sun), a light spectrum with a distribution matching the globally standard solar spectrum, and a device temperature of 298 K.

For characterizing solar cells, typically white light from a solar simulator is used as the light source. Due to the mismatch between the spectrum of artificial light sources and the solar spectrum, certain modifications (such as different filters) are required to achieve a reasonable spectrum. Further details about the standard conditions for solar cell characterization including the stability tests are presented in the reference[48, 50-52].

1.4. Hybrid organic-inorganic perovskites

1.4.1. Perovskite crystal structure

Initially “perovskite” was a term used for the inorganic compound calcium titanium oxide ($CaTiO_3$)[37, 53]. In 1839, $CaTiO_3$ was discovered by Gustave Rose and named after the Russian scientist Count Lev Alekseevich Perovski[37]. The first scientific paper on lead halide perovskites was published in 1892 by H. L. Wells[54]. However, the crystal structure of perovskites was deduced in 1958, 45 years after the invention of X-ray diffraction technique (XRD)[55].

Nowadays, all the materials with the chemical formula ABX_3 and the crystal structure of $CaTiO_3$ are termed ”perovskites”[53]. A crystalline perovskite compound with the composition of ABX_3 in ideal case has a simple cubic crystal structure consisting of corner-sharing TiO_6 octahedra in three dimensions with B-X-B bond angle of 180 ° and the cuboctahedral cavity in each unit cell is occupied by ‘A’ (Figure 1.5) [56, 57]. Perovskite materials are archetypal systems and depending on the distortion of the BX_6 octahedra, they may adopt a crystalline structure with lower symmetry than cubic phase[53, 57-60]. Other accessible phases for perovskites are cubic, tetragonal, orthorhombic, trigonal and monoclinic polymorphs[53, 58]. Induction of reversible phase transitions

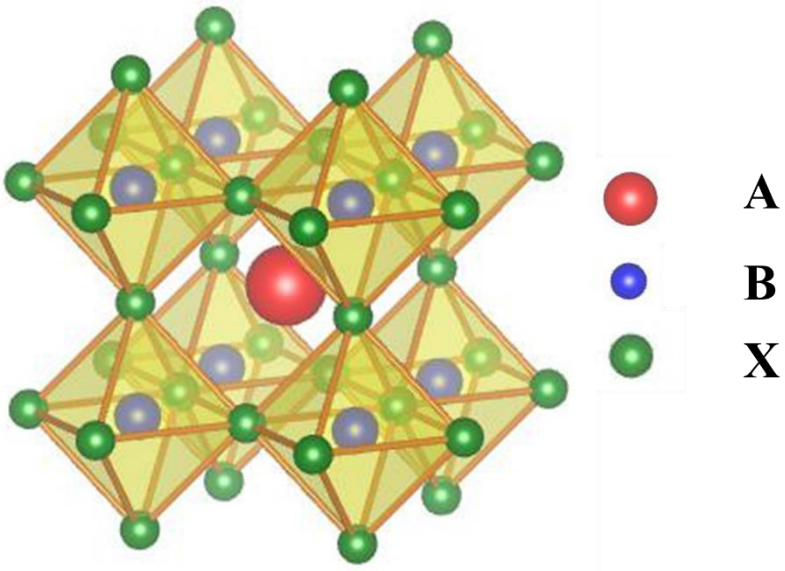

Figure 1.5. Cubic perovskite crystal structure with corner-sharing BX_6 octahedra with B-X-B bond angle of 180 ° and the cuboctahedral cavity occupied by A.

in perovskites can occur by several external stimuli, including temperature, pressure and magnetic or electric fields[53]. Depending on the nature of the A, B, and X ions the perovskite structured material can have different optoelectronic properties and can be insulating, semiconducting or superconducting[35, 37, 61, 62].

The criteria for formation of perovskite crystal structure, probable structure, and crystallographic stability are defined by the Goldsmidth tolerance factor in combination with the octahedral factor[37, 53, 63, 64]. In this idealized model, the A, B, and X ions are assumed as solid spheres and the tolerance factor is defined as the ratio of the distance between the X anion with A and B cations[35, 64]. The tolerance factor is defined as

$$t = \frac{R_A + R_X}{\sqrt{2}(R_B + R_X)} \qquad (1.9)$$

where R_A, R_B, and R_X are the radii of the corresponding cations and anions. In this formulation the octahedral factor μ is defined as $\frac{R_B}{R_X}$. Stable halide perovskite structures are formed under the conditions of $0.81 < t < 1.11$ and $0.44 < \mu < 0.90$. Formation of the cubic phase is more likely when t is in a narrower range of 0.89–1.0. Less symmetric crystal phases of tetragonal or orthorhombic can be formed with lower values of t[35, 37, 64].

1.4.2. Perovskite compositions

In a perovskite structure, A is a monovalent cation, B is a divalent cation, where A is larger than B, and X is a monovalent anion (Figure 1.5) [61, 62, 65]. There are numerous perovskite compounds with the structure of ABX_3 for different applications, in which A, B, and X are organic or inorganic ions. As previously mentioned, for formation of a perovskite crystal structure and fulfilling the conditions of the tolerance and octahedral factor, the size of the cations and the anion are of great importance. For optoelectronic applications, where the optical and electrical properties are of high importance, X is usually a halogen anion (F^-, Cl^-, Br^-, I^-)[35, 37, 57]. A can be an organic cation such as methylammonium ($CH_3NH_3^+$), ethylammonium ($CH_3CH_2NH_3^+$), and formamidinium ($NH_2CH{=}NH_2^+$)[35, 37, 57]. Several inorganic monovalent candidates for position A have been proposed that can fulfill the conditions of perovskite formation, including Cs^+ and Rb^+.[37] So far, the most efficient and common divalent cation for the position B has been Pb^{2+}. However, numerous studies have been conducted to substitute lead with a non-toxic or less toxic divalent cation that can form the perovskite crystal structure with desirable optoelectronic properties. Some of the alternative candidates are Sn^{2+}, Ge^{2+}, Mg^+, and Ca^+.[37]

The first reports on organic-inorganic lead halide perovskites were hybrid Pb ($CH_3NH_3PbX_3$, X=I, Cl, Br) and Sn ($CH_3NH_3SnBr_{1-x}I_x$, x=0.3) halide perovskites and published in 1978[61, 62].

Weber and coworkers investigated the fundamental optoelectronic properties of $CH_3NH_3PbX_3$ and $CH_3NH_3SnBr_{1-x}I_x$.[61, 62] In 1995, Mitzi et al. showed that layered organometal halide perovskites demonstrate outstanding performance as light-emitting diodes and transistors with charge carrier mobilities comparable to that in amorphous silicon[66]. About a decade ago, lead halide perovskites were successfully used in solar cells[33] and since then they have been widely used in solar cells[34, 35, 37, 39, 40, 42, 53, 67], light emitting diodes[68, 69], photodectectors[70-72], transistors[73], and lasers[74-76]. In this thesis, the standard $MAPbI_3$ perovskite compound, namely the most commonly used lead halide perovskite compound, is selected for studying the device physics of perovskite devices.

Crystal characterization of methylammonium lead iodide has shown three crystal phases that can be identified upon decreasing temperature, being cubic, tetragonal, and orthorhombic[53, 77]. The orthorhombic crystalline phase of $MAPbI_3$ is mostly stable at lower temperatures and it appears at temperatures below 165 K[53, 59, 65]. The first phase transition by increasing temperature occurs at 165 K from the orthorhombic phase to the tetragonal crystal phase[53, 59, 65]. Upon increasing the temperature, the crystal structure becomes more symmetric and the second phase transition appears at a temperature of 327 K from the tetragonal phase to the symmetric cubic phase[53, 59, 65].

For solar cells and optoelectronic applications of perovskites, normally a thin film of organic (-inorganic) halide perovskite is required. The thin films can be prepared by vapor deposition or solution processing[78-82]. Numerous techniques for solution processing and treatment of halide perovskite thin films from a variety of precursors have been introduced[78-82]. As an example, $MAPbI_3$ thin films can be processed by co-evaporation of a metal salt (such as PbI_2) and an organic halide salt (MAI) [78-82]. Additionally, it can be processed from a mixed solution of both salts dissolved in a solvent such as dimethylformamid (DMF), followed by a single-step or two-step

spin coating[78-82]. Further information about the processing and treatment techniques of thin films and nanocrystals of perovskites will be provided in chapter 2.

1.4.3. Band structure, band-gap, and exciton binding energy

Numerous experimental and theoretical studies have been accomplished to investigate optoelectronic properties of halide perovskites such as the band structure, band-gap, and exciton binding energy[57, 83]. The band structure of $MAPbI_3$ in the cubic crystal phase has been calculated using the many-body perturbation theory[83]. These calculations predicted a fundamental bandgap of ~ 1.7 eV for $MAPbI_3$. However, from experimental optical absorption an optical energy gap of ~ 1.6 eV has been measured at room temperature[84], which differs from the theoretically calculated fundamental energy gap by the exciton binding energy[57]. The optical gap of $MAPbI_3$ is very close to the optimal value of band gap ~ 1.1–1.5 eV in the Shockley–Queisser model for a single p–n junction solar cell under standard 1 Sun solar illumination[6, 57]. In addition, from the band structure of cubic $MAPbI_3$ it can be found that the minimum of the conduction band occurs at the same wavevector as the maximum of the valence band, meaning that the cubic phase of $MAPbI_3$ is a direct band-gap semiconductor and therefore photon absorption can occur without the assistance of a phonon[57, 83, 84]. It has to be noted that the optoelectronic properties of tetragonal and orthorhombic phases of $MAPbI_3$ are similar to the ones of the cubic phase[57, 85, 86]. Having a direct band gap close to the optimal value together with a high absorption coefficient of ~ 10^5 cm^{-1}, makes $MAPbI_3$ and the other hybrid perovskite compounds great candidates for PV technology[84]. With the aforementioned optoelectronic properties of hybrid perovskites, for full absorption solar radiation only a thin film of the material with a thickness of 300 nm is sufficient[57, 84].

Absorption of a photon with an energy higher than the optical band-gap of a semiconductor generates an electron-hole pair that is known as an exciton. The electron-hole pair is bound to each other by an electrostatic energy, the so-called exciton binding energy (E_B). Efficient exciton dissociation and therefore free electron-hole generation in a semiconductor, requires that the E_B is sufficiently low (in the order of the thermal energy kT)[57]. A range of values for E_B of $MAPbI_3$ have been reported from various experimental techniques[87]. Using high-field magneto-absorption measurements, an E_B of ~ 12 meV was extracted for $MAPbI_3$ in the tetragonal phase under a high magnetic field[57, 88]. By extrapolating the high magnetic field data, the zero field E_B was estimated to be lower than 5 meV[88]. Similar values of E_B have been predicted for other hybrid perovskite materials. Such low values of E_B for $MAPbI_3$ and other hybrid perovskite materials, show that PSCs are not excitonic and that free charge carriers are directly generated after light absorption[57].

1.4.4. Giant apparent permittivity

Another unique feature of hybrid perovskite compounds is their frequency dependent giant dielectric constant[89, 90]. The dielectric constant of hybrid perovskites is highly frequency dependent. At frequencies higher than 1 kHz, values in the order of tens have been reported for the dielectric constant. At lower frequencies, the dielectric constant shows a significant enhancement. The low frequency dielectric constant of lead halide perovskite reaches a value of 10^3-10^4. Under illumination, even larger values of the dielectric constant have been measured. At high frequencies under illumination, values similar to the dark values are obtained, namely in the order of tens. However, at low frequency, the dielectric constant increases to 10^6-10^7. Such a giant dielectric constant has been attributed to an excess of charge carriers due to charge injection or photo-generation[89]. In this thesis, the enhanced low frequency permittivity has been intensively

investigated both in dark conditions and under illumination. Moreover, the influence of the frequency dependent permittivity and the giant low frequency permittivity on the operation of $MAPbI_3$ devices has been studied and will be discussed in the following chapters.

1.4.5. Ferroelectricity of lead halide perovskites

The classical perovskite compounds are known as ferroelectric compounds and they have been widely used for memory applications[91]. In the early stage of the development of PSCs, ferroelectricity was introduced as one of the possible origins of the hysteresis in the *J-V* characteristics of PSCs[60, 92-94]. In addition, ferroelectricity was proposed as one of the potential reasons for the efficient performance of PSCs[95-97]. In this assumption, ferroelectric domains of the perovskite thin film facilitate efficient charge-carrier separation by means of aligned internal potential gradients across each domain, which could enhance the lifetimes of charge carriers[95-97].

In principle, the prerequisite of ferroelectricity of a compound is that the crystal structure must be non-centrosymmetric hence exhibiting a strong optical second harmonic generation (SHG)[98]. It is shown that the crystal structure of $MAPbI_3$ is not polar at room temperature down to 77 K[99]. Such none polar centrosymmetric crystal structure implies absence of ferroelectricity. On the other hand, at room temperature, some hybrid perovskite compounds have exhibited non-centrosymmetric crystal structures, which in principle allow for the presence of ferroelectricity[60]. Theoretically, this observation has also been confirmed by first-principles calculations[96].

Nevertheless, over the last years ferroelectricity of lead halide perovskites has been one of the most controversial topics in this field[100]. Such lack of clarity originates from the experimental challenges in distinguishing the ferroelectric behavior from a combination of the spatial, mechanical, and chemical effects present in the lead halide perovskite thin films[100]. Piezoelectric

force microscopy (PFM) technique has been widely used by several research groups exploring evidences of ferroelectricity in lead halide perovskites[100, 101]. Although the results of several PFM studies have claimed to provide evidence for ferroelectricity in lead halide perovskites[102], this was not observed in other studies[103]. Similar inconsistency can be observed in reports that used other methods such as polarization-voltage (*P-V*) measurements and dielectric measurements[100]. Experimentally, it has been shown that $MAPbBr_3$ crystals are not pyroelectric, implying that they cannot be ferroelectric[100, 104].

In this thesis, conventional ferroelectric electrical characterization tests, namely *P-V* and *I-V* measurements, are employed to investigate the ferroelectricity of $MAPbI_3$ thin films. In chapter 4 it will be discussed that at room temperature, no trace of ferroelectricity can be observed in $MAPbI_3$ thin films.

1.4.6. Ionic conduction in organic-inorganic perovskites

Transport of ionic species in halide perovskites has been widely investigated, referred to as ion displacement or migration, ion dynamics, and ion conduction[53, 105]. Motion of ionic species in halide perovskites was initially reported three decades ago by Mizusaki and coworkers (1983)[105]. Migration of ions draw the attention of the PV community since 2014, when together with ferroelectricity of perovskites and the trapping-detrapping of electronic charge carriers, ion migration was introduced as one of the potential origins of hysteresis in the *J-V* characteristics of PSCs by Unger et al.[106] and Snaith et al[92]. The *J-V* characteristics of a meso-structure based PSC in forward scan was different than the one in backward scan, meaning there was a discrepancy in the efficiency of the device between forward and backward scan. Due to the hysteretic *J-V*

characteristics of PSCs, accurate characterization of PSCs became controversial and more complicated.

During the last seven years, numerous attempts have been performed to investigate the nature and the mechanism of ion conduction in halide perovskites, which are known as solid ionic-electronic conductors[92, 107-129]. Intrinsic ion migration occurs under the influence of an electric field, regardless of the perovskite crystal structure. A variety of direct and indirect evidences of ion migration and its influence on anomalous *J*–*V* hysteresis[112, 122, 130-132], phase segregation, and long-term stability of PSCs has been reported. Ion migration in solids is defect mediated[53]. The ion migration rate depends on the available interstitial space, number of Schottky defects (vacancies), ion jumping distance, and size and charge of the ions. A physical quantity that describes the quality of ion migration in perovskite films is the activation energy of ions. In $MAPbI_3$ perovskites, in principle Pb^{2+}, MA^+, and I^- ions (or their vacancies) can possibly migrate[109]. Different values of activation energies have been obtained for the migration of Pb^{2+}, MA^+, and I^- ions (or their vacancies) from theoretical calculations and various experiments[109, 118, 128]. Among them, the heavy Pb^{2+} ion has the highest activation energy and is therefore less likely to migrate[109]. Migration of MA^+ and I^- ions (or their vacancies) is widely reported[109, 128]. With a lower activation energy, the I^- ion is suggested to be the most easily migrating ionic species[109, 128, 133, 134]. Migration of the MA^+ ion, with a higher activation energy than that of I^-, has also been confirmed[109, 128, 133, 134]. In this thesis, the migration of ions in $MAPbI_3$ thin films is explored by different methods. In the following chapters, experimental and simulation approaches will be introduced for quantification of the ion density and ion diffusion coefficient in $MAPbI_3$ thin films. More importantly, the influence of ionic conduction in $MAPbI_3$ thin films on the operation of $MAPbI_3$ devices will be intensively investigated.

1.4.7. Charge transport properties of organic-inorganic perovskite

The transport of electronic charge carriers in a semiconductor is directly dependent on the band structure of the semiconductor[49, 83]. One of the key features of a semiconductor is the diffusion coefficient D and the mobility μ of charge carriers. The two quantities are related to each other through the Einstein–Smoluchowski relation $D = \mu V_T$, where V_T is the thermal voltage $V_T = kT/q$. The mobility of charge carriers depends on the effective mass and the scattering rate of the carriers. The effective mass is the apparent mass of charge carriers in the crystal and can be determined from the curvature of the conduction and valence band in the electronic band structure[49, 83, 135]. Theoretically, from the curvature of the band structure of cubic $MAPbI_3$, the effective masses of $m_h^* \sim 0.1 m_0$ and $m_e^* \sim 0.15 m_0$ have been estimated for the holes and electrons, which are comparable to those of classical inorganic semiconductors[57, 83]. The predicted effective masses of the orthorhombic and the tetragonal phases of $MAPbI_3$ by first principles calculations[83, 85, 86] are in good agreement with the reduced mass measured by magneto-absorption in thin films ($\sim 0.1\ m_0$)[88]. Such low values of effective masses for electrons and holes, suggests that high charge carrier mobilities in the order of several hundreds of $\frac{cm^2}{V.S}$ can be achieved. However, the experimentally measured mobilities and diffusion coefficients are not in complete agreement with these predictions[57, 136, 137]. In fact, in spite of the low effective masses of charge carriers in hybrid perovskites that were theoretically predicted and experimentally measured, the values of the mobilities and diffusion coefficient are modest and lower than those of their inorganic counterparts. So far, a broad range of mobilities have been reported for single crystal and poly crystalline hybrid perovskites, from 10^{-7} to $10^3 \frac{cm^2}{V.S}$. [57, 136, 137] This clearly shows the significant discrepancy between the values measured by different methods on various samples[136].

Considering the modest and low values of mobility, long carrier lifetimes[138-140] of ~ 0.1- to > 1 μs in perovskites as direct-bandgap semiconductors seems to be the origin of the efficient carrier collection[57, 138]. Superposition of the two effects, namely the mobility and the long lifetime, results in long diffusion lengths of ~ 0.1- to > 1 μm in thin films[88, 139-141] and ~ 2 –15 μm in single crystals[138, 142, 143] of perovskite. The efficient carrier collection is a direct consequence of diffusion lengths that are several times longer than the absorption depth[57, 138, 142, 143].

Several methods have been employed for measuring the mobility of hybrid perovskites and they can be categorized in two different classes, namely with and without electrode[136]. The electrode-free or contactless methods are: transient absorption spectroscopy (TA)[136, 144], time-resolved photoluminescence spectroscopy (TRPL)[145], time-resolved terahertz absorption spectroscopy (TRTS)[136, 146], and time-resolved microwave conductivity (TRMC)[147-149]. The electrode-based methods are[136]: charge extraction by linearly increasing voltage (CELIV)[67, 150-152], (photocurrent) time-of-flight (TOF)[138, 142, 150, 153], field-effect transistor (FET) evaluation[73, 154], Hall effect (HE)[155, 156] and space-charge-limited current (SCLC) analysis[72, 138, 157, 158]. Although all the aforementioned techniques are individually self-consistent in evaluating the charge transport in perovskite materials, the comparison among those techniques reveals a significant inconsistency in the measured values of carrier mobility by different techniques. The mobility values extracted from the abovementioned techniques cover a broad range of ten orders of magnitude difference in the measured mobility (from 10^{-7} to $10^{3}\ \frac{cm^2}{V.S}$)[136, 137, 159].

The interactions of carriers with the lattice and imperfections of the perovskite materials are limiting factors for the mobility of charge carriers in perovskites[136, 137]. The carrier-lattice interactions are dominated by the intrinsic electronic structures of the material and therefore they are known as an intrinsic property of perovskites. The carrier-imperfections interactions are known

as extrinsic effects due to the fact that they originate from the grain boundaries, dopants, impurities, lattice defects, etc[49, 136, 137].

Comparison of the different transport measurement techniques reveals that the mobilities extracted from the CELIV, FET, and TOF methods are often below $10^{-2}\frac{cm^2}{V.s}$, while the mobility values obtained from the other techniques are usually a few orders of magnitude higher (Figure 1.6A)[67, 73, 136, 138, 142, 150-154, 159]. Remarkably, the TOF mobilities of perovskite single crystals that

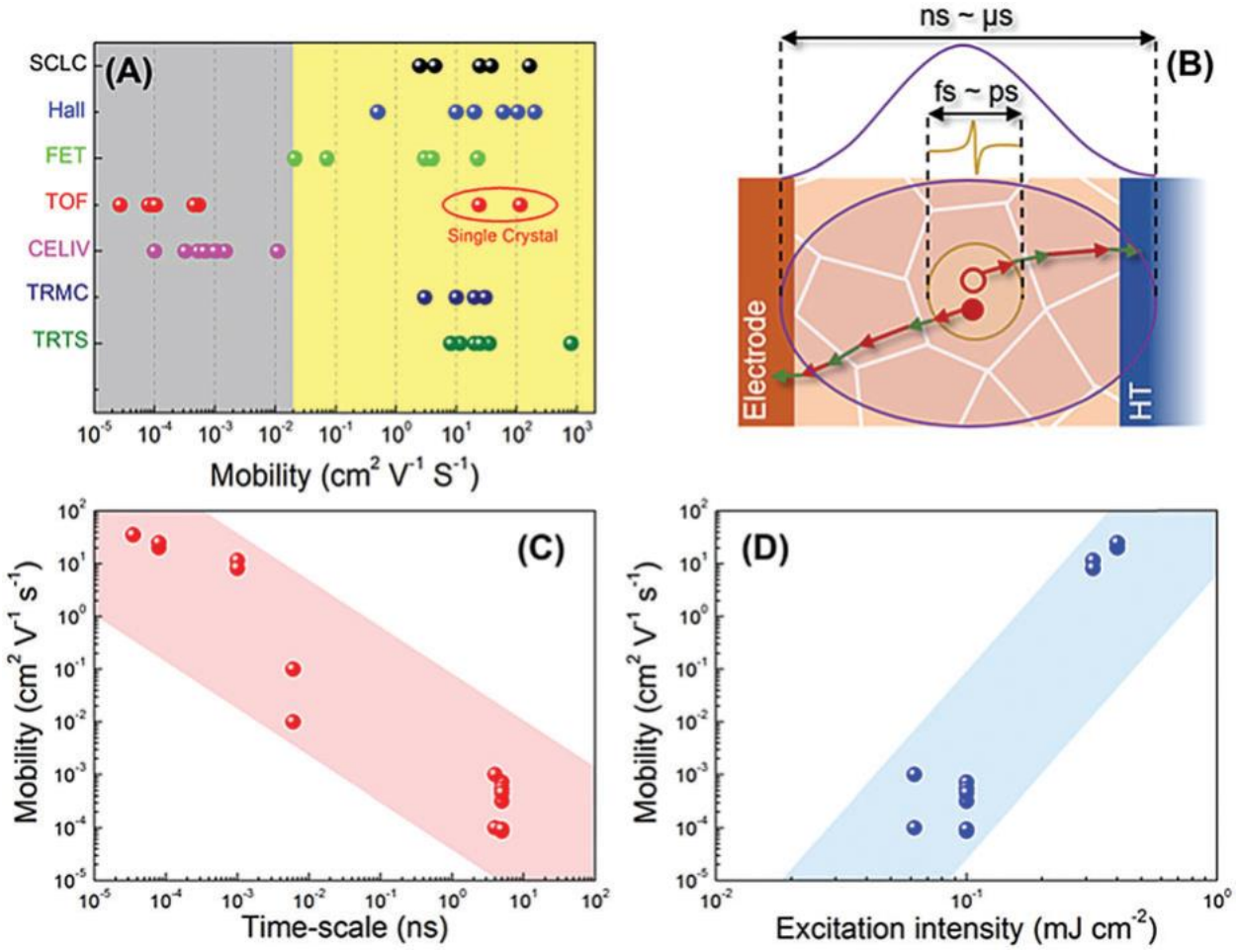

Figure 1.6. Comparison of the charge carrier mobilities measured via various techniques, including electrode-based and electrode-free techniques (**A**). The detection regime that shows the difference in time span of the pump–probe methods and the electrode based methods (**B**). The dependence of the mobilities measured by different techniques on the excitation time (**C**) and intensity (**D**)[136].

are expected to be comparatively defect-free, are within the same range as provided by the other techniques[136, 137]. This implies that the CELIV, FET, and TOF techniques are sensitive to the long-range order of perovskites and their outputs are highly influenced by a substantial contribution from the grain boundaries or other imperfections[67, 73, 136, 138, 142, 150-154, 159]. In contrast, other time-resolved approaches (such as TRMC and TRTS) mainly reflect the local intrinsic charge transport properties[136, 137, 144-149].

A study on the grain-size dependent mobilities demonstrated that pump–probe methods such as TRTS and TRMC reflect the intrinsic capabilities of the charge transport limited by the local carrier-acoustic photon scattering or carrier–phonon scattering (see Figure 1.6B)[136, 160]. In contrast to the pump–probe methods, the electrode-based methods like CELIV and TOF characterize charge carriers that pass through the entire transport path across the perovskite film within a much longer time span of nanoseconds to microseconds or longer[136, 150]. Therefore, the characteristic charge mobilities are most likely dominated by carrier scattering or trapping by defects, which is a bottleneck for charge transport[136, 150].

Additionally, the measured charge mobilities in perovskite films seem to be dependent on the probing time-scale used in different methods (see Figure 1.6C)[136]. Evidently, the mobility decreases upon the increase of the probing time-scale. It has to be noted that in methods such as SCLC and Hall effect, the inter-grain and cross-grain transportation of charge carriers can be well distinguished by modulating the applied voltage or magnetic field[136]. Therefore, the charge mobilities extracted using SCLC and Hall effect methods could potentially be close to the mobility values obtained from the TRTS and TRMC techniques[136].

The excitation intensity or the carrier concentration regime is another critical factor that needs to be taken into account for interpreting the charge-transport results of different methods[136]. It is

expected that at high carrier concentrations the rate of carrier-carrier scattering increases, which leads to a reduction of carrier mobilities[49, 136]. In contrast, as can be seen in Figure 1.6D[136], the charge carrier mobility in perovskites measured by different techniques exhibits an increasing trend with the excitation intensity. One potential reason could be the dynamic trap filling process at high carrier densities, which reduces the carrier–defect scattering of residual free charge carriers[136].

In this thesis electron and hole transport properties of $MAPbI_3$ thin films have been studied. Here a modified SCLC method has been applied for interpreting the electron and hole currents of $MAPbI_3$ thin films in single carrier device configurations. The combined experimental and simulation results are presented in chapter 7. It will be shown that the transport of electrons and holes in $MAPbI_3$ is highly influenced by the motion of ions.

1.5. Modelling of perovskite solar cells

There are different approaches for modelling perovskite materials and PSCs in different time and length scales. The most fundamental approach is density functional theory (DFT) simulations, which are often used to model physical systems on the atomic scale[83, 85, 86, 96, 135]. Principally, DFT calculations are widely used to evaluate the macroscopic properties of the materials from their atomistic structures by modelling a limited number of atoms over an extremely short time span[83, 85, 86, 96, 135]. As one might expect, DFT calculations are computationally extremely expensive and incapable of simulation of a complete device. For instance, the electronic band structure of a material can be predicted by DFT calculations, which gives several macroscopic properties of the material such as band gap and charge carrier mobility[83, 85, 86, 96, 135]. Equivalent circuit modeling is another approach for modeling the PSCs. This is a completely indirect method for describing the

behavior of PSCs, in which the collective behavior of the device is modeled by an equivalent circuit. Selecting the proper equivalent circuit is a very challenging and critical task that requires simplifying assumptions as well as reasonable knowledge of the device physics and the involved mechanisms. In this thesis, the equivalent circuit model has been used for interpreting the experimental impedance data of $MAPbI_3$ capacitors, which will be discussed in chapter 5.

Another approach for simulating PSCs is drift-diffusion modeling of the current flow in PSCs[112, 122, 161-164]. In contrast to DFT calculations and equivalent circuit methods, drift diffusion models are simply applicable on larger scales (nanometer length scale and higher) without requiring the simplifying assumptions of the equivalent circuit model. A drift-diffusion model is capable of simulating the transport of various charge carrier species including electrons, holes and ions in a full device. It also provides the possibility to include different effects such as charge trapping, mobile and immobile defects, and temperature dependent transport. Additionally, in combination with experimental data it can be used for evaluating the physical properties of the device. One of the critical points in the drift diffusion model is to choose the proper input parameters, which highly influences the output of the model. The basic parameters can be extracted from DFT calculations or directly measured by different experiments. Although drift diffusion models have been presented in several reports, the input parameters are often not validated by experiments[112, 122, 161-164]. In this thesis, a drift-diffusion model is presented which includes the ionic conduction property of perovskites. In the model, the dynamics of mobile ions, electrons, and holes are experimentally validated. The model is applied for simulating the behavior of the various $MAPbI_3$-based devices such as capacitors, electron-only, hole-only, and solar cells under different conditions. Although the model is validated for $MAPbI_3$, the concept is extendable to other perovskite based devices or mixed electronic-ionic systems. The device model will be

presented in chapter 3 and in following chapters the model validation and applications will be discussed.

1.6. Dissertation outline

The major objective of this dissertation is to study the device physics of PSCs, which assists to understand PSCs and perovskite materials for further improvement of the performance of PSCs. Experimental studies and device modelling have been followed as the two main approaches to study the physics of PSCs. Experimentally, the focus was on producing decent perovskite devices with different configurations, such as capacitors, electron-only, hole-only, and solar cells, for individual investigation of the transport of electrons, holes, and mobile ions in methylammonium lead iodide thin films. The second approach was to develop a device model based on the experimentally validated quantities for simulating the operation of PSCs. By combining the two approaches, realistic simulation of PSCs is feasible. After the introduction presented in this chapter, the different aspects of physics of PSCs will be discussed in the following chapters, including ferroelectricity, ionic properties, and electron-hole transport properties of methylammonium lead iodide perovskites.

Chapter 2. This chapter covers the experimental work accomplished in this thesis. Solution processing methods for producing crystalline $MAPbI_3$ thin films will be described. Fabrication and optimization methods for producing various $MAPbI_3$ device configurations, which have been fabricated for studying different features of $MAPbI_3$ thin films, are presented in chapter 2. Parallel plate $MAPbI_3$ capacitors are introduced and fabricated for investigation of ionic, dielectric, and ferroelectric properties of $MAPbI_3$ thin films. A route toward fabrication of efficient electron-only and hole-only devices for investigating charge transport properties of $MAPbI_3$ thin films is

described. Efficient perovskite solar cells are fabricated using the high quality perovskite thin films.

Chapter 3. The third chapter discusses the device modeling of perovskite devices. Due to the presence and significant role of the mobile ions in perovskite devices, the ion conduction is also included in the model. A device model for numerical simulations of perovskite devices is presented and formulated. The model is based on the drift-diffusion approach and includes the contribution of electronic and ionic charges. A code is programmed in MATLAB for solving the electronic-ionic drift-diffusion equations of a device based on a mixed electronic-ionic conductor. This model utilizes the finite difference method for discretization of the space and solves the current equations and continuity equations for electrons, holes, and mobile ions coupled with Poisson's equation.

Chapter 4. In this chapter, the ferroelectricity of perovskites as one of the most controversial topics in the field of perovskite solar cells is investigated. Frequency dependent electric displacement field-electric field (*D-E*) measurements were employed on $MAPbI_3$-based capacitors and solar cells. The *D-E* characteristic showed a frequency dependent behavior. At low frequencies large hysteresis in *D-E* was observed, while the high frequency *D-E* showed a linear behavior. In addition, from the frequency dependent *J-V* measurements no switching peak was observed in the current. Therefore, the ferroelectricity was ruled out as the origin of the frequency dependent *D-E* hysteresis in methylammonium lead iodide. Instead, the frequency dependent behavior of *D-E* was attributed to the mobile ionic charges.

Chapter 5. Ionic properties of $MAPbI_3$ thin films are quantified in this chapter. Impedance spectroscopy is employed to quantify the dynamics of mobile ions in $MAPbI_3$ thin films. The

impedance spectrum of $MAPbI_3$ capacitors is measured over a wide range of frequencies. Using an appropriate equivalent circuit, the impedance spectrum is analyzed. The characteristic frequencies of the impedance spectrum were extracted and using a physical model for ionic systems, the ion diffusion coefficient and ion density were estimated from the extracted characteristic frequencies.

Chapter 6. For verification of the ionic properties measured by impedance spectroscopy in chapter 5 in this chapter the electric displacement-voltage measurement was utilized as an independent and complementary method for quantification of ion dynamics in $MAPbI_3$. The frequency dependent *D-E* loops of $MAPbI_3$ capacitors were experimentally measured. Using the developed device model (chapter 3), the experimental *D-E* loops were excellently reproduced using the ionic properties that were extracted from impedance spectroscopy of $MAPbI_3$ capacitors. Combining the experimental results with numerical device simulations enabled us to introduce a device model with validated ion dynamics.

Chapter 7. Electron and hole transport properties of $MAPbI_3$ thin films are intensively investigated in this chapter. By optimizing electron and hole injection into $MAPbI_3$ thin films, decent electron-only and hole-only devices are fabricated. The space-charge-limited electron and hole currents were measured at different temperatures and voltage scan rates. Both the electron and hole current exhibit temperature and scan rate dependence. Using the experimentally validated device model, the temperature and scan rate dependent hysteretic *J-V* characteristics of the hole-only and electron-only devices were successfully simulated. Using the device model to fit the space charge limited currents (SCLC), the electron and hole mobility of the $MAPbI_3$ thin film are extracted. It is demonstrated that the frequency dependence of permittivity as well as the temperature dependence of ion dynamics and permittivity has to be considered in the SCLC

analysis of lead halide perovskites. Additionally, the sign of the hysteresis in the *J-V* characteristics showed that the mobile ionic species are positively charged.

Chapter 8. After individual quantification of transport properties of mobile ions, electrons and holes in $MAPbI_3$ thin films, a realistic simulation of $MAPbI_3$ PSCs is accomplished in this chapter. Decent inverted planar $MAPbI_3$ solar cells are fabricated by optimizing the selective layers for electron and hole collection. Impedance spectroscopy and electric displacement measurements are employed to analyze the ionic motion in $MAPbI_3$ PSCs in dark conditions and under illumination. It is shown that a second ionic species is activated under illumination. Due to this phenomenon, the permittivity of $MAPbI_3$ thin film shows a significant enhancement under illumination. The scan rate dependent *J-V* characteristics of the PSCs are measured in dark condition and under illumination. Using the device model with the experimentally quantified electronic-ionic charge transport properties, the experimental *J-V* characteristics of solar cells under illumination and in dark conditions were simulated by utilizing the frequency dependent permittivity.

1.7. References

1. World Energy Scenarios Composing energy futures to 2050. *World Energy Council* (2013).

2. Nazeeruddin, M.K. Twenty-five years of low-cost solar cells. *Nature* **538**, 463-464 (2016).

3. Gielen, D., *et al*. The role of renewable energy in the global energy transformation. *Energy Strateg Rev* **24,** 38-50 (2019).

4. IRENA. Global energy transformation: A roadmap to 2050. *International Renewable Energy Agency (IRENA)*, Abu Dhabi (2018).

5. Chapin, D.M., Fuller, C., & Pearson, G. A new silicon p-n junction photocell for converting solar radiation into electrical power. *J. App. Phys.* **25,** 676-677 (1954).

6. Shockley, W., & Queisser, H.J. Detailed balance limit of efficiency of p-n junction solar cells. *J. Appl Phys.* **32**, 510-519 (1961).

7. El-Shimy, M., & Abdo, T. Photovoltaic Technologies: History, Advances, and Characterization. *Encyclopedia of Energy Engineering and Technology,* 1397-1424 (2014).

8. https://www.nrel.gov/pv/assets/pdfs/best-research-cell-efficiencies.20200708.pdf.

9. El Chaar, L., & El Zein, N. Review of photovoltaic technologies. *Renew. Sust. Energ. Rev.* **15**, 2165-2175 (2011).

10. Gul, M., Kotak, Y., & Muneer, T. Review on recent trend of solar photovoltaic technology. *Energy Exploration & Exploitation*, **34**, 485-526 (2016).

11. Green, M.A. How did solar cells get so cheap? *Joule* **3**, 631-633 (2019).

12. Green, M.A. Photovoltaic technology and visions for the future. *Prog. Energy* **1**, 013001 (2019).

13. Green, M.A., *et al*. Solar cell efficiency tables (version 54). *Prog Photovolt Res Appl.* **27**, 565-575 (2019).

14. Archer, M.D. & Green, M.A. Clean electricity from photovoltaics. *Imperial College Press* **4** (2015).

15. Poullikkas, A. Technology and market future prospects of photovoltaic systems. *Int. J. Energy Environ.* **4**, (2010).

16. Liu, D.*, et al.* Impact of ultrathin C_{60} on perovskite photovoltaic devices. *ACS nano*, **12**, 876-883 (2018).

17. Mah, O. Fundamentals of Photovoltaic Materials. National Solar Power Research Institute. *Inc, California* (1998).

18. Iles, P.A. Evolution of space solar cells. *Sol. Energy Mater. Sol. Cells* **68**, 1-13 (2001).

19. Gielen, D. Renewable energy technologies: Cost analysis series. *International Renewable Energy Agency (IRENA)*, **1,** 52 (2012).

20. Britt, J. & Ferekides, C. Thin-film CdS/CdTe solar cell with 15.8% efficiency. *Appl. Phys. Lett.*, **62**, 2851-2852 (1993).

21. Fromer, N., Eggert, R.G., & Lifton, J. Critical materials for sustainable energy applications. *Resnick Sustainability Institute* (2011).

22. Fthenakis, V. Sustainability of photovoltaics: The case for thin-film solar cells. *Renew. Sust. Energ. Rev.* **13**, 2746-2750 (2009).

23. Green, M.A. Photovoltaic material resources. Semicond. Semimet. 87, 143-183 (2012).

24. Serrano, E., Rus, G., & Garcia-Martinez, J. Nanotechnology for sustainable energy. Renew. Sust. Energ. Rev. 13, 2373-2384 (2009).

25. Sethi, V., Pandey, M., & Shukla, M.P. Use of nanotechnology in solar PV cell. Int. J. Chem. Eng. Appl. 2, 77 (2011).

26. O'regan, B., & Grätzel, M. A low-cost, high-efficiency solar cell based on dye-sensitized colloidal TiO2 films. nature, 353, 737-740 (1991).

27. Jasim, K.E., "Quantum Dots Solar Cells," in Solar Cells- New Approaches and Reviews, edited by L. A. Kosyachenko, IntechOpen, 303-331 (2015).

28. Nozik, A.J. Quantum dot solar cells. Physica E: Low-dimensional Systems and Nanostructures 2002, 14(1-2): 115-120.

29. Nozik, A.J., et al. Semiconductor quantum dots and quantum dot arrays and applications of multiple exciton generation to third-generation photovoltaic solar cells. *Chem. Rev.* **110**, 6873-6890 (2010).

30. Koster, L.J., Smits, E., Mihailetchi, V., & Blom, P.W. Device model for the operation of polymer/fullerene bulk heterojunction solar cells. *Phys. Rev. B*, **72**, 085205 (2005).

31. Blom, P.W., Mihailetchi, V.D., Koster, L.J.A., & Markov, D.E. Device physics of polymer: fullerene bulk heterojunction solar cells. *Adv. Mater.* **19**, 1551-1566 (2007).

32. Pal K, Singh P, Bhaduri A, Thapa KB. Current challenges and future prospects for a highly efficient (> 20%) kesterite CZTS solar cell: A review. *Sol. Energy Mater. Sol. Cells,* **196,** 138-156 (2019).

33. Kojima, A., Teshima, K., Shirai, Y. & Miyasaka, T. Organometal halide perovskites as visible-light sensitizers for photovoltaic cells. *J. Am. Chem. Soc.* **131**, 6050-6051 (2009).

34. Snaith, H.J. Perovskites: the emergence of a new era for low-cost, high-efficiency solar cells. *J. Phys. Chem. Lett.* **4**, 3623-3630 (2013).

35. Green, M.A., Ho-Baillie, A., & Snaith, H.J. The emergence of perovskite solar cells. *Nature Photon* **8**, 506-514 (2014).

36. Snaith, H.J. Present status and future prospects of perovskite photovoltaics. *Nature Mater*, **17**, 372-376 (2018).

37. Jena, A.K., Kulkarni, A., & Miyasaka, T. Halide perovskite photovoltaics: background, status, and future prospects. *Chem. Rev.* **119**, 3036-3103 (2019).

38. Rowell, M.W., *et al.* Organic solar cells with carbon nanotube network electrodes. *Appl. Phys. Lett.* **88**, 233506 (2006).

39. Grätzel, M. The light and shade of perovskite solar cells. *Nature Mater*, **13**, 838-842 (2014).

40. Green, M.A., & Ho-Baillie, A. Perovskite solar cells: the birth of a new era in photovoltaics. *ACS Energy Lett.* **2**, 822-830 (2017).

41. Kojima, A.; Teshima, K.; Shirai, Y.; & Miyasaka, T. Novel Photoelectrochemical Cell with Mesoscopic Electrodes Sensitized by Lead-halide Compounds (5). Electrochem. Soc., 210th Meeting Abstr. MA2007-02, 352 (2007).

42. Miyasaka, T. Perovskite photovoltaics: rare functions of organo lead halide in solar cells and optoelectronic devices. *Chem. Lett.* **44**, 720-729 (2015).

43. Im, J-H., Lee, C-R., Lee, J-W., Park, S-W., & Park, N-G. 6.5% efficient perovskite quantum-dot-sensitized solar cell. *Nanoscale* **3**, 4088-4093 (2011).

44. Kim, H-S., *et al.* Lead iodide perovskite sensitized all-solid-state submicron thin film mesoscopic solar cell with efficiency exceeding 9%. *Sci Rep* **2**, 1-7 (2012).

45. Lee, M.M., Teuscher, J., Miyasaka, T., Murakami, T.N., & Snaith, H.J. Efficient hybrid solar cells based on meso-superstructured organometal halide perovskites. *Science* **338**, 643-647 (2012).

46. Heo, J.H., *et al.* Efficient inorganic–organic hybrid heterojunction solar cells containing perovskite compound and polymeric hole conductors. *Nature Photon* **7**, 486-491 (2013).

47. Liu, M., Johnston, M.B., & Snaith, H.J. Efficient planar heterojunction perovskite solar cells by vapour deposition. *Nature* **501**, 395-398 (2013).

48. Correa-Baena, J-P.*, et al.* The rapid evolution of highly efficient perovskite solar cells. *Energy Environ. Sci.* **10**, 710-727 (2017).

49. Sze, S.M., & Ng, K.K. Physics of semiconductor devices. *John wiley & sons*, (2006).

50. Emery, K.A., *et al.* Methods for measuring solar cell efficiency independent of reference cell or light source. (1985).

51. Dunlop, E.D.*, et al.* Guidelines for PV power measurement in industry. *European Commission Joint Research Centre* (2010).

52. Zimmermann, E.*, et al.* Characterization of perovskite solar cells: Towards a reliable measurement protocol. *APL Mater.* **4,** 091901 (2016).

53. Yuan, Y., Wang, Q. & Huang, J. Organic-Inorganic Halide Perovskite Photovoltaics: From Fundamentals to Device Architectures. (eds Park, N.-G., Grätzel, M. & Miyasaka, T.) *Springer* (2016).

54. Wells, H.L. Über die Cäsium-und Kalium-Bleihalogenide. *Zeitschrift für anorganische Chemie*, **3**, 195-210 (1893).

55. Møller, C. K. Crystal Structure and Photoconductivity of Cæsium Plumbohalides. *Nature* **182,** 1436−1436 (1958).

56. Wells, A.F. Structural inorganic chemistry. *Oxford university press*, (2012).

57. Brenner, T.M., Egger, D.A., Kronik, L., Hodes, G., & Cahen, D. Hybrid organic-inorganic perovskites: low-cost semiconductors with intriguing charge-transport properties. *Nature Rev Mater* **1**, 1-16 (2016).

58. Glazer, A. The classification of tilted octahedra in perovskites. *Acta Cryst. B* **28**, 3384-3392 (1972).

59. Weller, M.T., Weber, O.J., Henry, P.F., Di Pumpo, A.M., & Hansen, T.C. Complete structure and cation orientation in the perovskite photovoltaic methylammonium lead iodide between 100 and 352 K. *Chem. Commun.* **51**, 4180-4183 (2015).

60. Stoumpos, C.C., Malliakas, C.D., & Kanatzidis, M.G. Semiconducting tin and lead iodide perovskites with organic cations: phase transitions, high mobilities, and near-infrared photoluminescent properties. *Inorg. Chem.* **52**, 9019-9038 (2013).

61. Weber, D. $CH_3NH_3PbX_3$, ein Pb (II)-system mit kubischer perowskitstruktur/ $CH_3NH_3PbX_3$, a Pb (II)-system with cubic perovskite structure. *Zeitschrift für Naturforschung B* **33**, 1443-1445 (1978).

62. Weber, D. $CH_3NH_3SnBr_xI_{3-x}$ (x= 0-3), ein Sn (II)-System mit kubischer Perowskitstruktur/$CH_3NH_3SnBr_xI_{3-x}$ (x= 0-3), a Sn (II)-system with cubic perovskite structure. *Zeitschrift für Naturforschung B* **33**, 862-865 (1978).

63. Goldschmidt, V.M. Die gesetze der krystallochemie. *Naturwissenschaften* **14**, 477-485 (1926).

64. Li, C., *et al*. Formability of ABX_3 (X= F, Cl, Br, I) Halide Perovskites. *Acta Cryst.* B **64**, 702-707 (2008).

65. Poglitsch, A., & Weber, D. Dynamic disorder in methylammoniumtrihalogenoplumbates (II) observed by millimeter-wave spectroscopy. *J. Chem. Phys.* **87**, 6373-6378 (1987).

66. Mitzi, D., Wang, S., Field, C., Chess, C., & Guloy, A. Conducting layered organic-inorganic halides containing< 110>-oriented perovskite sheets. *Science* **267**, 1473-1476 (1995).

67. Lin, Q., Armin, A., Nagiri, R.C.R., Burn, P.L., Meredith, P. Electro-optics of perovskite solar cells. *Nature Photon* **9**, 106-112 (2015).

68. Lin, K.*, et al.* Perovskite light-emitting diodes with external quantum efficiency exceeding 20 per cent. *Nature* **562**, 245-248 (2018).

69. Tan, Z-K., *et al.* Bright light-emitting diodes based on organometal halide perovskite. *Nature Nanotech* **9**, 687-692 (2014).

70. Li, D., Dong, G., Li, W., & Wang, L. High performance organic-inorganic perovskite-optocoupler based on low-voltage and fast response perovskite compound photodetector. *Sci Rep* **5**, 1-6 (2015).

71. Dong, R.*, et al.* High-gain and low-driving-voltage photodetectors based on organolead triiodide perovskites. *Adv. Mater.* **27**, 1912-1918 (2015).

72. Liu, Y., *et al.* 20-mm-Large Single-Crystalline Formamidinium-Perovskite Wafer for Mass Production of Integrated Photodetectors. *Adv. Opt. Mater.* **4**, 1829-1837 (2016).

73. Chin, X.Y., Cortecchia, D., Yin, J., Bruno, A., & Soci, C. Lead iodide perovskite light-emitting field-effect transistor. *Nat Commun* **6,** 7383 (2015).

74. Xing, G., *et al.* Low-temperature solution-processed wavelength-tunable perovskites for lasing. *Nature Mater* **13**, 476 (2014).

75. Zhu, H.*, et al.* Lead halide perovskite nanowire lasers with low lasing thresholds and high quality factors. *Nature Mater* **14**, 636-642 (2015).

76. Deschler, F.*, et al.* High photoluminescence efficiency and optically pumped lasing in solution-processed mixed halide perovskite semiconductors. *J. Phys. Chem. Lett.* **5**, 1421-1426 (2014).

77. Onoda-Yamamuro, N., Matsuo, T., & Suga, H. Dielectric study of $CH_3NH_3PbX_3$ (X= Cl, Br, I). *J. Phys. Chem. Solids* **53,** 935-939 (1992).

78. Dubey, A.*, et al.* A strategic review on processing routes towards highly efficient perovskite solar cells. *J. Mater. Chem. A* **6**, 2406-2431 (2018).

79. Chen, Y., Zhang, L., Zhang, Y., Gao, H., & Yan, H. Large-area perovskite solar cells–a review of recent progress and issues. *RSC Adv.* **8**, 10489-10508 (2018).

80. Ashurov, N., *et al.* Current state and perspectives for organo-halide perovskite solar cells. Part 1. Crystal structures and thin film formation, morphology, processing, degradation, stability improvement by carbon nanotubes. A review. *Mod. Electron. Mater.* **3**, 1-25 (2017).

81. Bing, J., Huang, S., & Ho-Baillie A.W. A Review on Halide Perovskite Film Formation by Sequential Solution Processing for Solar Cell Applications. *Energy Technol.* **8**, 1901114 (2020).

82. Sharenko, A., & Toney, M.F. Relationships between lead halide perovskite thin-film fabrication, morphology, and performance in solar cells. *J. Am. Chem. Soc.* **138**, 463-470 (2016).

83. Brivio, F., Butler, .KT., Walsh, A., & Van Schilfgaarde, M. Relativistic quasiparticle self-consistent electronic structure of hybrid halide perovskite photovoltaic absorbers. *Phys. Rev. B* **89**, 155204 (2014).

84. De Wolf, S., *et al.* Organometallic halide perovskites: sharp optical absorption edge and its relation to photovoltaic performance. *J. Phys. Chem. Lett.* **5**, 1035-1039 (2014).

85. Umari, P., Mosconi, E., & De Angelis, F. Relativistic GW calculations on $CH_3NH_3PbI_3$ and $CH_3NH_3SnI_3$ perovskites for solar cell applications. *Sci Rep* **4,** 4467 (2014).

86. Menéndez-Proupin, E., Palacios, P., Wahnón, P., & Conesa, J. Self-consistent relativistic band structure of the $CH_3NH_3PbI_3$ perovskite. *Phys. Rev. B* **90**, 045207 (2014).

87. Collavini, S,. Völker, S.F., & Delgado, J.L. Understanding the outstanding power conversion efficiency of perovskite-based solar cells. *Angew. Chem. Int. Ed.* **54**, 9757-9759 (2015).

88. Miyata, A., *et al.* Direct measurement of the exciton binding energy and effective masses for charge carriers in organic–inorganic tri-halide perovskites. *Nature Phys* **11**, 582-587 (2015).

89. Juarez-Perez, E.J.*, et al.* Photoinduced giant dielectric constant in lead halide perovskite solar cells. *J. Phys. Chem. Lett.* **5**, 2390-2394 (2014).

90. Onoda-Yamamuro, N., Matsuo, T., & Suga, H. Dielectric study of $CH_3NH_3PbX_3$ (X= Cl, Br, I). *J. Phys. Chem. Solids* **53,** 935-939 (1992).

91. Kim, H., Han, J.S., Kim, S.G., Kim, S.Y., & Jang, H.W. Halide perovskites for resistive random-access memories. *J. Mater. Chem. C* **7**, 5226-5234 (2019).

92. Snaith, H., *et al.* Anomalous hysteresis in perovskite solar cells. *J. Phys. Chem. Lett.* **5,** 1511-1515 (2014).

93. Chen, B., *et al.* Interface band structure engineering by ferroelectric polarization in perovskite solar cells. *Nano Energy* **13,** 582-591 (2015).

94. Chen, H-W., Sakai, N., Ikegami, M., & Miyasaka, T. Emergence of hysteresis and transient ferroelectric response in organo-lead halide perovskite solar cells. *J. Phys. Chem. Lett.* **6**, 164-169 (2015).

95. Sherkar, T.S. & Koster, L.J.A. Can ferroelectric polarization explain the high performance of hybrid halide perovskite solar cells? *Phys. Chem. Chem. Phys.* **18**, 331-338 (2016).

96. Frost, J.M., &. Atomistic origins of high-performance in hybrid halide perovskite solar cells. *Nano Lett.* **14**, 2584-2590 (2014).

97. Liu, S., *et al*. Ferroelectric domain wall induced band gap reduction and charge separation in organometal halide perovskites. *J. Phys. Chem. Lett.* **6**, 693-699 (2015).

98. Asadi, K., & van der Veen, M.A. Ferroelectricity in metal-organic frameworks: characterization and mechanisms. *Eur. J. Inorg. Chem.* **2016,** 4332-4344 (2016).

99. Mahale, P., *et al.* Is $CH_3NH_3PbI_3$ polar? *J. Phys. Chem. Lett.* **7**, 2412-2419 (2016).

100. Liu, Y.*, et al.* Chemical nature of ferroelastic twin domains in $CH_3NH_3PbI_3$ perovskite. *Nature Mater.* **17**, 1013-1019 (2018).

101. Kutes, Y., *et al*. Direct observation of ferroelectric domains in solution-processed $CH_3NH_3PbI_3$ perovskite thin films. *J. Phys. Chem. Lett.* **5**, 3335-3339 (2014).

102. Röhm, H., Leonhard, T., Hoffmann, M.J., & Colsmann, A. Ferroelectric domains in methylammonium lead iodide perovskite thin-films. *Energy Environ. Sci.* **10**, 950-955 (2017).

103. Balke, N., *et al*, Exploring local electrostatic effects with scanning probe microscopy: implications for piezoresponse force microscopy and triboelectricity. *ACS nano*, **8**, 10229-10236 (2014).

104. Rakita, Y.*, et al.* $CH_3NH_3PbBr_3$ is not pyroelectric, excluding ferroelectric-enhanced photovoltaic performance. *APL Mater.* **4**, 051101 (2016).

105. Mizusaki, J., Arai, K., & Fueki, K. Ionic conduction of the perovskite-type halides. *Solid State Ionics*, **11**, 203-211 (1983).

106. Unger, E.L., *et al.* Hysteresis and transient behavior in current–voltage measurements of hybrid-perovskite absorber solar cells. *Energy Environ Sci.* **7**, 3690-3698 (2014).

107. Azpiroz, J.M., Mosconi, E., Bisquert, J., & De Angelis, F. Defect migration in methylammonium lead iodide and its role in perovskite solar cell operation. *Energy Environ. Sci.* **8**, 2118-2127 (2015).

108. Bag, M., *et al.* Kinetics of ion transport in perovskite active layers and its implications for active layer stability. *J. Am. Chem. Soc.* **137**, 13130-13137 (2015).

109. Eames, C., *et al*. Ionic transport in hybrid lead iodide perovskite solar cells. *Nat Commun* **6,** 7497 (2015).

110. Haruyama, J., Sodeyama, K., Han, L. & Tateyama, Y. First-principles study of ion diffusion in perovskite solar cell sensitizers. *J. Am. Chem. Soc.* **137**, 10048-10051 (2015).

111. Tress, W., *et al*. Understanding the rate-dependent J–V hysteresis, slow time component, and aging in $CH_3NH_3PbI_3$ perovskite solar cells: the role of a compensated electric field. *Energy Environ. Sci.* **8,** 995-1004 (2015).

112. van Reenen, S., Kemerink, M., & Snaith, H. Modeling anomalous hysteresis in perovskite solar cells. *J. Phys. Chem. Lett.* **6,** 3808-3814 (2015).

113. Yang, T.Y., Gregori, G., Pellet, N., Grätzel, M., & Maier, J. The significance of ion conduction in a hybrid organic–inorganic lead-iodide-based perovskite photosensitizer. *Angew. Chem. Int. Ed.* **54**, 7905-7910 (2015).

114. Yuan, Y.*, et al.* Photovoltaic switching mechanism in lateral structure hybrid perovskite solar cells. *Adv. Energy Mater.* **5**, 1500615 (2015).

115. Calado, P., *et al.* Evidence for ion migration in hybrid perovskite solar cells with minimal hysteresis. *Nat Commun* **7,** 13831 (2016).

116. Delugas, P., Caddeo, C., Filippetti, A., & Mattoni, A. Thermally activated point defect diffusion in methylammonium lead trihalide: anisotropic and ultrahigh mobility of iodine. *J. Phys. Chem. Lett.* **7**, 2356-2361 (2016).

117. DeQuilettes, D.W.*, et al.* Photo-induced halide redistribution in organic–inorganic perovskite films. *Nat Commun* **7,** 11683 (2016).

118. Frost, J.M., & Walsh, A. What is moving in hybrid halide perovskite solar cells? *Acc. Chem. Res.* **49**, 528-535 (2016).

119. Li, C., *et al.* Iodine migration and its effect on hysteresis in perovskite solar cells. *Adv. Mater.* **28**, 2446-2454 (2016).

120. Meloni, S., *et al.* Ionic polarization-induced current–voltage hysteresis in $CH_3NH_3PbX_3$ perovskite solar cells. *Nat Commun* **7,** 10334 (2016).

121. Mosconi, E., Meggiolaro, D., Snaith, H.J., Stranks, S.D., & De Angelis, F. Light-induced annihilation of Frenkel defects in organo-lead halide perovskites. *Energy Environ. Sci.* **9**, 3180-3187 (2016).

122. Richardson, G., *et al.* Can slow-moving ions explain hysteresis in the current–voltage curves of perovskite solar cells? *Energy Environ. Sci.* **9**, 1476-1485 (2016).

123. Xing, J., *et al*. Ultrafast ion migration in hybrid perovskite polycrystalline thin films under light and suppression in single crystals. *Phys. Chem. Chem. Phys.* **18**, 30484-30490 (2016).

124. Game, O.S., Buchsbaum, G.J., Zhou, Y., Padture, N.P., & Kingon, A.I. Ions matter: description of the anomalous electronic behavior in methylammonium lead halide perovskite devices. *Adv. Func. Mater.* **27**, 1606584 (2017).

125. Li, C., Guerrero, A., Huettner, S., & Bisquert, J. Unravelling the role of vacancies in lead halide perovskite through electrical switching of photoluminescence. *Nat Commun* **9**, 5113 (2018).

126. Meggiolaro, D*., et al.* Iodine chemistry determines the defect tolerance of lead-halide perovskites. *Energy Environ. Sci.* **11**, 702-713 (2018).

127. Ebadi, F., Taghavinia, N., Mohammadpour, R., Hagfeldt, A., & Tress, W. Origin of apparent light-enhanced and negative capacitance in perovskite solar cells. *Nat Commun* **10**, 1574 (2019).

128. Futscher, M. H., et al. Quantification of ion migration in $CH_3NH_3PbI_3$ perovskite solar cells by transient capacitance measurements. *Mater. Horiz.*, **6**, 1497-1503 (2019).

129. Moia, D*., et al.* Ionic-to-electronic current amplification in hybrid perovskite solar cells: ionically gated transistor-interface circuit model explains hysteresis and impedance of mixed conducting devices. *Energy Environ. Sci.* **12**, 1296-1308 (2019).

130. Riquelme, A., *et al.* Identification of recombination losses and charge collection efficiency in a perovskite solar cell by comparing impedance response to a drift-diffusion model. *Nanoscale*, **12,** 17385-17398 (2020).

131. Weber, S., *et al.* How the formation of interfacial charge causes hysteresis in perovskite solar cells. *Energy Environ. Sci.* **11,** 2404-2413 (2018).

132. Chen, B., Yang, M., Priya, S., & Zhu, K. Origin of J–V hysteresis in perovskite solar cells. *J. Phys. Chem. Lett.* **7,** 905-917 (2016).

133. Senocrate, A.*, et al.* The nature of ion conduction in methylammonium lead iodide: a multimethod approach. *Angew. Chem. Int. Ed.* **56**, 7755-7759 (2017).

134. Senocrate, A.*, et al.* Slow $CH_3NH_3^+$ Diffusion in $CH_3NH_3PbI_3$ under Light Measured by Solid-State NMR and Tracer Diffusion. *J. Phys. Chem. C,* **122**, 21803-21806 (2018).

135. Zhao, T., Shi, W., Xi, J., Wang, D., & Shuai, Z. Intrinsic and extrinsic charge transport in $CH_3NH_3PbI_3$ perovskites predicted from first-principles. *Sci Rep* **6**, 1-9 (2016).

136. Peng, J., Chen, Y., Zheng, K., Pullerits, T., & Liang, Z. Insights into charge carrier dynamics in organo-metal halide perovskites: from neat films to solar cells. *Chem. Soc. Rev.* **46**, 5714-5729 (2017).

137. Herz, L.M. Charge-carrier mobilities in metal halide perovskites: fundamental mechanisms and limits. *ACS Energy Lett.* **2**, 1539-1548 (2017).

138. Shi, D., *et al.* Low trap-state density and long carrier diffusion in organolead trihalide perovskite single crystals. *Science* **347**, 519-522 (2015).

139. Stranks, S.D.*, et al.* Electron-hole diffusion lengths exceeding 1 micrometer in an organometal trihalide perovskite absorber. *Science* **342**, 341-344 (2013).

140. Xing, G., *et al.* Long-range balanced electron-and hole-transport lengths in organic-inorganic $CH_3NH_3PbI_3$. *Science* **342**, 344-347 (2013).

141. Wehrenfennig, C., Eperon, G.E., Johnston, M.B., Snaith, H.J. & Herz, L.M. High Charge Carrier Mobilities and Lifetimes in Organolead Trihalide Perovskites. *Adv. Mater. Adv. Mater.* **26**, 1584-1589 (2014).

142. Dong, Q.*, et al.* Electron-hole diffusion lengths> 175 μm in solution-grown $CH_3NH_3PbI_3$ single crystals. *Science* **347**, 967-970 (2015).

143. Saidaminov, M., *et al.* High-quality bulk hybrid perovskite single crystals within minutes by inverse temperature crystallization. *Nat Commun* **6,** 7586 (2015).

144. Narra, S., Chung, C-C., Diau, E.W-G., & Shigeto, S. Simultaneous observation of an intraband transition and distinct transient species in the infrared region for perovskite solar cells. *J Phys. Chem. Lett.* **7**, 2450-2455 (2016).

145. Guo, Y.*, et al.* Enhanced performance of perovskite solar cells via anti-solvent nonfullerene Lewis base IT-4F induced trap-passivation. *J. Mater. Chem. A* **6**, 5919-5925 (2018).

146. Chen Y, *et al.* Tailoring Organic Cation of 2D Air-Stable Organometal Halide Perovskites for Highly Efficient Planar Solar Cells. *Adv. Energy Mater.* **7**, 1700162 (2017).

147. Colbeau-Justin, C., & Valenzuela, M. Time-resolved microwave conductivity (TRMC) a useful characterization tool for charge carrier transfer in photocatalysis: a short review. *Revista Mexicana de Física*, **59**, 191-200 (2013).

148. Ponseca, Jr C.S.*, et al.* Organometal halide perovskite solar cell materials rationalized: ultrafast charge generation, high and microsecond-long balanced mobilities, and slow recombination. *J. Am. Chem. Soc.* **136**, 5189-5192 (2014).

149. Hutter, E.M., Eperon, G.E., Stranks, S.D., & Savenije, T.J. Charge carriers in planar and meso-structured organic–inorganic perovskites: mobilities, lifetimes, and concentrations of trap states. *J. Phys. Chem. Lett.* **6**, 3082-3090 (2015).

150. Chen, Y., Peng, J., Su, D., Chen, X., & Liang, Z. Efficient and balanced charge transport revealed in planar perovskite solar cells. *ACS Appl. Mater. Interfaces*, **7**, 4471-4475 (2015).

151. Tsai, H., *et al.* High-efficiency two-dimensional Ruddlesden–Popper perovskite solar cells. *Nature* **536**, 312-316 (2016).

152. Petrović, M., Ye, T., Vijila, C., & Ramakrishna, S. Influence of charge transport and defects on the performance of planar and mesostructured perovskite solar cells. *Adv. Energy Mater.* **7**, 1602610 (2017).

153. Peng, J., Sun, Y., Chen, Y., Yao, Y., & Liang, Z. Light and thermally induced evolutional charge transport in $CH_3NH_3PbI_3$ perovskite solar cells. *ACS Energy Lett.* **1**, 1000-1006 (2016).

154. Zhang, M-J.*, et al.* Carrier transport improvement of $CH_3NH_3PbI_3$ film by methylamine gas treatment. *ACS Appl. Mater. Interfaces*, **8**, 31413-31418 (2016).

155. Takahashi, Y., Hasegawa, H., Takahashi, Y., & Inabe, T. Hall mobility in tin iodide perovskite $CH_3NH_3SnI_3$: evidence for a doped semiconductor. *J. Solid State Chem.* **205,** 39-43 (2013).

156. Yi, H.T., Wu, X., Zhu, X., & Podzorov, V. Intrinsic Charge Transport across Phase Transitions in Hybrid Organo-Inorganic Perovskites. *Adv. Mater.* **28,** 6509-6514 (2016).

157. Pospisil, J., *et al*. Density of bulk trap states of hybrid lead halide perovskite single crystals: temperature modulated space-charge-limited-currents. *Sci Rep* **9**, 1-8 (2019).

158. Lin, Y., *et al.* Unveiling the operation mechanism of layered perovskite solar cells. *Nat Commun* **10,** 1-11 (2019).

159. Zhou, S.*, et al.* Ag-doped halide perovskite nanocrystals for tunable band structure and efficient charge transport. *ACS Energy Lett.* **4**, 534-541 (2019).

160. Reid, O.G., Yang, M., Kopidakis, N., Zhu. K., & Rumbles, G. Grain-size-limited mobility in methylammonium lead iodide perovskite thin films. *ACS Energy Lett.* **1,** 561-565 (2016).

161. Zhou, Y., & Gray-Weale, A. A numerical model for charge transport and energy conversion of perovskite solar cells. *Phys. Chem. Chem. Phys.* **18**, 4476-4486 (2016).

162. O'Kane, S., *et al.* Measurement and modelling of dark current decay transients in perovskite solar cells. *J. Mater. Chem. C* **5,** 452-462 (2017).

163. Courtier, N.E., Richardson, G., & Foster, J.M. A fast and robust numerical scheme for solving models of charge carrier transport and ion vacancy motion in perovskite solar cells. *Appl. Math. Model.* **63**, 329-348 (2018).

164. Courtier, N., Cave, J., Foster, J., Walker, A., & Richardson, G. How transport layer properties affect perovskite solar cell performance: insights from a coupled charge transport/ion migration model. *Energy Environ. Sci.* **12,** 396-409 (2019).

Chapter 2

$MAPbI_3$ Thin Film Processing and Device Fabrication

Summary

Processing high-quality perovskite thin films is the main step for producing highly efficient perovskite optoelectronic devices. In this chapter the experimental techniques applied for producing $MAPbI_3$ thin films are explained. The fabrication and optimization procedure of $MAPbI_3$ capacitors, electron-only, and hole-only devices using high quality $MAPbI_3$ thin films are described. Ultimately, it is explained how to utilize high quality $MAPbI_3$ thin films and efficient charge extraction layers to produce high efficiency perovskite solar cells.

2.1. $MAPbI_3$ thin film processing

In order to fabricate a decent lead halide perovskite solar cell, the first step is to produce a high-quality perovskite film. In this context, high quality film stands for a homogeneous, compact, and pinhole free thin film, which leads to desirable optoelectronic properties. During the last decade, many efforts have been made to achieve this goal[1-20]. A variety of techniques have been introduced, from low temperature solution processing techniques to vapor deposition techniques[1-20]. Each perovskite thin film processing method has several advantages and disadvantages. In case of thermal evaporation in high vacuum, once the evaporation conditions are optimized, perovskite thin films with high quality and reproducibility can be obtained. However, the evaporation techniques require vacuum facilities which increases the ultimate production costs. On the other hand, solution processing methods are to some extent difficult to optimize. However, after optimization, solution processing techniques are relatively inexpensive and easier than their evaporation-based counterparts[1].

Solution processing techniques for producing perovskite thin films can also be categorized in two main categories, known as single step[5, 8, 10-12, 15-17, 19] and double step[3, 4, 6, 9, 15-17, 19] techniques. In the two- step lead halide seeded method[3, 4, 6, 9, 17], at first lead halide (PbI_2) solution is spin coated on a substrate and a thin layer of lead halide will be formed. It has to be noted that the lead halide layer can be also deposited by vapor deposition. In the second step, the deposited lead halide film has to be exposed to methylammonium iodide or formamidinium iodide (MAI or FAI) by spin coating or dip coating. Consequently, the perovskite compound will be formed. The film is required to be annealed for full crystallization[6].

In single step spin coating, a mixed solution of lead halide and MAI (FAI) will be spin coated on the substrate and the perovskite will form[1, 8, 12, 15, 16, 19, 20]. The film should be annealed for crystallization. However, producing a high quality and pinhole free film with large crystallites is not as straightforward as described here. In fact, in the majority of the cases the thin films produced by the aforementioned methods suffer from the existence of pinholes and poor crystal formation. Therefore, further modifications have to be done to obtain a perovskite film with desirable quality[1, 15-17, 19, 20]. So far, numerous modification techniques have been reported to improve the perovskite film quality[2, 10, 12, 15-17, 19, 20]. Among them, anti-solvent washing[1, 15, 17, 21], vacuum-flash assisted solution processing[19, 22], hot casting[5], and gas (or vapor) treatment[4, 9, 23] are among the successful and common modification methods.

In this thesis, single step spin coating was utilized to produce high quality solution processed $MAPbI_3$ thin films. Depending on the precursors, different approaches were applied for preparing the $MAPbI_3$ solution and processing the thin films. Here, lead iodide (PbI_2)[15, 16] and lead acetate trihydrate ($Pb(CH_3CO_2)_2 \cdot 3H_2O$ or $PbAc_2$)[11, 12, 15, 16] were used as two different sources of lead and methylammonium iodide (MAI) was utilized as the source of methyalammonium. In the following, the methods based on both PbI_2, as the most commonly used lead source, and $PbAc_2$ will be discussed in detail.

It has to be noted that for all the experiments that are described in this thesis, all the substrates were cleaned via a standard procedure prior to the experiment. For all the experiments, the entire cleaning process was accomplished in a clean room. The cleaning was carried out by rubbing the substrate in soap-water and consecutive sonication in soap-water, di-ionized water, Acetone, and Isopropanol. The substrates were dried with nitrogen flow and heated at 100 ºC for ten minutes. In all the experiments, the substrate surface was activated by UV-Ozone treatment

prior to spin coating of the solutions. The substrates were transferred to a nitrogen filled glovebox. The entire procedure of $MAPbI_3$ thin films processing, including weighing the precursors, preparing the solution, spin coating, and annealing, as well as the device fabrication procedure and electrical characterizations were accomplished in a nitrogen filled glovebox.

2.1.1. PbI_2-based $MAPbI_3$ thin films

In order to prepare $MAPbI_3$ thin films using a PbI_2 precursor, a mixed solution of 1.3 M PbI_2 and 1.3 M MAI with molar ratio of 1:1 in dimethylformamid (DMF) and dimethylsulfoxide (DMSO) with volume ratio of 4:1 was prepared. The solution was prepared in a nitrogen filled glovebox and stirred at room temperature for 2.5 hours, which was subsequently filtered using a 0.45 micron PTFE filter. Several approaches were used for spin coating the $MAPbI_3$ solution and modifying the spin coated thin films, which will be explained in the following.

Vacuum-Flash Assisted Solution Processing (VASP) method: the VASP method has been introduced for preparing decent mixed-cation mixed-halide perovskite thin films[22]. Therefore, this method was examined to improve the quality of our $MAPbI_3$ thin films. For this purpose, the $MAPbI_3$ solution was spin coated on a glass substrate. Immediately, after spin coating the sample was transferred to a vacuum chamber and kept under vacuum for 30 s. This action facilitates the removal of the residual solvent, which assists the crystallization of the thin films. The samples were annealed at 100 ^{o}C for 90 minutes. Figure 2.2 shows the SEM images of the thin films prepared with the VASP method. Although various parameters such as vacuum time and spin coating speeds were examined to improve the quality of the films, it can be observed that the films are inhomogeneous with large pinholes.

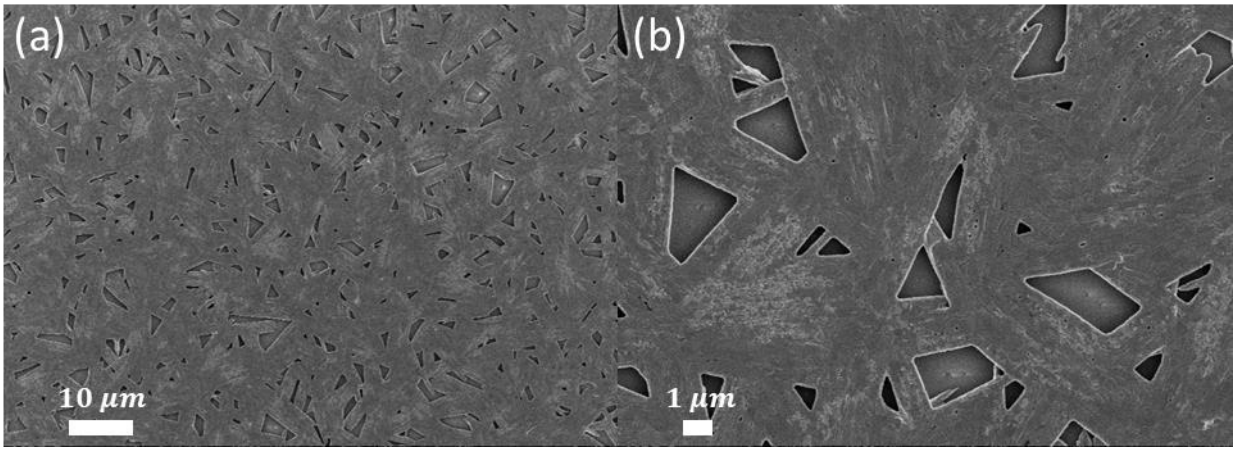

Figure 2.1. Scanning electron microscopy images of $MAPbI_3$ thin films fabricated using the hot-casting technique. Large pin holes are observable all over the thin film between large crystallites.

Hot-Casting: Hot casting has been introduced as a potential method for producing decent perovskite films with different material compositions[5]. This method was applied for producing $MAPbI_3$ thin films. For this purpose, the solution was heated at 70 ºC and the substrate was kept at 100 ºC. The heated solution was spin coated on the hot substrate and quickly the color of sample changed to dark brown. To make sure of full crystallization the samples were annealed at 100 ºC for 30 minutes. The SEM images of the samples are displayed in Figure 2.1, which clearly shows

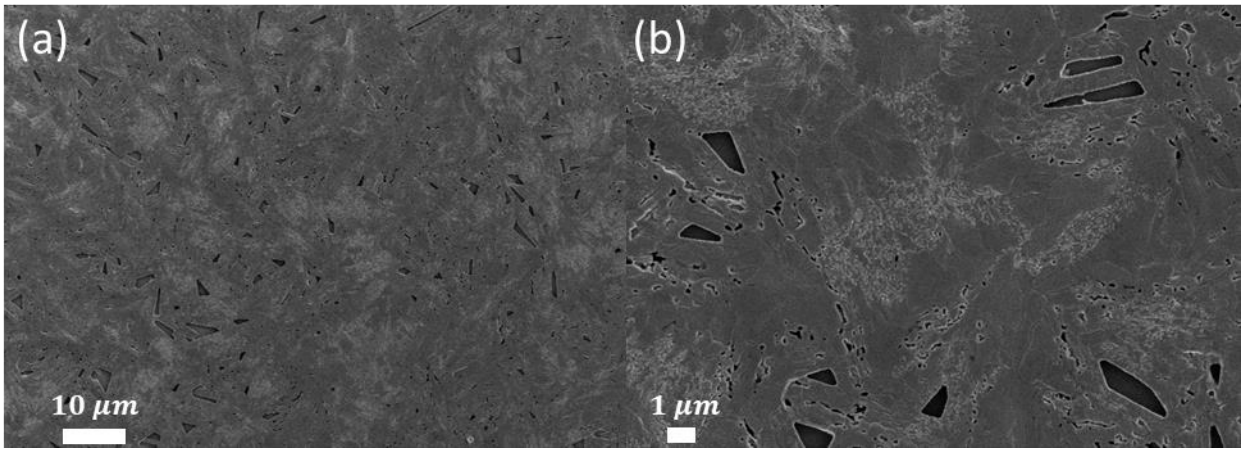

Figure 2.2. Scanning electron microscopy images of $MAPbI_3$ thin films fabricated via the VASP method. Large pin holes are observable throughout the thin film.

the poor quality of $MAPbI_3$ films with pin holes. All the attempts on examining different parameters for improving the poor quality of the films were not successful.

Double step spin-coating with anti-solvent washing: It has been shown that using an anti-solvent facilitates the rapid crystallization of mixed-cation mixed-halide perovskites[1, 9, 17, 21]. Here, this method was used to improve the quality of $MAPbI_3$ thin films. Therefore, the $MAPbI_3$ solution was spin coated at the spinning speed of 2000 rpm for 10 s and subsequently the spinning speed was increased to 6000 rpm. A few seconds after starting the second step of spin coating, 150 µL of chlorobenzene, as a common anti-solvent, was dropped on the spinning sample. It has to be noted that the timing for depositing the anti-solvent is of great importance for obtaining highly crystalline films. The $MAPbI_3$ films were annealed at 100 ºC for 90 minutes. Figure 2.3 shows the SEM images of $MAPbI_3$ thin films fabricated by the Anti-solvent Washing method. As can be observed using ant-solvent (chlorobenzene) treatment of $MAPbI_3$ thin films leads to compact, pinhole free, homogeneous, and highly crystalline thin films.

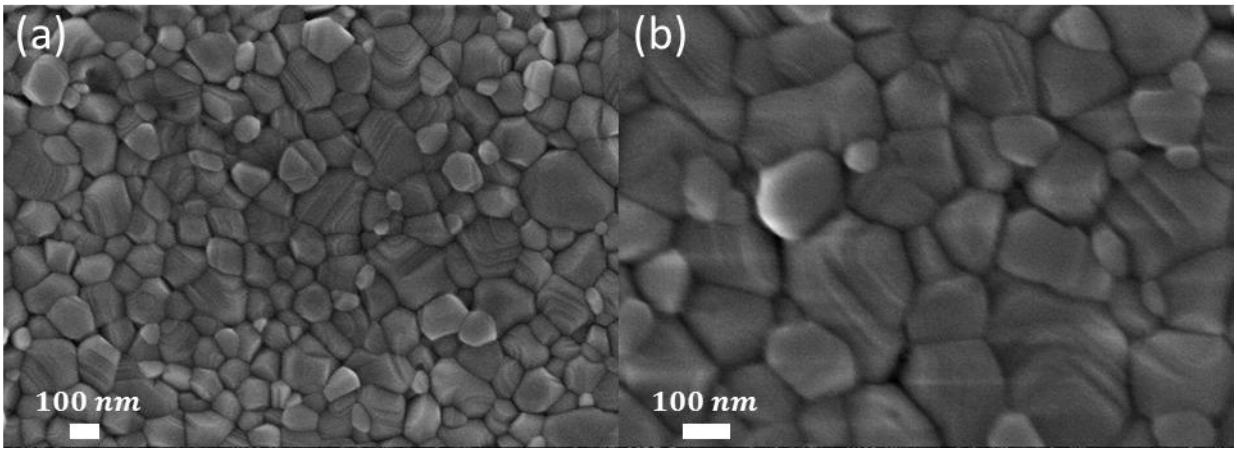

Figure 2.3. Scanning electron microscopy (SEM) image of $MAPbI_3$ thin film formed by double step spin-coating. The $MAPbI_3$ is homogeneous and free of pin holes

Despite the high quality of the $MAPbI_3$ thin films produced with the Anti-solvent Washing method, this method is to some extent suffering from a lack of reproducibility. As was mentioned previously, the main reason is the timing of the anti-solvent deposition, which is very critical to be accurate.

2.1.2. $PbAc_2$-based $MAPbI_3$ thin films

As explained above, in all the previous methods, a PbI_2 precursor was used as the lead source. Another method that has been successfully applied for processing mixed halide methylammonium ($MAPbI_xCl_{1-x}$) based perovskites, utilizes $PbAc_2$ as an alternative precursor[11-16]. In order to produce $MAPbI_3$ thin films with this method, a 30 wt.% mixed solution of $PbAc_2$ and MAI in DMF with molar ratio of 3:1 was prepared. The solution was filtered with a 0.45 µm PTFE filter. The yellow colored $MAPbI_3$ solution was spin coated at different spin coating speeds. The samples were annealed for 30 minutes to crystallize the $MAPbI_3$ thin films. Shiny $MAPbI_3$ thin films with dark brown color were achieved. Figure 2.4 displays the SEM images of the

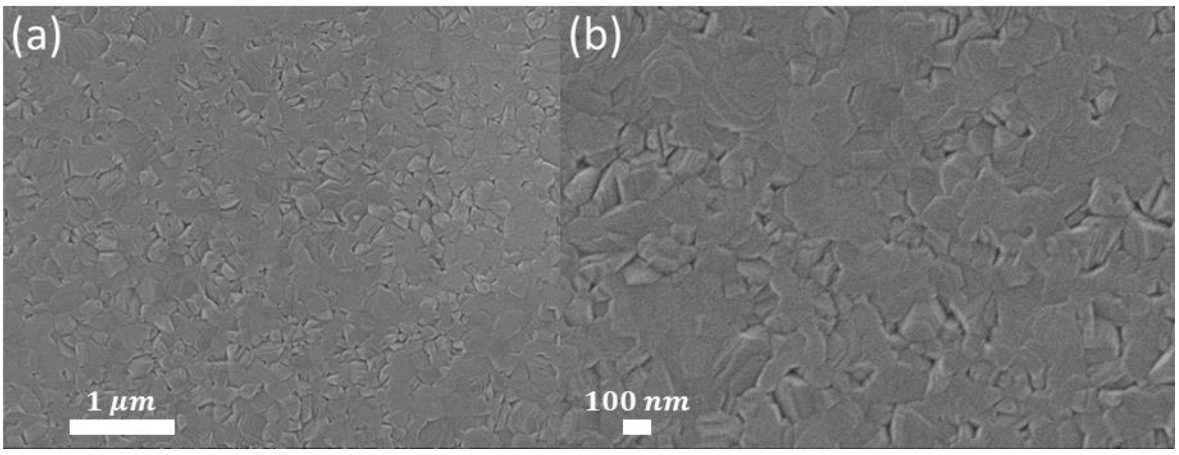

Figure 2.4. Scanning electron microscopy (SEM) image of $MAPbI_3$ thin film produced by Lead Acetate based method.

$MAPbI_3$ thin films produced using a lead acetate precursor. As can be observed, the $MAPbI_3$ thin films are highly homogeneous, compact and free of pin holes. These features are critical for perovskite thin films in order to achieve excellent optoelectronic properties of lead halide perovskites and also for fabricating decent perovskite solar cells. The absence of pinholes is of critical importance to fabricate perovskite capacitors and devices without or with ultrathin organic interlayers. The main advantage of the lead acetate based method is that the obtained $MAPbI_3$ thin films are highly reproducible. The reproducibility of $MAPbI_3$ thin films is critical for comparing the performance of different devices. Another key advantage of this method is that it is a single step spin coating technique and it requires no post modification.

2.2. $MAPbI_3$ parallel-plate capacitor

One of the most beneficial devices for studying the basic electronic-ionic properties of perovskites is a parallel-plate capacitor (see Figure 2.5). In this thesis metal (M)/$MAPbI_3$/metal (M) parallel plate capacitors were fabricated to explore different physical properties of $MAPbI_3$, including ferroelectricity, ionic properties, and dielectric characteristics. In order to fabricate $MAPbI_3$ capacitors, 1 nm of chromium (Cr) was thermally deposited on cleaned glass substrates to increase the adhesion of the gold (Au) electrode to the glass. Subsequently, a 50 nm layer of Au

Figure 2.5. Schematic of a M/$MAPbI_3$/M parallel plate capacitor.

was deposited on the Cr coated glass substrate as a bottom electrode. For the depositing the bottom electrode, a shadow mask with a special pattern was used, which in the end gives 4 individual devices on a single substrate. The substrates then were transferred to a nitrogen filled glovebox for depositing the $MAPbI_3$ layer. The $MAPbI_3$ solution was prepared by mixing $PbAc_2$ and MAI in DMF with a molar ratio of 3:1 and a concentration of 30 wt.%. The $MAPbI_3$ solution was spin coated on the Au covered substrate and subsequently annealed at 100 ºC for 30 minutes. The samples were kept under nitrogen atmosphere and using a specially designed and sealed container transferred to another glovebox for the top electrode deposition. The $MAPbI_3$ parallel plate capacitor was finished by depositing a 50 nm thick layer of Au as the top electrode. The prepared devices were transferred to the measurement glovebox for performing different electrical characterizations. Different measurements, such as electric displacement measurements, impedance spectroscopy, and current-voltage measurements were performed on $MAPbI_3$ capacitors to study the intrinsic electronic-ionic properties of $MAPbI_3$ which will be discussed in details in the following chapters.

2.3. Single-carrier devices

In order to experimentally study charge transport in $MAPbI_3$ perovskite thin films, one of the best approaches is to isolate electron and hole transport from each other to be able to individually investigate their transport in the material. For this purpose, single-carrier devices are the best candidate, which need to be specifically designed and fabricated. As can be recognized from the name, a single-carrier device is a type of device in which the majority of the carriers that participate in transport are from one type of carriers, namely either holes or electrons. In other words, in an electron-only device the majority of the carriers are electrons, whereas in a hole-only

device holes are the majority and the transport is majority carrier dominated. In order to ensure unipolarity in single-carrier devices, specially designed device configurations are required, in which only one type of carriers is injected and the opposite type is to a desirable extent blocked by utilizing an injection barrier. In this way, the electron and hole transport mechanism and properties of the material can be individually explored. Optimization of electron and hole transport in the device is highly beneficial to achieve highly efficient solar cells. In the following sections of this chapter, fabrication and optimization of $MAPbI_3$ electron-only and hole-only devices will be presented in details.

2.3.1. $MAPbI_3$ electron-only devices

Ideally, a $MAPbI_3$ electron-only device is a device in which electrons can be decently injected into the $MAPbI_3$ layer from the contacts and conduction is carried out by electrons as the majority carriers. This implies that the electron injection barrier between the contacts and $MAPbI_3$ has to be minimized to achieve excellent electron injection. In such a device, the electron injection rate has to be much higher than the rate of hole injection from the opposite electrode. In order to achieve these goals, the energy level alignment of the $MAPbI_3$ layer and the injecting contacts plays a critical role. In fact, to achieve efficient electron injection into the $MAPbI_3$ layer an ohmic junction between the $MAPbI_3$ and the contact is desirable. Such ohmic junction for efficient electron injection can be achieved when the conduction band of the perovskite layer is well aligned with the fermi level (E_f) of the conductive contacts or the conduction band of the semiconductor interlayer (see Figure 2.6). To ensure that hole injection is minimized, the counter electrode needs to exhibit a large barrier for hole injection, also requiring an electrode with a low work function. Therefore, in order fabricate decent $MAPbI_3$ electron-only devices choice of the contacts with

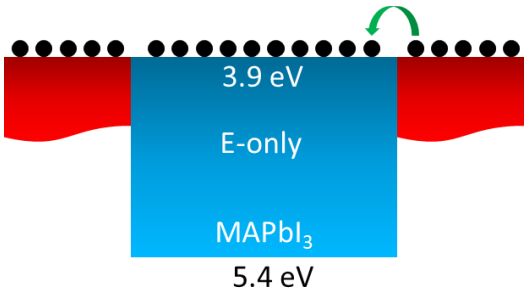

Figure 2.6. Schematic of a $MAPbI_3$ electron-only device. The schematic exhibits that for efficient electron injection the E_f (E_c) of the conductive (semiconductor) injecting contact has to be close the E_c of $MAPbI_3$ (-3.9 eV).

proper energy levels is of great importance. Another critical factor for fabricating $MAPbI_3$ electro-only device is material compatibility of the contacts and also the possible interlayers with $MAPbI_3$. Especially when it comes to solution processing, despite the energy level compatibility there are several difficulties for processing some of the materials underneath or on top of the $MAPbI_3$ layer.

In order to fabricate decent electron-only devices, a variety of device configurations and various electron transport layers, interlayers, and conductive contacts were examined in this thesis. In the following, a highlight of the electron-only device fabrication and optimization will be described.

As already mentioned, in order to fabricate $MAPbI_3$ electron-only devices, efficient electron injecting layers, interlayers or contacts are required. The first step is to find materials with energy levels matching $MAPbI_3$ layer. $MAPbI_3$ perovskite is a semiconductor with the conduction (E_C) and valence (E_V) level of -3.9 eV and -5.4 eV, respectively. Therefore, for efficient electron injection, semiconductors with E_C close that of $MAPbI_3$ ($E_C \sim -3.9\ eV$) are required. One of the best candidates for this purpose is titanium oxide (TiO_2) which has been widely used as electron transport layer in solar cells. TiO_2 is an n-type semiconductor with a band gap of $E_g \sim 3.2\ eV$ and

$E_c \sim -4\ eV$. Another suitable candidate is the fullerene derivative "phenyl-C61-butyric acid methyl ester" (PCBM), which has been widely used in OPVs and PSCs as a decent electron transport material. The highest occupied molecular orbital (HOMO) and the lowest unoccupied molecular orbital (LUMO) level of PCBM are almost similar to the conduction and valence band of TiO_2, respectively.

As a first attempt, a device configuration of Al/TiO_2/$MAPbI_3$/PCBM/Al was used to fabricate electron-only devices, as schematically presented in Figure 2.7a. As can be seen in this configuration the $MAPbI_3$ layer is sandwiched between two electron transport layers, namely TiO_2 and PCBM. For fabricating the device, 100 nm of Aluminum (Al) was thermally deposited on cleaned glass substrates as the conductive bottom electrode. It has to be noted that Al is a suitable electron injection contact due to its low work function. For Al deposition, a special shadow mask was used which gives four devices on a single glass substrate. Subsequently, a layer of TiO_2 was spin coated on an Al bottom electrode as the bottom electron injection layer. The titanium solution was prepared in ambient air by mixing titanium isopropoxide, ethanol, and acetic acid and stirred for 90 minutes. The solution was filtered by a 0.2 μm filter and spin coated on glass/Al samples. The Al/TiO_2 samples were annealed to crystallize the TiO_2 layer and evaporating the residual solvent. Various annealing conditions were examined for annealing the TiO_2 films to optimize the device performance. According to our experiments the best results were obtained from high temperature annealing of TiO_2 layer at 500 °C. For such a high temperature annealing a special furnace was used and temperature was gradually increased in several steps and finally the samples were heated at 500 °C for 30 minutes. After cooling, the Al/TiO_2 samples were transferred to a nitrogen filled glove box for $MAPbI_3$ deposition. A 30 wt% solution of $MAPbI_3$ was prepared by

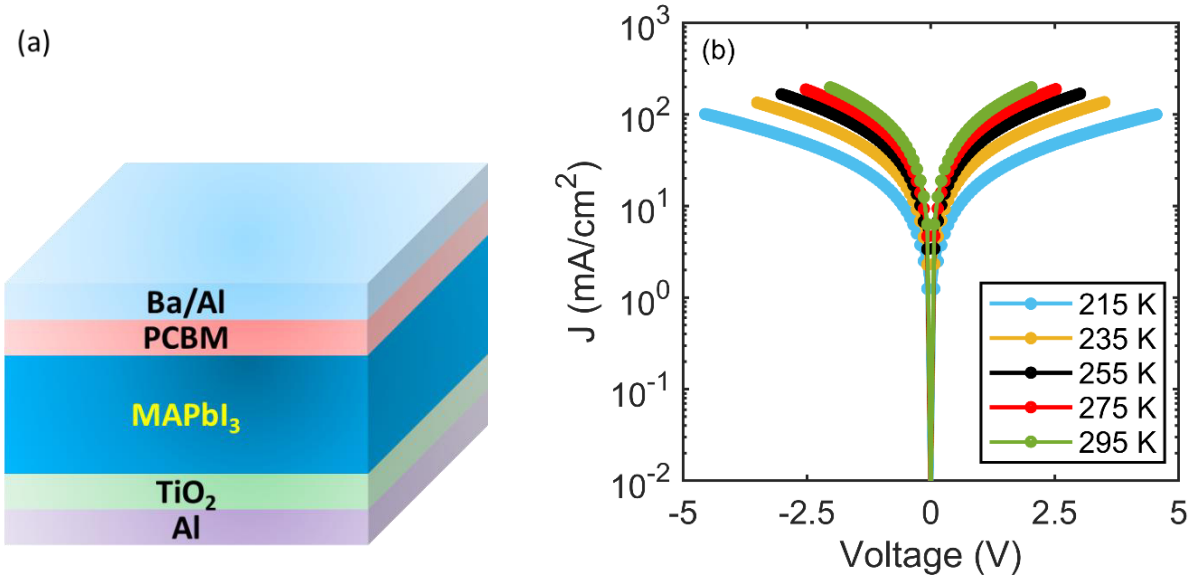

Figure 2.7. (**a**) Device layout and (**b**) temperature dependent electron current of Al/TiO_2/$MAPbI_3$/PCBM /Ba/Al electron-only device.

mixing MAI and $PbAc_2$ with the molar ratio of 3:1 in DMF. The solution was stirred for 15 minutes and the filtered by a 0.2 µm PTFE filter. The $MAPbI_3$ solution was spin coated on the TiO_2 coated samples (Al/TiO_2) and the Al/TiO_2/$MAPbI_3$ samples were annealed at 100 °C for 30 minutes.

In order to achieve a desirable electron injection from top side, PCBM was used as the top electron transport layer. 20 mg of PCBM was dissolved in 1 ml of chlorobenzene and the solution was stirred for 5 hours. The PCBM solution was filtered with a 0.45 µm filter and spin coated on Al/TiO_2/$MAPbI_3$ samples. Subsequently, the Al/TiO_2(20nm)/$MAPbI_3$(200nm)/ PCBM(35nm) samples were annealed at 100 °C for 10 minutes. The electron-only device fabrication was completed by evaporating 5 nm of barium (Ba) and 100 nm of Al as the conductive top electron injection electrode.

As already mentioned, various annealing conditions for TiO_2 were tried to optimize the electron-only device. Our results showed that the highest electron current can be only achieved

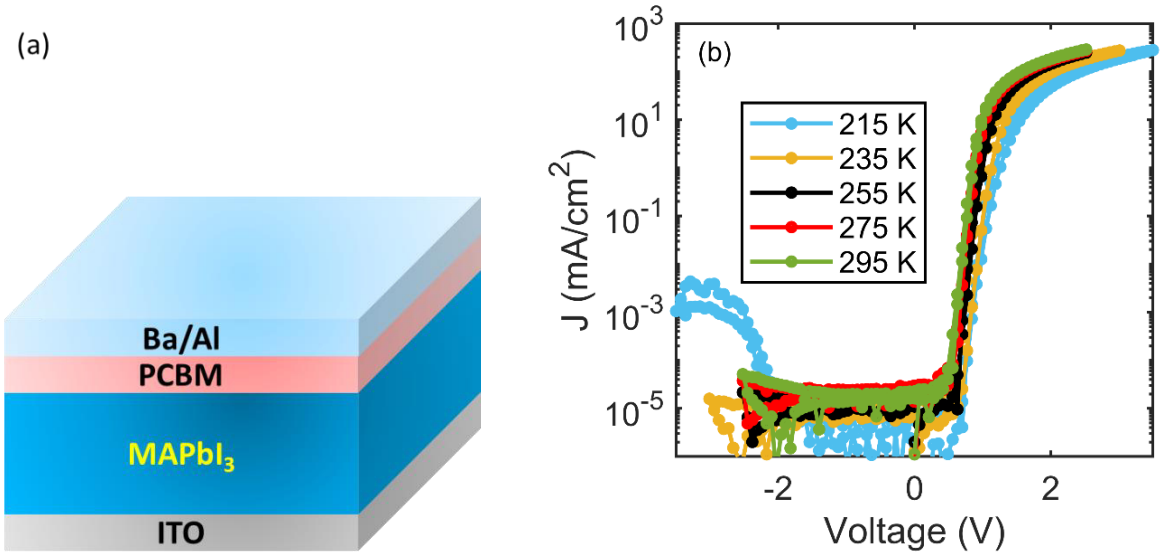

Figure 2.8. (**a**) Device layout and (**b**) electron current in ITO/$MAPbI_3$/PCBM/Ba/Al device at various temperatures.

when TiO_2 is annealed at high temperature of 500 °C. In Figure 2.7, the *J-V* characteristic of Al/TiO_2/$MAPbI_3$/PCBM/Ba/Al electron-only device is exhibited at various temperatures. It can be seen that the *J-V* characteristics are symmetric, meaning the electron injection rate from both side of $MAPbI_3$ (TiO_2 and PCBM) is approximately equal. In addition, in the temperature range of 215 K to 295 K the current is meaningfully temperature dependent and the electron current increases by increasing temperature. Furthermore, no hysteresis can be observed in the *J-V* characteristics in the whole range of temperature from 295 K to 215 K.

However due to the existence of the two electron transport layers, namely PCBM and TiO_2, the magnitude of the measured electron current might be affected by these surrounding layers. Additionally, due to the presence of these surrounding layers, the origin of the temperature dependence of electron current cannot be concluded. Therefore, to exclude any influence of the TiO_2 electron-transport layer on the magnitude and the temperature dependence of the measured

electron current, further experiments were carried out and alternative device layouts were examined.

In the next attempt for investigating the electron transport of $MAPbI_3$, the bottom electron transport layer (TiO_2) was eliminated from the device stack. Additionally, due to the incompatibility of Al with $MAPbI_3$, in the new configuration of the electron-only device the bottom electrode was replaced by ITO.

To fabricate the device, $MAPbI_3$ solution was spin coated on ITO-coated, cleaned substrates. After annealing, a layer of PCBM was spin coated on ITO/ $MAPbI_3$ samples. The solution preparation and film processing of both $MAPbI_3$ and PCBM was similar to the previous experiment. The device stack was completed by depositing 5 nm of Ba and 100 nm of aluminum on ITO/ $MAPbI_3$/PCBM as the top electrode.

The *J-V* characteristics of the ITO/$MAPbI_3$/PCBM/Ba/Al electron-only device is presented in Figure 2.8. In contrast to the previous device, here the *J-V* is asymmetric, as expected due to the higher work function of ITO compared to AL/TiO_2 stack. The difference in work function of the bottom and top contact results in a built-in potential which can be observed in *J-V* characteristics. Upon increasing the applied voltage beyond the built-in voltage, a rapid rise of the current can be seen. Moreover, here the temperature dependence is less pronounced as compared to the Al/TiO_2/$MAPbI_3$/PCBM/Ba/Al devices. Furthermore, as opposed to the Al/TiO_2/$MAPbI_3$/PCBM/Ba/Al electron-only device, the *J-V* characteristics of the ITO/$MAPbI_3$/PCBM/Ba/Al are hysteretic.

As expected, the electron current in the reverse bias is negligible. However, due to the fact that ITO is often used as a hole injector in organic electronic, the question rises whether the measured current is a pure electron current or not. In order to verify the nature of the measured

current, the electroluminescence of the ITO/ $MAPbI_3$/PCBM/Ba/Al electron-only device was measured. The luminescence of the device is compared with that of a solar cell (Figure 2.9), which has an additional polytriarylamine (PTAA) hole-injection and transport layer. It can be clearly seen that the device shows a very negligible light output, which confirms that current is electron dominated in the ITO/$MAPbI_3$/PCBM/Ba/Al device.

To explore the influence of the PCBM layer on the *J-V* characteristics of the ITO/$MAPbI_3$/PCBM/Ba/Al device, additional experiments were performed. For this purpose, ITO/$MAPbI_3$/PCBM/Ba/Al electron-only devices were fabricated and the thickness of the PCBM film was varied from 40 nm to 75 nm. The J-V characteristics of the devices are provided in Figure 2.10. For all the samples with three different thicknesses of PCBM, the *J-V* curves are approximately on top of each other. For the temperature dependence of the electron current exhibits a similar trend, even at lower temperatures. This observation suggests that the current in

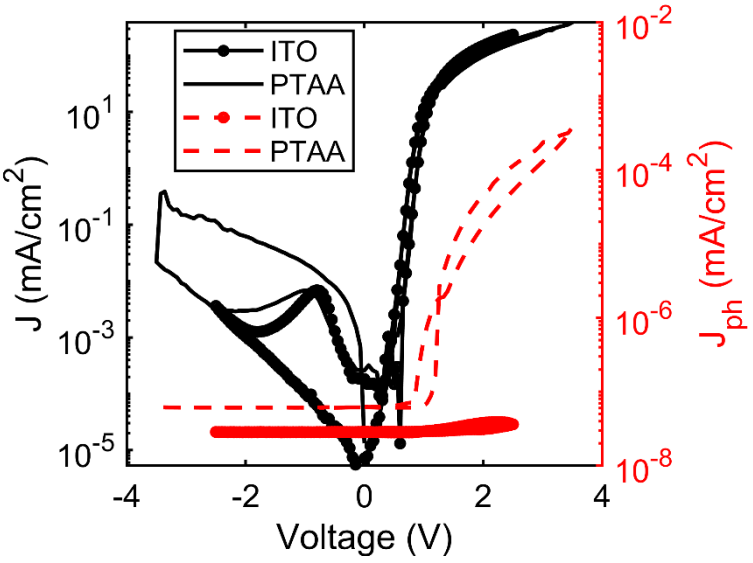

Figure 2.9. Current density-voltage (black, left axis) and photocurrent density-voltage (red, right axis) as measured by a silicon photodiode placed on top of the ITO/$MAPbI_3$/PCBM/Ba/Al and ITO/PTAA /$MAPbI_3$/PCBM/Ba/Al devices.

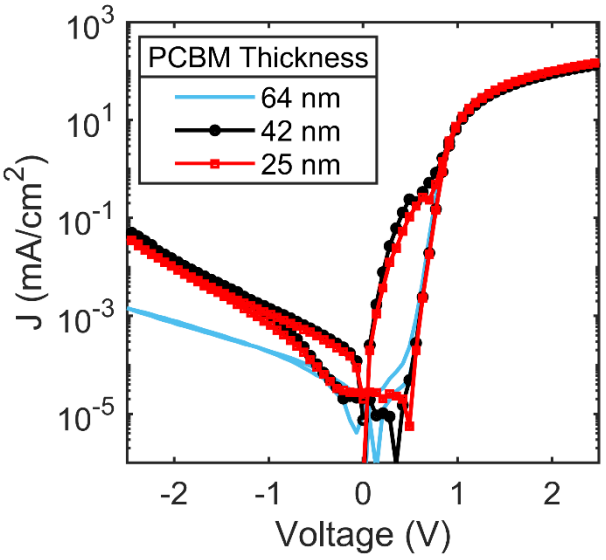

Figure 2.10. Current density voltage of ITO/$MAPbI_3$/PCBM/Ba/Al device for three different thickness of PCBM layer.

our ITO/$MAPbI_3$/PCBM/Ba/Al electron only device is not limited by PCBM layer. In other words, it suggests that the electron current in ITO/$MAPbI_3$/PCBM/Ba/Al device is either limited by the conductive contacts or by the $MAPbI_3$ layer.

In order to clarify the effect of contacts on the measured electron current, the bottom electrode in ITO/$MAPbI_3$/PCBM/Ba/Al device stack, namely ITO, was replaced by the more conductive silver (Ag). For this purpose, 2 nm of Cr followed by 50 nm of Ag were thermally deposited on glass substrates. The $MAPbI_3$ and PCBM layer were processed and deposited with the previously described conditions. The top contact was a 100 nm film of aluminum. Figure 2.11 shows the *J-V* characteristics of the device at various temperatures. The observed current densities are now substantially higher, implying that the resistance of ITO limited the current. The clear temperature dependence of the current suggests that the current is no longer limited by the resistance of the electrodes when ITO is replaced by silver. However, the PCBM layer may now be the limiting factor in the observed current.

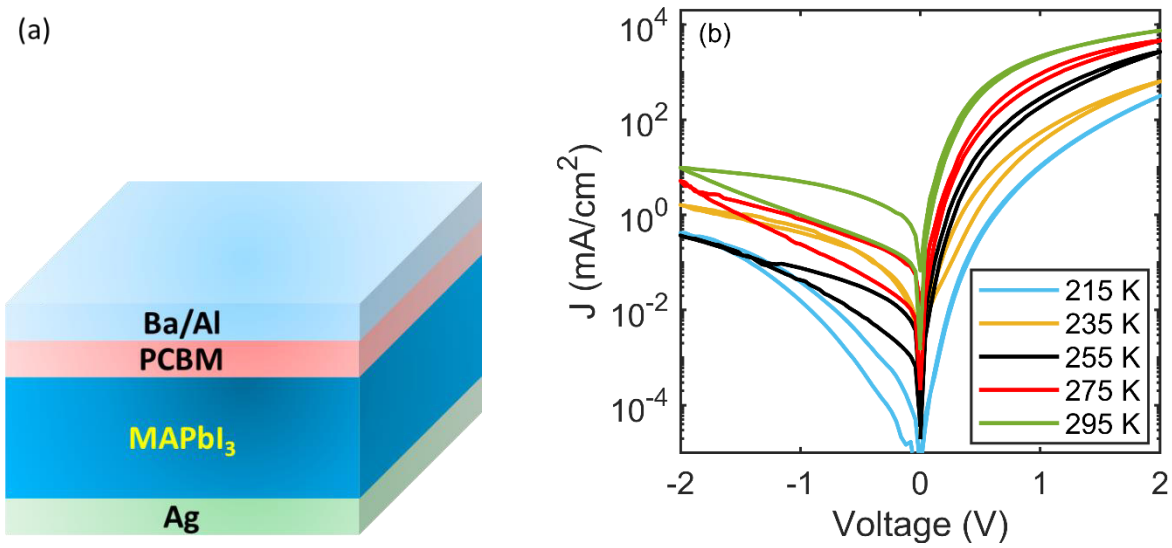

Figure 2.11. (**a**) Device layout and (**b**) electron current density voltage of Ag/$MAPbI_3$/PCBM/Ba/Al electron-only device.

In order to exclude the effect of PCBM layer from the measured electron current of $MAPbI_3$, the PCBM layer was eliminated from the device stack. For this purpose, a thin film of $MAPbI_3$ was deposited on an Ag coated glass substrate. For efficient electron injection 5 nm of C_{60} and 5 nm of TPBi were evaporated on Ag/$MAPbI_3$ samples. The LUMO of C_{60} aligns well with $MAPbI_3$ and the minimal thickness of the C_{60} layer ensures minimal resistance. A TPBi tunneling interlayer is used to create an ohmic electron contact between aluminum and C_{60}.The device was completed by thermal deposition of 100 nm of Al as the top electrode. The temperature-dependent *J-V* characteristics of the device are presented in Figure 2.12. Higher currents are observed as compared to the device with a PCBM electron-transport layer, indicating that the PCBM-based devices were limited by electron transport through the PCBM layer.

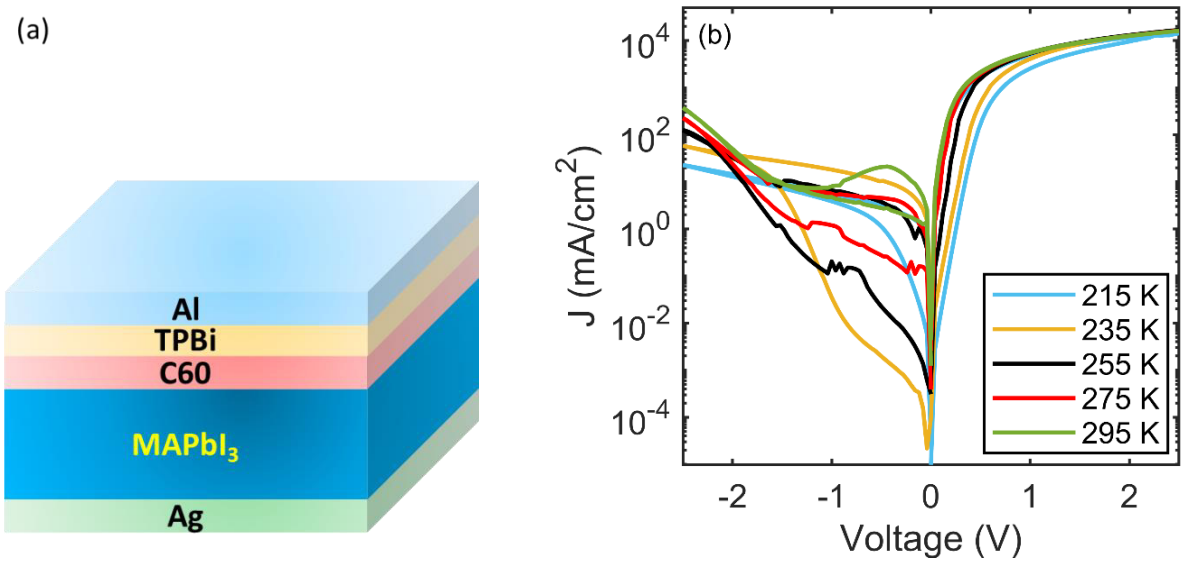

Figure 2.12. (**a**) Device configuration and (**b**) electron current-voltage of Ag/$MAPbI_3$/C60/TPBi/Al at different temperatures.

2.3.2. $MAPbI_3$ hole-only devices

A $MAPbI_3$ hole-only device in the ideal case is a device in which holes are injected into the $MAPbI_3$ layer from the contacts and conduction is carried out by holes as the majority carriers. This implies that the hole injection rate has to be sufficiently higher than the electron injection from the opposite electrode. Similar to the case of electron-only devices, to fabricate efficient hole-only devices the energy level alignment of the layer and the hole injecting contacts play a critical

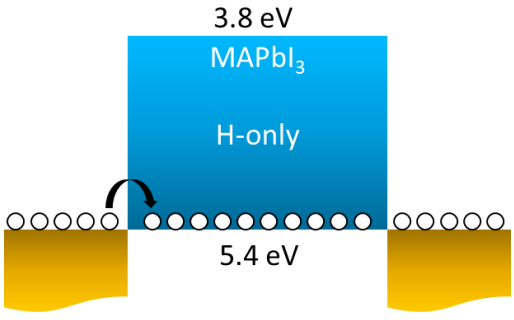

Figure 2.13. Schematic of a $MAPbI_3$ hole-only device.

role. For efficient hole injection into the $MAPbI_3$ layer ohmic junction between the $MAPbI_3$ and the contact is desirable. This can be achieved when the valence band of the perovskite layer is well aligned with the fermi level (E_f) of the conductive contacts or the valence band of the semiconductor interlayer (see Figure 2.13). Therefore, the choice of the contacts with proper energy levels is of great importance for fabricating efficient $MAPbI_3$ hole-only devices. Material compatibility of the contacts and the interlayers with $MAPbI_3$ is another critical factor for fabricating $MAPbI_3$ hole-only devices.

In this thesis, a variety of device configurations and various hole transport layers, interlayers, and conductive contacts were examined for fabricating decent hole-only devices. In the following a highlight of the hole-only device fabrication and optimization will be described.

One of the most popular hole transport materials in the field of perovskite solar cells is PTAA. Here, PTAA was used for producing hole-only devices. For this purpose, a solution of PTAA in toluene was prepared and spin coated on ITO coated glass substrates. The film was

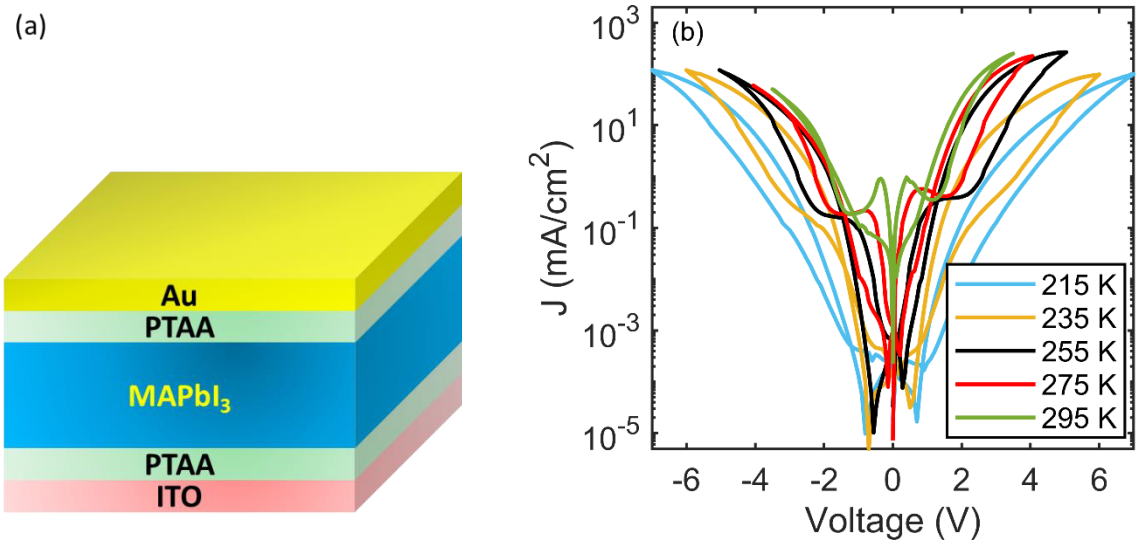

Figure 2.14. (**a**) Device layout and (**b**) temperature dependence of hole current-voltage ITO/PTAA/$MAPbI_3$ /PTAA/Au hole-only device.

annealed at 100 °C for 5 minutes. The $MAPbI_3$ solution was prepared with the lead acetate based method and processed on ITO/PTAA samples. The second layer of PTAA was spin coated on ITO/PTAA/$MAPbI_3$ and annealed at 100 °°C for 5 minutes. The device was completed by evaporating 50 nm of Au on ITO/PTAA/$MAPbI_3$/PTAA. All the steps were accomplished in a nitrogen filled Glovebox. The device stack and the *J-V* characteristics of the ITO/PTAA/$MAPbI_3$/PTAA/Au hole-only device are provided in Figure 2.14. The hole current shows a considerable hysteresis and clear temperature dependence. Due to the strong hysteresis, the analysis of the hole current is not trivial.

In order to understand the operation of the hole-only device, the top PTAA layer was eliminated. The ITO/PTAA/$MAPbI_3$/Au hole only device was prepared using the similar protocol as the ITO/PTAA/$MAPbI_3$/PTAA/Au device. The device layout and the *J-V* of this hole-only device are displayed in Figure 2.15. As can be seen, the *J-V* characteristics now show some level of asymmetry, a lower level of hysteresis, and hysteresis with a different shape than in the

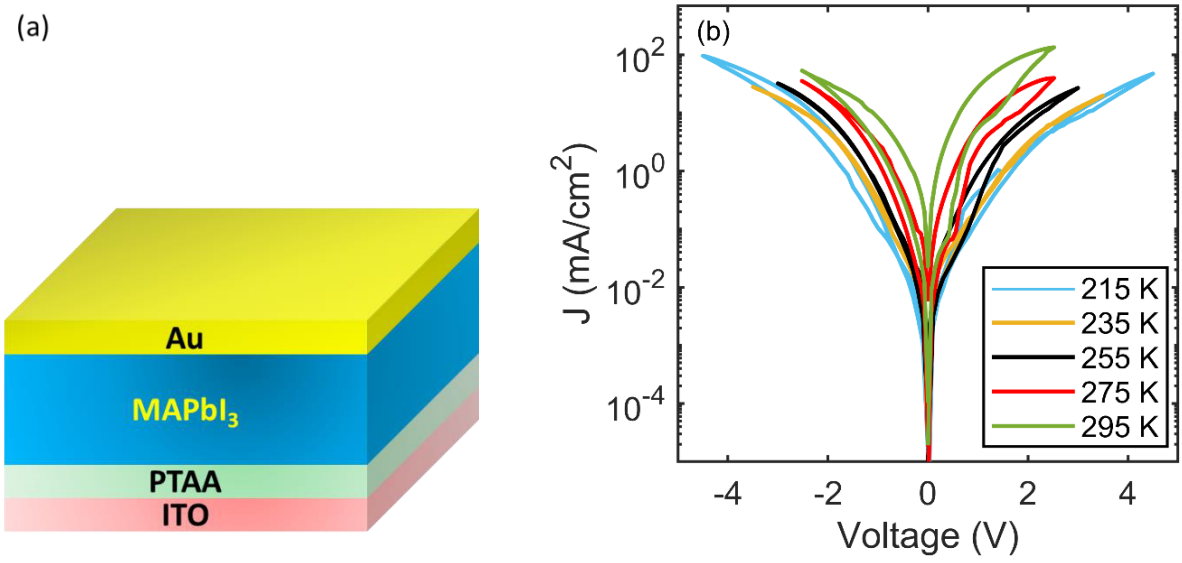

Figure 2.15. (**a**) Device structure and (**b**) temperature dependent hole current in ITO/PTAA/$MAPbI_3$/Au hole-only device.

ITO/PTAA/$MAPbI_3$/PTAA/Au device. This shows that the top PTAA layer highly impacts the hole current.

In the next step the bottom PTAA layer was replaced by a layer of PEDOT:PSS, which is a commonly used hole transport material in organic electronics. The PEDOT:PSS was spin coated on ITO and annealed at 140 °C for 10 minutes. The $MAPbI_3$ layer and Au electrode were deposited as described previously. The device configuration and the hole current-voltage of ITO/PEDOT:PSS/$MAPbI_3$/Au is displayed in Figure 2.16. Positive bias corresponds to hole injection from the PEDOT:PSS electrode, negative bias to hole injection from the Au top electrode. As can be seen, the *J-V* characteristics are hysteretic and temperature dependent. In addition, the hole current from the Au electrode seems to be higher than the hole injection from the PEDOT:PSS.

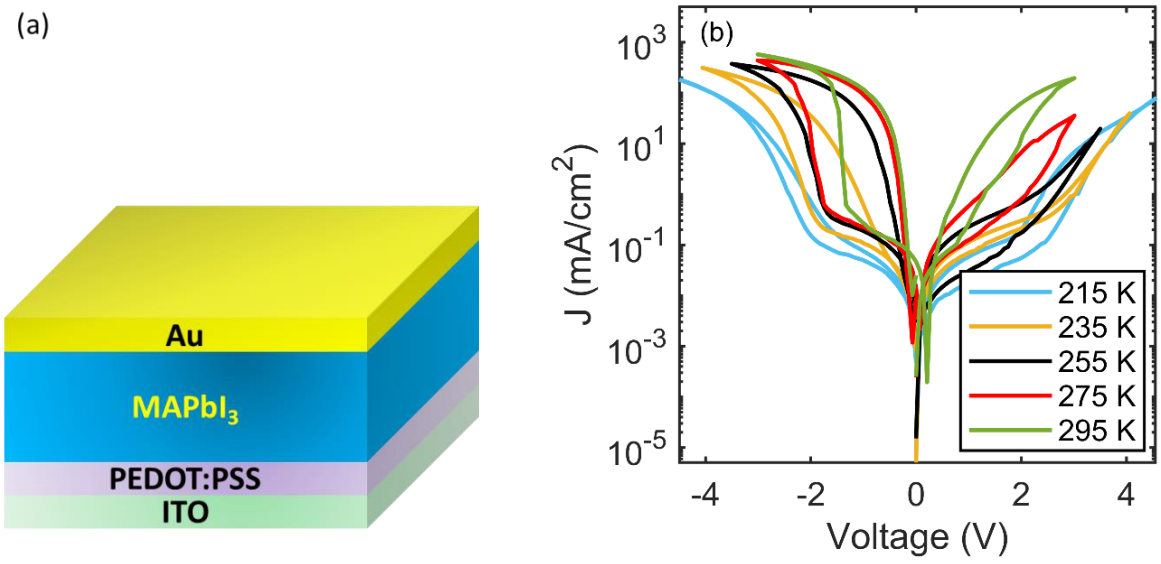

Figure 2.16. **(a)** Device structure and **(b)** temperature dependence of hole current in ITO/PEDOT:PSS/ $MAPbI_3$/Au hole-only device.

To verify the efficient hole injection from the Au electrode, the PEDOT:PSS layer was eliminated from the device layout and hole-only device with the configuration of ITO/$MAPbI_3$/Au were fabricated (Figure 2.17a). The processing of the $MAPbI_3$ layer and Au electrode was as described before. The temperature dependent *J-V* characteristics of this device are presented in Figure 2.17b. Similar to the previous device configurations, the hole current is hysteretic and temperature dependent. Additionally, similar to the ITO/PEDOT:PSS/$MAPbI_3$/Au sample, the ITO/$MAPbI_3$/Au device also confirms that the hole injection rate from the gold electrode is higher than the injection rate from ITO.

As the Au electrode showed the best hole injection rate into $MAPbI_3$, hole-only devices with a configuration of Au/$MAPbI_3$/Au were fabricated (see Figure 2.18a). The bottom electrode was prepared by depositing 2 nm of Cr followed by 50 nm of Au. The $MAPbI_3$ thin film and top Au electrode were processed as described before. Figure 2.18b presents the current-voltage characteristics of an Au/$MAPbI_3$/Au hole-only device. In contrast to previous hole-only devices

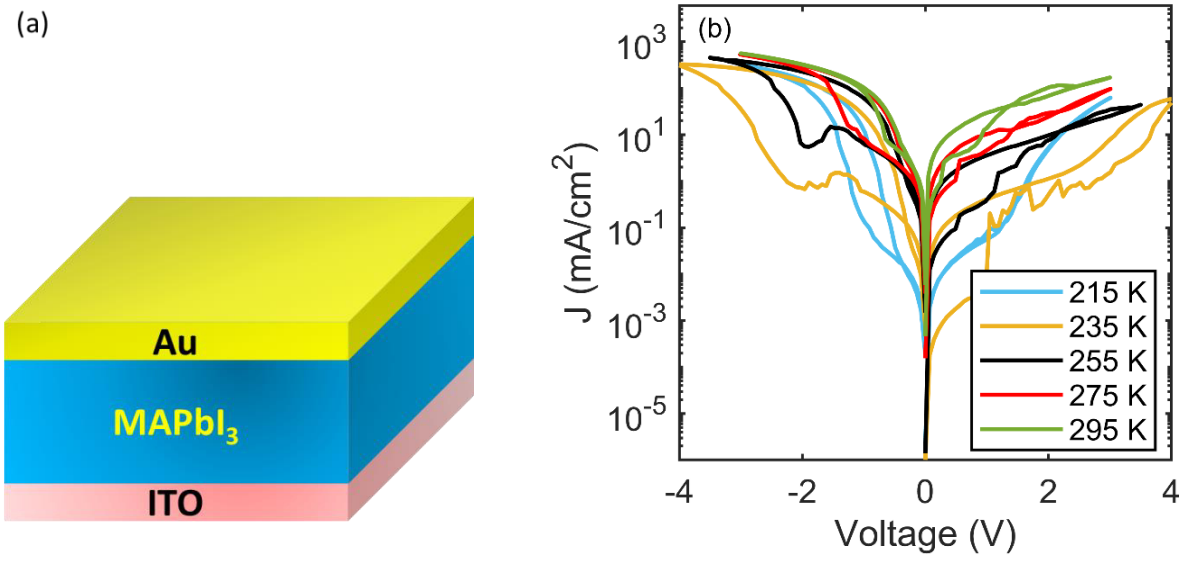

Figure 2.17. (**a**) Device layout and (**b**) temperature dependent hole current-voltage in ITO/$MAPbI_3$/Au hole-only device.

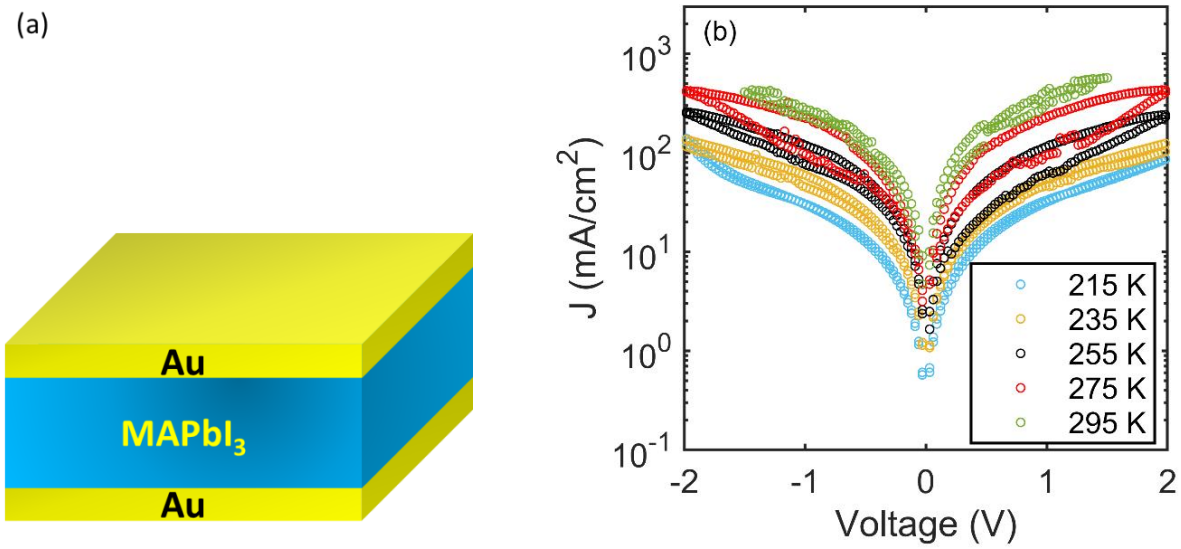

Figure 2.18. (**a**) Device configuration and (**b**) hole current-voltage of Au/$MAPbI_3$/Au hole-only device.

the hole current in Au/$MAPbI_3$/Au is symmetric with lower hysteresis. It can be seen that the hysteresis in hole current is temperature dependent. At room temperature and low temperatures the hysteresis is negligible and it reaches its maximum at an intermediate temperature of 275 K. Detailed analysis of the hole current will be presented in the following chapters.

A comparison of the hole current in different hole-only devices is presented in Figure 2.19. It can be observed that the hole current of Glass/Au/$MAPbI_3$/Au device is higher than all the other devices. In other words, among all the examined hole injectors, including PTAA, PEDOT:PSS and ITO, Au shows the best hole injection performance.

2.4. $MAPbI_3$ solar cells

One of the key points for fabricating efficient solar cells is to select proper electron and hole blocking layers to minimize the power loss. To achieve efficient electron and hole blocking properties, the energy level alignment of the electron and hole transport layers with respect to the

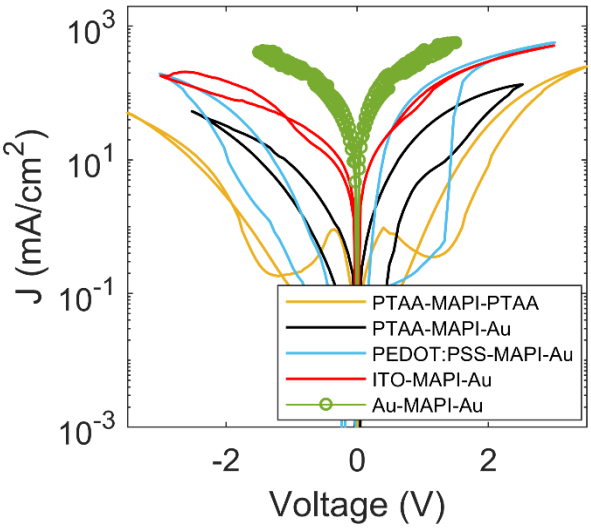

Figure 2.19. Comparison of the hole current into $MAPbI_3$ from various hole injectors. The hole current in Au/$MAPbI_3$/Au device is larger than the other investigated hole-only device layouts.

absorption layer, namely the perovskite layer, is of great importance. Figure 2.20 presents a schematic depiction of a perovskite solar cell, in which the required energy levels of the electron and hole transport layers are provided. As is shown in the Figure 2.20, the incident photon is absorbed by the perovskite layer and generates an electron and hole pair or exciton. The exciton dissociates into individual electron and holes. The separated electrons and holes move towards the electron and hole transport layers. Considering the energy levels, the electrons transfer from the conduction band of $MAPbI_3$ to the electron transport layer, which has a lower conduction edge. At the same interface, the holes are blocked due to the low valence band of the electron transport layer with respect to that of $MAPbI_3$. On the other hand, the holes are extracted from the hole transport layer. At the same interface, the electrons are blocked due to the high conduction band of hole transport layer respect to the $MAPbI_3$ layer. In this way, the electrons and holes are efficiently extracted at the corresponding transport layers and they are blocked at the opposite transport layer.

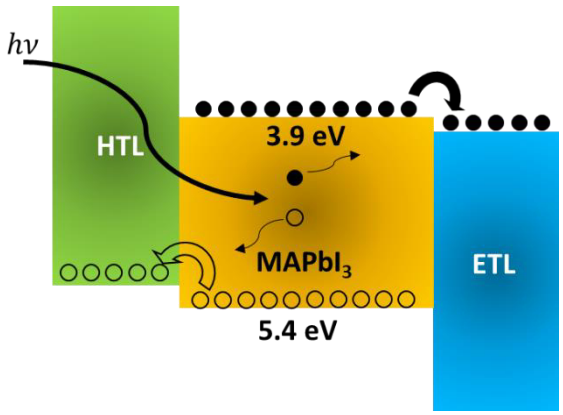

Figure 2.20. Schematic of a $MAPbI_3$ solar cell which indicates the alignment of the energy levels of ETL and HTL with respect to the conduction and valence band of $MAPbI_3$.

After optimizing the $MAPbI_3$ thin films and optimizing the electron-only and hole-only devices, the next step was to produce highly efficient $MAPbI_3$ solar cells. Our focus for solar cell fabrication is on low temperature solution processing. Therefore, the electron and hole transport materials that require high temperature processing, such as TiO_2, are not applicable for low temperature processing. The device configuration that we used is known as the inverted planar structure, in which the cell is illuminated from the hole collection side.

Based on the electron-only devices, the best candidates for efficient electron-only device were PCBM/Ba/Al and C60/TPBi/Al. Therefore, these layouts are considered for solar cell fabrication. Although the best candidate for hole only device was Au, it does not provide optical transparency and electron blocking. Therefore, hole transport layers such as PTAA and PEDOT:PSS that were examined for hole only devices were used for solar cell fabrication.

To fabricate $MAPbI_3$ solar cells, a layer of PEDOT:PSS was spin coated on ITO in a clean room and annealed at 140 °C for 10 minutes. The samples were transferred to a nitrogen filled glovebox for depositing the perovskite layer. The $MAPbI_3$ layer was deposited and processed on ITO/PEDOT:PSS samples with the previously described recipe. The PCBM solution was prepared

by dissolving 20 mg of PCBM in 1 ml chlorobenzene. The solution was stirred overnight at 55 °C and finally filtered by a PTFE filter. A thin layer of PCBM was formed on ITO/PEDOT:PSS/$MAPbI_3$ stack by spin coating the PCBM solution. The samples were annealed at 100 °C for 10 mins. The device was completed by evaporating 5 nm of Ba and 100 nm of Al.

Figure 2.21 displays the *J-V* characteristics of the ITO/PEDOT:PSS/$MAPbI_3$/PCBM /Ba/Al solar cell in dark conditions and under 1 sun illumination. The device shows a desirable short circuit current density of $J_{SC} = 20.4\ \frac{mA}{cm^2}$, a low open-circuit voltage of $V_{OC} = 0.7\ V$, a high fill factor of $FF = 75.6\%$, and a relatively low power conversion efficiency of $PCE = 10.8\ \%$. Additionally, no hysteresis can be observed in the current-voltage characteristics of the device. However, as can be seen the device suffers from low V_{OC} which results in low PCE. This is consistent with the observation of a barrier at the PEDOT:PSS hole contact in the hole-only devices. Additionally, as PEDOT:PSS is a highly doped conducting polymer, it does not provide electron blocking.

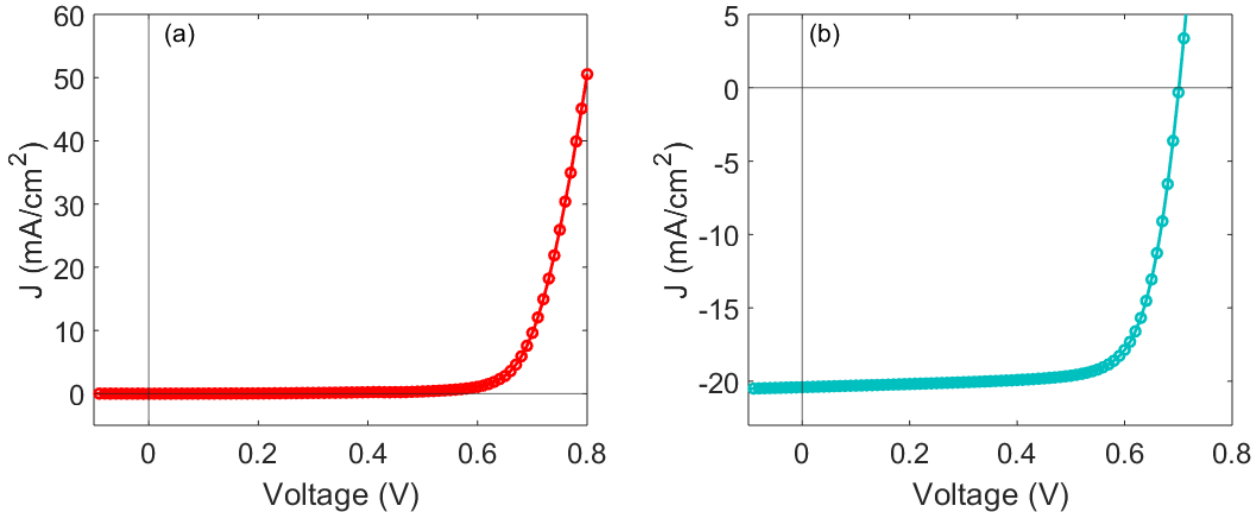

Figure 2.21. Dark (**a**) and under illumination (**b**) *J-V* characteristics of $MAPbI_3$ solar cell with the device configuration of ITO/PEDOT:PSS/$MAPbI_3$/PCBM/Ba/Al.

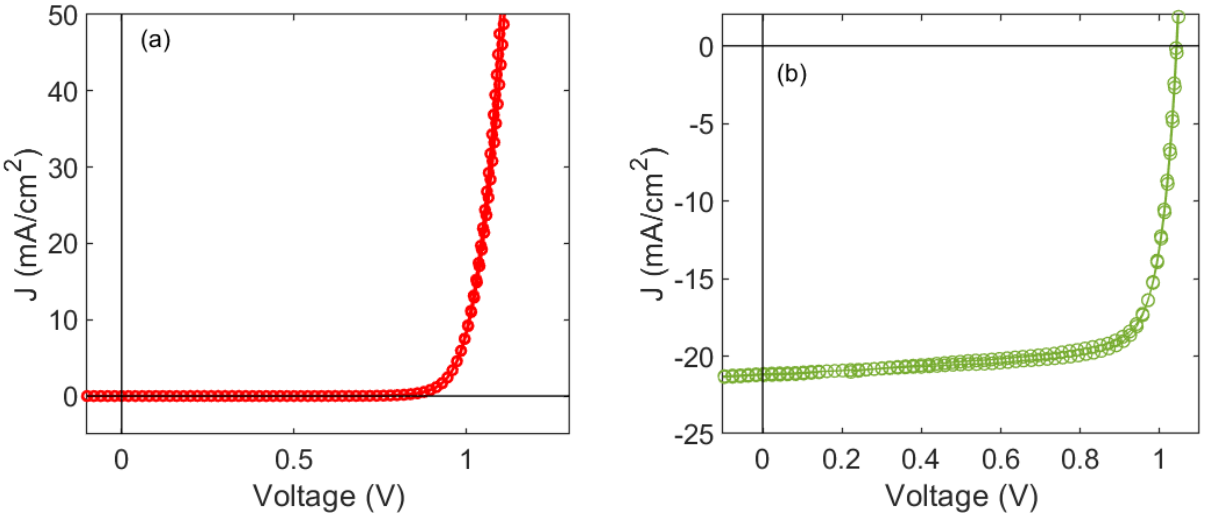

Figure 2.22. Dark (**a**) and under illumination (**b**) J-V characteristics of $MAPbI_3$ solar cell with the device configuration of ITO/PTAA/$MAPbI_3$/C60/TPBi/Al.

In order to improve the performance of the $MAPbI_3$ solar cells, the PEDOT:PSS hole transport layer was replaced by a 10 nm thin film of PTAA, which provides electron blocking functionality. The PTAA solution and thin film was prepared as described in the hole-only section. The $MAPbI_3$ layer thin film processing was similar to the previous samples. As electron extraction layer, 5 nm of C_{60} and 5 nm TPBi were respectively deposited on ITO/PTAA/$MAPbI_3$ samples by thermal evaporation. The device was completed by depositing 100 nm of Al as the top electrode. The *J-V* characteristics of the device under 1 Sun illumination is presented in Figure 2.22. The device exhibits decent performance with output characteristics of $J_{SC} = 21.3\ \frac{mA}{cm^2}$, $V_{OC} = 1.04\ V$, $FF = 78\%$, and $PCE = 17.3\ \%$. Compared to the device with a PEDOT:PSS layer, utilization of a PTAA hole-transport layer raises the open-circuit voltage substantially.

2.5. References

1. Jeon, N.J., *et al*. Solvent engineering for high-performance inorganic–organic hybrid perovskite solar cells. *Nature Mater* **13**, 897-903 (2014).

2. Kim, J., *et al.* Solvent and intermediate phase as boosters for the perovskite transformation and solar cell performance. *Sci Rep* **6,** 25648 (2016).

3. Li, D.*, et al.* Size-dependent phase transition in methylammonium lead iodide perovskite microplate crystals. *Nat Commun* **7**, 1-8 (2016).

4. El-Henawey, M., Gebhardt, R.S., El-Tonsy, M., & Chaudhary, S. Organic solvent vapor treatment of lead iodide layers in the two-step sequential deposition of $CH_3NH_3PbI_3$-based perovskite solar cells. *J. Mater. Chem. A* **4**, 1947-1952 (2016).

5. Nie, W.*, et al.* High-efficiency solution-processed perovskite solar cells with millimeter-scale grains. *Science* **347**, 522-525 (2015).

6. Xiao, Z.*, et al.* Efficient, high yield perovskite photovoltaic devices grown by interdiffusion of solution-processed precursor stacking layers. *Energy Environ. Sci.* **7**, 2619-2623 (2014).

7. Tavakoli, M.M.*, et al.* Fabrication of efficient planar perovskite solar cells using a one-step chemical vapor deposition method. *Sci. Rep* **5,** 14083 (2015).

8. Noel, N.K., *et al.* A low viscosity, low boiling point, clean solvent system for the rapid crystallisation of highly specular perovskite films. *Energy Environ. Sci.* **10**, 145-152 (2017).

9. Shi, D., *et al.* Low trap-state density and long carrier diffusion in organolead trihalide perovskite single crystals. *Science* **347,** 519-522 (2015).

10. Wang, JT-W., *et al.* Efficient perovskite solar cells by metal ion doping. *Energy Environ. Sci.* **9**, 2892-2901 (2016).

11. Zhang, W., *et al.* Ultrasmooth organic–inorganic perovskite thin-film formation and crystallization for efficient planar heterojunction solar cells. *Nat Commun* **6**, 1-10 (2015).

12. Zhang, W.*, et al.* Enhanced optoelectronic quality of perovskite thin films with hypophosphorous acid for planar heterojunction solar cells. *Nat Commun* **6**, 1-9 (2015).

13. Qiu, W.*, et al.* Pinhole-free perovskite films for efficient solar modules. *Energy Environ. Sci.* **9**, 484-489 (2016).

14. Aldibaja, F.K., *et al*. Effect of different lead precursors on perovskite solar cell performance and stability. *J. Mater. Chem. A* **3**, 9194-9200 (2015).

15. Ashurov, N.*, et al.* Current state and perspectives for organo-halide perovskite solar cells. Part 1. Crystal structures and thin film formation, morphology, processing, degradation, stability improvement by carbon nanotubes. A review. *Mod. Electron. Mater.* **3**, 1-25 (2017).

16. Bing, J., Huang, S., & Ho-Baillie, A.W. A Review on Halide Perovskite Film Formation by Sequential Solution Processing for Solar Cell Applications. *Energy Technol.* **8**, 1901114 (2020).

17. Sharenko, A., & Toney, M.F. Relationships between lead halide perovskite thin-film fabrication, morphology, and performance in solar cells. *J. Am. Chem. Soc.* **138**, 463-470 (2016).

18. Palazon, F.*, et al.* Room-temperature cubic phase crystallization and high stability of vacuum-deposited methylammonium lead triiodide thin films for high-efficiency solar cells. *Adv. Mater.* **31**, 1902692 (2019).

19. Chen, Y., Zhang, L., Zhang, Y., Gao, H., & Yan, H. Large-area perovskite solar cells–a review of recent progress and issues. *RSC Adv.* **8**, 10489-10508 (2018).

20. Tai, Q., Tang, K-C., & Yan, F. Recent progress of inorganic perovskite solar cells. *Energy Environ. Sci.* **12**, 2375-2405 (2019).

21. Bi, D.*, et al.* Efficient luminescent solar cells based on tailored mixed-cation perovskites. *Sci Adv* **2**, e1501170 (2016).

22. Li, X., *et al.* A vacuum flash–assisted solution process for high-efficiency large-area perovskite solar cells. *Science* **353**, (2016).

23. Zhang, M-J.*, et al.* Carrier transport improvement of $CH_3NH_3PbI_3$ film by methylamine gas treatment. *ACS Appl. Mater. Interfaces*, **8**, 31413-31418 (2016).

Chapter 3

Device Model for Mixed Electronic-Ionic Systems*

Summary

Lead halide perovskites are known as mixed electronic-ionic semiconductors. Coexistence of electronic and ionic charges complicates the understanding of the perovskite devices. To facilitate the comprehension of the device physics of perovskite devices, realistic numerical device models are required. To this end, a numerical drift-diffusion device model has been developed for perovskites. The device model includes the contribution of electronic and ionic charges. The model can be utilized for exploring the device physics of mixed electronic-ionic systems.

*Publication: Sajedi Alvar, M., Blom, P. W. M., & Wetzelaer, G.-J. A. H., *Adv. Electron. Mater.* 1900935 (2020).

3.1. Introduction

Understanding of the operation mechanism of perovskite solar cells (PSCs) has been hampered by the coexistence of electronic and ionic conduction in lead halide perovskites[1, 2]. The presence of mobile ions and their accumulation at the interfaces has a large effect on the electric-field distribution inside the perovskite layer[3-7], which affects the charge extraction in a solar cell[4, 6]. In addition, knowledge of the electric-field distribution is also vital for quantifying the steady-state charge-carrier mobility. Furthermore, the occurrence of hysteresis in the current-voltage characteristics, which affects the accuracy of the solar-cell efficiency measurement[8-10], has been attributed to slow-moving ions[4, 11-13]. Candidates such as iodine vacancies and methylammonium ions have been proposed as being responsible for ion motion in lead halide perovskites[2, 5]. The hysteresis in the *J-V* characteristics are in accordance with such slow moving positive vacancies[14]. Moreover, ion migration has been introduced as one of the degradation mechanisms of perovskite devices. Therefore, to improve the understanding of the device physics of perovskite solar cells, a numerical device model that includes both the electronic and ionic properties, is indispensable.

Thus, in this chapter a mixed electronic-ionic numerical device model will be introduced and formulated. The finite difference discretization method is used for solving the coupled differential equations. A code has been programmed for solving the drift-diffusion current equations, together with the current-continuity equations and the Poisson equation. The experimental verification and validation of the input parameters will be presented in the following chapters.

3.2. Numerical device model

In order to model the operation and behavior of perovskite capacitors, single-carrier devices, and solar cells, an electronic-ionic model is developed. The device model is based on solving the drift-diffusion equations coupled with Poisson's equation for electronic and ionic charge carriers. Here, the model will be described for a perovskite capacitor, formed by sandwiching a perovskite layer between two metal electrodes. In the configuration of this capacitor, the perovskite is treated as a mixed electronic-ionic conductor. The junction between the perovskite layer and the surrounding electrodes can be of ohmic or Schottky type. The perovskite layer includes a certain density of electron and holes as the intrinsic charge carriers. It is also possible to include doping of the perovskite layer in the model by adding more charges. Additionally, photogenerated charge carriers can be introduced in the perovskite layer by tuning the charge generation rate. Charge carriers can recombine at different rates via different recombination mechanisms. In addition to electrons and holes, the perovskite layer contains a certain density of negative and positive ions. The ions can be mobile or stationary. As it will be discussed in the following chapters, to model the behavior of the perovskite devices in dark conditions only the positive ions are considered as mobile, whereas the negative ionic charges are assumed to be immobile. In this electronic-ionic system, the mobile ionic charges are blocked at the interfaces with the two blocking contacts. In the following chapters the effect of ions in the perovskite layers on operation of the perovskite devices will be explained in detail. Transport of mobile ions, electrons, and holes occurs via diffusion and drift mechanisms. The corresponding equations will be described in the following. The distribution of the potential in the perovskite layer is described by the Poisson's equation.

For ease of computation the perovskite device is approximated as a one-dimensional system. The one-dimensional continuity equations of the system are summarized as follows[11, 15-22]:

$$\frac{\partial n(x,t)}{\partial t} - \frac{1}{q}\frac{\partial j_n}{\partial x} = G - R \tag{3.1}$$

$$\frac{\partial p(x,t)}{\partial t} + \frac{1}{q}\frac{\partial j_p}{\partial x} = G - R \tag{3.2}$$

$$\frac{\partial N(x,t)}{\partial t} - \frac{1}{q}\frac{\partial J_N}{\partial x} = 0 \tag{3.3}$$

$$\frac{\partial P(x,t)}{\partial t} + \frac{1}{q}\frac{\partial J_P}{\partial x} = 0 \tag{3.4}$$

Eqs. (3.1), (3.2), (3.3), and (3.4) represent the continuity equation for electrons, holes, and the negatively charged and positively charged ionic species, respectively. Here, n and p are the electron and hole density, t represents the time, x is the distance with respect to the left-side electrode, q is the elementary charge, j_n and j_p are the electron and hole current density, and G and R the generation and recombination rate, respectively. N, P, J_N, and J_P represent the charge densities and the current densities of the negative and positive ions, respectively.

The current densities of the electronic and ionic charge carriers are described by the following equations:

$$j_n = qD_n\left(\frac{\partial n(x,t)}{\partial x} - \frac{n(x,t)}{k_B T}\frac{\partial \varphi}{\partial x}\right) \tag{3.5}$$

$$j_p = -qD_p\left(\frac{\partial p(x,t)}{\partial x} + \frac{p(x,t)}{k_B T}\frac{\partial \varphi}{\partial x}\right) \tag{3.6}$$

$$J_N = qD_N\left(\frac{\partial N(x,t)}{\partial x} - \frac{N(x,t)}{k_B T}\frac{\partial \varphi}{\partial x}\right) \tag{3.7}$$

$$J_P = -qD_P\left(\frac{\partial P(x,t)}{\partial x} + \frac{P(x,t)}{k_B T}\frac{\partial \varphi}{\partial x}\right) \tag{3.8}$$

where Eqs. (3.5), (3.6), (3.7), and (3.8) represent the current equations for electrons, holes, negatively charged, and positively charged mobile ions, respectively, with their diffusion coefficients denoted as D_n, D_p, D_N, and D_P. Here, k_B is Boltzmann's constant, T is the temperature, and φ is the electrostatic potential.

The electrostatic potential inside the device is described by Poisson's equation:

$$\frac{\partial^2 \varphi}{\partial x^2} = \frac{q}{\varepsilon_r \varepsilon_0}(N - P + n - p) \tag{3.9}$$

with ε_r and ε_0 the relative and vacuum permittivity, respectively.

The charge carrier recombination rate R can be of radiative or non-radiative type. The radiative recombination rate (also known as bimolecular recombination) is described by the following equation

$$R = B_{pre}\left(\frac{q}{\varepsilon_r \varepsilon_0}\right)(\mu_n + \mu_p)(np - n_i^2) \tag{3.10}$$

Here, B_{pre} is the bimolecular recombination perfactor, n_i is the intrinsic charge density, μ_n and μ_p are the electron and hole mobility, respectively. The non-radiative recombination rate (also known as Shockley-Read-Hall (SRH)) for electrons and holes is given by

$$R = \frac{np - n_i^2}{n\tau_p + p\tau_n + k_3} \tag{3.11}$$

With τ_n and τ_p the electron and hole lifetime, respectively. n_i is the intrinsic charge density. Additionally, the generation rate G of electrons and holes is described by the Beer-Lambert law

$$G = G_0 \exp(-\alpha x) \tag{3.12}$$

where α represents the absorption coefficient of the perovskite layer. The equations (3.1) to (3.12) describe the injection, generation, recombination, distribution, and transport of electrons, holes, and mobile ions inside the perovskite layer in the capacitor.

After formulating the perovskite device model, a proper method is required for solving the abovementioned equations. In order to solve this system of coupled equations, a numerical approach has to be applied. To numerically solve the electronic-ionic equations of the perovskite device, the Finite Difference method was used to discretize the space in one dimension. Here, the space is defined as the distance between the left and the right contact. For this purpose, a one-dimensional computational grid with sufficiently small grid point spacing was selected (Figure 3.1). After defining the computational grid, the equations have to be written in finite difference form to be able to solve them at each grid point. As an example, the finite difference form of Poisson's equation for calculating the electric field can be written as

$$\frac{E_{i+1}^k - E_{i-1}^k}{x_{i+1} - x_{i-1}} \approx \frac{q}{\varepsilon\varepsilon_0}\left(P_i^k - N_i^k + p_i^k - n_i^k\right) \tag{3.13}$$

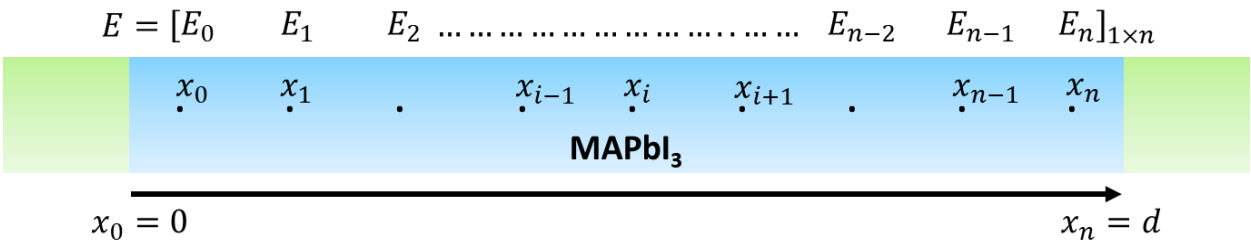

Figure 3.1. One dimensional computational grid for finite discretization of the space.

Where i is representing the grid point index and k is the time index. In this formulation, the variables with indices of i and k are representing the value of the variables at time k and position i. E_{i+1} represents the electric field at the position of x_{i+1} inside the perovskite layer (see Figure 3.1). Using the same approach all the equations ((3.1) to (3.12)) can be written in finite difference form. This enables us to solve the equations on each grid point.

In order to solve the system of equations, proper boundary and initial conditions are required. As can be seen in Figure 3.1, in this one-dimensional system the boundaries are applied at $x_0 = 0$ and $x_n = d$. The electric potential at left and right electrode is set at $\frac{V_b - V}{2}$ and $\frac{V - V_b}{2}$, respectively. Here, V is the applied voltage and $V_b$is the built-in potential. The electrons are injected from the left contact and holes are injected from the right contact. Electron and hole injection from the contacts into the perovskite layer are described by the Boltzmann injection equation:

$$n_0 = N_C . \exp\left(-\frac{q\varphi_n}{kT}\right) \qquad (3.14)$$

$$p_0 = N_V . \exp\left(-\frac{q\varphi_p}{kT}\right) \qquad (3.15)$$

n_0 and p_0 are the electron and hole density at left and right contact, respectively. N_C and N_V are respectively the conduction band and valence band density of states. φ_n and φ_p are the injection

barriers for electrons and holes. Furthermore, due to the assumption of ion blocking contacts the mobile ions cannot leave the perovskite layer, meaning there is no ion flow through the interfaces.

As initial condition it is assumed that all the electronic and ionic charges are uniformly distributed across the perovskite film. Therefore, at the time zero, at every single point in the $MAPbI_3$ layer, the net amount of electric charge is zero. Upon variation of the applied bias, the negative and the positive ionic charges can move toward the contacts and redistribute across the film. By applying a voltage to the device the electrons and holes that are injected from the corresponding contacts move across the perovskite layer. Further details about the device model can be found in the references[7, 11, 15-23].

In this thesis, MATLAB was used for solving the aforementioned system of equations. With the aforementioned boundary and initial conditions, the system of equations can be solved in time and space. The time dependent equations are solved by forward integration in time. Due to the presence of mobile ions and formation of narrow Debye layers at the interfaces, there are rapid spatial variations in the calculated charge and potential profiles. Therefore, the grid point spacing has to be sufficiently small to reach a converged solution. Another key criterion for convergence of the solution is an extremely small time step. However, using a constant small time step dramatically increases the computation costs. Therefore, an adaptive time step was employed to reach a converged solution with low computation cost.

After developing the model and solving the governing equations of the system, the next step is the validation of the model. As explained previously, the output of the model is highly dependent on the inputs. For this purpose, in the following chapters different methods have been utilized to experimentally determine various ionic and electronic properties of the $MAPbI_3$ thin

films in different device configurations. Subsequently, these experimental results are combined with the device simulations to describe the operation of different perovskite devices.

3.3. Conclusion

In conclusion, we have developed a numerical device model for describing the electronic and ionic transport in perovskites as a class of mixed electronic ionic semiconductors. The charge-transport physics of perovskites was described and the device model was formulated. The finite difference method was applied to discretize the space and numerically solve the system of equations. A code was programmed in MATLAB for solving the equations. The experimental results for determining the input parameters and validation of the model will provided in the following chapters.

3.4. References

1. Snaith, H., *et al.* Anomalous hysteresis in perovskite solar cells. *J. Phys. Chem. Lett.* **5,** 1511-1515 (2014).

2. Frost, J., & Walsh, A. What is moving in hybrid halide perovskite solar cells? *Acc. Chem. Res.* **49,** 528-535 (2016).

3. Belisle, R., *et al.* Interpretation of inverted photocurrent transients in organic lead halide perovskite solar cells: proof of the field screening by mobile ions and determination of the space charge layer widths. *Energy Environ. Sci.* **10,** 192-204 (2017).

4. Tress, W., *et al*. Understanding the rate-dependent J–V hysteresis, slow time component, and aging in $CH_3NH_3PbI_3$ perovskite solar cells: the role of a compensated electric field. *Energy Environ. Sci.* **8,** 995-1004 (2015).

5. Eames, C., *et al*. Ionic transport in hybrid lead iodide perovskite solar cells. *Nat Commun* **6,** 7497 (2015).

6. Weber, S., *et al.* How the formation of interfacial charge causes hysteresis in perovskite solar cells. *Energy Environ. Sci.* **11,** 2404-2413 (2018).

7. Calado, P., *et al.* Evidence for ion migration in hybrid perovskite solar cells with minimal hysteresis. *Nat Commun* **7,** 13831 (2016).

8. Kim, H-S. & Park, N-G. Parameters affecting I–V hysteresis of $CH_3NH_3PbI_3$ perovskite solar cells: effects of perovskite crystal size and mesoporous TiO_2 layer. *J. Phys. Chem. Lett.* **5**, 2927-2934 (2014).

9. Chen, B., Yang, M., Priya, S., & Zhu, K. Origin of J–V hysteresis in perovskite solar cells. *J. Phys. Chem. Lett.* **7,** 905-917 (2016).

10. Unger, E.L*., et al.* Hysteresis and transient behavior in current–voltage measurements of hybrid-perovskite absorber solar cells. *Energy Environ. Sci.* **7**, 3690-3698 (2014).

11. van Reenen, S., Kemerink, M., & Snaith, H. Modeling anomalous hysteresis in perovskite solar cells. *J. Phys. Chem. Lett.* **6,** 3808-3814 (2015).

12. Chen, B*., et al.* Impact of capacitive effect and ion migration on the hysteretic behavior of perovskite solar cells. *J. Phys. Chem. Lett.* **6**, 4693-4700 (2015).

13. Haruyama, J., Sodeyama, K., Han, L. & Tateyama, Y. First-principles study of ion diffusion in perovskite solar cell sensitizers. *J. Am. Chem. Soc.* **137**, 10048-10051 (2015).

14. Bertoluzzi, L., *et al*. In Situ Measurement of Electric-Field Screening in Hysteresis-Free PTAA/$FA_{0.83}Cs_{0.17}Pb(I_{0.83}Br_{0.17})_3$/$C_{60}$ Perovskite Solar Cells Gives an Ion Mobility of~ 3×10^{-7} $cm^2/(V\ s)$, 2 Orders of Magnitude Faster than Reported for Metal-Oxide-Contacted Perovskite Cells with Hysteresis. *J. Am. Chem. Soc.* **140**, 12775-12784 (2018).

15. Sze, S.M., Ng K.K. *Physics of semiconductor devices*. John wiley & sons (2006).

16. Sherkar, T.S. & Koster, L.J.A. Can ferroelectric polarization explain the high performance of hybrid halide perovskite solar cells? *Phys. Chem. Chem. Phys.* **18**, 331-338 (2016).

17. Richardson, G., *et al.* Can slow-moving ions explain hysteresis in the current–voltage curves of perovskite solar cells? *Energy Environ. Sci.* **9,** 1476-1485 (2016).

18. O'Kane, S., *et al.* Measurement and modelling of dark current decay transients in perovskite solar cells. *J. Mater. Chem. C* **5,** 452-462 (2017).

19. Sherkar, T.S.*, et al.* Recombination in perovskite solar cells: significance of grain boundaries, interface traps, and defect ions. *ACS Energy Lett.* **2**, 1214-1222 (2017).

20. Sherkar, T.S., Momblona, C., Gil-Escrig, L., Bolink, H.J., & Koster, L.J.A. Improving perovskite solar cells: Insights from a validated device model. *Adv. Energy Mater.* **7**, 1602432 (2017).

21. Courtier, N., Cave, J., Foster, J., Walker, A., & Richardson, G. How transport layer properties affect perovskite solar cell performance: insights from a coupled charge transport/ion migration model. *Energy Environ. Sci.* **12,** 396-409 (2019).

22. Courtier, N.E., Richardson, G., & Foster, J.M. A fast and robust numerical scheme for solving models of charge carrier transport and ion vacancy motion in perovskite solar cells. *Appl. Math. Model.* **63**, 329-348 (2018).

23. Neukom, M., *et al.* Consistent Device Simulation Model Describing Perovskite Solar Cells in Steady-State, Transient and Frequency Domain. *ACS Appl. Mater. Interfaces* **11,** 23320-23328 (2019).

Chapter 4

Absence of Ferroelectricity in $MAPbI_3$ Thin Films*

Summary

Ferroelectricity has been proposed as one of the potential origins of the observed hysteresis in photocurrent-voltage characteristics of perovskite based solar cells. Measurement of ferroelectric properties of lead halide perovskites in a solar-cell configuration is hindered by the presence of (in)organic charge-transport layers. Here, we fabricate metal-perovskite-metal capacitors and unambiguously show that methylammonium lead iodide is not ferroelectric at room temperature. We propose that the hysteresis in electric displacement field originates from the movement of positive ions rather than ferroelectric switching.

*Publication: Sajedi Alvar, M., Kumar, M., Blom, P., Wetzelaer, G., & Asadi, K., *AIP Adv.* **7,** 095110 (2017).

4.1. Introduction

As discussed in chapter 1, despite the great progress in device performance of hybrid organic-inorganic lead halide perovskites, understanding of the device physics is still in the early stages. For instance, observation of a hysteretic behavior in current-voltage (*I-V*) characteristics has been one of the controversial issues around PSCs[1] as the presence of hysteresis hampers arriving at reliable values for the fill factor (*FF*), short-circuit current density (J_{SC}), open-circuit voltage (V_{OC}). Understanding of the origin of the hysteretic *I-V* characteristics in PSCs is therefore crucial to arrive at reliable values for the PCE of the PSCs with hysteretic *I-V*. It has been shown that various parameters such as, applied voltage, sweep rate, polarity [2], bias history [3, 4], light-exposure[3, 4], and even device configuration can affect the hysteresis in the *I-V* characteristics. Several mechanisms have been proposed to explain the hysteretic *I-V* characteristics of PSCs, namely slow transient capacitive current [2, 5, 6], trapping-detrapping of charge carriers at the various interfaces and grain boundaries [7, 8], ion migration [3, 5, 8-11], and finally ferroelectricity of the lead halide perovskite layer[4, 12, 13].

As discussed in chapter 1, there have recently been numerous conflicting reports regarding ferroelectricity in lead halide perovskites [14-17]. The controversy over the ferroelectricity of methylammonium lead iodide ($MAPbI_3$) perovskite layer closely resembles the dispute over the ferroelectricity of bananas[18] and highlights the extra care that should be taken in the interpretation of electrical polarization loops and the claim of ferroelectricity[19]. The prerequisite of ferroelectricity of a compound is that the crystal structure must be non-centrosymmetric hence exhibiting a strong optical second harmonic generation (SHG). It has been recently shown that $MAPbI_3$ does not have a polar crystal structure at room temperature down to 77 K[20]. None polar

centrosymmetric crystal structure implies absence of ferroelectricity. On the other hand there are reports that based on dielectric constant measurements[21], or piezoelectric force microscopy (PFM)[22] claim ferroelectricity in $MAPbI_3$. Typically, a solar cell device layout, wherein the perovskite is sandwiched between a layer of transparent conductive metal-oxide (typically FTO or ITO) and a top metallic contact, is used to probe ferroelectricity of the perovskite layer. Presence of the several non-metallic layers in the device stack complicates interpretation of the electrical measurements due to charge trapping at the interfaces and ion movements to name a few. Reliable tests of ferroelectricity of the perovskite layer carried out with noble metallic contacts such as gold in a metal/perovskite/metal device structure are still missing.

Here, we address the controversial issue related to ferroelectricity in methylammonium lead iodide ($MAPbI_3$) perovskites. In order to disentangle effects from charge carriers trapped at the various interfaces in perovskite solar cells we fabricated parallel-plate capacitors based on Au/$MAPbI_3$/Au. Conventional ferroelectric tests were performed to obtain the displacement loops as a function of electric field (*D-E* loop) at different frequencies. Hysteretic *D-E* loops were only observed at low frequencies and disappeared at frequencies above 100 Hz. Displacement loops of the multi-layer solar cells show similar behavior. We therefore clearly rule out the occurrence of ferroelectricity in $MAPbI_3$ at room temperature as the origin of the hysteretic behavior in PSCs. Instead, we suggest slow dynamic of positive mobile ions as the origin of the observed hysteresis.

4.2. Results and discussion

4.2.1. Device fabrication

$MAPbI_3$ parallel-plate capacitors were fabricated first. A layer of Cr/Au (1 nm/50 nm) was deposited as the bottom contact. A mixture of lead acetate trihydrate ($Pb(Ac)_2$) and methylammonium iodide (MAI) in a 1:3 molar ratio in N,N-dimethylformamide (DMF) was prepared and spin coated on the substrate inside a nitrogen-filled glovebox. The films were annealed at 100 °C for 30 minutes. As a ferroelectric reference test material we used the random copolymer P(VDF-TrFE) (65%–35%), purchased from Solvay. P(VDF-TrFE) thin-films of 750±10 nm were spin coated on glass substrates with Au electrodes (50 nm) and annealed at 140 °C in vacuum. Both types of capacitors were finished by deposition of 50 nm top Au electrodes. The device area of all capacitors was 0.16 mm^2. The solar cells were prepared on ITO-coated glass substrates. The substrates were thoroughly cleaned with soap, water, acetone and isopropanol in clean-room environment. After 20 minutes UV-ozone treatment, a layer of poly(3,4-ethylenedioxythiophene)-poly(styrenesulfonate) (PEDOT:PSS) was spin coated on ITO-coated glass substrates as hole transport layer. Subsequently PEDOT:PSS was annealed at 140 °C for 10 minutes. The perovskite solution was spin coated on to PEDOT:PSS inside the glovebox and then annealed at 100 °C for 30 minutes. To form the electron transport layer, a 20 mg/mL solution of [6,6]-Phenyl C_{61} butyric acid methyl ester (PCBM) (Solenne BV) in chlorobenzene was prepared and spin coated on top of the annealed perovskite films. Finally, a top electrode of Ba(5 nm)/Al(100 nm) was deposited by thermal evaporation. We also fabricated solar cells with the device layout of ITO/PCBM/$MAPbI_3$/Poly-TPD/Au. The PCBM and $MAPbI_3$ layers were prepared with the same method as described above. In this device configuration Poly(4-

butyltriphenylamine) (Poly-TPD) was used as hole transport material. For this purpose, 20 nm of Poly-TPD was spin coated on ITO/PCBM/$MAPbI_3$ and the samples were annealed at 100 °C for 10 minutes. The devices were completed by thermal evaporation of 50 nm of Au as top electrode. All chemicals were used as received.

4.2.2. *D-V* and *J-V* of ferroelectric P(VDF-TrFE) capacitors

A typical counter clockwise hysteretic *D-E* loop of a ferroelectric material, here P(VDF-TrFE), is shown in Figure 4.1a. At high positive bias, P(VDF-TrFE) is fully polarized. As the bias is reduced toward zero, the ferroelectric polarization persists, and at zero bias, the remanent polarization amounts to 64 mC/m^2. As the bias further decreases toward negative values, the polarization slowly goes down and suddenly at 45 MV/m goes through zero and changes the sign. The switching of polarization is associated with a peak in the displacement current, as shown in Figure 4.1b. The negative coercive field and the remanent polarization amounts to -45 MV/m and -64 mC/m^2, respectively. The hysteretic response of P(VDF-TrFE) is consistently observed at different frequencies ranging from 1 Hz to 10 kHz, albeit a slight shift in the coercive field. As the

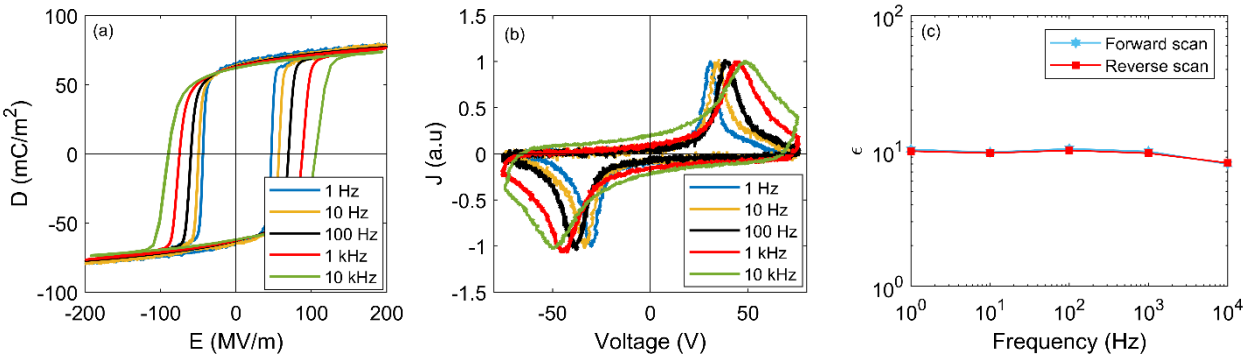

Figure 4.1. (**a**) *D-E* and (**b**) *J-V* loops of a P(VDF-TrFE) ferroelectric capacitor at different frequencies ranging from 1 Hz to 10 kHz. (**c**) Dielectric constant of P(VDF-TrFE) obtained from *D-E* loops as a function of frequency.

field sweep frequency increases the remanent polarization remains unaffected, whereas the coercive field increases.[23] Observation of a hysteretic *D-E* loop is typically assumed as an evidence for ferroelectricity. A ferroelectric material shows also hysteretic *J-V* characteristics, as shown in Figure 4.1b. In both negative and positive biases there is a peak in the current, which appears at the coercive voltage. The peaks are due to switching of the remanent polarization under applied bias, which leads to a displacement current.

The electric displacement, D, is defined as $D= \varepsilon\varepsilon_0 E+P$ where in ε is the dielectric constant, ε_0 is vacuum permittivity, E is the electric field and P is (remanent) polarization. The dielectric constant ε can be estimated as $\partial D/\partial E$ from those part of the *D-E* loop where there is no polarization reversal $(\partial P/\partial E=0)$. Taking the positively polarized upper branch, (equally holds for the negatively polarized lower branch), a dielectric constant of ten was obtained for P(VDF-TrFE), in good agreement with literature reports.[23] The dielectric constant does not show a significant frequency dependence up to 10 kHz, Figure 4.1c.

4.2.3. *D-V* and *J-V* of $MAPbI_3$ parallel plate capacitors

To test whether $MAPbI_3$ is ferroelectric, $MAPbI_3$ parallel-palate capacitors were fabricated. The conventional ferroelectric measurements were carried out in the dark. *D-E* and *J-V* loops of the Au/$MAPbI_3$/Au based capacitors are given in Figure 4.2a-b. The dielectric constant of $MAPbI_3$ obtained from the *D-E* loop is presented in Figure 4.2c as a function of frequency. At 1 Hz a hysteretic *D-E* loop is observed, as shown in Figure 4.2a. The shape of the *D-E* hysteresis loop is different from that of a conventional ferroelectric. At first glance one might, although mistakenly, even derive a value of 100-200 mC/m^2 for the remanent polarization. By increasing the frequency

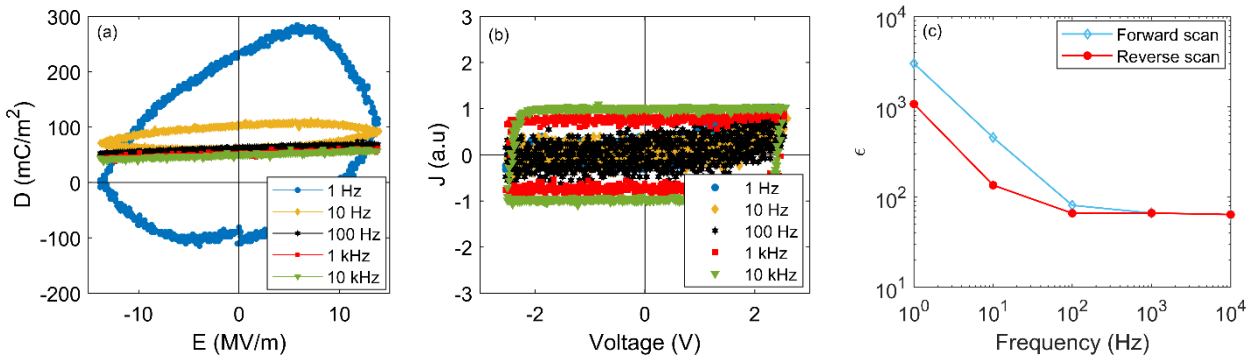

Figure 4.2. (**a**) The *D*-*E* and (**b**) *J*-*V* curves of Au/$MAPbI_3$/Au capacitors for a range of frequencies from 1 Hz to 10 kHz. (**c**) Calculated dielectric constants from the slope of *D*-*E* curve (**a**) as a function of frequency.

however, the hysteresis in the displacement and nonlinearity decreases and eventually disappears at frequencies higher than 1 kHz where *D*-*E* is linear. For a dielectric free of moving charges and ions, *D*-*E* measurement produces a line that passes through origin at zero field, the slope of which is determined by the dielectric constant. The displacement at zero field, however, is shifted toward positive value. The high-frequency value of *D* at zero field amounts to 50 mC/m^2. Moreover, for the relevant voltages typically used in the study of perovskite solar cells, the $MAPbI_3$ based capacitor does not show any switching peak in its *J*-*V* characteristics, in agreement with the *D*-*E* measurement. Room-temperature *D*-*E* and *J*-*V* loops of $MAPbI_3$ capacitors and its frequency behavior are in sharp contrast with the *D*-*E* and *J*-*V* loops obtained for the ferroelectric P(VDF-TrFE). Hence the observed hysteresis for $MAPbI_3$ is not related to the ferroelectricity. Therefore, ferroelectricity can be ruled out as the origin of hysteretic *I*-*V* characteristics in $MAPbI_3$ perovskite solar cells.

The shift of *D* towards positive values at high frequencies shows that there are slow moving positively charged species in the perovskite layer, which are not able to follow the applied high frequency electric field. Presence of such slow dynamic ionic charges in $MAPbI_3$ perovskites has

been reported in literature[3, 5, 8-11]. It has been proposed that the slow current response in $MAPbI_3$ perovskites is either due to $CH_3NH_3^+$ or Pb^{2+} ions[24]. Later it was confirmed that $CH_3NH_3^+$ is the slowly migrating ionic species in the layer[25].

Theoretical calculations predicted that I^- ions to be the most mobile ions in the $MAPbI_3$ films[26]. However, the migration of I^- ion at room temperature and under device operation conditions has not been verified yet[27]. The experimental procedure applied here gives only an account of the total number of ions and their sign, showing that the hysteretic behavior can only be attributed the positive ions. As a result of these moving ions, the apparent dielectric constant obtained at low frequencies is very high. At 1 Hz the dielectric constant amounts to around 3000 in forward scan and 1000 in reverse scan. At high frequency, however, the ions cannot follow the electric field modulation and are fixated. Then, the electronic contribution to the dielectric constant of the $MAPbI_3$ can be reliably determined and amounts to 64, comparable to reported values in literature [28-30].

4.2.4. *D-V* and *J-V* of $MAPbI_3$ solar cells

In the next step, $MAPbI_3$ solar cells with both conventional and inverted planar structures were fabricated. Figure 4.3a shows the forward and reverse scan. Under irradiation, an open-circuit voltage of 0.75 V, a short-circuit current density of 20.67 mA/cm^2, and a fill factor of 68% were obtained, resulting in a PCE of 10.58%. We note that the PCE of the cell is not comparable to the state-of-the-art cells, but of sufficient quality for a reliable comparison with the capacitors. The ferroelectric tests were carried out in dark on the solar cells. The *D-E* and *J-V* results for the solar cells in dark at different frequencies are shown in Figure 4.3b-c. At low frequency of 1 Hz, a hysteretic loop in the *D-E* curves can be clearly seen in Figure 4.3b. Upon increasing the frequency,

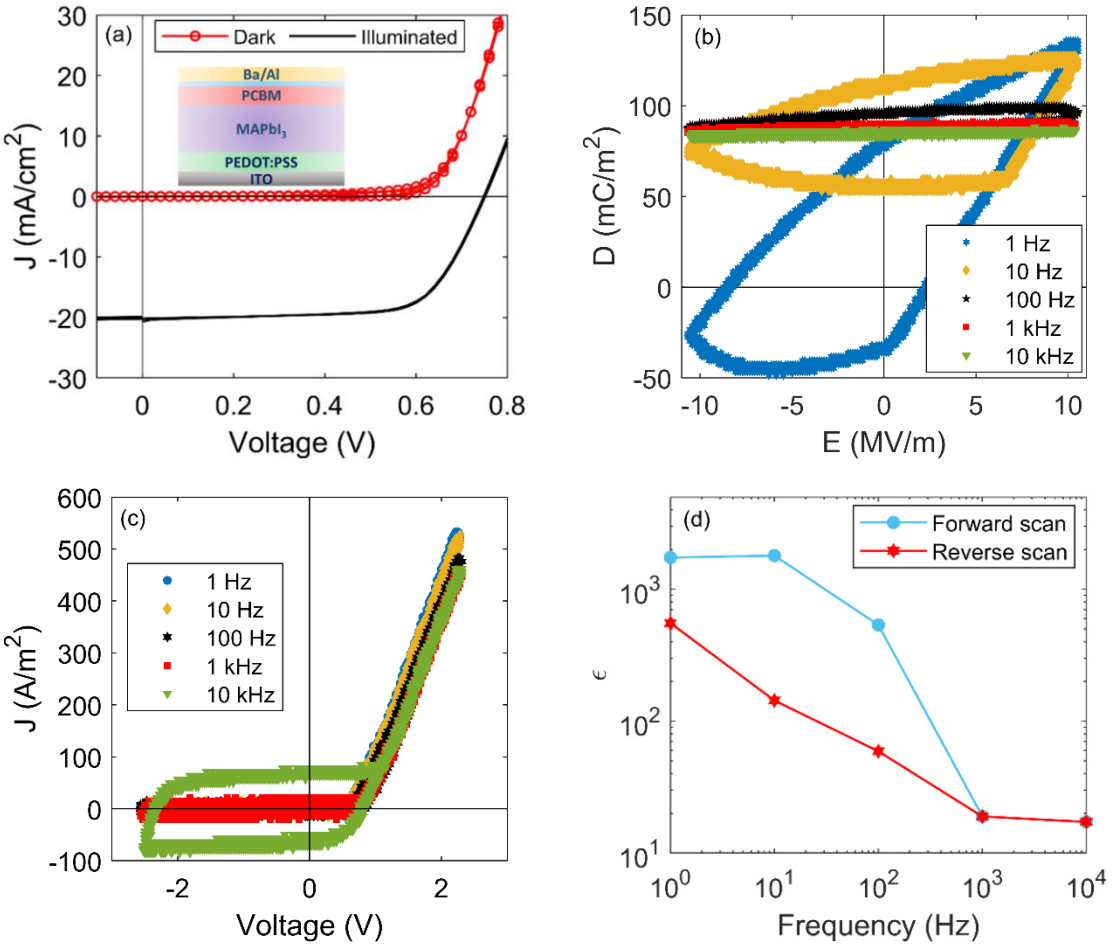

Figure 4.3. (**a**) PSC with inverted architecture in dark (red line) and under AM 1.5 G illumination (black line). The inset shows the performance parameters and the device. (**b**) The *D-E* and (**c**) *J-V* loops at different frequencies from 1 Hz to 10 kHz. (**d**) The effective dielectric constant obtained from the slope of *D-E* loop.

the hysteresis in the displacement decreases and eventually disappears at frequencies ≥100 Hz. The displacement at zero field is again shifted towards a positive value for both scan directions and amounts to 87 mC/m^2. At frequencies beyond 100 Hz, displacement again shows a linear dependence on the applied field. This behavior is in good agreement with the *D-E* loops presented in Figure 4.2 for the $MAPbI_3$ capacitors. Similar to $MAPbI_3$ capacitors, the *J-V* curves of the solar cells at various frequencies, Figure 4.3c, do not show any sign of a switching peak. The only

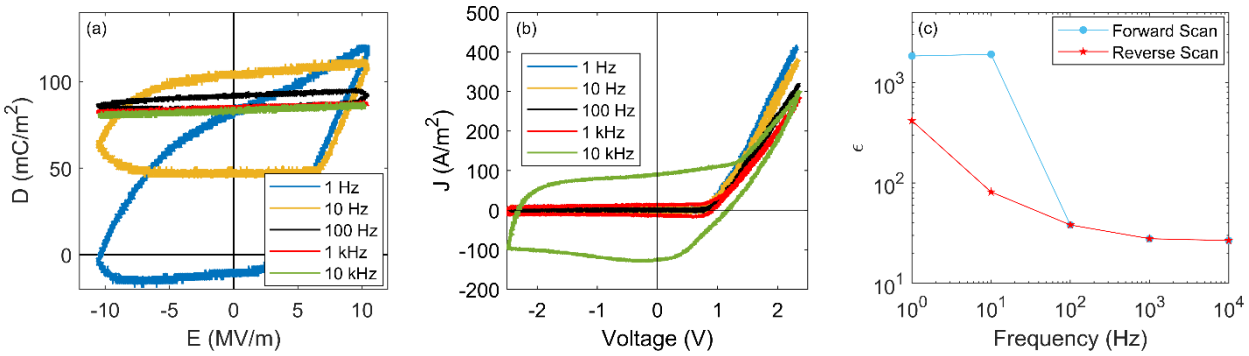

Figure 4.4. Conventional ferroelectric measurements performed on ITO/PCBM/$MAPbI_3$/Poly-TPD/Au. (**a**) The electric displacement field versus voltage at different frequencies from 1 Hz to 10 kHz. (**b**) *J-V* curves of the device for the same range of frequency. (**c**) Calculated effective dielectric constant from the slope of *D-V* curves.

difference here is that at forward bias, the cells are conductive. Similar results were obtained with the cells with regular planar structure as shown in Figure 4.4.

The calculated dielectric constant from the *D-E* loops, Figure 4.3d, shows again similar behavior as the $MAPbI_3$ capacitors. We note that in the case of the solar cell only the "effective" dielectric constant of the whole stack *i.e.* $MAPbI_3$/PCBM can be determined. The effective dielectric constant of the stack at 1 Hz is around 1900 in forward scan and 600 in reverse scan and it decreases to about 19 at frequencies ≥ 1 kHz. The solar cell can be considered as a configuration of two capacitors in in series (ignoring PEDOT:PSS due to its high conductivity). Assuming a dielectric constant of 64 for the $MAPbI_3$ layer (as determined from the capacitors) and 3.9 for PCBM, and by taking their respective layer thickness into account, the effective dielectric constant of 17 for the $MAPbI_3$/PCBM stack is obtained, which is in a good agreement with the value of 19 directly obtained from the *D-E* measurement.

Figure 4.4 shows the results for the ferroelectricity measurements on a $MAPbI_3$ perovskite solar cell with a regular planar architecture. The layout of the device was

ITO/PCBM/$MAPbI_3$/Poly-TPD/Au. Despite the difference in the device configuration, the hysteresis in *D*-*E* (Figure 4.4a) and *J*-*V* (Figure 4.4b) of the regular planar solar cell exhibits similar behavior to that of the inverted planar solar cell (Figure 4.3b-c). Moreover, as can be observed in Figure 4.4c, the frequency-dependent effective permittivity of $MAPbI_3$ in a regular planar solar cell stack of ITO/PCBM/$MAPbI_3$/Poly-TPD/Au presents the same trend as that of the inverted planar device (Figure 4.3d).

4.3. Conclusion

In conclusion, using capacitors we have shown that solution processed $MAPbI_3$ is not ferroelectric at room temperature. Furthermore, we obtained a high frequency dielectric constant of 64 for the $MAPbI_3$ perovskite layer. At low frequencies surface charges as high as 50 mC/m^2 have been observed, which we attributed to the motion of positive ions. Presence of positive ions can drastically influence the steady state (DC) current-voltage characteristics of the perovskite solar cells.

4.4. References

1. Chen, B., Yang, M., Priya, S., & Zhu, K. Origin of J–V hysteresis in perovskite solar cells. *J. Phys. Chem. Lett.* **7,** 905-917 (2016).

2. Kim, H-S. & Park, N-G. Parameters affecting I–V hysteresis of $CH_3NH_3PbI_3$ perovskite solar cells: effects of perovskite crystal size and mesoporous TiO_2 layer. *J. Phys. Chem. Lett.* **5**, 2927-2934 (2014).

3. Unger, E.L.*, et al.* Hysteresis and transient behavior in current–voltage measurements of hybrid-perovskite absorber solar cells. *Energy Environ. Sci.* **7**, 3690-3698 (2014).

4. Chen, B.*, et al.* Interface band structure engineering by ferroelectric polarization in perovskite solar cells. *Nano Energy* **13**, 582-591 (2015).

5. Chen, B.*, et al.* Impact of capacitive effect and ion migration on the hysteretic behavior of perovskite solar cells. *J. Phys. Chem. Lett.* **6**, 4693-4700 (2015).

6. Almora, O., *et al*. Capacitive dark currents, hysteresis, and electrode polarization in lead halide perovskite solar cells. *J. Phys. Chem, Lett.* **6**, 1645-1652 (2015).

7. Wojciechowski, K.*, et al.* Heterojunction modification for highly efficient organic–inorganic perovskite solar cells. *Acs Nano* **8**, 12701-12709 (2014).

8. van Reenen, S., Kemerink, M., & Snaith, H. Modeling anomalous hysteresis in perovskite solar cells. *J. Phys. Chem. Lett.* **6,** 3808-3814 (2015).

9. Haruyama, J., Sodeyama, K., Han, L. & Tateyama, Y. First-principles study of ion diffusion in perovskite solar cell sensitizers. *J. Am. Chem. Soc.* **137**, 10048-10051 (2015).

10. Snaith, H., *et al.* Anomalous hysteresis in perovskite solar cells. *J. Phys. Chem. Lett.* **5,** 1511-1515 (2014).

11. Meloni, S.*, et al.* Ionic polarization-induced current–voltage hysteresis in $CH_3NH_3PbX_3$ perovskite solar cells. *Nat Commun* **7**, 10334 (2016).

12. Chen, H-W., Sakai, N., Ikegami, M., & Miyasaka, T. Emergence of hysteresis and transient ferroelectric response in organo-lead halide perovskite solar cells. *J. Phys. Chem. Lett.* **6**, 164-169 (2014).

13. Stoumpos, C.C., Malliakas, C.D., & Kanatzidis, M.G. Semiconducting tin and lead iodide perovskites with organic cations: phase transitions, high mobilities, and near-infrared photoluminescent properties. *Inorg. Chem.* **52**, 9019-9038 (2013).

14. Beilsten-Edmands, J., Eperon, G., Johnson, R., Snaith, H., & Radaelli, P. Non-ferroelectric nature of the conductance hysteresis in CH3NH3PbI3 perovskite-based photovoltaic devices. *Appl. Phys. Lett.* **106**, 173502 (2015).

15. Fan, Z.*, et al.* Ferroelectricity of $CH_3NH_3PbI_3$ perovskite. *J. Phys. Chem. Lett.* **6**, 1155-1161 (2015).

16. Rakita, Y.*, et al.* $CH_3NH_3PbBr_3$ is not pyroelectric, excluding ferroelectric-enhanced photovoltaic performance. *APL Mater.* **4**, 051101 (2016).

17. Kutes, Y., *et al*. Direct observation of ferroelectric domains in solution-processed $CH_3NH_3PbI_3$ perovskite thin films. *J. Phys. Chem. Lett.* **5**, 3335-3339 (2014).

18. Scott, J. Ferroelectrics go bananas. *J. Phys.: Condens. Matter* **20**, 021001 (2007).

19. Asadi, K., & van der Veen, M.A. Ferroelectricity in Metal–Organic Frameworks: Characterization and Mechanisms. *Eur. J. Inorg. Chem.* **2016**, 4332-4344 (2016).

20. Mahale, P.*, et al.* Is $CH_3NH_3PbI_3$ Polar? *J. Phys. Chem. Lett.* **7**, 2412-2419 (2016).

21. Rakita Y*, et al.* Tetragonal $CH_3NH_3PbI_3$ is ferroelectric. *Proceedings of the National Academy of Sciences*, 201702429 (2017).

22. Röhm, H., Leonhard, T., Hoffmann, M.J., & Colsmann, A. Ferroelectric domains in methylammonium lead iodide perovskite thin-films. *Energy Environ. Sci.,* **10**, 950-955 (2017).

23. Zhao, D., Katsouras, I., Asadi, K., Blom, P.W., & de Leeuw, D.M. Switching dynamics in ferroelectric P (VDF-TrFE) thin films. *Phys. Rev. B* **92**, 214115 (2015).

24. Azpiroz, J.M., Mosconi, E., Bisquert, J., & De Angelis, F. Defect migration in methylammonium lead iodide and its role in perovskite solar cell operation. *Energy Environ. Sci.* **8**, 2118-2127 (2015).

25. Yuan, Y.*, et al.* Photovoltaic switching mechanism in lateral structure hybrid perovskite solar cells. *Adv. Energy Mater.* **5**, (2015).

26. Eames, C., *et al*. Ionic transport in hybrid lead iodide perovskite solar cells. *Nat Commun* **6,** 7497 (2015).

27. Yuan, Y., & Huang, J. Ion migration in organometal trihalide perovskite and its impact on photovoltaic efficiency and stability. *Acc. Chem. Res.* **49**, 286-293 (2016).

28. Yang, T.Y., Gregori, G., Pellet, N., Grätzel, M., & Maier, J. The Significance of Ion Conduction in a Hybrid Organic–Inorganic Lead-Iodide-Based Perovskite Photosensitizer. *Angew. Chem.* **127**, 8016-8021 (2015).

29. Hoque, M.N.F.*, et al.* Polarization and Dielectric Study of Methylammonium Lead Iodide Thin Film to Reveal its Nonferroelectric Nature under Solar Cell Operating Conditions. *ACS Energy Lett.* **1**, 142-149 (2016).

30. Juarez-Perez, E.J.*, et al.* Photoinduced giant dielectric constant in lead halide perovskite solar cells. *J. Phys. Chem. Lett.* **5**, 2390-2394 (2014).

Chapter 5

Quantification of Ion Dynamics in $MAPbI_3$ Thin Films*

Summary

Being based on mixed ionic-electronic semiconductors, the operation of perovskite solar cells depends on many parameters. To comprehend the physics of perovskite devices, it is therefore necessary to isolate individual physical phenomena. To this end, in this chapter the dynamics of ion motion in $MAPbI_3$ perovskite is investigated by measuring impedance spectra of Au/$MAPbI_3$/Au capacitors under dark conditions. By analyzing the characteristic frequencies of slow moving ions, the concentration and the diffusivity of ions are quantified. The frequency dependence of the apparent dielectric constant of $MAPbI_3$ is investigated.

*Publication: Sajedi Alvar, M., Blom, P. W. M., & Wetzelaer, G.-J. A. H., *Adv. Electron. Mater.* 1900935 (2020).

5.1. Introduction

The importance of ion motion in the operation of perovskite devices has been discussed in chapters 1 and 3. In this chapter, a novel and simple method is presented for quantification of the ion dynamics in $MAPbI_3$ thin films.

Several candidates for ion motion in lead halide perovskites have been identified[1, 2]. Experimentally, motion of I^- ions with a diffusion coefficient of 2.4×10^{-12} m^2/s was proposed as well as movement of positive MA^+ with a diffusion coefficient of only ~ 10^{-16} m^2/s [3, 4]. Theoretically, from density functional theory vacancy assisted I^- diffusion was predicted as the fastest diffusion, where positively charged I^- vacancies are the mobile species instead of I^- ions[1]. For these vacancies, a room temperature diffusion coefficient of 10^{-16} m^2/s was calculated. Using transient ion-drift measurements on $MAPbI_3$ PSCs, Futscher et al. observed that both MA^+ and I^- are mobile and reported an ion density of $10^{21\text{-}22}$ m^{-3} and diffusion coefficient of 10^{-16} m^2/s and 10^{-13} m^2/s, respectively[5]. The hysteresis in the *J-V* characteristics $MAPBI_3$ solar cells are in accordance with such slow moving positive vacancies[6].

Due to the significant impact of ion motion on the electric field distribution in PSCs, all physical phenomena in PSCs can be influenced by the ionic properties of perovskites. As an example, the movement of ions towards a biased electrode has a strong effect on the electronic properties of a PSC[7]. In a PSC with electron- and hole selective contacts the built-in electric field at zero bias will for example move positive ions towards the negatively charged electrode, as schematically indicated in Figure 5.1a. Consequently, the electric field is not homogeneous but mainly drops at the electrode, such that the electric field in the bulk of the active layer is (partially)

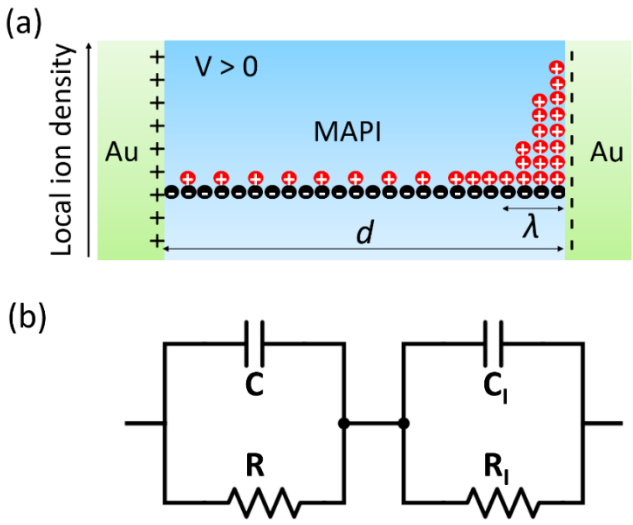

Figure 5.1**.** Ion movement in a biased Au/$MAPbI_3$/Au device. (**a**) Accumulation of positive ions at the negatively charged electrode, resulting in an accumulation layer with width λ. (**b**) Equivalent circuit with R_I and C_I the resistance and capacitance of the accumulation layer, R and C the resistance and capacitance of bulk $MAPbI_3$.

screened. The amount of screening depends on the dielectric constant, the ion concentration and its ability to follow the applied field, which is governed by the ion diffusion coefficient. In case of weak screening, the photogenerated charge carriers at short-circuit conditions are swept out by the built-in field, the photocurrent is drift dominated. In contrast, for complete screening the photogenerated carriers are driven towards the contacts by diffusion. Since metal-halide perovskites are affected by both electronic charge-carrier and ion movement, many parameters are simultaneously influencing the solar-cell current-voltage characteristics, such as the ion concentration and diffusion coefficient, the dielectric constant, charge-carrier mobilities, charge trapping, contact barriers, and recombination rates.

In this chapter we present a combined experimental and equivalent circuit modelling study on $MAPbI_3$, providing quantification of the ion dynamics, governed by the dielectric constant, ion diffusion coefficient and ion concentration. We demonstrate that the ion diffusion, ion density, and

the apparent dielectric constant of $MAPbI_3$, can be directly quantified from impedance spectroscopy measurements on Au/$MAPbI_3$/Au parallel-plate capacitors, independent of the electronic properties.

5.2. Results and discussion

5.2.1. Impedance spectroscopy analysis of $MAPbI_3$ parallel plate capacitors

To obtain the ion concentration, ion-diffusion coefficient, and frequency-dependent apparent dielectric constant, we used impedance spectroscopy. In order to avoid parasitic effects on the measurements from surrounding electron and hole transport layers that are typically existing in solar cells, we fabricated bare $MAPbI_3$ parallel-plate capacitors based on an Au/$MAPbI_3$/Au. As studied by Courtier et al.[8], charge-transport layers significantly affect the electrical characteristics of perovskite-based devices. We have therefore purposely avoided such layers to isolate the ionic parameters of $MAPbI_3$ thin films. Au/$MAPbI_3$/Au parallel plate capacitors were fabricated with the method that was described in chapter 2. A schematic depiction of the bare perovskite parallel-plate capacitors, along with the employed equivalent circuit for the analysis, is displayed in Figure 5.1. Impedance measurements were conducted under controlled nitrogen atmosphere, using a computer-controlled Solartron 1260 impedance analyzer. All measurements were carried out under dark conditions. In Figure 5.2a the measured real and imaginary part of the complex impedance Z are shown at zero bias as a function of frequency, together with the resulting dielectric loss ε_r'' and constant ε_r' (Figure 5.2b and c), defined as $\varepsilon_r' - j\varepsilon_r'' = 1/j\omega Z$, and dielectric loss tangent $\varepsilon_r''/\varepsilon_r'$ (Figure 5.2c) with ω the angular frequency $\omega = 2\pi f$. The amplitude of the ac voltage used for the

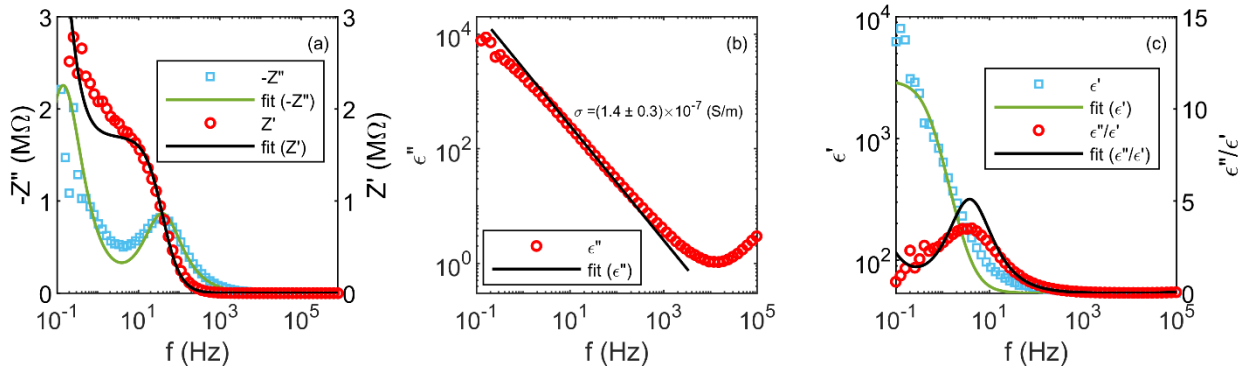

Figure 5.2**.** Impedance measurements on Au/$MAPbI_3$/Au capacitor. (**a**) Real (Z') and imaginary (Z'') part of the complex impedance Z as a function of frequency, (**b**) Apparent dielectric constant ε_r' and loss ε_r'' and (**c**) ε_r' and dielectric loss tangent ($\varepsilon_r''/\varepsilon_r'$) as a function of frequency f for a Au/$MAPbI_3$/Au capacitor with layer thickness L of 240 nm. The $1/f$ dependence of ε_r'' (Jonscher's law) is indicated by the solid line (**b**), the calculated frequency dependence of ε_r' (Eq. (5.8)) is given by the solid line (**c**).

impedance measurement was 100 mV. The real part Z' strongly decreases for frequencies higher than 70 Hz, whereas the imaginary part Z'' is characterized by a maximum at f_1=34.4 Hz and a minimum at f_2=5.3 Hz. At f = 1 Hz we obtain an apparent dielectric constant ε_r' of 990, which is identical to earlier reported values[9-11]. With increasing frequency ε_r' strongly decreases to a value of 67 for frequencies higher than 1 kHz. Furthermore, the dielectric loss ε_r'' exhibits a $1/f$ dependence in the frequency range 1 Hz to 1 kHz, in agreement with Jonscher's law for ionic conductors[12]. Jonscher's law behavior has been reported previously for $MAPbI_3$[13].

5.2.2. Equivalent-circuit model for $MAPbI_3$ parallel plate capacitors

For further analysis of the data and extraction of the ion mobility we use a model for ionic liquids and electrolytes developed by Bandara and Mellander[14]. We assume that positively charged defects (i.e. iodide vacancies) are mobile, whereas negative defects are fixed. The electrical behavior of our $MAPbI_3$ thin films between two (ion) blocking contacts can be described by an

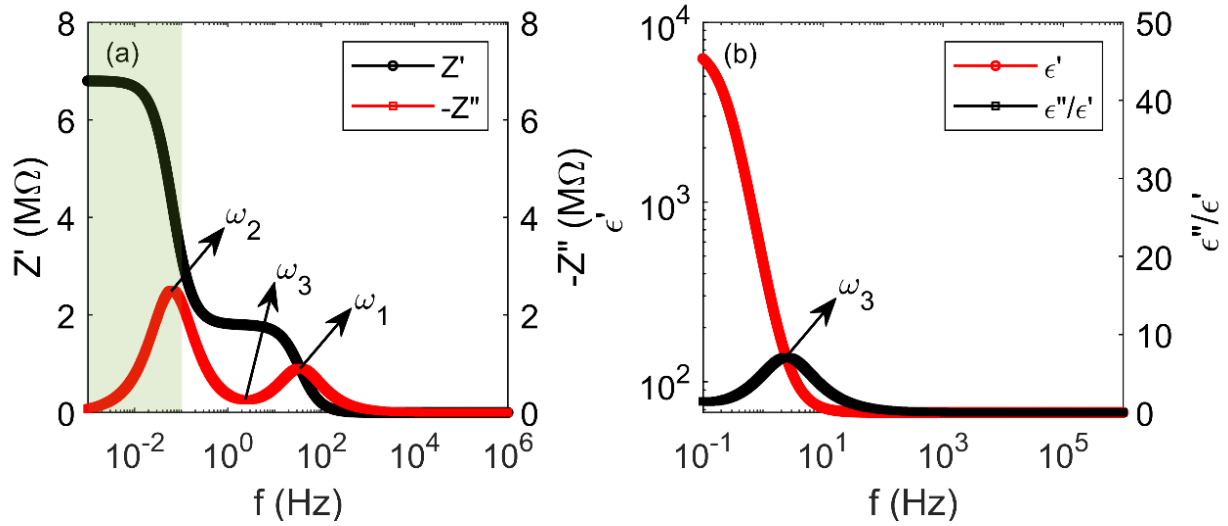

Figure 5.3**.** Calculated impedance and dielectric properties for the equivalent circuit of Figure 5.1b. (**a**) Schematic representation of the real Z' and imaginary Z'' part of the impedance as function of frequency *f* for R_I = 5 MΩ, C_I = 0.5 µF, *R*= 1.8 MΩ and *C* = 2.5 nF. (**b**) Corresponding ε_r' and dielectric loss tangent ($\varepsilon_r''/\varepsilon_r'$) as function of frequency.

equivalent circuit as shown in Figure 5.1b. We assume that the positively charged ionic species are mobile, and the negatively charged species are immobile. Upon application of an electrical signal with frequency *f* (or angular frequency $\omega = 2\pi f$) positive ions will move to the negatively biased electrode, leaving fixed negatively charged ions behind. As schematically indicated in Figure 5.1a, the accumulated positive ions at the electrode form a Helmholz double layer and behave as a parallel RC circuit, where C_I and R_I represent the capacitance and resistance of the Helmholz layer. This parallel RC element is placed in series with another parallel *RC*-circuit, where *C* and *R* represent the capacitance and resistance of the bulk $MAPbI_3$, respectively ($C_I >> C$). We note that the equivalent circuit of Figure 5.1b can only be applied to analyze the impedance data under the condition that $C_I >> C$, meaning that accumulation of ions at the electrode should take place[15]. When ions are absent or immobile the corresponding equivalent circuit would further simplify to a parallel *RC* circuit. For $C_I >> C$ the calculated *Z'* and *Z''* of such a circuit for a

hypothetical case of R_I = 5 MΩ C_I = 0.5 μF, R = 1.8 MΩ and C = 2.5 nF are shown in Figure 5.3a. For such a circuit Z' and $Z^{"}$ are given by

$$Z' = \frac{R}{1 + R^2\omega^2C^2} + \frac{R_I}{1 + R_I^2\omega^2C_I^2} \quad (5.1)$$

$$Z'' = -\left(\frac{R^2\omega C}{1 + R^2\omega^2C^2} + \frac{R_I^2\omega C_I}{1 + R_I^2\omega^2C_I^2}\right) \quad (5.2)$$

In the ideal case, the Nyquist plot of a double parallel *RC* circuit would give two semicircles in the whole range of frequency. The time constants of the two parallel *RC* elements are given by

$$\tau_1 = \frac{1}{\omega_1} = RC \quad (5.3)$$

$$\tau_2 = \frac{1}{\omega_2} = R_IC_I \quad (5.4)$$

For the frequency range of $\omega > \frac{1}{R_IC_I}$, τ_1 can be calculated using Z' = *R*/2. For the low frequency regime, where $\omega < \frac{1}{RC}$, the characteristic time constant of τ_2 occurs at Z' $= R + \frac{R_I}{2}$.

Figure 5.3 shows the total Z'' as a function of frequency. From the Figure 5.3 two peaks at ω_1 and ω_2 can be distinguished, corresponding to each of parallel RC elements. Between the two peaks, Z" exhibits a minimum at a frequency of ω_3, which obviously appears at the frequencies higher than ω_2. The time constant for this characteristic minimum is given by

$$\tau_3 = \frac{1}{\omega_3} = \frac{1}{\omega_1}\sqrt{\frac{C_I}{C}} \quad (5.5)$$

The maximum at ω_1 and minimum at ω_3 thus provides us with two characteristic time constants, representing relaxation of the space charge in the bulk and interface, τ_1 and τ_3 respectively, which are related via

$$\tau_3 = \tau_1 \sqrt{\delta} \tag{5.6}$$

with δ defined as L/λ, where L is the sample thickness and λ is the Debye length. The Debye length is equal to $\sqrt{(D\tau_3)}$. As a result, with τ_1 and τ_3 known, the ion diffusion coefficient D_{ion} is then directly given by

$$D_{ion} = \frac{L^2}{\tau_3 \delta^2} \tag{5.7}$$

For the equivalent circuit (RC-R_IC_I) shown in Figure 5.1b Z'' exhibits a maximum at angular frequency $\omega_1=1/\tau_1=1/RC$ and a minimum at $\omega_3=1/\tau_3=1/RC\times\sqrt{(C/C_I)}$, as also shown in Figure 5.3a and Figure 5.4a, using $R_I = 10$ MΩ, $C_I = 0.5$ µF, $R = 1.8$ MΩ and $C = 2.5$ nF. When trying to describe the impedance data with an alternative circuit R-RC ($R_1 = 1.8$ MΩ, $R_2 = 10$ kΩ and $C = 2.5$ nF), shown in the inset of Figure 5.4a, that was proposed to describe the impedance data for 0.6 mm thick $MAPbI_3$ pellets[16], it is observed that a difference only occurs at low frequencies. Here, due to the large impedance of C_I at low frequencies in case of RC-R_IC_I the impedance is governed by C_I, whereas for R-RC it will be dominated by R_1. As a result, for low frequencies for the RC-R_IC_I circuit Z'' will increase with $1/f$, whereas for the R-RC circuit Z'' will go to zero. Typically, the resistance R is given by $R = \rho d/A$, with ρ the resistivity, d the sample thickness and A the device area. Furthermore, the capacitance C is given by $C = \varepsilon_0\varepsilon_r A/d$, with $\varepsilon_0\varepsilon_r$ the permittivity. As a result, for very thick samples R will increase and C will decrease, but the RC product will not change, since $RC = \rho\varepsilon_0\varepsilon_r$ is independent of the sample dimensions. However, because $\omega_3 = 1/\tau_3 = 1/RC\times\sqrt{(C/C_I)}$ a lowering of C with constant RC means that ω_3 will shift to lower frequencies for thick samples. Figure 5.4b represents Z'' for a thick sample where R has increased and C has decreased by two orders of magnitude as compared to the values used in Figure 5.4 (C_I

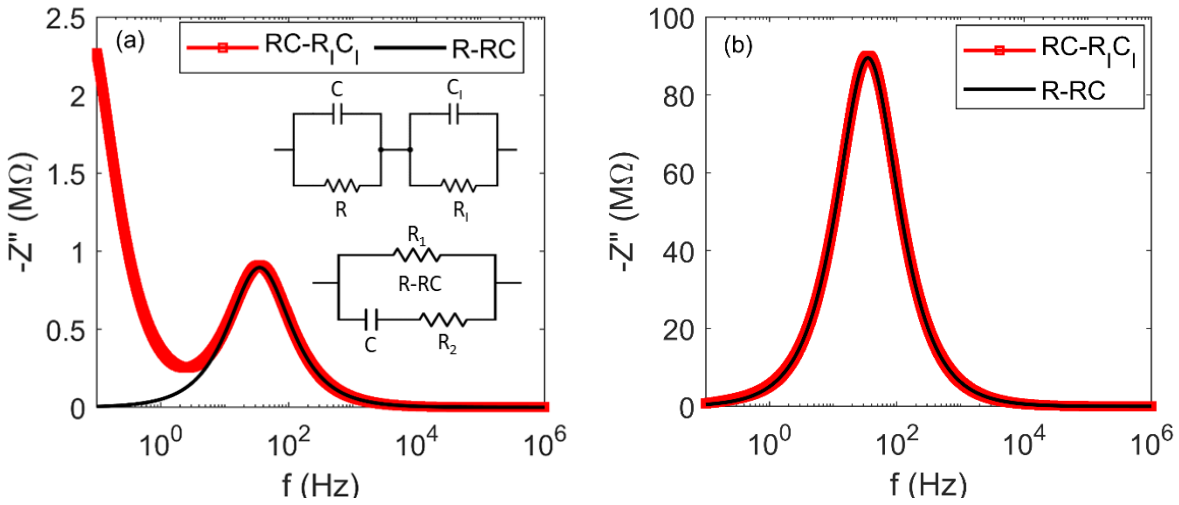

Figure 5.4**.** Calculated imaginary impedance Z'' for the equivalent circuits RC-R_IC_I and R-RC as shown in the inset of Figure 5.4. (**a**) Z'' as function of frequency *f* for R_I = 10 MΩ, C_I = 0.5 µF, R = 1.8 MΩ and C = 2.5 nF (RC-R_IC_I, red symbols) and R_1 = 1.8 MΩ, R_2 = 10 kΩ and C = 2.5 nF (R-RC, black line). (**b**) Imaginary Z'' for a thick device as function of frequency *f* using R_I = 10 MΩ, C_I = 0.5 µF, R = 180 MΩ and C = 25 pF (RC-R_IC_I, red symbols) and for R_I = 180 MΩ, R_2 = 1 MΩ and C = 25 pF (R-RC, black line).

is still taken as 1 µF, whereas R_2 also increased by two orders of magnitude). Since ω_3 is now outside the measuring regime (<0.1 Hz) the minimum in *Z''* cannot be observed. In that case, both circuits RC-R_IC_I and R-RC give an identical description of *Z''* and cannot be discriminated. Therefore, the occurrence of a minimum in Z'' that validates the applicability of the RC-R_IC_I circuit can only be observed for thin films (< 1 µm).

Furthermore, as displayed in Figure 5.3b, the frequency dependence of the apparent dielectric constant ε_r' in the model of Bandara and Mellander[14] is given by

$$\varepsilon_r' = \varepsilon'_\infty \left(1 + \frac{\delta}{1 + (\omega\tau_1\delta)^2}\right) \qquad (5.8)$$

The experimental impedance data shown in Figure 5.2 qualitatively exhibit the same functional dependence on frequency as compared to the proposed equivalent circuit. Not only *Z''* exhibits a minimum (ω_3) and a

maximum (ω_1), but also Z' is equal to Z'' at ω_1. The second maximum occurs in a very low frequency regime, which is out of experimentally accessible frequency range.

In Figure 5.2, the experimental impedance data are fitted with an equivalent circuit model with values of $C = 2.7$ nF, $C_I = 0.115$ µF, $R = 1.7$ MΩ, $R_I = 4.5$ MΩ, showing that this simple equivalent circuit captures most of the essential physics. We note that more complex circuits have been used for describing the interfaces in solar cells including charge transport layers[17]. The agreement between theory and experiment allows determination of the ion diffusion coefficient directly from the characteristic frequencies. From the observed frequencies $f_1 = 34.4$ Hz and $f_3 = 5.3$ Hz it follows that $\tau_1 = 4.6$ ms and $\tau_3 = 30$ ms, resulting in $\delta = 42$. With a sample thickness $L = 240$ nm, an ion diffusion coefficient D_{ion} of 1×10^{-15} m^2/s is obtained via Eq. (5.7). This value is in the same range as the diffusion coefficient obtained from fitting a circuit including a Warburg element[18] (3×10^{-16} m^2/s), as well as the coefficient needed to simulate the hysteresis in the *J-V* characteristics[19], and furthermore also in agreement with the value obtained from ab initio theory[1]. Using the obtained values for δ and τ_1 we also compare the expected frequency dependence of ε_r' according to Eq. (5.8) (solid line) with the experimentally obtained results (symbols), as shown in Figure 5.2c. The high frequency value ε_∞' amounts to 67, in agreement with earlier reported results[11, 13]. The calculated increase of ε_r' at lower frequencies is in reasonable agreement with experiment, given the fact that we approximate the ion conduction in $MAPbI_3$ by a relatively simple equivalent circuit. Furthermore, the model predicts a static (DC) ε_r' of about 2900.

As a next step, we show that also the ion concentration N_{ion} can be obtained from the impedance data. With the ion diffusion coefficient D_{ion} and thus ion mobility μ known via the Nernst-Einstein relation ($\mu = eD/kT$), knowledge of the ion conductivity σ would suffice to calculate $N_{ion} = \sigma/e\mu$. The conductivity can be obtained from Jonscher's law for ionic conductors, via the equation $\varepsilon_r'' = \sigma/\varepsilon_0\omega$. A fit using this relation is shown by the black solid line in Figure 5.2b. Considering a slight deviation from $1/\omega$ behavior in the experimental data, the fit yields an ionic conductivity of $\sigma = (1.4 \pm 0.3) \times10^{-7}$ S m^{-1}, accounting for the fitting error. The ion diffusion coefficient D_{ion} of 1×10^{-15} m^2/s yields an ion mobility μ of 4×10^{-14} m^2/Vs.

Using $\sigma = eN_{ion}\mu$, an ion concentration N_{ion} of 2×10^{25} m^{-3} is obtained, remarkably similar to the value predicted by ab initio theory[20]. From the impedance data we obtain R_I = 4.5 MΩ and R =1.7 MΩ, showing that there is a large resistance present both in the bulk and at the interfaces, most likely due to the presence of an injection barrier[7]. As a result, the electronic current at steady state is very low, having negligible influence on the extracted ionic parameters.

5.2.3. Verification of the impedance measurements

To verify that the deduced ion diffusion coefficient is not influenced by the intensity of the perturbation signal, the impedance spectra of the $MAPbI_3$ capacitor were measured for different amplitudes of the AC voltages. We note that in order to extract reliable results from impedance measurements, the amplitude of the perturbation signal has to be sufficiently small. In this way, the system is still close to its steady-state condition. Figure 5.5 shows the spectra of the imaginary (a) and real (b) part of the impedance and the dielectric loss (c) as a function of frequency, as well as the extracted ion diffusion coefficient (d) for five different values of V_{AC}. By varying V_{AC} from 10 mV to 100 mV, the positions of the maximum and minimum in the spectra are approximately constant, yielding similar time constants and, as a result, similar values for the extracted ion diffusion coefficient. However, at a higher V_{AC} of 200 mV, the height of the low frequency peak decreases and the position of the minimum between peaks shifts to lower frequencies. Consequently, the extracted diffusion coefficient at high V_{AC} deviates from the value of diffusion coefficient determined from measurements with lower V_{AC}. These measurements demonstrate that the diffusion coefficient can be extracted reliably for voltage amplitudes of 100 mV and lower. The extracted conductivity was not affected by changing V_{AC}.

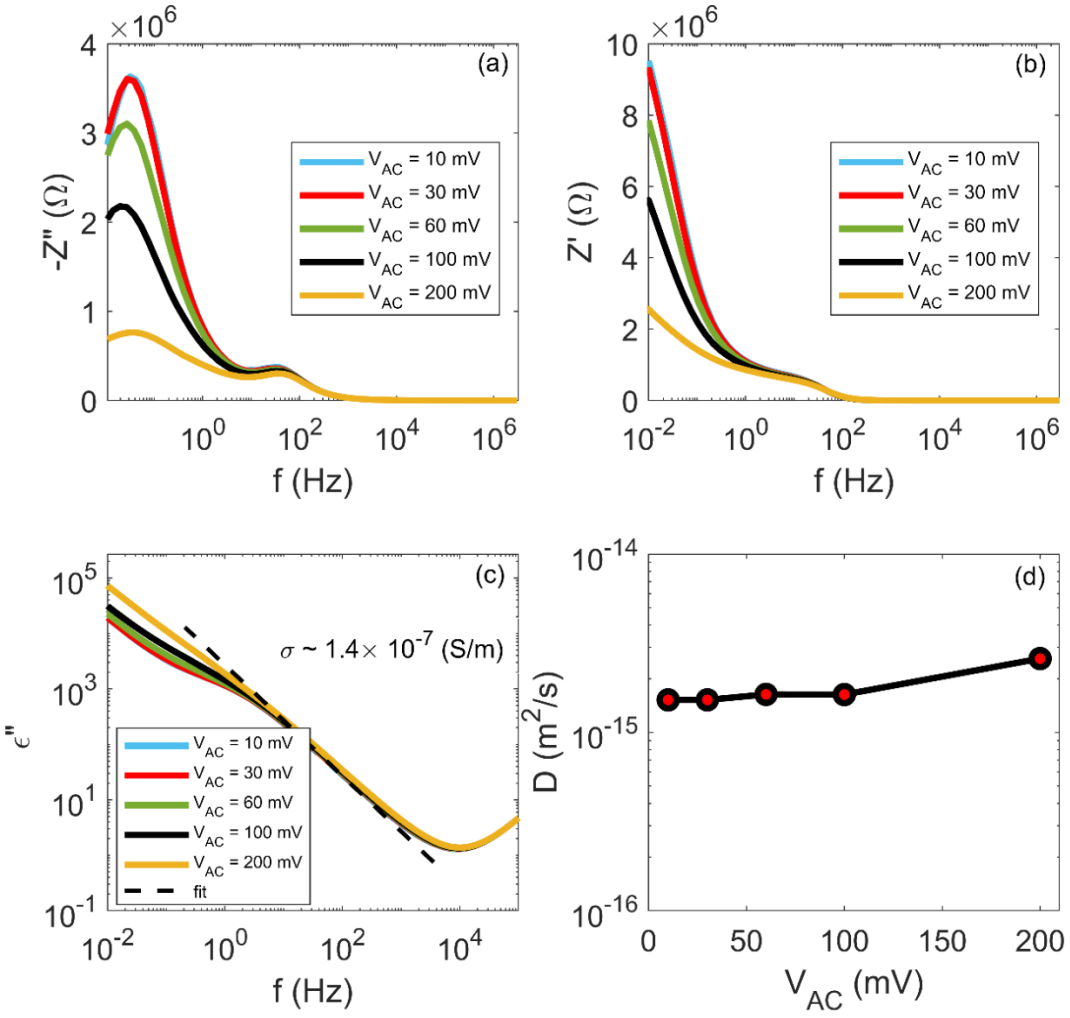

Figure 5.5**.** (**a**) The spectrum of the imaginary and (**b**) real part of the impedance for different amplitudes of the AC voltage. (**c**) The dielectric loss with the 1/f behavior which gives a conductivity of $\sigma \sim 1.4 \times 10^{-7} (S/m)$ independent of the ac field. (**d**) The extracted ion diffusion from the impedance spectrum as a function of the applied ac voltage. For V_{AC} of 100 mV and lower, the ion diffusion coefficient is approximately independent of the amplitude of the applied AC voltage.

5.3. Conclusion

In conclusion, we have developed a method for experimental quantification of ion dynamics in $MAPbI_3$ thin films. The apparent dielectric constant, diffusion coefficient and concentration of ions in $MAPbI_3$ were quantified using impedance spectroscopy. An ion diffusion coefficient $D_{ion} = 1\times10^{-15}$ m^2/s and an ion concentration $N_{ion} = 2\times10^{25}$ m^{-3} were obtained. The apparent dielectric constant of $MAPbI_3$ thin film was quantified as a function of frequency. It was shown that at low frequencies, the dielectric constant drastically increases due to the presence of the slow moving mobile ions.

5.4. References

1. Eames, C., *et al*. Ionic transport in hybrid lead iodide perovskite solar cells. *Nat Commun* **6,** 7497 (2015).

2. Frost, J., & Walsh, A. What is moving in hybrid halide perovskite solar cells? *Acc. Chem. Res.* **49,** 528-535 (2016).

3. Senocrate, A.*, et al.* The nature of ion conduction in methylammonium lead iodide: a multimethod approach. *Angew. Chem. Int. Ed.* **56**, 7755-7759 (2017).

4. Senocrate, A.*, et al.* Slow $CH_3NH_3^+$ Diffusion in $CH_3NH_3PbI_3$ under Light Measured by Solid-State NMR and Tracer Diffusion. *J. Phys. Chem. C* **122**, 21803-21806 (2018).

5. Futscher, M. H., et al. Quantification of ion migration in $CH_3NH_3PbI_3$ perovskite solar cells by transient capacitance measurements. *Mater. Horiz.*, **6**, 1497-1503 (2019).

6. Bertoluzzi, L., *et al*. In Situ Measurement of Electric-Field Screening in Hysteresis-Free PTAA/$FA_{0.83}Cs_{0.17}Pb$ $(I_{0.83}Br_{0.17})_3/C_{60}$ Perovskite Solar Cells Gives an Ion Mobility of$\sim 3\times 10^{-7}$ $cm^2/(V\ s)$, 2 Orders of Magnitude Faster than Reported for Metal-Oxide-Contacted Perovskite Cells with Hysteresis. *J. Am. Chem. Soc.* **140**, 12775-12784 (2018).

7. Ebadi, F., Taghavinia, N., Mohammadpour, R., Hagfeldt, A., & Tress, W. Origin of apparent light-enhanced and negative capacitance in perovskite solar cells. *Nat Commun* **10**, 1574 (2019).

8. Courtier, N., Cave, J., Foster, J., Walker, A., & Richardson, G. How transport layer properties affect perovskite solar cell performance: insights from a coupled charge transport/ion migration model. *Energy Environ. Sci.* **12,** 396-409 (2019).

9. Onoda-Yamamuro, N., Matsuo, T., & Suga, H. Dielectric study of $CH_3NH_3PbX_3$ (X= Cl, Br, I). *J. Phys. Chem. Solids* **53,** 935-939 (1992).

10. Juarez-Perez, E.J.*, et al.* Photoinduced giant dielectric constant in lead halide perovskite solar cells. *J. Phys. Chem. Lett.* **5**, 2390-2394 (2014).

11. Hoque, M.N.F.*, et al.* Polarization and Dielectric Study of Methylammonium Lead Iodide Thin Film to Reveal its Nonferroelectric Nature under Solar Cell Operating Conditions. *ACS Energy Lett.* **1**, 142-149 (2016).

12. Jonscher, A. Analysis of the alternating current properties of ionic conductors. *J. Mater. Sci.* **13**, 553-562 (1978).

13. Lin, Q., Armin, A., Nagiri, R.C.R., Burn, P.L., & Meredith, P. Electro-optics of perovskite solar cells. *Nature Photon* **9**, 106 (2015).

14. Bandara, T., & Mellander, B. Evaluation of mobility, diffusion coefficient and density of charge carriers in ionic liquids and novel electrolytes based on a new model for dielectric response. *Ionic liquids: theory, properties, new approaches*, 383-406 (2011).

15. Almora, O., *et al*. Capacitive dark currents, hysteresis, and electrode polarization in lead halide perovskite solar cells. *J. Phys. Chem. Lett.* **6**, 1645-1652 (2015).

16. Senocrate, A.*, et al.* Slow $CH_3NH_3^+$ Diffusion in $CH_3NH_3PbI_3$ under Light Measured by Solid-State NMR and Tracer Diffusion. *J. Phys. Chem. C,* **122**, 21803-21806 (2018).

17. Moia, D.*, et al.* Ionic-to-electronic current amplification in hybrid perovskite solar cells: ionically gated transistor-interface circuit model explains hysteresis and impedance of mixed conducting devices. *Energy Environ. Sci.* **12**, 1296-1308 (2019).

18. Bag, M.*, et al.* Kinetics of ion transport in perovskite active layers and its implications for active layer stability. *J. Am. Chem. Soc.* **137**, 13130-13137 (2015).

19. Richardson, G., *et al.* Can slow-moving ions explain hysteresis in the current–voltage curves of perovskite solar cells? *Energy Environ. Sci.* **9,** 1476-1485 (2016).

20. Walsh, A., Scanlon, D.O., Chen, S., Gong, X., & Wei, S.H. Self-regulation mechanism for charged point defects in hybrid halide perovskites. *Angew. Chem. Int. Ed.,* **54**, 1791-1794 (2015).

Chapter 6

Device Model for $MAPbI_3$ Perovskite with Experimentally Validated Ion Dynamics*

Summary

The operation of perovskite solar cells depends on many parameters due to the coexistence of electronic and ionic charges. To develop an experimentally-validated numerical device model, it is therefore necessary to isolate individual physical phenomena. To this end, the dynamics of ion motion in lead halide perovskites is investigated by measuring the electric displacement field as a function of frequency in dark conditions. The displacement response is fully reproduced by a numerical device model that combines electronic and ionic conduction. For a quantitative description of the displacement, it is critical to consider the frequency-dependent apparent dielectric constant, the ion concentration and the ion diffusion coefficient. The numerical simulations enable us to quantify the effect of ion motion and voltage scan speed on the electric field distribution in $MAPbI_3$ based devices, laying the foundations for an experimentally-validated perovskite device model. The extracted ionic properties are in excellent agreement with results obtained from impedance spectroscopy in chapter 5.

---

*Publication: Sajedi Alvar, M., Blom, P. W. M., & Wetzelaer, G.-J. A. H., *Adv. Electron. Mater.* 1900935 (2020).

6.1. Introduction

As discussed in chapter 1 and chapter 3, in order to improve the understanding of the device physics of perovskite device, it is indispensable to have a numerical device model that includes both electronic and ionic properties. In the presented device model in chapter 3, it is clear that the device model requires several input parameters. Therefore, for such a model to be accurate, the large amount of input parameters should be carefully quantified. So far, several device models have been reported for describing the operation of PSCs[1-9]. Van Reenen et al. explained the hysteretic I-V of PSCs by combining ion motion and charge trapping at the interfaces of perovskite layer[2]. However, their choice of ion density (10^{24} m^{-3}) and relative dielectric constant (6.5) is not consistent with other reports[1, 4, 10]. Calado et al. simulated optoelectronic transient measurements on PSCs and reported the same mechanisms for hysteretic I-V, but with higher ion density (10^{25} m^{-3}) and much lower ion diffusivity (2.5×10^{-18} m^2/s) [1]. Richardson et al. reported the motion of iodide vacancies as the origin of I-V hysteresis and estimated the ion diffusion coefficient to be around 10^{-16} m^2/s [4]. Another device model was developed by Sherkar et al, where they studied the influence of ferroelectric polarization and grain boundaries on the performance of PSCs[8, 9]. However, ion dynamics were not included in their model[9]. Recently, Neukom et al. applied an electronic-ionic device model to simulate a series of experiments, but a validation of the multiple fit parameters was missing[5]. In all the aforementioned models, the question remains what are the proper input parameters for the ionic and electronic properties.

In this chapter, we present a combined experimental and device modelling study on $MAPbI_3$, providing an independent quantification and validation of the ion dynamics, governed by the dielectric constant, ion diffusion coefficient and ion concentration. In the previous chapter,

impedance spectroscopy was used to quantify the ion diffusion, ion density, and the apparent dielectric constant of $MAPbI_3$ thin films in a parallel-plate capacitor configuration, independently of the electronic properties. In this chapter the ion dynamics are further investigated by measuring and modeling the electric displacement loops of Au/$MAPbI_3$/Au parallel-plate capacitors. With a numerical device model combining electronic and ionic conduction, both the magnitude and frequency dependence of the electric displacement as a function of electric field are excellently described using an ion diffusion coefficient and concentration similar to the impedance data. The mixed electronic-ionic model, with the ionic parameters independently validated by impedance and displacement measurements, is employed to simulate the time-dependent electric field distribution in $MAPbI_3$ based devices and paves the way for a device model based on experimentally-validated input parameters.

6.2. Results and discussion

6.2.1. Device fabrication and *D-V* measurements

In chapter 4, the ionic properties of $MAPbI_3$ thin films were obtained from impedance spectroscopy measurements on parallel plate capacitors. An independent confirmation of these ionic properties by directly modelling the current-voltage characteristics of solar cells is not trivial since a device model contains many additional parameters, such as contact barriers, charge-carrier mobilities and concentrations, trap concentrations and trap depths, and even an apparent dielectric constant that depends on the frequency and thus the scan rate. Highly desirable is a method that characterizes the ionic properties independently, such that the ionic part of the device model can be validated. Therefore, we measure the electric displacement with a Sawyer-Tower circuit in

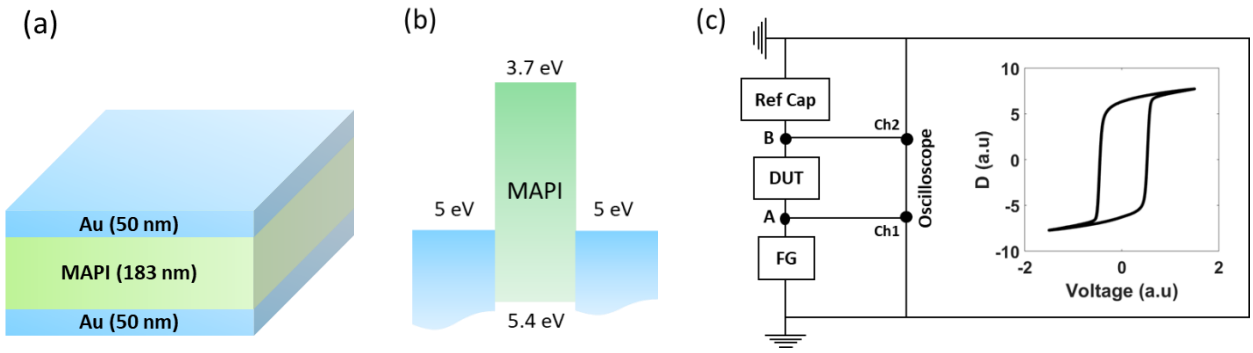

Figure 6.1**.** (**a**) Device layout of an Au/MAPI/Au capacitor. (**b**) The energy diagram of the device. (**c**) The Sawyer Tower circuit used for electric displacement measurements and a typical hysteresis loop for a ferroelectric material.

Au/$MAPbI_3$/Au perovskite based capacitors (Figure 6.1a and b) under dark conditions. A schematic diagram of the Sawyer Tower setup is shown in Figure 6.1c. A Sawyer-Tower setup is typically used to measure the polarization of ferroelectric capacitors. In this figure, a typical hysteretic electric displacement D as function of voltage V (D-V) loop of a ferroelectric material is presented as an output of the Sawyer Tower method. As shown in Figure 6.1c, in this method, a function generator (FG) applies an AC bias with certain frequency and amplitude to the device under test (DUT). At the same time, the oscilloscope records the applied bias as input voltage (V_A). There is a reference capacitor (Ref Cap) with a certain capacitance in contact with the DUT. The oscilloscope also records the output voltage ($V_B = V_{Ref}$). Knowing the capacitance and the voltage across the reference capacitor, gives the total amount of charges on this capacitor. Since the two capacitors are connected in series, the amount of charges on the plates of DUT is equal to the charge on the reference capacitor. The charge density on the plates of DUT equals the electric displacement field D. Therefore, utilizing the Sawyer Tower test, the electric displacement field D of the MAPI-based capacitor can be recorded as a function of the applied bias.

As mentioned above, upon application of a bias voltage positive ions drift towards the negatively biased electrode and form an accumulation layer. This accumulation layer screens the electric field in device generated by the amount of electronic charge on the capacitor plates. For large ion concentrations the electric field is almost completely screened. In that case, the amount of ionic charge at the perovskite surface is nearly equal to the amount of (free) electronic charge on the plate, which is represented by the electric displacement *D*. Consequently, the amount of free charges on the electrodes of the Au/$MAPbI_3$/Au capacitors is directly linked to the build-up of ionic charges at the negatively biased electrode. The measured amount of free charges then depends on the ion concentration *N*, whereas the frequency dependence of the *D*-*E* loops depends on how fast ions can follow the applied field, which is governed by the ion diffusion coefficient D_I. We note that the use of two gold electrodes prevents the results from being affected by a large built-in electric field as well as chemical reaction between the electrode and perovskite.

To fabricate Au/$MAPbI_3$/Au capacitors a layer of Cr/Au (1 nm/50 nm) was deposited as the bottom contact on a glass substrate. A mixture of lead acetate trihydrate ($Pb(Ac)_2$) and methylammonium iodide (MAI) in a 1:3 molar ratio in N,N-dimethylformamide (DMF) was prepared and spin coated on the substrate inside a nitrogen-filled glovebox. The films were annealed at 100 °C for 30 minutes. Finally, the capacitors were finished by the deposition of 50 nm top Au electrodes, giving rise to a device area of 1 mm^2. Electric displacement measurements were carried out via Sawyer-Tower method (Figure 6.1). As function generator, a Tektronix AFG 3022B has been used, the input voltage and output voltage were recorded with a Waverunner LT374 LeCroy Digital Oscilloscope.

6.2.2. Frequency dependence of the experimental *D-V* characteristics

The experimental *D-V* characteristics of the $MAPbI_3$-based capacitor as a function of frequency are presented in Figure 6.2a. The measurements have been carried out in dark conditions. A large hysteresis loop can be observed at 1 Hz, which shows a different shape from a typical loop of a ferroelectric material, excluding ferroelectricity as the origin of the hysteresis[11]. Depending on the applied voltage, at 1 Hz the magnitude of the electric displacement varies between +150 mC/m^2 to -200 mC/m^2. At a frequency of 10 Hz, the hysteresis in the electric displacement reduces, with the loop only showing negative displacement. In addition, the magnitude of the electric displacement at 10 Hz compared to 1 Hz decreases by almost one order of magnitude. Upon increasing the frequency to 100 Hz, the hysteresis almost disappears. At higher frequencies of 1 kHz and 10 kHz the hysteresis is absent and the electric displacement of the device exhibits a linear dependence on the electric field with a slope of $\varepsilon_0\varepsilon_r$ (see Eq. (10)). It

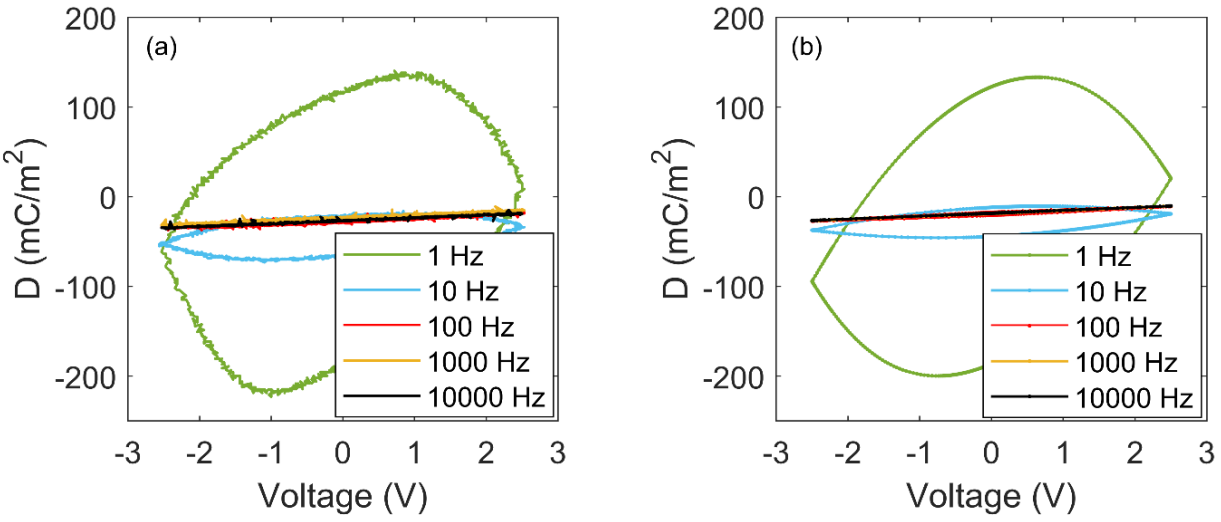

Figure 6.2**.** Electric displacement as function of voltage at various frequencies. (**a**) Experimental and (**b**) corresponding simulated *D-V* characteristics using a combined ionic-electronic drift diffusion model with an ion diffusion coefficient of 8×10^{-16} m^2/s and an ion concentration of 1.9×10^{25} m^{-3}.

has to be noted that in chapter 3 the same measurement was conducted to study the ferroelectricity of $MAPbI_3$ thin films.

6.2.3. Numerical simulation of *D-V* characteristics

In chapter 3, an electronic-ionic drift-diffusion model was presented for modeling perovskite devices. Here, this model was applied to model the electric displacement loops of the $MAPbI_3$ capacitors. For modeling the $MAPbI_3$ capacitor, it is assumed that the $MAPbI_3$ layer is a mixed electronic-ionic conductor which includes a certain density of negative and positive ionic charges. Here the positive ionic species are considered to be mobile inside the $MAPbI_3$ layer whereas the negative ionic species are assumed to be immobile. The Au-$MAPbI_3$ interfaces of the Au/$MAPbI_3$/Au parallel-plate capacitor are considered to be ion blocking. The assumption of ion blocking contacts implies that there is no ion flow through the interfaces. The recombination mechanism is assumed to be of the Shockley-Read-Hall (non-radiative) type. However, in the frequency regime of the electric displacement study in this chapter, the recombination does not influence the electric displacement of the device. Since all the experimental measurements on the $MAPbI_3$ capacitors have been performed in the dark, the generation rate is considered to be zero. For initial conditions, it is assumed that all the electronic and ionic charges are uniformly distributed across the $MAPbI_3$ film. Therefore, at time zero, at every single point in the $MAPbI_3$ layer, the net amount of electric charge is zero. Upon variation of the applied bias, the negative ionic charges remain immobile and uniformly distributed across the $MAPbI_3$ layer, while the positive ionic charges can move toward the contacts and redistribute across the film. By applying a voltage to the device the electrons and holes will be injected from the corresponding contacts and move across the device. As discussed in chapter 3, in this thesis a program was developed in

MATLAB for solving the aforementioned system of equations. With the aforementioned boundary and initial conditions, the system of equations was solved over time and space.

In order to calculate the *D-V* characteristics corresponding to the experimental results in Figure 6.2a, numerical simulations were performed using the described device model. Due to the fast dynamics of electronic charges and considering the frequency regime of our study, namely 1 Hz to 10 kHz, the transport of electrical charges does not play a significant role in the electric displacement. Therefore, the choice of electronic properties does not significantly influence the simulation results. Importantly, in this frequency regime, the results are a direct consequence of the ionic properties of the perovskite. This enables us to isolate the effect of ion diffusion on the ion distribution and electric field inside the device. In a system in which both ions and charge carriers are present, the electric displacement has two components. One component is related to the polarization charges and the second component is the ionic part. The total electric displacement is the summation of the polarization and ionic contribution and can be described by following equation:

$$D = D_{polarization} + D_{Ionic} \tag{6.1}$$

Where D is the total electric displacement and $D_{polarization}$ and D_{Ionic} are the polarization and ionic portion of the electric displacement. The polarization part of the displacement is defined as follows:

$$D_{polarization} = \varepsilon_{\infty}\varepsilon_0 E \tag{6.2}$$

Here, $\varepsilon_{\infty}$is the high frequency dielectric constant of $MAPbI_3$, ε_0 is vacuum permittivity, and E is the electric field. In addition, the ionic electric displacement can be defined by the following equation:

$$D_{Ionic} = \varepsilon_r \varepsilon_0 \Delta E \quad (6.3)$$

Where $\varepsilon_r$is the apparent dielectric constant and ΔE is difference between the electric field at the interface, where the ions accumulate, respect to the bulk electric field.

$$\Delta E = E_{interface} - E_{bulk} \quad (6.4)$$

For a quantitative simulation of the perovskite capacitors, the key parameters are the ion concentration, ion diffusion coefficient, and the apparent dielectric constant ε_r. The experimentally measured values for ε_r, shown in Figure 5.2c, were used as input parameters in the drift-diffusion model to simulate the *D-V* characteristics. Using an ion diffusion coefficient of 8×10^{-16} m^2/s and an ion concentration of 1.9×10^{25} m^{-3} the calculated *D-V* characteristics are shown in Figure 6.2b for a range of frequencies from 1 Hz to 10 kHz. Similar to the experimental results, the simulated electric displacement shows strong frequency dependence, with the simulations being in excellent agreement with the experimentally-obtained characteristics. The simulations reveal that the large hysteresis observed at 1 Hz is due to the slow dynamics of ionic charges. At such low frequency, the ionic component of the electric displacement is dominant, while the polarization part does not play a significant role. In addition, the magnitude of the electric displacement is voltage dependent and similar to the experimental results it varies between +150 to -200 mC/m^2. Moreover, in accordance with experiments, the hysteresis and also the magnitude of the electric displacement drastically reduce at a frequency of 10 Hz. In fact, at a frequency of 10 Hz, the slow ions can marginally follow the variations of the applied electric field. Therefore, the ionic portion of the displacement has a small voltage-dependent variation, which leads to a small hysteresis in the *D-V* characteristics of the device. For frequencies above 100 Hz, no significant hysteresis can be observed. In this frequency regime, the ionic charges are not sufficiently mobile to respond to the

applied electric field. Thus, the ionic portion of the electric displacement becomes constant and the polarization part of the electric displacement is the only voltage-dependent term.

6.2.4. Position-dependent distribution of positive ions, holes, and electric field

To explain the observed displacement loops, the rearrangement of ionic and electronic charges inside $MAPbI_3$ under the applied bias is visualized in Figure 6.3. Figure 6.3a shows the distribution of ions as a function of position at 1 Hz for different bias voltages. After an initial *D*-*V* sweep (0 V→+2.5 V→-2.5 V→0 V) at 0 V a population of ions is accumulated at the interface of $MAPbI_3$ and the right electrode (blue line), which has a slightly higher work function. This results in a large and negative electric displacement of ~ -200 mC/m^2. As the bias again increases to +2.5 V, the ions start moving toward the opposite (left) electrode. Therefore, the population of the ions at the right electrode gradually decreases, while the ionic population starts increasing on the left electrode. As a result, the electric displacement also reduces (see Figure 6.2). At a bias voltage of +2.5 V, a certain number of ions accumulate at the left electrode (red line), which leads to a positive electric displacement of approximately +20 mC/m^2. In the subsequent downward scan, from +2.5 V to 0 V, the bias remains positive and consequently the number of accumulated ions at the left electrode increases (green line). As a result, at 0 V the electric displacement has further increased to approximately +130 mC/m^2. Upon further decreasing the applied bias, the ions start moving toward the right electrode again and concomitantly the electric displacement gradually decreases. At the maximum bias voltage of -2.5 V, the presented distribution of charges (black line) gives a negative electric displacement of approximately -100 mC/m^2. This displacement continues to decrease while sweeping back to 0 V.

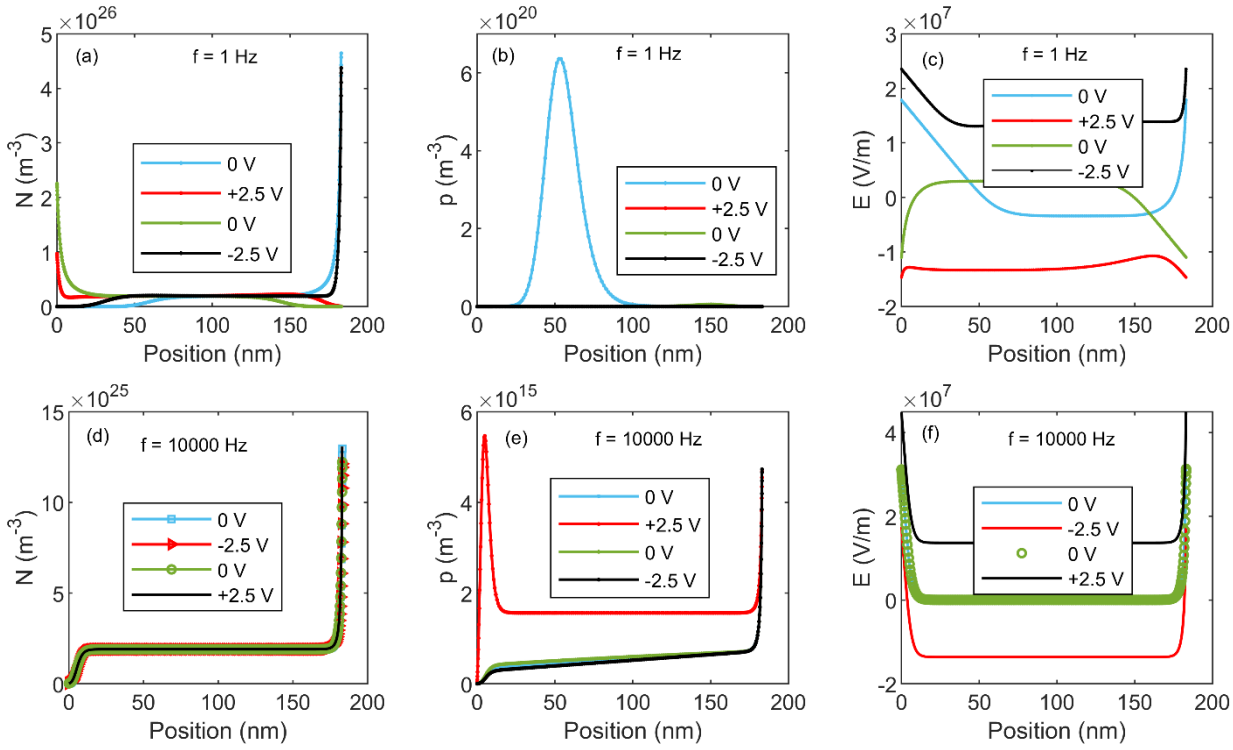

Figure 6.3**.** Simulated distribution of mobile ionic charges, holes, and electric field across the $MAPbI_3$ layer. (**a**) ion distribution in the $MAPbI_3$ capacitor at different applied voltages in downward and upward scan for low frequency (1 Hz) and (**d**) high frequency regime (10 kHz). (**b**) Distribution of holes inside the $MAPbI_3$ capacitor for various bias voltages in downward and upward scan at frequency of 1 Hz and (**e**) 10 kHz. (**c**) Electric field distribution inside the capacitor for different applied voltages in downward and upward scan at frequency of 1 Hz and (**f**) 10 kHz.

Figure 6.3d shows the position-dependent distribution of mobile ions at various applied biases at frequency of 10 kHz, for which the displacement loops do not show hysteresis. Due to a small built potential, some ions are accumulated at the higher work function (right) electrode. In contrast to what is observed at 1 Hz, in the high frequency regime the distribution of ions approximately persists at all voltages and the hysteresis in the *D*-*V* loops disappears. This is a result of the ions not being able to follow the changing electric field at high frequency. Therefore, the ionic part of the electric displacement remains constant, which in combination with the polarization part gives rise to a linear dependence of the electric displacement on the electric field

with a slope of $\varepsilon_\infty \varepsilon_0$. From the measurements a slope of $67\varepsilon_0$ is obtained, which is the high frequency permittivity of $MAPbI_3$ (Figure 6.7a).

Figure 6.3b and Figure 6.3e present the position-dependent distribution of holes at different applied biases at frequencies of 1 Hz and 10 kHz. The density of holes inside the device is several orders of magnitude lower than the density of mobile ions. Furthermore, the dynamics of electronic charge carriers is much faster than the frequency regime of our study. In other words, the response time of the electronic charges is much faster than the variation of applied bias. The low density and the fast dynamics of holes mean that the displacement response is dominated by ionic charges.

The simulated distribution of the electric field inside the $MAPbI_3$ capacitor at 1 Hz and at 10 kHz is shown in Figure 6.3c and Figure 6.3f, respectively. At 10 kHz, the ions are not sufficiently mobile to respond the applied voltage, upon variation of the applied voltage the difference between electric field at the interface with respect to the bulk value, resulting from ion movement as a result of the small built-in voltage, persists. This effect results in a constant (negative) ionic component in the electric displacement, as shown in Figure 6.2. At 1 Hz, when no bias is applied at steady state, the ions are mostly accumulated at the higher work function (right) electrode interface and consequently a narrower Debye layer is formed at this interface ($\lambda = \sqrt{\frac{\varepsilon\varepsilon_0 k_\beta T}{Ne^2}}$) (blue line). From 0 to +2.5 V, the ions start to move toward the opposite electrode. Therefore, the number of ions at the high work function electrode decreases, while it enhances on the opposite electrode. Consequently, the sign of the electric field at the electrodes changes and the screening effect is strongly reduced when an applied bias of +2.5 V is reached, the field is nearly constant (red line). From +2.5 V to 0 V, more ions reach the left electrode and the screening effect again increases, while the sign of the electric field in the bulk changes from negative to

positive value (green line). As the applied voltage increases from 0 V to -2.5V, the direction of ion motion changes toward the right electrode, meaning the ion density at the low work function (left) electrode decreases and the (positive) electric field in the bulk is further enhanced due to reduced screening (black line).

6.2.5. Position-dependent distribution of electrons

The position-dependent distribution of electrons is presented in Figure 6.4. The injection barrier for electrons is assumed to be about 1 eV, meaning the electron density in the $MAPbI_3$ layer is negligible compared to the density of holes and ions. Therefore, it has no effect on the observed displacement. Furthermore, the sensitivity of the calculated displacement on the hole-injection barrier was examined. The electric displacement at a frequency of 1 Hz was simulated for a range of injection barriers from 0.2 to 0.5 eV. The results are shown in Figure 6.8c. It can be seen that the magnitude of the hole injection barrier does not have a major effect on the electric displacement

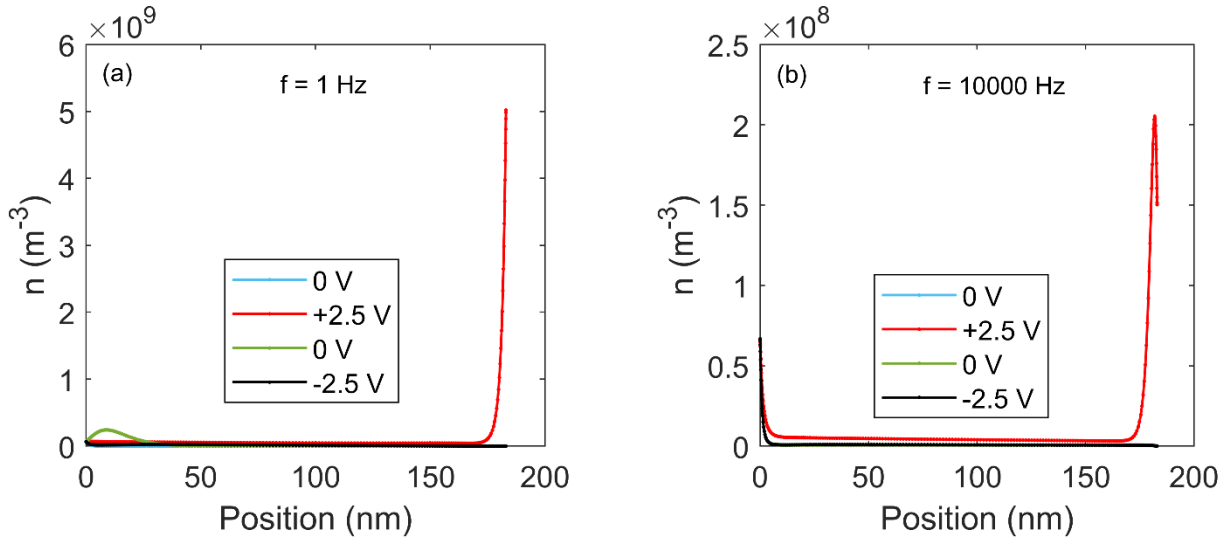

Figure 6.4**.** Simulated distribution of electrons across the $MAPbI_3$ layer at different applied voltages in downward and upward scan for (**a**) low frequency (1 Hz) and (**b**) high frequency regime (10 kHz).

loop. This demonstrates that the displacement response of the device is dominated by the ionic contribution.

6.2.6. Frequency dependence of *J-V* characteristics

In order to investigate the contribution of the electronic current experimentally, the *J-V* characteristics of the $MAPbI_3$-based capacitor were measured at different frequencies. For the *J-V* measurements, the reference capacitor in the Sawyer-Tower circuit (Figure 6.1c) was replaced by a reference resistor. Figure 6.5 shows the *J-V* characteristics of the device at different frequencies ranging from 1 Hz to 10 kHz, shown in more detail in Figure 6.6. Here the frequency *f* refers to the frequency of the applied voltage which is related to the scan rate via $f = \frac{1}{t}\frac{scan\ rate\ \left(\frac{V}{s}\right)}{4\times V_m}$ (where *t* and V_m are the period and the amplitude of the applied voltage, respectively). At a low frequency

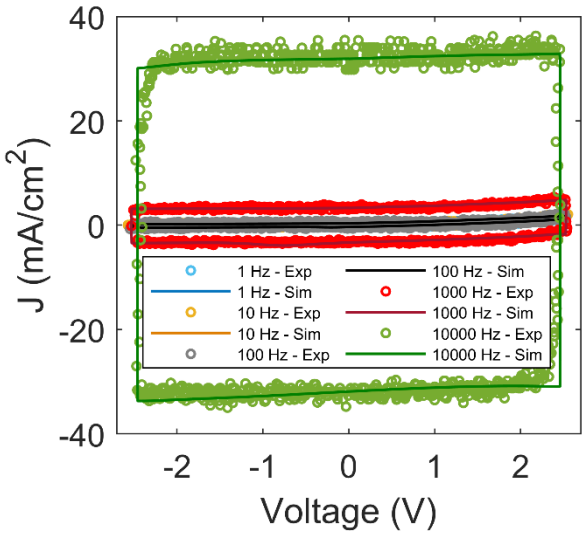

Figure 6.5**.** Experimental (circles) and simulated (solid lines) current density-voltage characteristics of an $MAPbI_3$ capacitor at different frequencies ranging from 1 Hz to 10 kHz. At low frequencies, the total current is small and dominated by the electronic current. At 10 kHz, the current is fully dominated by the displacement current.

of 1 Hz, the current is dominated by the low electronic current and the displacement current is negligible. However, as the frequency increases the contribution of the displacement current increases. At a high frequency of 10 kHz, the current is fully dominated by the displacement contribution, while the electronic current has a negligible contribution to the total current. This is evident from the large rectangular hysteretic loops appearing at higher frequencies.

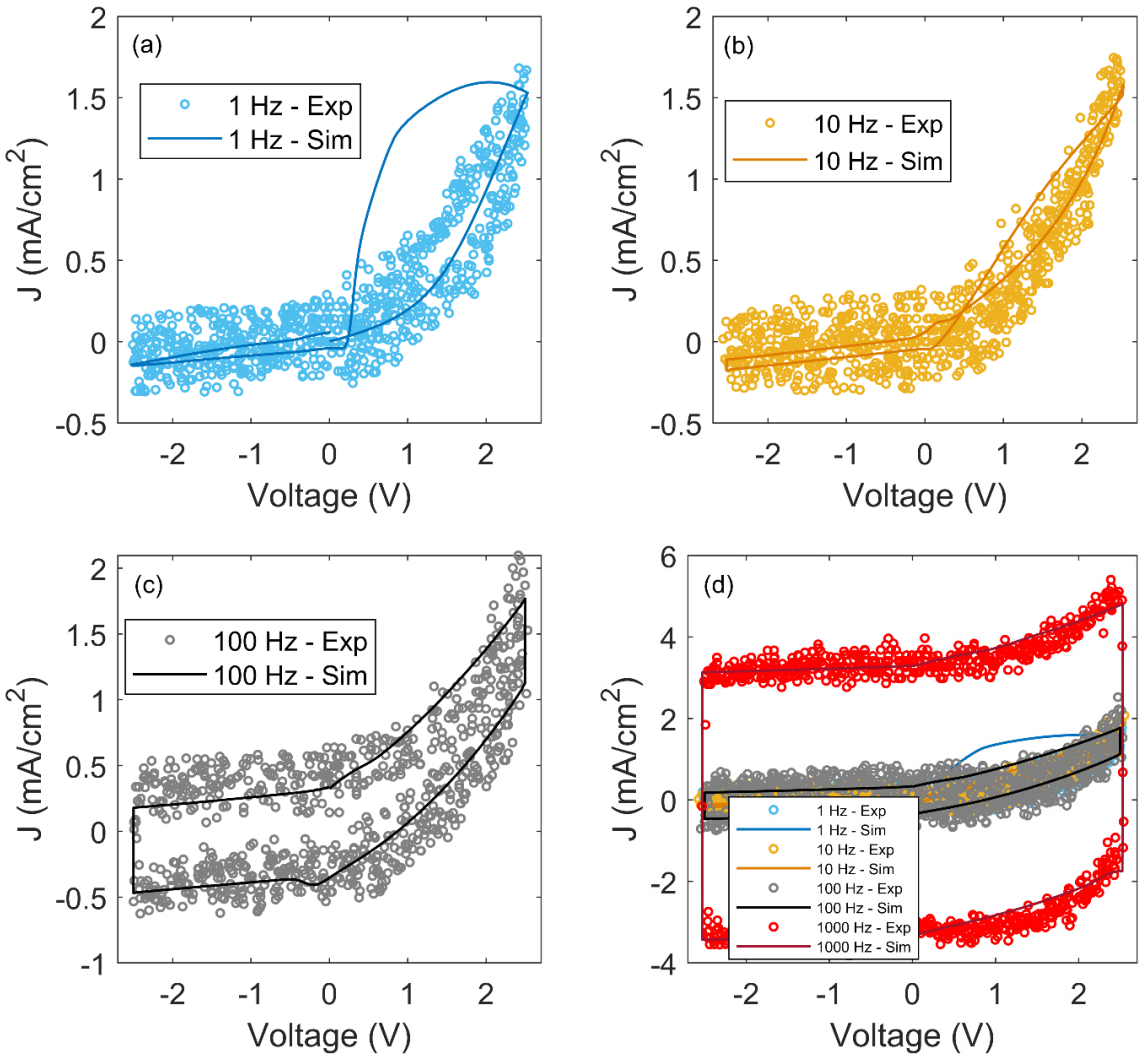

Figure 6.6**.** (**a**) The J-V of the $MAPbI_3$ capacitor at frequencies of 1 Hz, (**b**) 10 Hz, (**c**) 100 Hz, and (**d**) 1 kHz. The markers show the experimental J-V and the solid lines show the simulated J-V using the drift diffusion device model.

Using the device model with the same set of parameters that were used for calculating the *D*-*V* loops, the *J*-*V* characteristics of the $MAPbI_3$-based capacitor were simulated at different frequencies. The simulations reproduce the experiments, showing the appearance of large hysteresis with increasing frequency.

6.2.7. Importance of frequency-dependent permittivity of $MAPbI_3$

We also verified the need for taking into account a frequency dependent apparent dielectric constant[12] to model the displacement loops. As an example, we have re-calculated the electric displacement as a function of frequency with a fixed apparent dielectric constant of 67 (Figure 6.7b). This value of the dielectric constant can be directly obtained from the slope of the D-E graph at 10 kHz, as shown in Figure 6.7a. Keeping the rest of the input parameters similar we observe that for an apparent dielectric constant of 67 the magnitude of *D* at 1 Hz has strongly decreased to

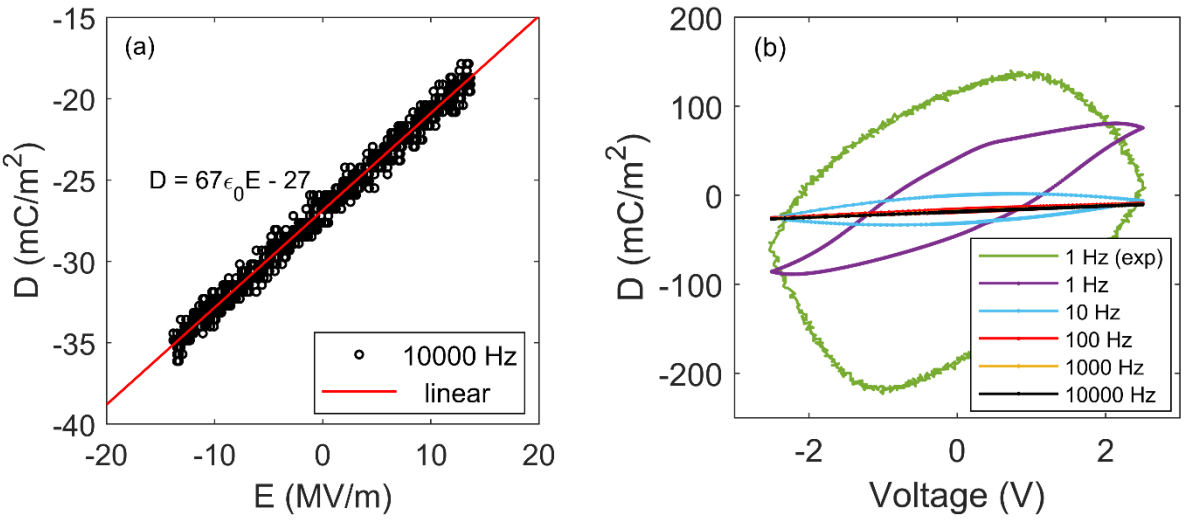

Figure 6.7**.** (**a**) Experimental electric displacement of the $MAPbI_3$-based capacitor as a function of electric field at frequency of 10 kHz. (**b**) *D*-*V* characteristics calculated with the high frequency apparent dielectric constant of $67\varepsilon_0$. Also shown is the experimental displacement loop at 1 Hz for comparison (green symbols).

a range of +80 to -90 mC/m^2, which is much lower than the experimental observations. When using the frequency dependent apparent dielectric constant as measured with impedance spectroscopy, the correct value for the electric displacement is obtained at all frequencies. As a result, a frequency dependent apparent dielectric constant is required to reproduce the experimental electric displacements.

6.2.8. Ion density, ion diffusion, and hole injection barrier dependence of *D-V* loops

In order to demonstrate the sensitivity of the calculated displacement loops on ion concentration and diffusion coefficient, the electric displacement at 1 Hz was calculated for a range of ion densities and diffusion coefficients (Figure 6.8a and Figure 6.8b). It is observed that changing the ion concentration within an order of magnitude drastically modifies the magnitude of the electric displacement. For example, an ion density of 5×10^{24} m^{-3} gives a variation in electric

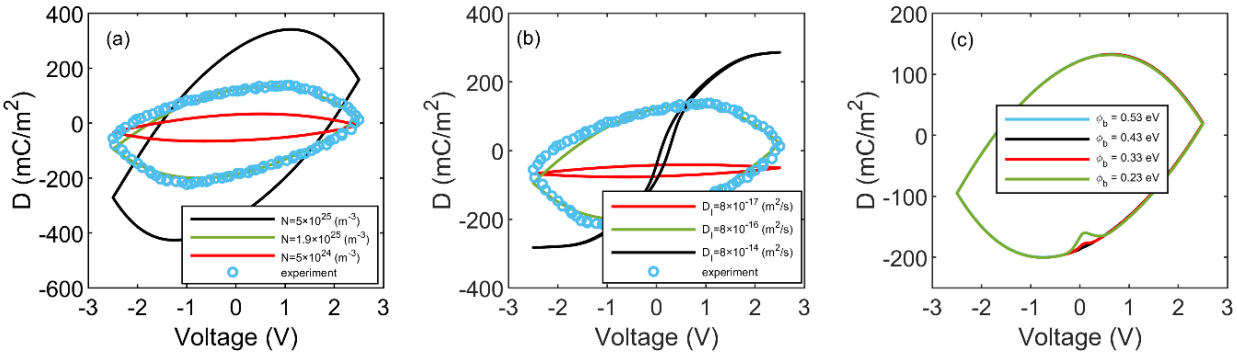

Figure 6.8. (**a**) Simulated electric displacement in a $MAPbI_3$ based capacitor as a function of voltage for different charge densities at 1 Hz compared with the experimental data. (**b**) Computed *D-V* characteristics of the $MAPbI_3$ based capacitor for various ionic diffusivity at frequency of 1 Hz. Also shown is the experimental displacement loop at 1 Hz for comparison (blue symbols). (**c**) simulated electric displacement in a $MAPbI_3$ based capacitor as a function of voltage for a range of injection barrier from 0.2 eV to 0.5 eV at 1 Hz.

displacement of +20 to -50 mC/m^2 which is much smaller than what is observed in experiment. Conversely, a large ion density of 5×10^{25} m^{-3} results in a much larger electric displacement ranging from +350 to -400 mC/m^2, much larger than the experimental values. The best fit of the experimental results is obtained with an intermediate ion concentration of 1.9×10^{25} m^{-3}.

As a next step the electric displacement was calculated for a range of ion diffusion coefficients, the ion density and the apparent dielectric constant were kept at the optimum value (Figure 6.8b). For a low ion diffusion coefficient to 8×10^{-17} m^2/s, there is only small hysteresis in the electric displacement, since the ions are not able to follow the variations in the applied electric field. An ion diffusivity of 8×10^{-16} m^2/s gives the maximum hysteresis, which quantitatively matches the corresponding experimental *D*-*V* loop. In this case, the ionic charges can partially follow the alteration of the electric field with some delay, giving rise to the characteristic hysteresis observed in experiment. By further increasing the ion diffusivity to than 8×10^{-14} m^2/s. the interface charge density can immediately follow the applied field and consequently negligible hysteresis in the electric displacement is observed. Most importantly, the obtained ion density of 1.9×10^{25} m^{-3} and diffusion coefficient of 8×10^{-16} m^2/s from modelling of the electric displacement are in excellent agreement with the values of 2×10^{25} m^{-3} and 1×10^{-15} m^2/s obtained from impedance analysis performed on the same device layout. As a result, the electric displacement measurements and device modelling independently confirm the ionic parameters directly obtained from impedance measurements.

We note that for ion diffusion coefficients > 10^{-13} m^2/s hysteresis is fully absent at a measurement frequency of 1 Hz, since the ions are sufficiently fast to follow the modulation completely. We note that from theoretical and experimental studies for I^- ions (or iodide vacancy) a broad range of activation energies (~ 0.1 to 0.6 eV)[10, 13-22] and diffusion coefficients ranging from

10^{-16} to 10^{-7} m^2/s, have been reported[10, 16, 20, 23-28]. For MA^+ ions, activation energies of ~ 0.4 eV to 1.1 eV and diffusion coefficients in the range of 10^{-15} m^2/s to 10^{-20} m^2/s have been reported[10, 13-15, 22-25, 27]. Due to the much higher activation energy and lower diffusivity of Pb^{2+} ions, they are approximately immobile at room temperature[10]. Here we observed that for high ion diffusion coefficients (>10^{-12} m^2/s) the maximum hysteresis in the electric displacement loops would occur around 10 kHz or higher, which is not observed in our experimental data. Although we cannot accurately distinguish the type of ions with our techniques, our experimental and simulation data show only ionic species with a diffusion coefficient of about 10^{-15} m^2/s are present in the perovskite layer. Such slow moving ions are consistent with the observed hysteresis in both electric displacement and *J-V* characteristics[4] at low frequencies.

Regarding ion concentrations reported values from simulations and theoretical models are rather high in the range of 10^{24} (m^{-3}) to 10^{25} (m^{-3}) [1, 4, 7, 10], whereas the experimentally measured values are often a few order of magnitude lower (in the range of 10^{21} m^{-3} to 10^{23} m^{-3}) [12, 17, 25, 26, 29-31]. As stated above, measurement of the electric displacement is a direct method to quantify ion concentrations, since the number of free carriers on the capacitor plate is nearly equal to the amount of accumulated ions at the interface. The obtained ion concentration of 2×10^{25} m^{-3} is furthermore verified by another independent experimental method. Our experiments combined with simulations show that the observed high electric displacement cannot be generated by ion densities in the range of only 10^{21} m^{-3} to 10^{23} m^{-3}. Only the higher range of ion density is consistent with both experiment and simulation.

6.2.9. Simulation of time-dependent electric potential across PSCs

Having demonstrated that the displacement characteristics can be accurately reproduced by simulations when using the correct apparent dielectric constant, ion concentration, and ion diffusion coefficient, we now turn to the implications of ionic movement for the potential distribution in perovskite solar cells. The potential profile of PSCs has been experimentally measured and numerically simulated[1, 2, 4, 6, 30]. Richardson et al. simulated the potential profile of a PSC and they reported an extremely narrow Debye layer with the width of 1.5 nm[4, 6]. Weber et al. successfully measured the potential distribution across a PSC based on mixed- cation mixed halide and recorded the time dependence of electric field distribution after a voltage step[30]. According to their observations, the relaxation time for the ions is slightly below one second. In addition, they reported a much larger value of Debye length[30]. Using our device model with experimentally-validated ion dynamics, we have simulated the "time-dependent" potential profile

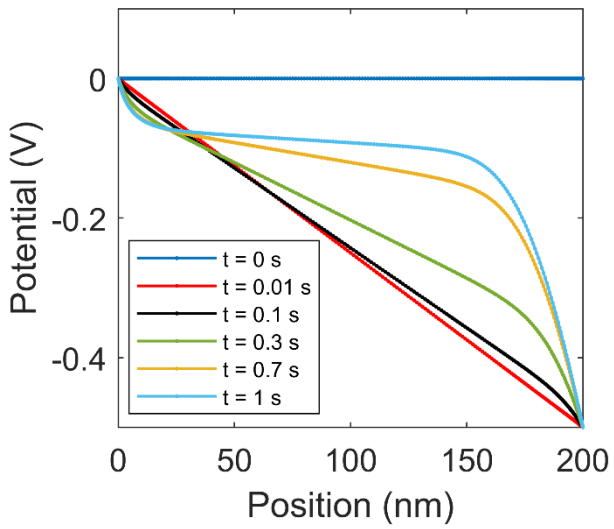

Figure 6.9**.** Simulated time-dependent electric potential across a perovskite layer in a solar cell. Potential distribution after reducing the applied voltage from 1 V (built-in voltage) to 0.5 V at $t = 0$. Here, the left and right sides are the hole and electron injecting, respectively.

in a perovskite solar cell after applying a voltage step. We assumed a solar cell device with built-in potential of 1 V. Initially, the device was kept under a bias of 1 V to compensate the effect of the built-in potential on the distribution of ionic charges. Then, a voltage step was applied to reduce the applied voltage to 0.5 V across the device. The potential profile across the device in response to the voltage step was calculated as a function of time, as displayed in Figure 6.9. At short timescales (10 ms) the ions are not sufficiently mobile to redistribute across the film. As a result, the electric potential linearly decreases across the device, which is equivalent to a uniformly distributed electric field across the perovskite layer. After a longer period of time the positive ions gradually reorganize and partially move toward the biased contact. For a relaxation time of 1 s, the system reaches to a steady state and the ions are approximately settled down in a new arrangement with a large population of ions accumulated at the interface. Although Weber et al. used a different composition of perovskite in their solar cell, this relaxation time is in the same range as their experimental value of 0.7 s[30]. As a result, we here demonstrate that the dynamical potential profile across a perovskite solar cell can be simulated with our device model. Qualitative comparison of the simulated potential profile by our device model and other reports of the experimental potential profile, shows that our validated ionic parameters are realistic.

6.3. Conclusion

In conclusion, we have developed a numerical device model with experimentally validated ion dynamics. In the previous chapter, the apparent dielectric constant, diffusion coefficient (D_{ion}=1×10^{-15} m^2/s) and concentration of ions (N_{ion}= 2×10^{25} m^{-3}) in $MAPbI_3$ were quantified using impedance spectroscopy. These numbers were confirmed independently by frequency-dependent displacement measurements and simulations. Using the developed electronic-ionic drift-diffusion

model, the experimental *D-V* loops of perovskite-based capacitors were accurately reproduced with identical ion concentration and diffusion coefficient as extracted from the impedance measurements. The frequency dependence of the impedance (previous chapter) and displacement measurements allows us to isolate the ionic contribution from the electronic contribution by the charge carriers.

The accurate description of the experimental electric displacement loops by our numerical simulations is an important step in the development of an experimentally-validated perovskite device model. As such a device model consists of many parameters, it is important to first isolate the ionic contribution to the device physics, prior to model the charge transport and full current-voltage characteristics of a perovskite solar cell. As first application of the model we have simulated the time-dependent potential profile in a $MAPbI_3$ solar cell, based on experimentally-validated parameters, which is dominated by the movement of ions in the layer.

6.4. References

1. Calado, P., *et al.* Evidence for ion migration in hybrid perovskite solar cells with minimal hysteresis. *Nat Commun* **7,** 13831 (2016).

2. van Reenen, S., Kemerink, M., & Snaith, H. Modeling anomalous hysteresis in perovskite solar cells. *J. Phys. Chem. Lett.* **6,** 3808-3814 (2015).

3. Sherkar, T.S. & Koster, L.J.A. Can ferroelectric polarization explain the high performance of hybrid halide perovskite solar cells? *Phys. Chem. Chem. Phys.* **18**, 331-338 (2016).

4. Richardson, G., *et al.* Can slow-moving ions explain hysteresis in the current–voltage curves of perovskite solar cells? *Energy Environ. Sci.* **9,** 1476-1485 (2016).

5. Neukom, M., *et al.* Consistent Device Simulation Model Describing Perovskite Solar Cells in Steady-State, Transient and Frequency Domain. *ACS Appl. Mater. Interfaces* **11,** 23320-23328 (2019).

6. O'Kane, S., *et al.* Measurement and modelling of dark current decay transients in perovskite solar cells. *J. Mater. Chem. C* **5,** 452-462 (2017).

7. Courtier, N.E., Richardson, G., & Foster, J.M. A fast and robust numerical scheme for solving models of charge carrier transport and ion vacancy motion in perovskite solar cells. *Appl. Math. Model.* **63**, 329-348 (2018).

8. Sherkar, T.S.*, et al.* Recombination in perovskite solar cells: significance of grain boundaries, interface traps, and defect ions. *ACS Energy Lett.* **2**, 1214-1222 (2017).

9. Sherkar, T.S., Momblona, C., Gil-Escrig, L., Bolink, H.J., & Koster, L.J.A. Improving perovskite solar cells: Insights from a validated device model. *Adv. Energy Mater.* **7**, 1602432 (2017).

10. Eames, C., *et al*. Ionic transport in hybrid lead iodide perovskite solar cells. *Nat Cmmun* **6,** 7497 (2015).

11. Sajedi Alvar, M., Kumar, M., Blom, P., Wetzelaer, G., & Asadi, K. Absence of ferroelectricity in methylammonium lead iodide perovskite. *AIP Adv.* **7,** 095110 (2017).

12. Almora, O., *et al*. Capacitive dark currents, hysteresis, and electrode polarization in lead halide perovskite solar cells. *J. Phys. Chem. Lett.* **6**, 1645-1652 (2015).

13. Haruyama, J., Sodeyama, K., Han, L. & Tateyama, Y. First-principles study of ion diffusion in perovskite solar cell sensitizers. *J. Am. Chem. Soc.* **137**, 10048-10051 (2015).

14. Azpiroz, J.M., Mosconi, E., Bisquert, J., & De Angelis, F. Defect migration in methylammonium lead iodide and its role in perovskite solar cell operation. *Energy Environ. Sci.* **8**, 2118-2127 (2015).

15. Meloni, S.*, et al.* Ionic polarization-induced current–voltage hysteresis in $CH_3NH_3PbX_3$ perovskite solar cells. *Nat Commun* **7**, 10334 (2016).

16. Delugas, P., Caddeo, C., Filippetti, A., & Mattoni, A. Thermally activated point defect diffusion in methylammonium lead trihalide: anisotropic and ultrahigh mobility of iodine. *J. Phys. Chem. Lett.* **7**, 2356-2361 (2016).

17. DeQuilettes, D.W.*, et al.* Photo-induced halide redistribution in organic–inorganic perovskite films. *Nat Commun* **7**, 11683 (2016).

18. Yu, H., Lu, H., Xie, F., Zhou, S., & Zhao, N. Native defect-induced hysteresis behavior in organolead iodide perovskite solar cells. *Adv. Funct. Mater.* **26**, 1411-1419 (2016).

19. Xing, J., *et al*. Ultrafast ion migration in hybrid perovskite polycrystalline thin films under light and suppression in single crystals. *Phys. Chem. Chem. Phys.* **18**, 30484-30490 (2016).

20. Yang, T.Y., Gregori, G., Pellet, N., Grätzel, M., & Maier, J. The Significance of Ion Conduction in a Hybrid Organic–Inorganic Lead-Iodide-Based Perovskite Photosensitizer. *Angew. Chem.* **127**, 8016-8021 (2015).

21. Pockett, A., *et al*. Microseconds, milliseconds and seconds: deconvoluting the dynamic behaviour of planar perovskite solar cells. *Phys. Chem. Chem. Phys.,* **19**, 5959-5970 (2017).

22. Game, O.S., Buchsbaum, G.J., Zhou, Y., Padture, N.P., & Kingon, A.I. Ions matter: description of the anomalous electronic behavior in methylammonium lead halide perovskite devices. *Adv. Funct. Mater.* **27**, 1606584 (2017).

23. Senocrate, A.*, et al.* The nature of ion conduction in methylammonium lead iodide: a multimethod approach. *Angew. Chem. Int. Ed.* **56**, 7755-7759 (2017).

24. Senocrate, A.*, et al.* Slow $CH_3NH_3^+$ Diffusion in $CH_3NH_3PbI_3$ under Light Measured by Solid-State NMR and Tracer Diffusion. *J. Phys. Chem. C,* **122**, 21803-21806 (2018).

25. Futscher, M. H., et al. Quantification of ion migration in $CH_3NH_3PbI_3$ perovskite solar cells by transient capacitance measurements. *Mater. Horiz.*, **6**, 1497-1503 (2019).

26. Bertoluzzi, L., *et al*. In Situ Measurement of Electric-Field Screening in Hysteresis-Free PTAA/$FA_{0.83}Cs_{0.17}Pb(I_{0.83}Br_{0.17})_3$/$C_{60}$ Perovskite Solar Cells Gives an Ion Mobility of~ 3×10^{-7} $cm^2/(V\ s)$, 2 Orders of Magnitude Faster than Reported for Metal-Oxide-Contacted Perovskite Cells with Hysteresis. *J. Am. Chem. Soc.* **140**, 12775-12784 (2018).

27. Yuan, Y., *et al.* Photovoltaic switching mechanism in lateral structure hybrid perovskite solar cells. *Adv. Energy Mater.* **5**, (2015).

28. Li, C., Guerrero, A., Huettner, S., & Bisquert, J. Unravelling the role of vacancies in lead halide perovskite through electrical switching of photoluminescence. *Nat Commun* **9**, 5113 (2018).

29. Belisle, R., *et al.* Interpretation of inverted photocurrent transients in organic lead halide perovskite solar cells: proof of the field screening by mobile ions and determination of the space charge layer widths. *Energy Environ. Sci.* **10,** 192-204 (2017).

30. Weber, S., *et al.* How the formation of interfacial charge causes hysteresis in perovskite solar cells. *Energy Environ. Sci.* **11,** 2404-2413 (2018).

31. Birkhold, S.T., *et al*. Direct observation and quantitative analysis of mobile frenkel defects in metal halide perovskites using scanning Kelvin probe microscopy. *J. Phys. Chem. C* **122**, 12633-12639 (2018).

Chapter 7

Space-Charge-Limited Electron and Hole Currents in Hybrid Organic-Inorganic Perovskites*

Summary

Hybrid organic-inorganic perovskites are promising materials for the application in solar cells and light-emitting diodes. However, the basic current-voltage behavior for electrons and holes is still poorly understood in these semiconductors due to their mixed electronic-ionic character. Here, we present the analysis of space-charge-limited electron and hole currents in the archetypical perovskite methyl ammonium lead iodide ($MAPbI_3$). We demonstrate that the frequency dependence of the permittivity plays a crucial role in the analysis of space-charge-limited currents and their dependence on voltage scan rate and temperature. Using a mixed electronic-ionic device model based on experimentally determined parameters, the current-voltage characteristics of single-carrier devices are accurately reproduced. Our results reveal that in our solution processed $MAPbI_3$ thin films transport of electrons dominates over holes. Furthermore, we show that the direction of the hysteresis in the current-voltage characteristics provide a fingerprint for the sign of the dominant moving ionic species.

*Publication: Sajedi Alvar, M., Blom. P.W.M., & Wetzelaer, G-J.A.H., *Nature Commun* **11**, 4023 (2020).

7.1. Introduction

As discussed in previous chapters, understanding the device physics of perovskite-based devices has proven not to be straightforward, which can mainly be traced back to the mixed ionic-electronic conduction behavior of these materials[1-9]. One particularly important aspect in understanding the behavior of perovskite-based electronic devices, is the characterization of the transport of electronic charges. As reviewed in chapter 1, over recent years, many techniques have been employed to measure the charge-carrier mobility in perovskites[10-21], giving a vast range of different numbers[22, 23]. The large differences observed in the measured charge-carrier mobility may, in part, be the result of different perovskite formulations and processing conditions, resulting in different film morphologies. However, also experimental techniques to measure the mobility can give rise to different values[22, 23]. For instance, time-resolved techniques may only probe fast charge carriers within crystal grains, while the slower transport of charges across grain boundaries and those affected by defect sites may be disregarded in these measurements. Such slower charge carriers may considerably impact the device performance.

A powerful technique that has proven its value in determining the time-averaged steady-state mobility of organic semiconductors, is the measurement of space-charge-limited currents[24, 25]. Space-charge-limited currents are observed in so-called electron- and hole-only devices, in which, by careful choice of the electrodes, either only electrons or holes are injected into the semiconductor. The maximum electrostatically allowed current in such a device is limited by the buildup of space charge. The space-charge density depends on the permittivity of the semiconductor, similar to a parallel-plate capacitor. The current will then be determined by the conductivity, being a product of the space-charge density and the charge-carrier mobility. In perovskites, classical space-charge-limited current (SCLC) theory has been used previously to

estimate the density of defects, or trapping sites, from measured current-voltage characteristics[10]. An important feature in the SCLC model is that the electric field resulting from the injected space charge exhibits a square-root dependence on distance from the injecting contact. However, it is well established that ion movement plays an important role in the shape, magnitude and hysteresis of the current-voltage characteristics of perovskite solar cells[5, 8, 26-28]. As slow-moving ions modify the electric field distribution in the device as a function of time it is evident that classical SCLC models are not applicable to mixed ionic-electronic semiconductors, such as perovskites. The ion dynamics and resulting field distributions will strongly affect the current-voltage characteristics in single-carrier devices, greatly complicating their analysis. Application of the SCLC model disregarding the effects of ions on permittivity and field distribution then leads to erroneous results regarding charge-carrier mobility and trapping sites. Although, there are numerous publications on SCLC measurements of perovskite single crystals and thin films, the effect of mobile ions, permittivity, and temperature on the current-voltage behavior are missing[10, 29-46]. To date, an accurate description of space-charge-limited currents in perovskite thin films does not exist. In this chapter, we investigate space-charge-limited currents in single-carrier devices of $MAPbI_3$, the work-horse material in perovskite solar cell research. As a central result, in this chapter, it is demonstrated that the frequency and temperature dependence of the apparent dielectric constant is of paramount importance in understanding the magnitude, the scan-rate dependence, and temperature dependence of space-charge-limited currents in perovskites. The developed device model with experimentally validated ion dynamics that was described in previous chapters, can consistently reproduce the scan-rate dependence and temperature dependence of the current voltage characteristics of electron-only and hole-only devices. The quantitative agreement allows for reliable determination of the electron and hole mobility from SCLC measurements on $MAPbI_3$

thin films. It is also demonstrated that the direction of the hysteresis in the electron and hole currents reveals the sign of the dominant mobile ionic species.

7.2. Results and Discussion

7.2.1. Device fabrication and characterization

For fabricating electron-only (hole-only) devices layers of Cr/Ag (Cr/Au) (1 nm/60 nm) was deposited as the bottom contact on a glass substrate by thermal evaporation in high vacuum. For Au/PTAA/$MAPbI_3$/Au hole only devices, a thin layer (10 nm) of polytriaryl amine (PTAA) was spin coated on the bottom Au electrode. A solution of Methylammonium Iodide (MAI) and Lead Acetate Trigydrate ($PbAc_2$) with a molar ratio of 3:1 in N,N-dimethylformamide (DMF) was prepared and spin coated on the substrate inside a nitrogen-filled glovebox[3]. The $MAPbI_3$ films were annealed at 100 °C for 30 minutes on a hot plate. The hole-only devices were finished by thermally evaporating a layer of Au (60 nm) as top electrode. For electron-only devices, 5 nm of C_{60} and 5 nm of TPBi were evaporated to achieve efficient electron injection into the $MAPbI_3$ layer. On top of that, a capping layer of Al (100 nm) was deposited by thermal evaporation. The area of the devices was 1 mm^2. Impedance measurements were performed using a computer-controlled Solartron impedance analyzer. The current-voltage measurements were carried out using a Keithley 2400 source meter. The scan rate dependent measurements were conducted using a Paios system from Fluxim. All the measurements were performed inside a nitrogen-filled glovebox.

Device simulations were performed using the formerly described experimentally validated electronic-ionic drift-diffusion model. The model includes both electronic and ionic conduction.

The ions are confined inside the perovskite layer by the ion-blocking contacts. The input ionic properties were experimentally quantified by impedance spectroscopy and electric displacement measurements as described in previous chapters[18]. For modelling the single-carrier devices, the injection barrier for the majority carriers is taken to be zero and the injection of the minority carriers was minimized by applying large injection barriers. Current-voltage calculations were conducted with the same protocol as the experimental measurements, including the voltage scan range and scan rate as well as the temperature. The effects of the electrode series resistance on the electron-only data were included in the simulation results.

7.2.2. Analysis of the relative permittivity of $MAPbI_3$

In the analysis of the current-voltage characteristics of $MAPbI_3$ perovskite solar cells in literature thus far, the dielectric constant (ε') was assumed to be frequency independent, having constant values typically ranging from 6 to 117[10, 26, 28-35, 37, 39-43, 45-51]. Also for other perovskites, the relative permittivity in the space-charge-limited current analysis was taken to be constant[10, 29-31, 33-35, 37, 39-43, 45, 46, 50, 51]. In Figure 7.1a, the frequency dependence of the dielectric constant is displayed, as obtained by impedance spectroscopy on $MAPbI_3$ capacitors. The relative permittivity is observed to be rather constant for frequencies above 100 Hz, having a value of 65, much higher than used in most device-modeling studies but consistent with earlier impedance results[52]. However, at lower frequencies, the dielectric constant increases considerably, up to two orders of magnitude higher. This apparent high dielectric constant at low frequencies is the result of slow moving ions[9].

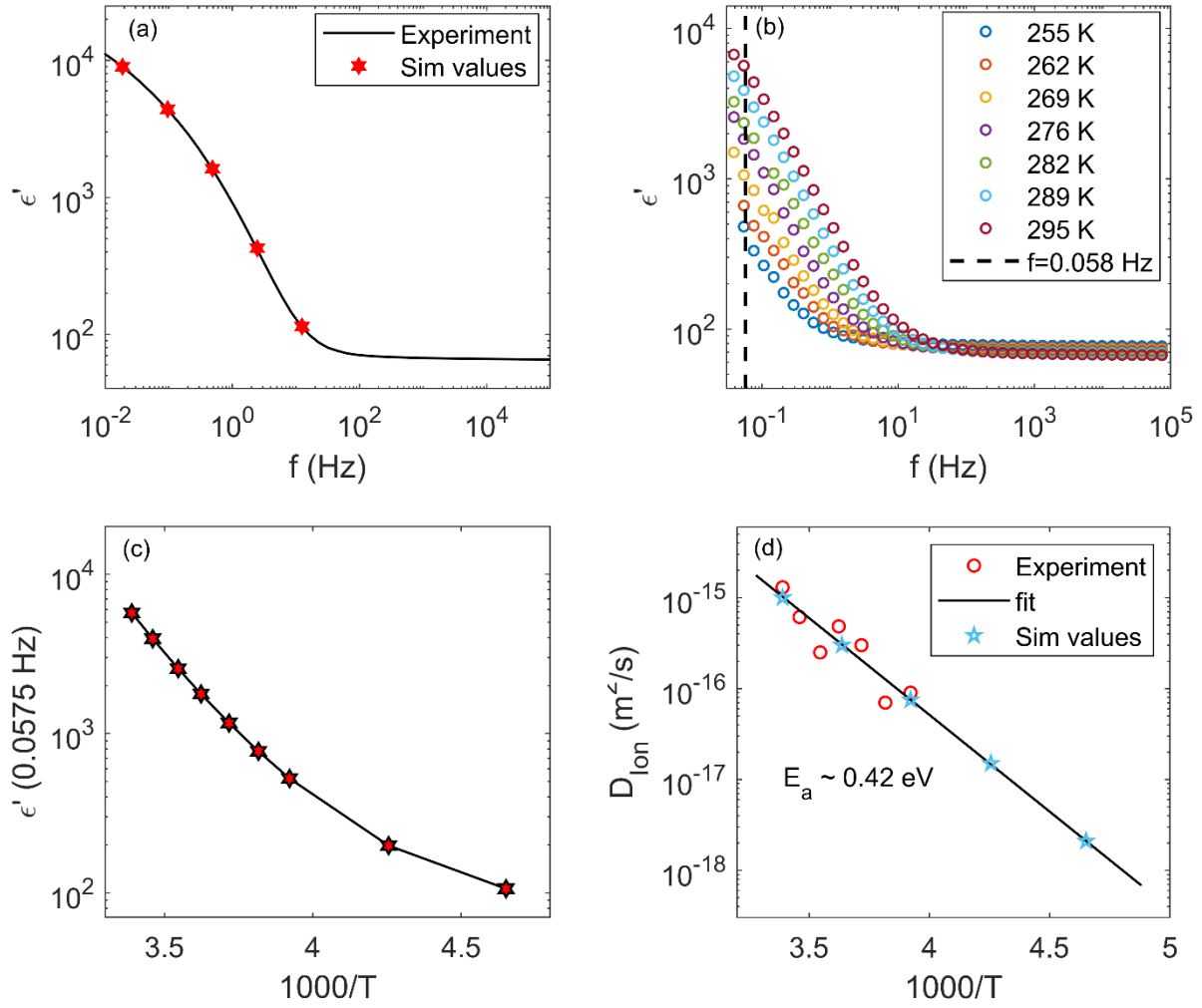

Figure 7.1**.** (**a**) The apparent dielectric constant of a $MAPbI_3$ thin films a function of frequency, obtained by impedance spectroscopy (black solid line). The red stars correspond to the apparent dielectric constant at the voltage scan rates used in the simulations (Sim values) in Figure 7.7. (**b**) Permittivity of $MAPbI_3$ thin film at different temperatures obtained by impedance spectroscopy. The low frequency permittivity significantly decreases by decreasing the temperature, which is accordance with the temperature dependence of ion diffusivity. High frequency exhibits a slight increase upon decreasing the temperature. (**c**) Temperature dependence of the apparent dielectric constant (red filled stars) at 0.0575 Hz (vertical dashed line in (**b**), corresponding to the scan rate of the temperature-dependent *J-V* measurements in Figure 7.2 and Figure 7.9. (**d**), Ion diffusion coefficient as a function of temperature, obtained from impedance spectroscopy (red circles). The measurements are fitted with an Arrhenius law with an activation energy of 0.42 eV (black line). The blue stars represent the ion diffusion coefficients used in the simulations.

As stated above, the dielectric constant has a direct influence on the magnitude of the space-charge-limited current, as it determines the amount of space charge that builds up in the semiconductor layer.

7.2.3. Characterization of electron- and hole-only devices

To measure space-charge-limited electron and hole currents, we have fabricated electron- and hole-only devices, as displayed in Figure 7.2. To optimize electron injection, a thin (5 nm) C_{60} layer was used, capped with a 5 nm TPBi buffer layer[53, 54]. The corresponding current density-voltage characteristics are displayed in Figure 7.2(c) and Figure 7.2(d). The electron-only device shows asymmetric current-voltage characteristics, which is due to the electron-injection barrier at the Ag bottom electrode (see Figure 7.3), resulting in a lower, injection-limited current in reverse bias. The hole-only device displays almost symmetric *J-V* characteristics. The hole current is observed to be lower than the electron current. We note that we observed this behavior for many similarly prepared samples over the course of several years.

When measuring a space-charge limited current in a single-carrier device, the scan rate is typically low (0.1 V s^{-1} to 1 V s^{-1}). As a result, slow moving ions can follow the changes in applied voltage, leading to small hysteresis in the measured current-voltage characteristics. This is shown for electron- and hole-only devices of $MAPbI_3$ in Figure 7.2. Considering the slow scan rate of 0.46 V s^{-1}, the question arises which value should be taken for the dielectric constant in the space-charge-limited-current analysis. Another important factor in the analysis is the influence of the moving ions on the electric-field distribution in the device, and thus the current. In many device modeling studies, the ion diffusivity and concentration are not known, and literature values are

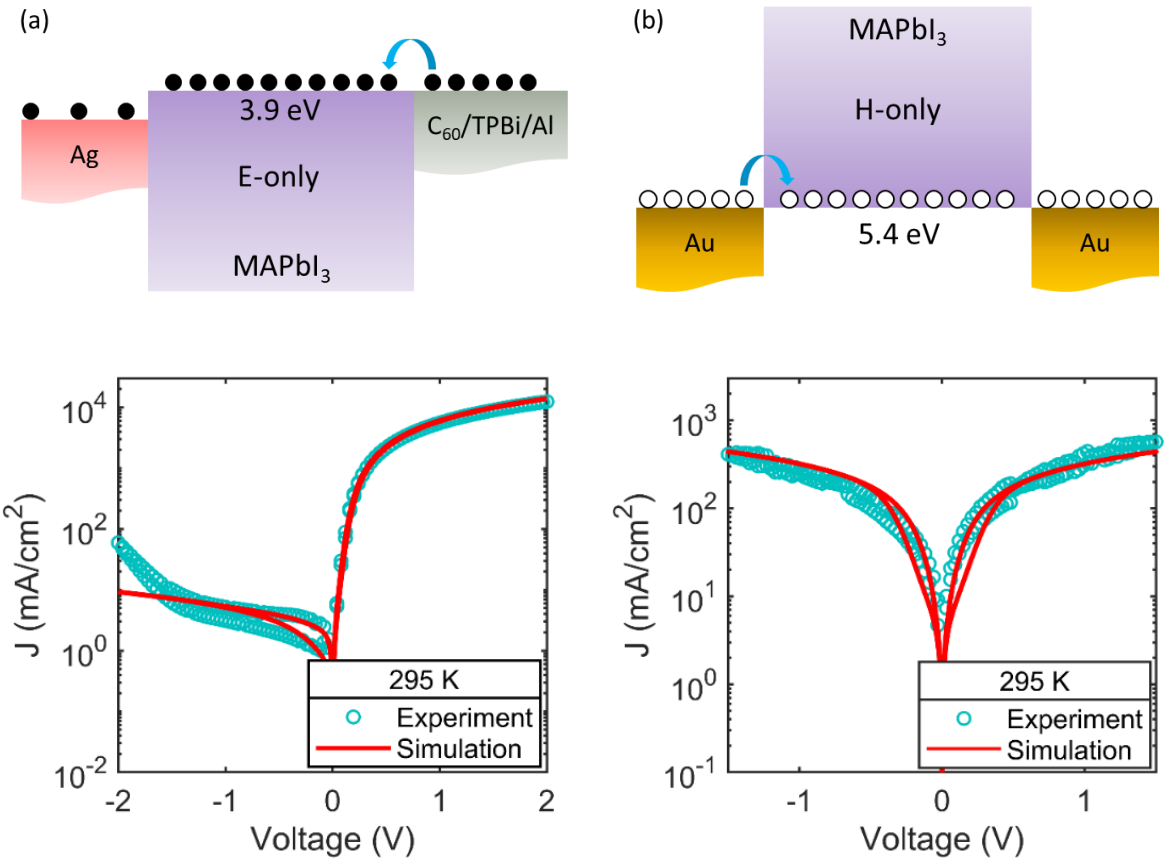

Figure 7.2. Schematic device structure and current density-voltage characteristics. (**a**) Electron-only device, using a C_{60}(5 nm)/TPBi(5 nm)/Al electron injection layer. Due to the barrier at the Ag bottom electrode, the current in reverse bias is injection limited. The dark cyan circles represent the electron current measured at room temperature, with a scan rate of 0.46 V s^{-1}. The red solid line shows the simulated electron current using the electronic-ionic drift-diffusion model with an apparent dielectric constant of 5700. (**b**) Schematic of the hole-only device, using Au bottom and top electrodes. The symbols and solid line represent the measured and simulated hole current, respectively, under the same conditions as the electron current (a).

taken, compromising the analysis. The situation is even more complicated when modeling complete solar cells including charge-transport layers, as the electron and hole mobility of all materials, the recombination rate, and possible charge-trapping effects are also not known accurately. By using all of these quantities as fit parameters, a reasonable agreement with experiment may be obtained, although a reliable analysis is near impossible without experimentally validating the input parameters in the model.

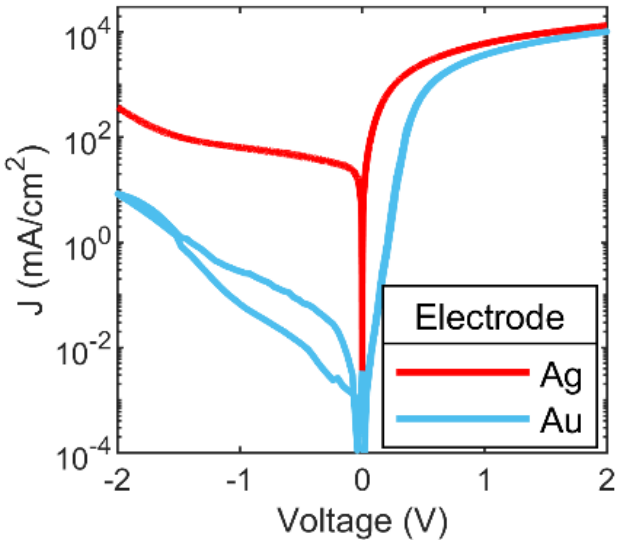

Figure 7.3. Current density-voltage characteristics of electron-only devices with different bottom electrodes. The work functions of Ag (4.6 eV) and Au (5.0 eV) result in different electron-injection barriers in reverse bias, which give rise to differences in the reverse-bias current and the built-in voltage. This shows that the asymmetric current-voltage characteristics in the electron-only devices are caused by the barrier at the bottom electrode.

Therefore, as described in previous chapters, in this thesis the ion diffusion coefficient (1×10^{-15} m^2 s^{-1}) and ion concentration (2×10^{25} m^{-3}) in similarly prepared $MAPbI_3$ films were determined and verified by using two independent techniques[9]. These techniques involved the analysis of impedance spectroscopy with a simple equivalent circuit for ionic conductors, and measurement of the electric displacement as a function of frequency, which could be reproduced with a mixed ionic-electronic drift diffusion model. It was demonstrated that the movement of ions completely dominates the displacement characteristics. Furthermore, it was observed that the drift-diffusion model could only reproduce the displacement characteristics when a frequency-dependent permittivity was used, as displayed in Figure 7.1a. In the analysis, it was assumed that positive ions are mobile and negative ions are fixed[9], based on previous studies. Likely candidates for the mobile positive ions are methylammonium ions or iodine vacancies[6, 28, 55].

Since in this thesis the dielectric constant, ion diffusivity, and ion concentration have been characterized experimentally, we can now fit the current-voltage characteristics of our single-carrier devices by tuning only the charge-carrier mobility. In this case, we have used an apparent relative dielectric constant of 5700, as measured at a frequency of 0.0575 Hz. This frequency corresponds to the voltage scan rate of the *J-V* measurements, $f = \frac{scan\ rate}{4 \times V_m}$, where V_m is the amplitude of the applied voltage (see Figure 7.4). We obtain a mobility of 1.2×10^{-6} $m^2\ V^{-1}s^{-1}$ for electrons and 3.5×10^{-10} $m^2\ V^{-1}s^{-1}$ for holes. We note that our extracted mobilities are comparable to values obtained by electrode-based mobility measurement techniques[22, 31, 34, 56, 57] and lower than the ones obtained by electrode-free techniques[18, 19, 22]. We note that the large variation in reported mobilities are likely the result of differences in sample morphologies, measurement techniques (e.g., different timescales), and their interpretation. For instance, as demonstrated here, classical SCLC analysis is not applicable to semiconductors with mobile ions. We further note that similarly low hole mobilities have been reported in $MAPbI_3$ field-effect transistors, also being a steady-state technique[58, 59].

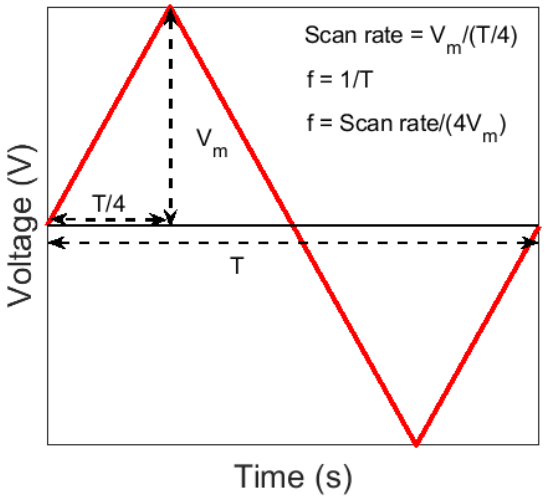

Figure 7.4. Applied voltage for current voltage measurements. The correlation between the scan rate and frequency is presented.

Although our electron and hole mobilities are in a range similar to earlier reported values for $MAPbI_3$ thin films of $\sim 4 \times 10^{-8}\ m^2\ V^{-1}\ s^{-1}$ obtained from time-of-flight measurements[56], we do not find ambipolar transport, but a clearly higher mobility for electrons as compared to holes. We verified that our hole currents are not limited by a contact barrier by comparing the hole injection from Au, PEDOT:PSS and PTAA into $MAPbI_3$ (Figure 7.5). Furthermore, with the inclusion of an injection barrier in the device model the shape of the *J-V* characteristics cannot be reproduced. We note that we cannot fully exclude that the low hole mobility originates from the presence of shallow hole traps[60], which in the classical model would give rise to an SCLC in which the mobility is replaced by an 'effective mobility' defined by the product $\mu\theta$. Here, μ is the mobility without shallow traps, which is reduced by a factor θ, being the fraction of free carriers with regard to the total amount of injected carriers. The effective mobility $\mu\theta$ can thus be considerably lower than the free charge-carrier mobility μ. In this case the measured current has

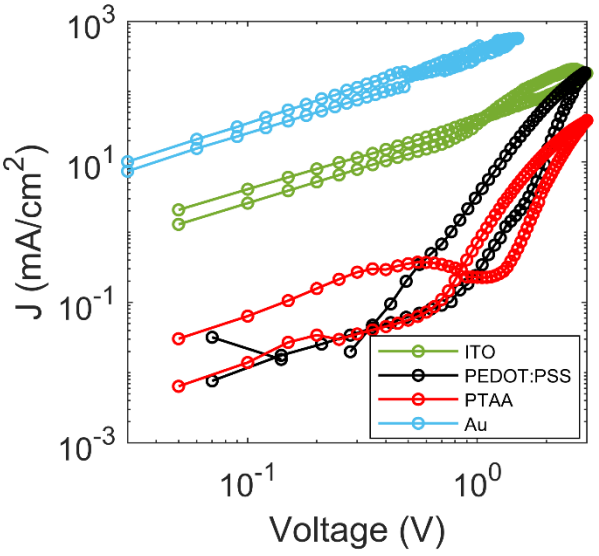

Figure 7.5. Comparison of hole injection from different hole injection layers. The Au contact shows the highest current as compared to ITO, PEDOT:PSS and PTAA. Furthermore, at low voltage the current density for the Au contact shows a linear dependence on voltage, whereas the injection-limited currents from the other electrodes show a steeper dependence.

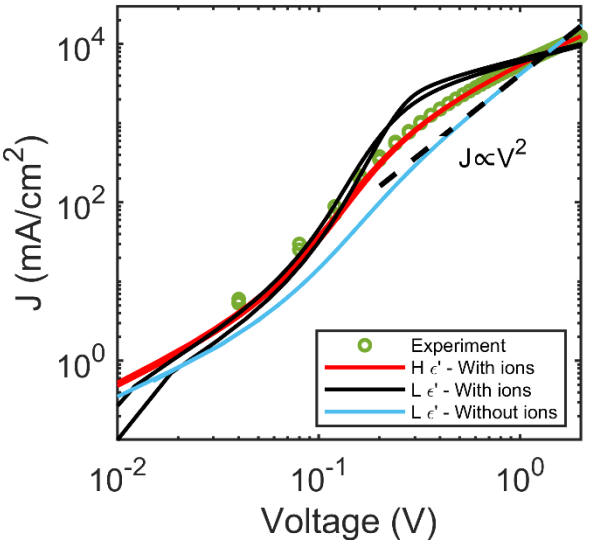

Figure 7.6. Experimental (symbols) and modelled electron-only current. The modelled electron currents include a high permittivity and ion movement (red line), a low permittivity and ion movement (black line) and a low permittivity without ions (classical SCLC model) (blue line).

all the features of an SCLC, except that the obtained mobility represents an effective mobility. However, this does not change our conclusion that the charge transport is highly unbalanced and electron dominated. Furthermore, it should be noted that the high current in forward bias in the electron-only device is limited by the series resistance of the electrodes, despite our attempts to reduce this resistance as much as possible in the fabricated devices. Therefore, the determined electron mobility should be viewed as a lower limit.

Since a space-charge-limited current is essentially determined by the product of the permittivity and the (effective) mobility, a question is whether a fit could also be obtained when assuming a lower value for the permittivity, as obtained at higher frequencies (Figure 7.1). As shown in Figure 7.6, by assuming a lower value of the permittivity the shape of the *J*-*V* characteristics cannot be reproduced, irrespective of the chosen mobility.

7.2.4. Scan-rate dependence of the SCLC

To further confirm whether the frequency-dependent permittivity should be used in the space-charge-limited current analysis, we have performed current-voltage measurements as a

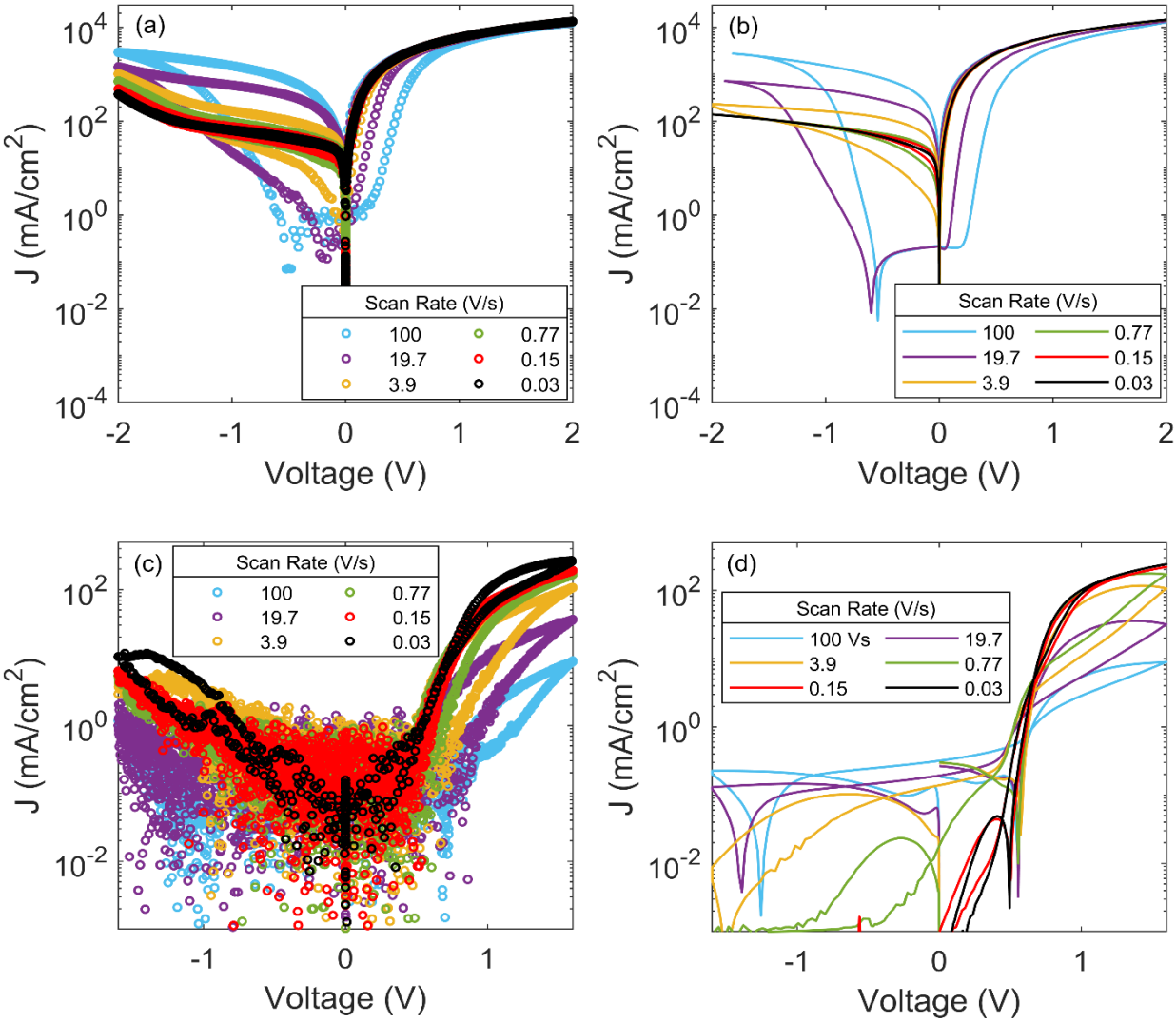

Figure 7.7. Current density-voltage characteristics of single-carrier devices for different voltage scan rates. The measurements (symbols) for the electron-only (**a**) and hole-only (**c**) device are reproduced by the corresponding simulations (solid lines) in panel (**b**) and (**d**), respectively. The hole-only device in an Au/$MAPbI_3$/PTAA/Au configuration shows slightly asymmetric characteristics. The simulations incorporate a scan rate-dependent dielectric constant, resulting in a correct description of both the magnitude of the current and the hysteresis behavior.

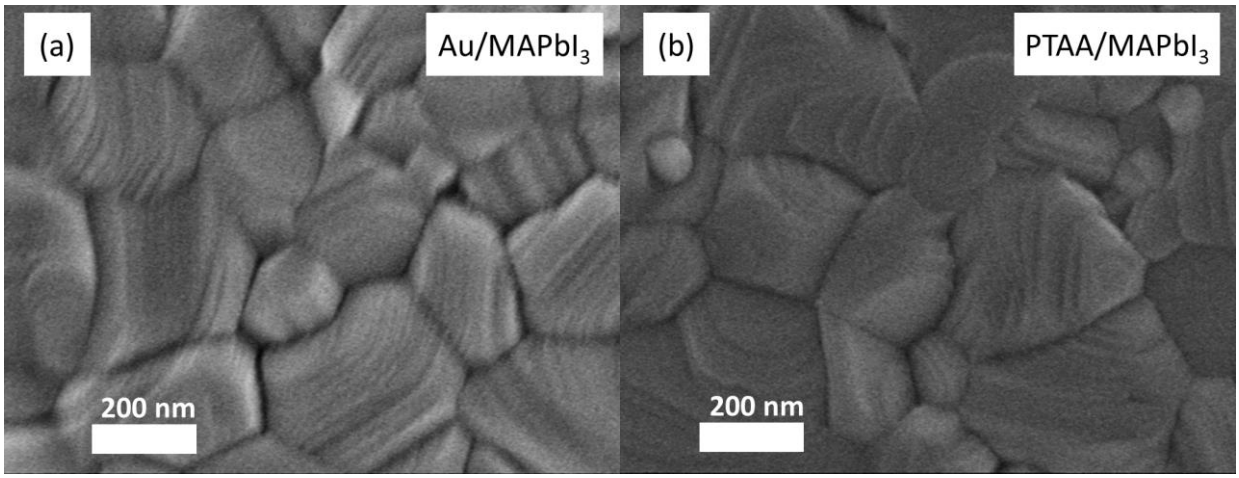

Figure 7.8 | Scanning electron microscopy images of the perovskite film on top of Au (**a**) and PTAA (**b**).

function of scan rate, as displayed in Figure 7.7a and Figure 7.7c. As shown in Figure 7.7b and Figure 7.7d the scan-rate dependence of the current-voltage characteristics can only be completely reproduced by considering the frequency dependence of the permittivity for every scan rate (red stars in Figure 7.1a). While the electron current in forward bias is limited by the electrode series resistance at higher applied voltages, it is observed that the hole current in the hole-only device increases with decreasing scan rate, in accordance with the higher permittivity measured at lower frequencies. This increase cannot be reproduced by assuming a constant, scan-rate independent permittivity. The quality of the $MAPbI_3$ thin films formed on Au and PTAA covered substrate is provided in Figure 7.8. It can be recognized that the morphology and grain size of the films produced on both substrates is similar.

7.2.5. Temperature dependence of the SCLC

The relative permittivity also controls the temperature dependence of the electron and hole currents. As displayed in Figure 7.1b and Figure 7.1c, the quasi-static dielectric constant at a frequency of 0.0575 Hz decreases with decreasing temperature, which is associated with a decrease

in ion diffusivity, as shown in Figure 7.1d. Both these quantities are determined by impedance spectroscopy on $MAPbI_3$ capacitors. The temperature-dependent dielectric constant directly results in a temperature dependence of the space-charge-limited currents, as displayed in Figure 7.9. The device simulations correctly reproduce the temperature dependence, using the measured

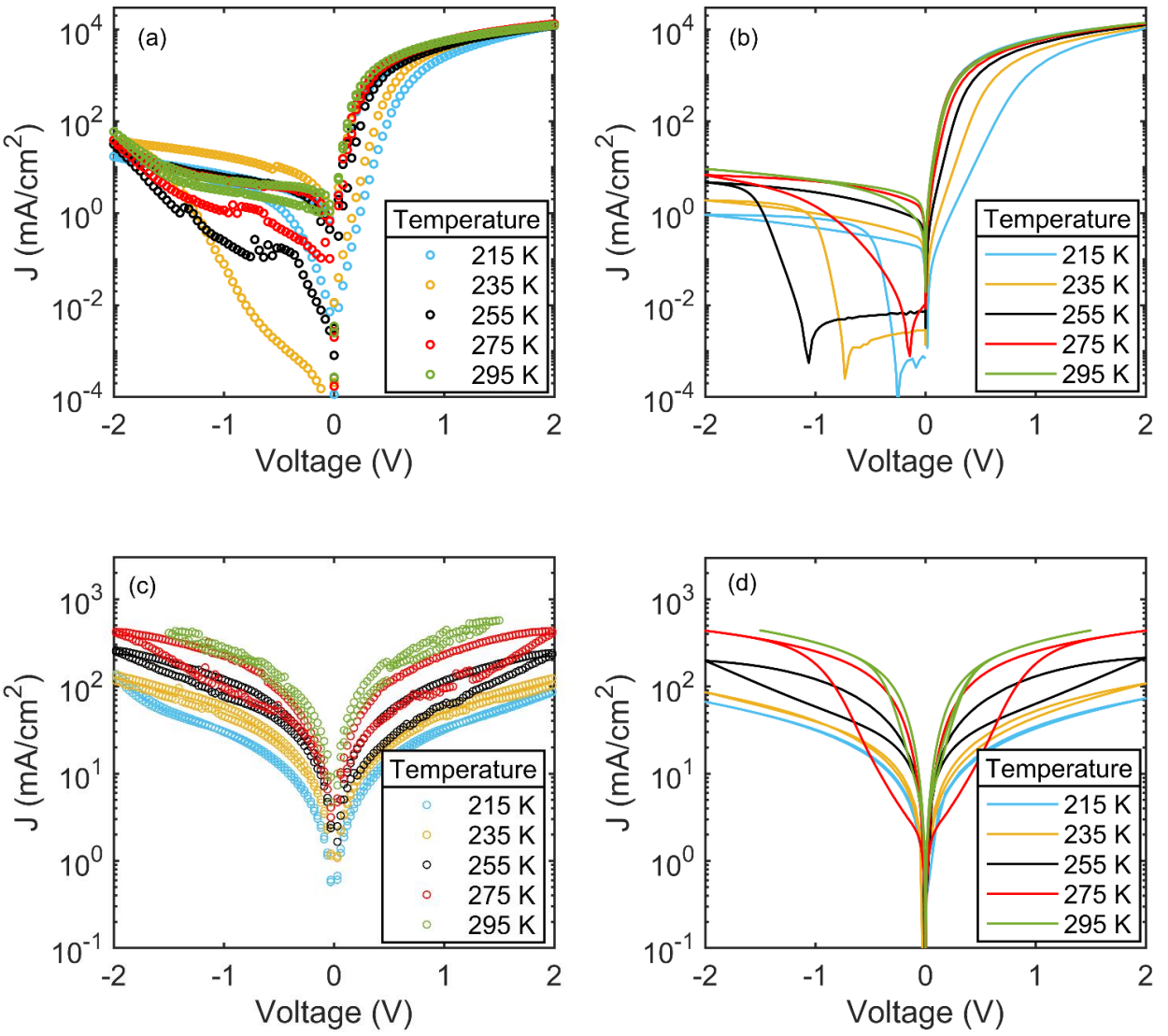

Figure 7.9. Temperature-dependent current density-voltage characteristics of single-carrier devices. The electron (**a**) and hole (**c**) currents (symbols) were measured from 295 K to 215 K at a scan rate of 0.46 V s^{-1}. The simulations (solid lines) of the electron-only (**b**) and hole-only (**d**) device reproduce the experiments by using a temperature-dependent dielectric constant and ion diffusion coefficient, using the values as displayed in Figure 7.1c and Figure 7.1d.

temperature-dependent permittivity (Figure 7.1c) as input, while keeping the charge-carrier mobility constant. In addition, the hysteresis behavior is also correctly reproduced by the model, using the temperature-dependent diffusivity as shown in Figure 7.1d. With regard to the hole-only current at low temperatures the ions are so slow that they cannot follow the voltage scan, resulting in the absence of hysteresis. With increasing temperature the ions become more mobile and the hysteresis increases. At room temperature the further increased ion mobility reduces the hysteresis again, since the ions are sufficiently fast to follow the applied voltage signal. The hysteresis behavior of the electron-only is more complex due to the presence of a built-in voltage. The built-in voltage leads to diffusion of ions, in this case positive ions to the exiting contact, already at zero applied bias. At low temperatures the immobile ions stay at this contact, independent of the applied voltage, which can give rise to negative electric fields in the device and large hysteresis. The effect of ion movement on the hysteresis will be discussed in more detail below. We note that a sharp

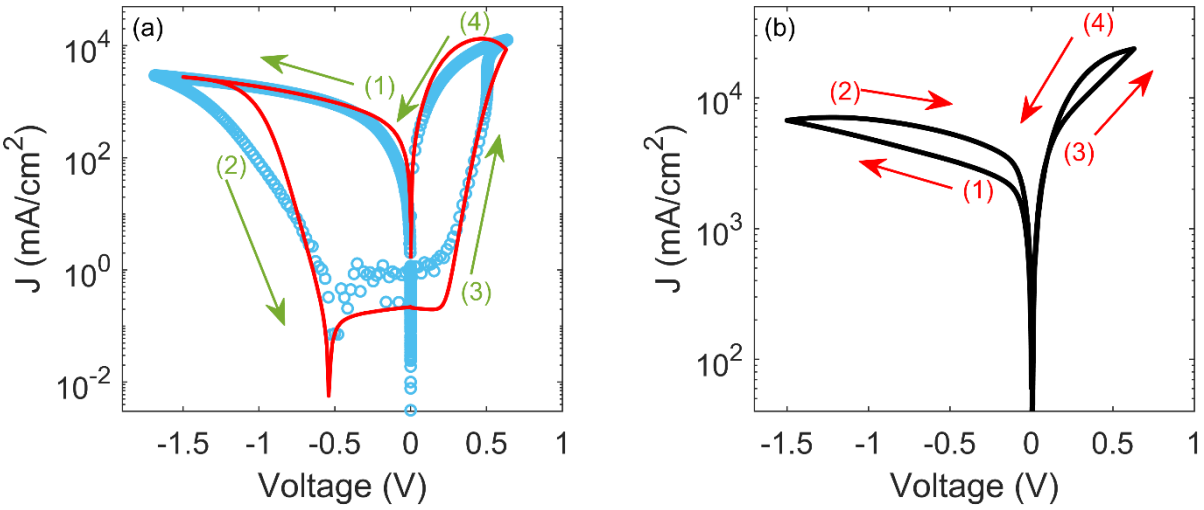

Figure 7.10. Experimental (symbols) and calculated current density-voltage characteristics of an electron-only device at 295 K at a high scan rate (100 V/s). The electron current is simulated with the same set of parameters under two different conditions for ionic charges: mobile positive ions and a uniform distribution of immobile negative ions (**a**) and mobile negative ions and a uniform distribution of immobile positive ions (**b**).

increase is present in the experimental injection-limited current in high reverse bias, especially noticeable in the electron-only devices at higher temperatures. This might be associated with field-assisted charge injection, which will be enhanced by the accumulation of ions at the contact.

The accurate agreement between our experiments and simulations, based on experimentally determined parameters, demonstrates that the space-charge-limited current behavior in perovskites is completely governed by the temperature dependence of ion dynamics and the associated temperature and frequency-dependent permittivity. We note that temperature dependent mobilities have been reported using different techniques, but in all cases the frequency and temperature dependence of permittivity due to ion dynamics-were not taken into account in the interpretation of the data[15, 19, 20, 45, 56, 57, 61-64]. We cannot fully exclude a very small temperature dependence of the charge carrier mobility, but if present, is fully overwhelmed by the temperature dependence of the permittivity and therefore of no relevance for the description of the SCLC.

7.2.6. Influence of ion motion on SCLCs

Thus far, we have assumed that only positive ions are mobile in the simulations, which excellently reproduces the direction of hysteresis in the experimental data, as displayed in Figure 7.11a. Here, the arrows and numbers represent the voltage scan direction. A question is whether this assumption also has an effect on the analysis of the space-charge-limited currents. For this reason, we have also performed simulations by assuming negative ions to be mobile and positive ions to be fixed, but keeping all other parameters the same. As a first case, we consider the hole transport at 275 K, where the hysteresis is maximal. Strikingly, as shown in Figure 7.11b, the direction of the hysteresis is reversed when assuming mobile negative ions. A similar observation is obtained for electron-only devices (Figure 7.10). Also here, only mobile positive carriers provide

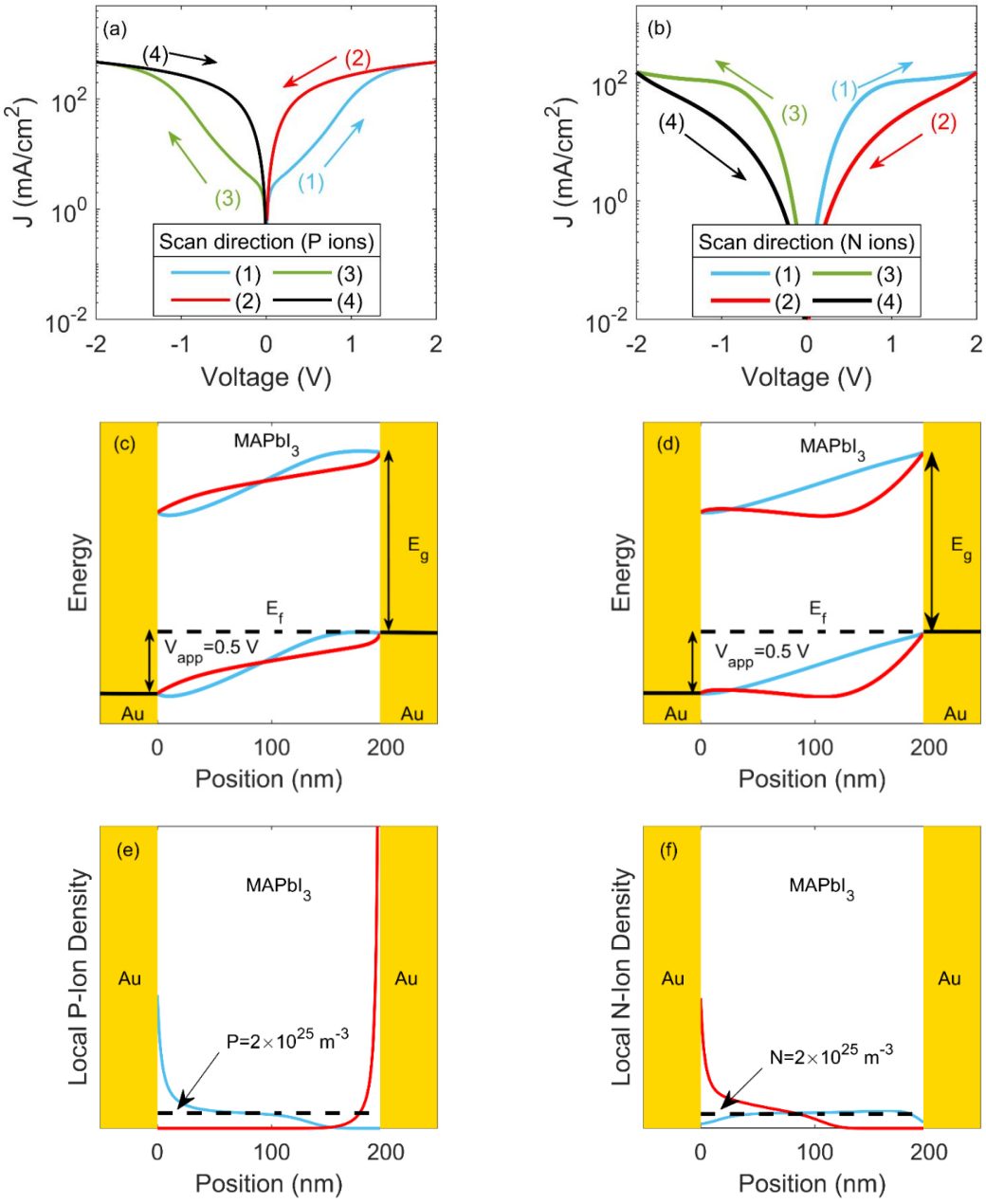

Figure 7.11. Current density-voltage characteristics of a hole-only device at 275 K. The current-density voltage characteristics (solid lines) are simulated with the same set of parameters under two different conditions for ionic charges: mobile positive ions and a uniform density of immobile negative ions (**a**) and mobile negative ions and immobile positive ions (**b**). The corresponding energy band diagrams and ion distributions for mobile positive ions (**c**) and (**e**) as well as mobile negative ions (**d**) and (**f**) are displayed at a forward bias of 0.5 V for the up scan (blue solid lines) and down scan (red solid lines). The dashed lines in (e) and (f) indicate the average ion densities.

the correct direction of the hysteresis. We note that for the electron-only we modeled experiments at higher scan rate, since the hysteresis is there more pronounced.

To explain this behavior in more detail, the energy band diagrams of the hole-only device at an applied voltage of 0.5 V are displayed in Figure 7.11c and Figure 7.11d. Consider the example of a hole-only device with positive ions. On the up scan (from 0 to 2 V, forward bias), the positive ions will migrate in the direction of the negatively-biased (right) electrode, at which the holes are extracted. Since these ions move slowly, the accumulation of ions at the extracting electrode at a bias voltage of 0.5 V is still rather limited, (Figure 7.11a, (1)), having a minor influence on the electric-field distribution across the device (Figure 7.11c). However, on the down scan (Figure

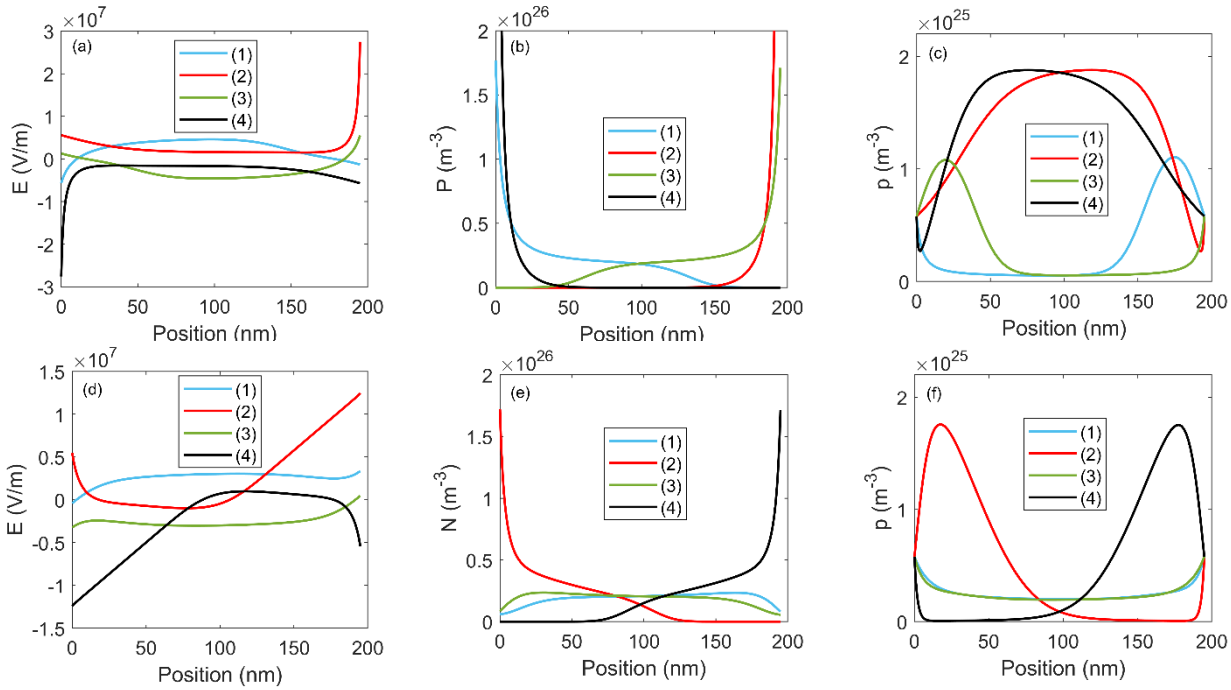

Figure 7.12. Electric field, ion and hole concentration profiles. The electric fields (**a**), ion (**b**) and hole (**c**) distributions for mobile positive ions at forward (blue and red) and reverse (green and black) bias of 0.5 V corresponding to the Figure 7.11a. The electric fields (**d**), ion (**e**) and hole (**f**) distributions for mobile negative ions at forward (blue and red) and reverse (green and black) bias of 0.5 V corresponding to the Figure 7.11b.

7.11a, (2)), the positive ions have migrated further away from the positively biased electrode (Figure 7.11c), resulting in positive ion depletion and an associated positive field near the hole injection electrode, enhancing the injection of holes. This results in a higher current in the down scan (Figure 7.11a, (2). In the case of negative ions, the ions migrate toward the positively biased, hole injecting electrode, where they screen the applied field (Figure 7.11b, (1)). Also in this case, the ions are distributed relatively uniformly on the up scan (Figure 7.11d), whereas the field screening limits hole injection on the down scan, and, in turn, a decreased hole current is observed (Figure 7.11b, (2)). The corresponding electric field, hole and ion concentration profiles for both cases are shown in Figure 7.12. As a result, the direction of the hysteresis in $MAPbI_3$ single-carrier devices directly reveals the sign of the moving ionic species.

7.3. Conclusion

In conclusion, in this chapter we have demonstrated the importance of temperature-dependent ion dynamics and a temperature as well as frequency-dependent apparent dielectric constant on the analysis of space-charge-limited currents in hybrid organic-inorganic perovskites. We have developed a device model that can reproduce the scan-rate and temperature dependent current-voltage characteristics with only experimentally validated parameters as input. The sign of the dominant mobile ionic species can be determined by the direction of the hysteresis in electron- and hole-only devices. The basic understanding of electron and hole currents in perovskite layers is an important step in the direction of unravelling the device physics of perovskite solar cells and light-emitting diodes, in which charge recombination is an additional factor that needs to be taken into account. Only by successive experimental validation of separate factors, such as ion dynamics

and charge transport, perovskite device models can be built up with increasing complexity, containing a large body of input variables.

7.4. References

1. Snaith, H., *et al.* Anomalous hysteresis in perovskite solar cells. *J. Phys. Chem. Lett.* **5,** 1511-1515 (2014).

2. Frost, J., & Walsh, A. What is moving in hybrid halide perovskite solar cells? *Acc. Chem. Res.* **49,** 528-535 (2016).

3. Sajedi Alvar, M., Kumar, M., Blom, P., Wetzelaer, G., & Asadi, K. Absence of ferroelectricity in methylammonium lead iodide perovskite. *AIP Adv.* **7,** 095110 (2017).

4. Belisle, R., *et al.* Interpretation of inverted photocurrent transients in organic lead halide perovskite solar cells: proof of the field screening by mobile ions and determination of the space charge layer widths. *Energy Environ. Sci.* **10,** 192-204 (2017).

5. Tress, W., *et al*. Understanding the rate-dependent J–V hysteresis, slow time component, and aging in $CH_3NH_3PbI_3$ perovskite solar cells: the role of a compensated electric field. *Energy Environ. Sci.* **8,** 995-1004 (2015).

6. Eames, C., *et al*. Ionic transport in hybrid lead iodide perovskite solar cells. *Nat Commun* **6,** 7497 (2015).

7. Calado, P., *et al.* Evidence for ion migration in hybrid perovskite solar cells with minimal hysteresis. *Nat Commun* **7,** 13831 (2016).

8. Weber, S., *et al.* How the formation of interfacial charge causes hysteresis in perovskite solar cells. *Energy Environ. Sci.* **11,** 2404-2413 (2018).

9. Sajedi Alvar, M., Blom, P. W. M., & Wetzelaer, G.-J. A. H. Device Model for Methylammonium Lead Iodide Perovskite With Experimentally Validated Ion Dynamics. *Adv. Electron. Mater.* 1900935 (2020).

10. Shi, D., *et al.* Low trap-state density and long carrier diffusion in organolead trihalide perovskite single crystals. *Science* **347,** 519-522 (2015).

11. DeQuilettes D.*, et al.* Photo-induced halide redistribution in organic–inorganic perovskite films. *Nat Commun* **7,** 11683 (2016).

12. Wang, K., *et al.* P-type mesoscopic nickel oxide/organometallic perovskite heterojunction solar cells. *Sci Rep* **4,** 4756 (2015).

13. Stranks, S., *et al.* Electron-hole diffusion lengths exceeding 1 micrometer in an organometal trihalide perovskite absorber. *Science* **342**, 341-344 (2013).

14. Labram, J., *et al.* Charge transport in a two-dimensional hybrid metal halide thiocyanate compound. *J. Mater. Chem. C* **5,** 5930-5938 (2017).

15. Milot, R., Eperon, G., Snaith, H., Johnston, M., & Herz, L. Temperature-dependent charge-carrier dynamics in $CH_3NH_3PbI_3$ perovskite thin films. *Adv. Funct. Mater.* **25,** 6218-6227 (2015).

16. Leijtens, T., *et al.* Mapping Electric Field-Induced Switchable Poling and Structural Degradation in Hybrid Lead Halide Perovskite Thin Films. *Adv. Energy Mater.* **5,** 1500962 (2015).

17. Takahashi, Y., Hasegawa, H., Takahashi, Y., & Inabe, T. Hall mobility in tin iodide perovskite $CH_3NH_3SnI_3$: evidence for a doped semiconductor. *J. Solid State Chem.* **205,** 39-43 (2013).

18. Lim, J., *et al.* Elucidating the long-range charge carrier mobility in metal halide perovskite thin films. *Energy Environ. Sci.* **12,** 169-176 (2019).

19. Biewald, A., *et al*. Temperature-Dependent Ambipolar Charge Carrier Mobility in Large-Crystal Hybrid Halide Perovskite Thin Films. *ACS Appl. Mater. interfaces* **11,** 20838-20844 (2019).

20. Yi, H.T., Wu, X., Zhu, X., Podzorov, V. Intrinsic Charge Transport across Phase Transitions in Hybrid Organo-Inorganic Perovskites. *Adv. Mater.* **28,** 6509-6514 (2016).

21. Shrestha, S., *et al.* High-performance direct conversion X-ray detectors based on sintered hybrid lead triiodide perovskite wafers. *Nature Photon* **11,** 436-440 (2017).

22. Peng, J., Chen, Y., Zheng, K., Pullerits, T., & Liang, Z. Insights into charge carrier dynamics in organo-metal halide perovskites: from neat films to solar cells. *Chem. Soc. Rev.* **46,** 5714-5729 (2017).

23. Herz, L. Charge-carrier mobilities in metal halide perovskites: fundamental mechanisms and limits. *ACS Energy Lett.* **2,** 1539-1548 (2017).

24. Lampert, M. Simplified theory of space-charge-limited currents in an insulator with traps. *Phys. Rev.* **103,** 1648 (1956).

25. J. V. D. Electronic processes in ionic crystals (Mott, N. F.; Gurney, R. W.). *J. Chem. Educ.* **42,** A692 (1965).

26. van Reenen, S., Kemerink, M., & Snaith, H.. Modeling anomalous hysteresis in perovskite solar cells. *J. Phys. Chem. Lett.* **6,** 3808-3814 (2015).

27. Chen, B., Yang, M., Priya, S., & Zhu, K. Origin of J–V hysteresis in perovskite solar cells. *J. Phys. Chem. Lett.* **7,** 905-917 (2016).

28. Richardson, G., *et al.* Can slow-moving ions explain hysteresis in the current–voltage curves of perovskite solar cells? *Energy Environ. Sci.* **9,** 1476-1485 (2016).

29. Pospisil, J., *et al*. Density of bulk trap states of hybrid lead halide perovskite single crystals: temperature modulated space-charge-limited-currents. *Sci Rep* **9,** 3332 (2019).

30. Duijnstee, E.A., *et al*. Towards Understanding Space-charge Limited Current Measurements on Metal Halide Perovskites. *ACS Energy Lett.* **5,** 376-384 (2020).

31. Lin, Y.*, et al.* Unveiling the operation mechanism of layered perovskite solar cells. *Nat Commun* **10,** 1008 (2019).

32. Gu, Z., Huang, Z., Li, C., Li, M., & Song, Y. A general printing approach for scalable growth of perovskite single-crystal films. *Sci. Adv.* **4,** eaat2390 (2018).

33. Ju, D., *et al.* Tunable Band Gap and Long Carrier Recombination Lifetime of Stable Mixed $CH_3NH_3Pb_xSn_{1-x}Br_3$ Single Crystals. *Chem. Mater.* **30,** 1556-1565 (2018).

34. Zheng, G., *et al.* Manipulation of facet orientation in hybrid perovskite polycrystalline films by cation cascade. *Nat Commun* **9,** 2793 (2018).

35. Wu, X., Li, H., Wang, K., Sun, X., & Wang, L. $CH_3NH_3Pb_{1-x}Eu_xI_3$ mixed halide perovskite for hybrid solar cells: the impact of divalent europium doping on efficiency and stability. *RSC Adv.* **8,** 11095-11101 (2018).

36. Rao, H.S., Li, W.G., Chen, B.X., Kuang, D.B., & Su, C.Y. In Situ Growth of 120 cm2 $CH_3NH_3PbBr_3$ Perovskite Crystal Film on FTO Glass for Narrowband-Photodetectors. *Adv. Mater.* **29,** 1602639 (2017).

37. Huang, Y., *et al.* The intrinsic properties of $FA_{(1-x)}MA_xPbI_3$ perovskite single crystals. *J. Mater. Chem. A* **5,** 8537-8544 (2017).

38. Röhr, J., Kirchartz, T., & Nelson, J. On the correct interpretation of the low voltage regime in intrinsic single-carrier devices. *J Phys Condens Matter.* **29,** 205901 (2017).

39. Murali, B., *et al.* The surface of hybrid perovskite crystals: a boon or bane. *ACS Energy Lett.* **2,** 846-856 (2017).

40. Liu Y*, et al.* 20-mm-Large Single-Crystalline Formamidinium-Perovskite Wafer for Mass Production of Integrated Photodetectors. *Advanced Optical Materials* **4**, 1829-1837 (2016).

41. Zhumekenov, A., *et al.* Formamidinium lead halide perovskite crystals with unprecedented long carrier dynamics and diffusion length. *ACS Energy Lett*. **1,** 32-37 (2016).

42. Han, Q., *et al.* Single crystal formamidinium lead iodide ($FAPbI_3$): insight into the structural, optical, and electrical properties. *Adv. Mater.* **28,** 2253-2258, (2016).

43. Liu, Y., *et al.* Thinness-and shape-controlled growth for ultrathin single-crystalline perovskite wafers for mass production of superior photoelectronic devices. *Adv. Mater.* **28,** 9204-9209 (2016).

44. Liu, Y., *et al.* Two-inch-sized perovskite $CH_3NH_3PbX_3$ (X= Cl, Br, I) crystals: growth and characterization. *Adv. Mater.* **27,** 5176-5183 (2016).

45. Saidaminov, M., *et al.* Planar-integrated single-crystalline perovskite photodetectors. *Nat Commun* **6,** 8724 (2015).

46. Saidaminov, M., *et al.* High-quality bulk hybrid perovskite single crystals within minutes by inverse temperature crystallization. *Nat Commun* **6,** 7586 (2015).

47. Courtier, N., Cave, J., Foster, J., Walker, A., & Richardson, G. How transport layer properties affect perovskite solar cell performance: insights from a coupled charge transport/ion migration model. *Energy Environ. Sci.* **12,** 396-409 (2019).

48. Neukom, M., *et al.* Consistent Device Simulation Model Describing Perovskite Solar Cells in Steady-State, Transient and Frequency Domain. *ACS Appl. Mater. Interfaces* **11,** 23320-23328 (2019).

49. O'Kane, S., *et al.* Measurement and modelling of dark current decay transients in perovskite solar cells. *J. Mater. Chem. C* **5,** 452-462 (2017).

50. Lian, Z., *et al.* Perovskite $CH_3NH_3PbI_3$ (Cl) single crystals: rapid solution growth, unparalleled crystalline quality, and low trap density toward 108 cm^{-3}. *J. Am. Chem. Soc*. **138,** 9409-9412 (2016).

51. Yang, D.*, et al.* High efficiency planar-type perovskite solar cells with negligible hysteresis using EDTA-complexed SnO_2. *Nat Commun* **9,** 3239 (2018).

52. Onoda-Yamamuro, N., Matsuo, T., & Suga, H. Dielectric study of $CH_3NH_3PbX_3$ (X= Cl, Br, I). *J. Phys. Chem. Solids* **53,** 935-939 (1992).

53. Liu, D., *et al.* Impact of ultrathin C_{60} on perovskite photovoltaic devices. *ACS nano* **12,** 876-883 (2018).

54. Schulz, P., *et al*. Electronic level alignment in inverted organometal perovskite solar cells. *Adv. Mater. Interfaces* **2,** 1400532 (2015).

55. Futscher, M. H., et al. Quantification of ion migration in $CH_3NH_3PbI_3$ perovskite solar cells by transient capacitance measurements. *Mater. Horiz.*, **6**, 1497-1503 (2019).

56. Chen, Y., Peng, J., Su, D., Chen, X., & Liang Z. Efficient and balanced charge transport revealed in planar perovskite solar cells. *ACS Appl. Mater. Interfaces* **7,** 4471-4475 (2015).

57. Petrovic, M., Ye, T., Chellappan, V., & Ramakrishna, S. Effect of Low Temperature on Charge Transport in Operational Planar and Mesoporous Perovskite Solar Cells. *ACS Appl. Mater. Interfaces* **9,** 42769-42778 (2017).

58. Li, D.*, et al.* Size-dependent phase transition in methylammonium lead iodide perovskite microplate crystals. *Nat Commun* **7**, 1-8 (2016).

59. Chin, X. Y., Cortecchia, D., Yin, J., Bruno, A., & Soci, C. Lead iodide perovskite light-emitting field-effect transistor. *Nat Commun* **6**, 7383 (2015).

60. Meggiolaro, D., *et al.* Iodine chemistry determines the defect tolerance of lead-halide perovskites. *Energy Environ. Sci.* **11,** 702-713 (2018).

61. Gélvez-Rueda, M., Renaud, N., & Grozema, F. Temperature dependent charge carrier dynamics in formamidinium lead iodide perovskite. *J. Phys. Chem. C* **121,** 23392-23397 (2017).

62. Shrestha, S., *et al*. Assessing Temperature Dependence of Drift Mobility in Methylammonium Lead Iodide Perovskite Single Crystals. *J. Phys. Chem. C* **122,** 5935-5939 (2018).

63. Ma, J., Wang, L-W. The nature of electron mobility in hybrid perovskite $CH_3NH_3PbI_3$. *Nano Lett.* **17,** 3646-3654 (2017).

64. Zhao, T., Shi, W., Xi, J., Wang, D., & Shuai, Z. Intrinsic and extrinsic charge transport in $CH_3NH_3PbI_3$ perovskites predicted from first-principles. *Sci Rep* **6**, 19968 (2016).

Chapter 8

Scan-Rate and Temperature Dependence of the Photocurrent in $MAPbI_3$ Solar Cells*

Summary

The operation of methylammonium lead iodide ($MAPbI_3$) based solar cells is governed by a number of interdependent properties, such as ion migration, permittivity, charge transport and recombination, resulting in a large number of device parameters. In previous chapters we demonstrated that the frequency dependence of the permittivity, governed by a slow-moving positive ion and fixed negative ionic charge, plays a vital role in understanding the ionic and electronic transport in the dark. Impedance and electric displacement measurements on $MAPbI_3$ solar cells reveal that upon illumination the fixed negative ion becomes mobile with a two orders of magnitude higher diffusion coefficient as compared to the slow positive ion. We demonstrate that the resulting enhancement of the permittivity of $MAPbI_3$ and corresponding frequency and temperature dependence governs the magnitude, scan-rate and temperature dependence of the photogenerated current in $MAPbI_3$ solar cells. The enhanced permittivity under illumination also weakens the recombination between charge carriers, enabling low losses and high fill factors in $MAPbI_3$ solar cells. Incorporation of a frequency- and temperature-dependent permittivity, so far not considered in modeling of perovskite solar cells, is an essential prerequisite to quantitatively describe the photocurrent of $MAPbI_3$ solar cells.

*Publication: Sajedi Alvar, M., Wetzelaer, G-J.A.H., & Blom, P.W.M., (Submitted, 2020)

8.1. Introduction

Typically, for semiconducting devices like solar cells, parameters such as charge-carrier mobility, density, trapping and recombination are required to describe the device operation[1-14]. With the charge transport properties known, the *J-V* characteristics of solar cells can be reproduced using numerical device simulations, also providing information on the distribution of electric field and charge carriers[1-14]. However, analysis of the current-voltage (*I-V*) characteristics of $MAPbI_3$ PSCs is strongly hindered by the occurrence of hysteresis[15, 16]. The occurrence of hysteresis originates from ion migration[3, 4, 17-20], attributed to the movement of iodide ion vacancies[21-23]. In chapter 7 it was demonstrated that such movement of ion vacancies towards a biased electrode has a strong effect on the electronic properties of a perovskite device[11, 12]. In an ion-free semiconductor exhibiting a trap-free space-charge-limited current (SCLC), the electric field increases with the square-root of distance from the injecting contact[24]. As presented in chapters 5, 6, and 7, in a mixed ionic-electronic semiconductor as $MAPbI_3$ accumulation of ions at a contact due to an applied electric field will not only affect the injection properties, but will also screen the electric field in the rest of the device[11, 12, 19, 25, 26]. In such a case, as described in chapter 7, the standard SCLC theory is not applicable to determine the charge-carrier mobility of the semiconductor[12, 27]. Consequently, a device model for perovskite solar cells should include both electronic and ionic properties[9, 11].

In the last years several electronic-ionic device models for perovskite based solar cells have been proposed, mainly focused on understanding of the *J-V* hysteresis[3, 4, 8-10, 13, 14, 25]. However, although describing similar *J-V* characteristics, already in the ionic part alone large variations of several orders of magnitude in parameters as ion diffusion coefficient and ion centration have been

used in the various models to explain experimental data. Similarly, with regard to the charge-carrier mobilities values ranging from 10^{-2} to 100 $cm^2\ V^{-1}\ s^{-1}$ have been implemented in the various models. Furthermore, in all models a fixed relative dielectric constant, typically ranging from 6.5 to 117, has been used to calculate space-charge effects[3-5, 7-10, 13, 14, 25, 27-46]. In contrast, as also presented in previous chapters, impedance measurements on $MAPbI_3$ show a frequency dependent relative dielectric constant, ranging from ~60 at high frequencies to values of ~1000 at low frequency (~1 Hz)[11, 47-50].

The major challenge for the development of an electronic-ionic device model for perovskite devices is that it contains many parameters, such that a good fit of experimental data is readily obtained. Next to parameters for charge injection also electron and hole mobilities, trap densities and their energy distribution, recombination processes, ion concentrations and diffusion coefficients all need to be considered, leading easily to ~15 input parameters[4, 8-10, 13, 14]. However, with so many parameters a good fit does not necessarily mean that the chosen input parameters provide a unique solution. What has been missing so far is a systematic combined experimental-modelling study where most of the input parameters have been validated by independent measurements. With regard to the ionic part of the device model, in chapters 5 and 6 we characterized the ion dynamics in $MAPbI_3$ by two experimental methods, namely impedance spectroscopy and electric displacement as function of frequency[11]. Both measurements, carried out on Au/$MAPbI_3$/Au capacitors, independently revealed a diffusion coefficient for positive ions of $1\times10^{-15}\ m^2\ s^{-1}$ combined with an ion concentration of $2\times10^{25}\ m^{-3}$ and equal concentration of a fixed negative ionic charge. The electric displacement response was fully reproduced by a numerical device model, validating the ionic device parameters of $MAPbI_3$.[11]

As a next step, in chapter 7 we measured the electronic transport properties of electrons and holes in $MAPbI_3$ thin films using single-carrier devices[12]. These SCLC experiments revealed that the ion dynamics and the high low-frequency permittivity played a significant role in the observed electron and hole currents[12]. By including the ion dynamics and permittivity as experimentally determined parameters, the electron and hole mobility could be obtained[12]. Furthermore, the direction of the observed hysteresis in the hole-only and electron-only devices was consistent with the movement of positive ionic charges and fixed negative charge. Next to the magnitude of the SCLC also its dependence on scan rate and temperature is governed by the frequency and temperature dependence of the effective dielectric constant, which in turn originates from the ion dynamics[11, 12]. As a result, the effective dielectric constant is a crucial parameter that links the ionic and electrical properties. Having identified that the effective dielectric constant is the crucial parameter for the electrical behavior of $MAPbI_3$ based devices, the important question remains if and how it is affected by illumination. Earlier studies have reported that the dielectric constant of $MAPbI_3$ strongly increases under illumination, which had been attributed to structural fluctuations induced by photogenerated carriers[50]. Recently, also the enhancement and blocking of charge injection due to moving ions has been taken into account to explain the appearance of a high capacitance under illumination[51, 52]. In this chapter, we first investigate the dielectric behavior of $MAPbI_3$ solar cells under illumination. We observe that next to the slow positive ion dominating the dark permittivity in the ~s time regime a second faster ion appears under illumination in the ~ms time regime, leading to an enhanced dielectric response as compared to the dark. The occurrence of both such a slow and faster ion under illumination is in agreement with recent findings of Futscher et al. from transient capacitance measurements[53]. Here, we obtain the sign, concentration and diffusion coefficient of this second ion directly from electric displacement

measurements. The difference in electric displacement between the dark and illuminated case is fully consistent with the release of the fixed negative ion by light. The obtained diffusion coefficient is subsequently linked to the increase of the permittivity in the kHz regime. Taking the enhanced permittivity under illumination into account we are able to describe the photocurrent of $MAPbI_3$ based solar cells only using experimentally validated input parameters. The revelation that the magnitude, scan rate and temperature dependence of the permittivity governs the operation of perovskite solar cells is a major step forward in understanding and quantitative description of their device characteristics.

8.2. Results and discussion

8.2.1. Device fabrication and characterization

Au/$MAPbI_3$/Au parallel plate capacitors were fabricated using the lead acetate method as described in previous chapters. The fabrication procedure of the ITO/PTAA/$MAPbI_3$/C_{60}/TPBi/Al solar cell is comprehensively described in chapter 2. All the measurements were performed inside a nitrogen-filled glovebox. Impedance measurements were carried out using a Solartron impedance analyzer. The current-voltage measurements at slow scan rates were performed using a Keithley 2400 source meter. The scan rate dependent measurements were conducted using a Paios system from Fluxim.

8.2.2. Frequency dependence of illuminated and dark permittivity

As a first step, we have performed impedance spectroscopy measurements on ITO/PTAA/$MAPbI_3$/C_{60}/TPBi/Al solar cells under 1 Sun illumination. In Figure 8.1 the resulting

dielectric constant ε_r' is shown at zero bias as a function of frequency. For comparison, the dielectric constant obtained from Au/$MAPbI_3$/Au capacitors in the dark is also shown[11].

We observe, similar to Juarez-Perez et al.[50], that at low frequencies ε_r' is enhanced by a few orders of magnitude under 1 sun illumination. Furthermore, whereas in the dark ε_r' only starts to increase from its high frequency value $\varepsilon_{r\infty}'$ at frequencies below 10 Hz, under illumination already at 1 kHz an enhancement of the permittivity is observed.

8.2.3. Frequency dependence of dark and illuminated D-V characteristics

To further elucidate the enhanced permittivity under illumination we have investigated the dielectric displacement as a function of frequency and voltage for $MAPbI_3$ based solar cells using a Sawyer-Tower setup. As displayed in Figure 6.1 c, in the Sawyer-Tower setup a reference capacitor C_{ref} is placed in series with the solar cell, the latter being termed device under test (DUT).

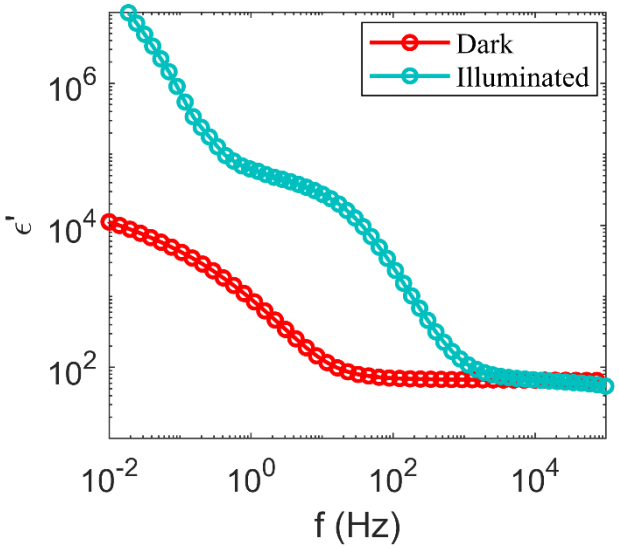

Figure 8.1. Frequency dependent of permittivity of 200 nm MAPbI3 thin film in the dark and under 1 sun illumination at zero bias.

A detailed description of electric displacement measurements on Au/$MAPbI_3$/Au capacitors is provided in chapter 6 [11]. Upon application of a bias voltage V ions in the perovskite drift towards the electrodes and form an accumulation layer. These accumulated ions screen the electric field inside the perovskite, such that the amount of ionic charge at the perovskite surface is nearly equal to the amount of (free) electronic charge on the electrodes, represented by the electric displacement D. As a result, the magnitude of D is governed by the ion concentration N_{ion}, whereas its frequency dependence is determined by the ion diffusion coefficient D_{ion}. In chapter 6, analysis of the D-V loops of Au/$MAPbI_3$/Au capacitors in the dark using an ionic-electronic drift-diffusion model revealed that the electric displacement can be reproduced by a mobile positive ion of which the concentration N_{ion}^+ amounts to 1.9×10^{25} m^{-3} and D_{ion}^+ equals 1×10^{-15} m^2 s^{-1} [11]. In contrast, the negative charge required for charge neutrality is considered immobile. This slow ion diffusion coefficient resulted in a large hysteresis in the D-E loops at 1 Hz, whereas for frequencies of 100 Hz and higher the hysteresis disappeared since the positive ions can no longer follow the modulation. As shown in Figure 8.2a, similar behavior for $MAPbI_3$ solar cells measured in the dark is observed.

The D-E loops could be reproduced with the device model using the same values for N_{ion}^+ and D_{ion}^+ as obtained from Au/$MAPbI_3$/Au capacitors for the slow positive ion, shown in Figure 8.2b. At 1 Hz the magnitude of the electric displacement varies between -50 mC m^{-2} to +150 mC m^{-2}, so a total variation of 200 mC m^{-2}. We note that the vertical asymmetry of the loops is the result of the presence of a built-in voltage due to the selective extracting contacts in the solar cell configuration. The increase of the dielectric constant at low frequency is also directly reflected in the voltage drop over the $MAPbI_3$ solar cell V_{DUT}: At 1 Hz, the capacitance of the solar cells is nearly equal to C_{ref}, such that about half of the applied voltage drops over the solar cell (V_{DUT}).

With increasing frequency the dielectric constant and therefore the solar cell capacitance drops such that its capacitance becomes smaller than C_{ref}, resulting in an increased voltage drop over the solar cell (V_{DUT}) and thus broader loop.

In contrast, shown in Figure 8.2c, the *D-E* loops of the illuminated $MAPbI_3$ solar cells are very narrow at low frequencies and show an additional strong response at 1 KHz. Due to the strongly enhanced dielectric constant at low frequencies (Figure 8.1) the capacitance of the solar cell is much larger than C_{ref} in this frequency range, such that most of the applied voltage drops over C_{ref}, resulting in a small V_{DUT} and narrow loop. At around 1 kHz the dielectric constant has dropped so much that the capacitance of the solar cell is lower than C_{ref}, such that most of the voltage now drops over the solar cell, resulting in broadening of the loop. Furthermore, at low frequencies the magnitude of the electric displacement varies between -250 mC m^{-2} to +150 mC m^{-2}, so a total variation of 400 mC m^{-2}.

The *D-V* loops clearly point towards the presence of a second ion in illuminated $MAPbI_3$ solar cells, providing direct information on its properties. The additional response at 1 kHz shows that this faster ion has a diffusion coefficient D_{ion} that is 2-3 orders of magnitude larger as compared to the slow ion that dominates the dark electric displacement. Furthermore, the difference in the magnitude of the displacement at 1 Hz between the dark (200 mC m^{-2}) and illuminated (400 mC m^{-2}) condition, where both the slow and fast ion contribute, is about 200 mC m^{-2}, directly showing that the slower and faster ions remarkably have similar concentration. As a result, the concentration of the faster ion is equal to the concentration of immobile negative charges in the dark required for maintaining charge neutrality.

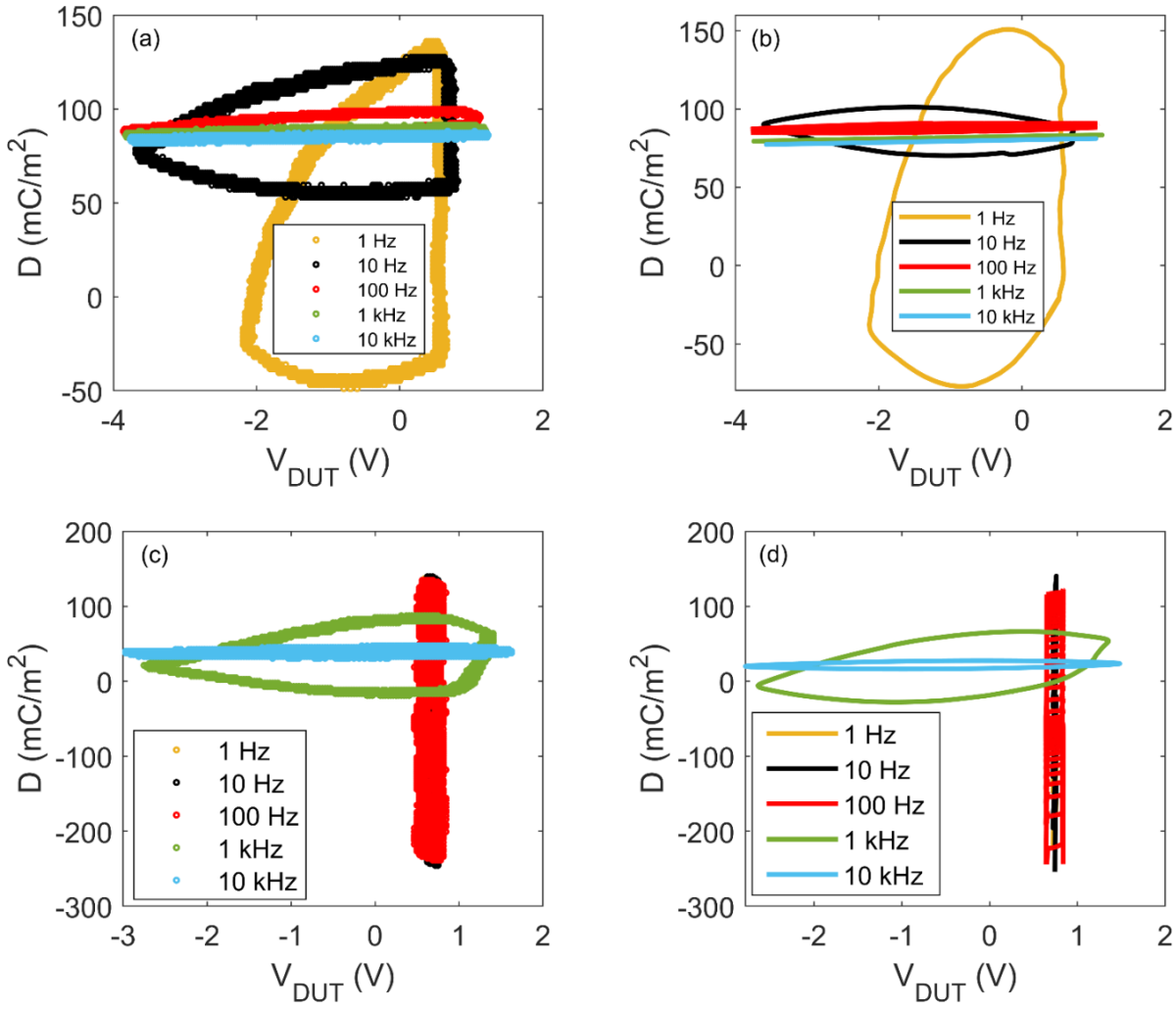

Figure 8.2. Electric displacement as function of voltage at various frequencies. (**a**) Experimental and (**b**) corresponding simulated *D-V* characteristics of an ITO/PTAA/$MAPbI_3$/C60/TPBi/Al solar cell in the dark using a combined ionic-electronic drift diffusion model with an ion diffusion coefficient D_{ion}^+ of 1×10^{-15} $m^2\ s^{-1}$ and an ion concentration N_{ion}^+ of 1.9×10^{25} m^{-3}. (**c**) Experimental *D-V* characteristics of an ITO/PTAA/$MAPbI_3$/C60/TPBi/Al solar cell under 1 sun illumination and (**d**) simulation of the electric displacement under illumination showing the additional contribution at 1 and 10 kHz using a D_{ion}^- of 2×10^{-13} $m^2\ s^{-1}$ and N_{ion}^- of 1.9×10^{25} m^{-3}.

We can fully describe all *D-V* loops both in dark and under illumination by only modifying, next to the permittivity, the diffusion coefficient of the negatively charged species from $D_{ion}^- = 0$ $m^2\ s^{-1}$ (dark) to $D_{ion}^- = 2\times10^{-13}$ $m^2\ s^{-1}$ (illuminated), in combination with $N_{ion}^- = 1.9\times10^{25}$ m^{-3} and

$D_{ion}^{+} = 1\times10^{-15}$ m^2 s^{-1}. The obtained diffusion coefficient D_{ion}^{-} is in the same range as reported for negatively charged iodine ions of ~10^{-12} m^2 s^{-1} by analyzing ionic conduction in $MAPbI_3$ [21]. Subsequent NMR studies[22] confirmed the dominant role of negatively charged I^- ions and the absence of MA related transport[54] with estimated diffusion coefficients below 10^{-18} m^2 s^{-1}. Theoretically, from density-functional-theory calculations it was found[23] that vacancy assisted I^- movement is dominant, where the mobile species are positively charged I^- vacancies with a diffusion coefficient of 10^{-16} m^2 s^{-1}, which is in the range of our $D_{ion}^{+} = 1\times10^{-15}$ m^2 s^{-1}. Furthermore, ab-initio theory[55] predicted an equilibrium positively charged I^- vacancy density of 1.6×10^{25} m^{-3}, which is in close agreement with the density of positive ions we find from impedance and dielectric measurements.

The fact that our measurements show that both positive and negative ions have equal concentrations also indicates that they might originate from the same chemical species. For a stoichiometric composition iodine moving away from its crystal site simultaneously creates a negatively charged I^- interstitial and a positively charged I^- vacancy, such that their concentrations are automatically equal. The occurrence of such a pair of defects, known as Frenkel pairs, is well known in halides[56] including leadiodide[57]. In a combined experimental and theoretical investigation by Mosconi et al.[58] it was proposed that illumination annihilates these Frenkel pairs, which would explain the occurrence of a second ion. Furthermore, they showed that the formation energy of these defect pairs is low such that they might occur in high concentrations. We therefore postulate that the slow ions that dominate the dark ionic conduction are positively charged I^- vacancies, of which the density and diffusion coefficients well agree with theoretical predictions. The faster ionic contribution activated by light might come from negatively charged I^- interstitials or I^- ions. Interestingly, in a recent paper of Kim et al. it has also been shown that the ionic

conductivity in $MAPbI_3$ is enhanced by two orders of magnitude upon illumination[59]. This is in excellent agreement with our result, where the mobile negative ionic charges created by light have equal concentration but a two order of magnitude higher diffusion coefficient than the positive ions that dominate the ionic conductivity in the dark. They attribute this effect to an interaction between electronic charge carriers and the iodine sublattice that allows for rapid exchange between the regular and interstitial lattice.

8.2.4. Analysis of the illumination-induced enhanced permittivity

Next, we investigate how the occurrence of a faster negative second ion contributes to the enhancement of the permittivity. In chapter 5 [11] we have shown that the frequency dependence of the effective dielectric constant ε_r' due to ion motion can be approximated by a model of Bandara and Mellander[60] for ionic liquids and electrolytes, given by

$$\varepsilon_r' = \varepsilon'_{r\infty}\left(1 + \frac{\delta}{1 + (\omega\tau_1\delta)^2}\right) \tag{8.1}$$

Here, τ_2 is a time constant characteristic for relaxation of the space-charge in the ion accumulation layer at the interface. The space-charge relaxation in the bulk is characterized by a time constant τ_1, which is related to τ_2 as

$$\tau_2 = \tau_1\sqrt{\delta} \tag{8.2}$$

These characteristic times show up as a maximum ($1/\tau_1$) and minimum ($1/\tau_2$) in the complex part of the impedance. Typically, with τ_1 and τ_2 known, the ion diffusion coefficient D_{ion} is then obtained by[11]

$$D_{ion} = \frac{L^2}{\tau_2\delta^2} \tag{8.3}$$

with L the sample thickness. Furthermore, the ion concentration is obtained from the ion conductivity σ, given by $N_{ion}=\sigma/e\mu$, with the ion mobility μ known via the Nernst-Einstein relation ($\mu=eD/kT$) and σ given by Jonscher's law[61] $\varepsilon_r''=\sigma/\varepsilon_0\omega$. However, given the fact that we already have obtained D_{ion} and N_{ion} from electric displacement measurements, it is instructive to see how they affect the frequency dependence of ε_r'. With N_{ion} and D_{ion} known also σ is known via:

$$\sigma = \frac{e^2 N_{ion} D_{ion}}{kT} \tag{8.4}$$

which is directly related to τ_1 by

$$\tau_1 = \frac{\varepsilon_0 \varepsilon_{r\infty}'}{\sigma} \tag{8.5}$$

With now D_{ion} and τ_1 known combining Eqs. (8.2) and (8.3) leads to an expression for δ given by

$$\delta = \left(\frac{L^2}{\frac{D_{ion}}{\tau_1}} \right)^{0.4} \tag{8.6}$$

which together with Eq. (8.2) provides τ_2 and then by Eq. (8.1) the effective relative permittivity as function of frequency. This analytical model is derived for the presence of one kind of ion, but since the diffusion coefficient of the two ions in $MAPbI_3$ differ by more than two orders of magnitude their contribution can be separated in frequency space. In Figure 8.3a the frequency dependence of the effective dielectric constant ε_r' in the dark using $N_{ion} = 2\times10^{25}$ m^{-3} and $D_{ion} = 1\times10^{-15}$ m^2 s^{-1}, combined with the high frequency relative dielectric constant $\varepsilon_{r\infty}' = 65$, is well reproduced at low frequencies. Under illumination the frequency dependence of ε_r' in the kHz regime is well described using $N_{ion} = 2\times10^{25}$ m^{-3} and $D_{ion} = 2\times10^{-13}$ m^2 s^{-1} as obtained from the

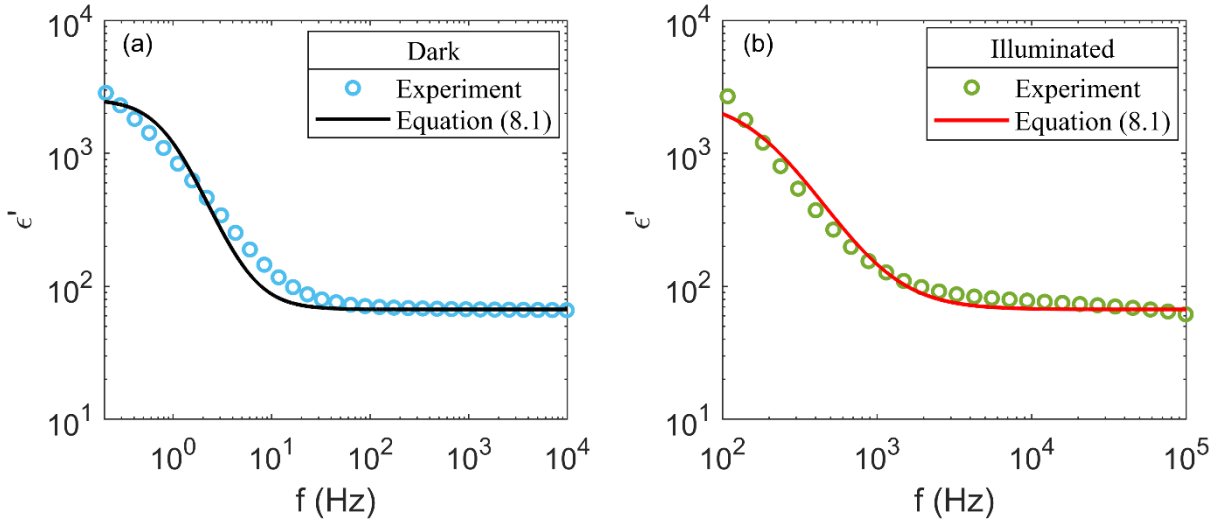

Figure 8.3. Frequency dependence of permittivity in dark and under illumination**.** Effective dielectric constant ε_r' of $MAPbI_3$ in the dark (**a**) and under illumination (**b**) as function of frequency. The lines represent the predicted ε_r' from Equation 1 using $D_{ion} = 1\times10^{-15}$ m^2 s^{-1} and $N_{ion} = 2\times10^{25}$ m^{-3} in the dark (**a**) and $D_{ion} = 2\times10^{-13}$ m^2 s^{-1} and $N_{ion} = 2\times10^{25}$ m^{-3} under illumination (**b**).

electric displacement measurements, shown in Figure 8.3b. In this frequency regime the slow ion does not contribute to the permittivity.

The agreement between these two independent experimental methods confirms the validity of our approach, showing that the enhancement of ε_r' under illumination arises from the presence of a photogenerated faster ion. We note that a description of ε_r' under illumination over the full frequency range including the contributions from both ions cannot be done analytically and is outside the scope of this work.

8.2.5. Operation of $MAPbI_3$ solar cell at slow scan rates

Having established the frequency dependence of the effective dielectric constant we now model the dark current and photocurrent of the ITO/PTAA/$MAPbI_3$/C_{60}/TPBi/Al solar cells. For the dark current we use as input parameters the measured SCLC electron and hole mobilities of μ_n

$= 1.2 \times 10^{-6}$ m^2 $V^{-1}s^{-1}$ and $\mu_p = 3.5 \times 10^{-10}$ m^2 $V^{-1}s^{-1}$, as described in chapter 7, as well as the N_{ion}^+ and D_{ion}^+ of the slow positive ion that dominates in dark condition[12]. These mobilities are at the lower end of scale of reported mobilities, which are affected by the timescale at which mobilities are measured. In a steady-state experiment like SCLC, a time-averaged mobility is obtained, relevant to steady-state devices like solar cells. For simulation of the dark current, we take the measured value of $\varepsilon_r' = 6000$ (Figure 8.1, dark) at the frequency that corresponds to the voltage scan rate of the *J-V* measurements, $f = \frac{scan\ rate}{4 \times V_m}$, where V_m is the amplitude of the applied voltage. Furthermore, knowledge on the recombination mechanism is required in order to model the bipolar dark current.

From time-delayed collection field experiments on $MAPbI_3$ solar cells it was shown by Paulke et al. that the recombination followed second order bimolecular recombination dynamics[62]. Considering the magnitude of the mobilities, Langevin recombination would be the expected mechanism for bimolecular recombination. The measured mobilities and dielectric constant then determine the bimolecular Langevin recombination coefficient, given by $e\,(\mu_n + \mu_p)/\varepsilon_r'$, such that with ε_r' and μ_n,μ_p known[12] there is no adjustable parameter in the device model. As shown in Figure 8.4a, the solar cell dark current is well reproduced by the numerical simulations without any adjustable parameter. We note that the bimolecular recombination rate according to the Langevin equation is lower than what has been measured by time-resolved techniques, such as transient absorption[63-65]. However, such techniques typically measure the recombination at short timescales, which may be significantly faster than recombination at longer timescales. Paulke et al.[62] showed that the bimolecular recombination coefficient is strongly time-dependent, reducing by over an order of magnitude already within the first 100 ns, trending towards even larger

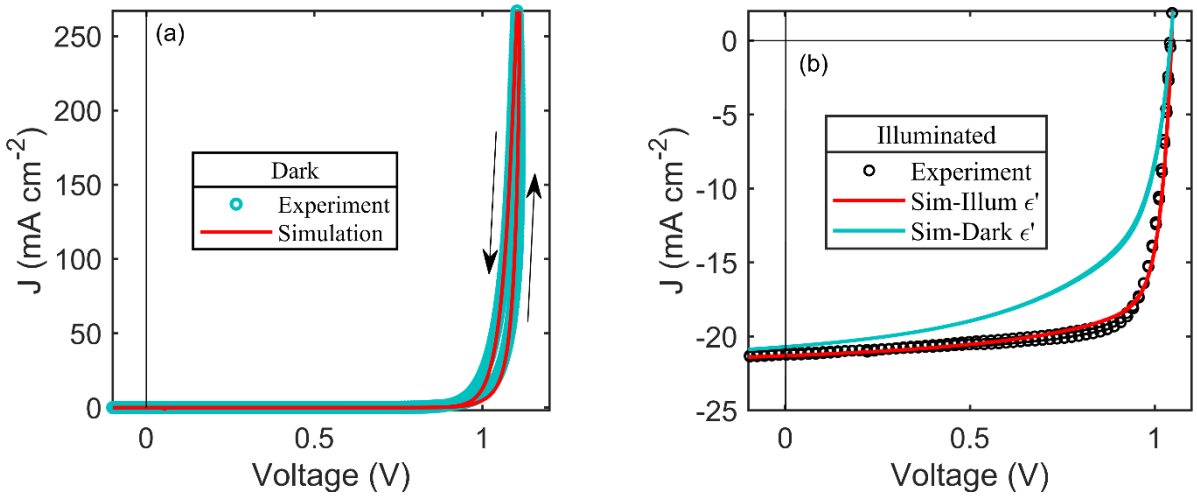

Figure 8.4. Current density-voltage characteristics of $MAPbI_3$ based solar cell**.** Current density-voltage characteristics of an ITO/PTAA/$MAPbI_3$/C60/TPBi/Al solar cell in the dark (**a**) and under 1 sun illumination (**b**). The simulations (lines) reproduce the solar cell characteristics using the obtained mobilities, dielectric constant in dark (**a**) and under illumination (**b**), while assuming Langevin-type recombination without a Langevin reduction factor.

reductions for longer timescales[62]. Such a time-dependent bimolecular recombination rate would be expected when bimolecular recombination occurs via a Langevin process, considering that reported charge-carrier mobilities also strongly depend on the time scale of the measurement technique[66].

As a next step, the current under illumination of the ITO/PTAA/$MAPbI_3$/C60/TPBi/Al solar cells is measured and modelled using the same input parameters, so with ε_r'= 6000 measured under dark conditions, Langevin recombination and the presence of two kind of mobile ions. The experimental current under illumination is characterized by a short-circuit current density J_{sc}=21.2 mA cm^{-2}, open-circuit voltage V_{oc}=1.04 V and a fill factor FF=78%, corresponding to a power conversion efficiency of 17.2%. As shown in Figure 8.4b the modelling (light-blue line) does not reproduce the measured photocurrent and leads to a much smaller fill factor (FF~60%), indicative of too strong recombination in the model. However, when using the enhanced ε_r'=3.5×10^6 that is

measured under illumination, the modelling (red line) is in excellent agreement with experiment, without any adjustable parameter. The enhanced ε_r' under illumination strongly weakens the Langevin recombination, such that an additional Langevin reduction factor[8] is not necessary to describe the experimental data. Incorporation of such a reduction factor, required when in the modelling only the constant high frequency $\varepsilon_{r\infty}$' is being used, is an artificial correction for the negligence of the enhancement of the effective dielectric constant due to ion motion.

8.2.6. Temperature and scan-rate dependence of the photocurrent of $MAPbI_3$ solar cells

As a further test of the device model we investigate the scan-rate and temperature dependence of the photocurrent of $MAPbI_3$ based solar cells. In chapter 7 we have demonstrated that the measured frequency dependence of the effective dielectric constant in dark enabled us to predict the scan-rate and temperature dependence of the space-charge-limited electron and hole current in $MAPbI_3$[12]. Here, we use the measured frequency dependence of ε_r' under illumination to describe the dependence of the photocurrent of $MAPbI_3$ based solar cells on voltage scan rate. Figure 8.5a shows the measured photocurrent as function of scan rate. The measured scan-rate dependence can be well reproduced by the model using the measured frequency-dependent permittivity, shown in Figure 8.5b. As next step the measured temperature dependence of the photocurrent is shown in Figure 8.5c. From impedance measurements we determined that the ion motion in $MAPbI_3$ is thermally activated with an activation energy of 0.42 eV, which in turn gives rise to a strong temperature dependence of the effective permittivty[12]. Using the experimental activation energy

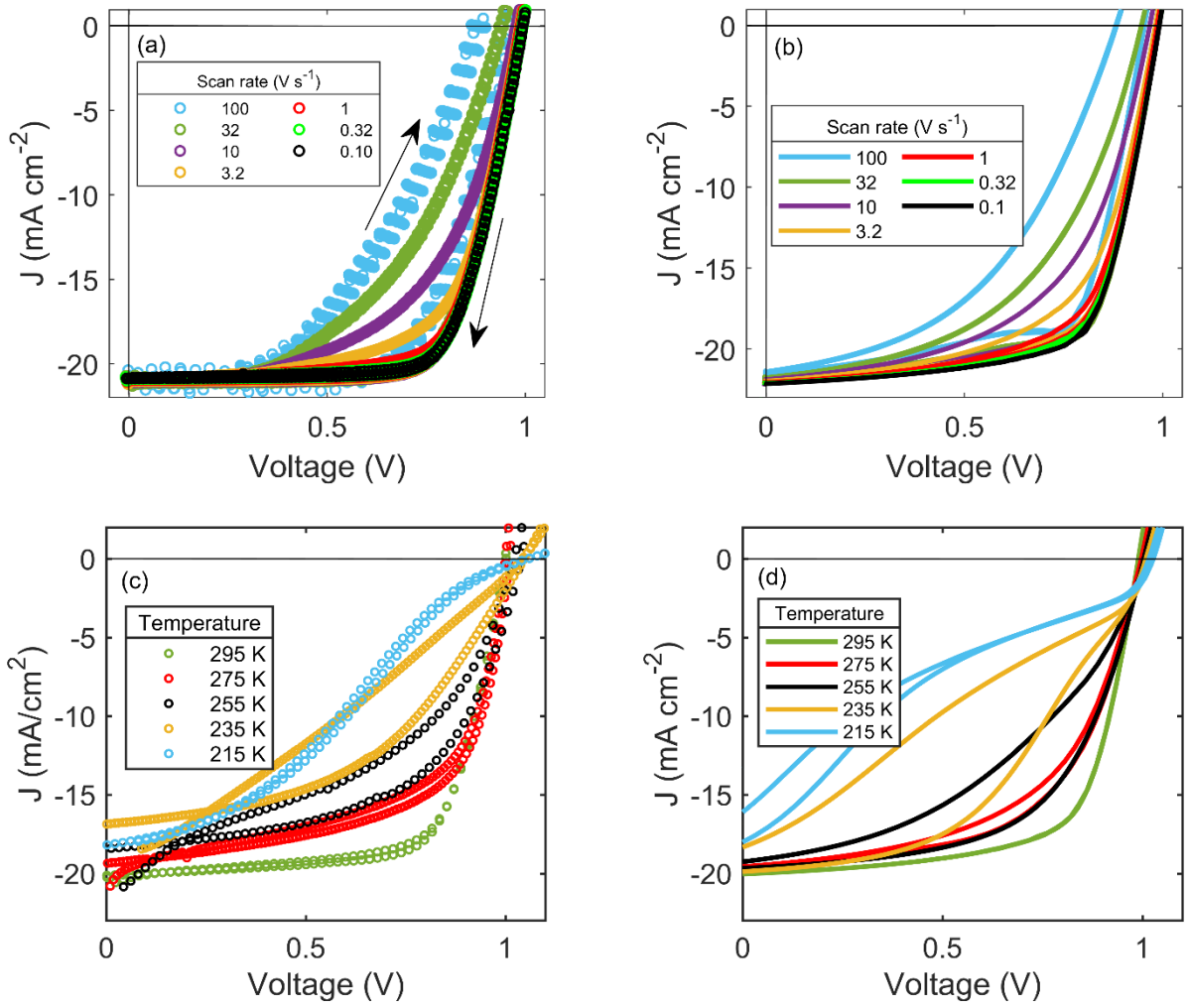

Figure 8.5. Current density-voltage characteristics of an ITO/PTAA/MAPbI3/C60/TPBi/Al solar cell under 1 sun illumination for different voltage scan rates and temperatures. The scan-rate (**a**) and temperature dependent measurements (**c**) are well reproduced by the corresponding simulations in panels (**b**) and (**d**), respectively. Incorporation of the measured frequency and temperature dependence of the dielectric constant results in a correct description of both the magnitude of the current as well as the hysteresis behavior.

for ion motion in the device model we can also reproduce very well the temperature dependence of the measured photocurrent of the $MAPbI_3$ based solar cells, as shown in Figure 8.5d. Again, next to the magnitude of the photocurrent also the behavior of the hysteresis is correctly reproduced. These results show that in order to understand the device characteristics of $MAPbI_3$

solar cells it is essential to take the frequency and temperature dependence of the permittivity into account.

We note that next to Langevin recombination also non-radiative recombination via trap states in the bulk as well as at the interface between the perovskite and the organic transport layers has been identified as important recombination mechanism[67-69]. The occurrence of these recombination mechanisms strongly depend on the combination of materials as well as their processing. Although our model calculations show that the magnitude, scan-rate and temperature dependence of the photocurrent are all consistently explained using bimolecular Langevin recombination for our materials system, we cannot rule out the occurrence of trap-assisted recombination. However, it should be noted that trap-assisted recombination in low mobility materials, either in the bulk or at the interface is also a diffusion driven Langevin-like process, limited by the diffusion of the free charge towards a trapped countercharge. As a result, for recombination of trapped electrons and free holes or recombination of trapped holes with free electrons the Shockley-Read-Hall[70, 71] capture coefficient is given by $e\mu_p/\varepsilon_r'$ or $e\mu_n/\varepsilon_r'$ respectively, which equals the Langevin coefficient with one of the mobilities set to zero[72]. As a result, also for trap-assisted recombination a strong enhancement of ε_r' upon illumination will strongly reduce the recombination rate, enabling a high FF and efficiency, in a similar way as for Langevin recombination. Therefore, the choice of the recombination mechanism in our model does not change the main message of our work, namely that the frequency and temperature dependence of the enhanced dielectric constant under illumination governs the scan-rate and temperature dependence of the photocurrent of $MAPbI_3$ based solar cells.

8.2.7. Scan-rate dependence of electric potential distribution

Next to a quantitative description of the electrical characteristics of $MAPbI_3$ solar cells our numerical ionic-electronic device model considering ion motion and resulting frequency dependent dielectric constant also provides insight in the distribution of electric fields, photogenerated carriers and ions as function of voltage and scan rate. As an example, in Figure 8.6 the energy band diagram of the solar cell is given for a slow (0.1 V/s) and fast (100 V/s) scan rate. It is observed that due to the high ε_r' at low scan speeds there is no build-up of space-charge, leading to a constant electric field in the solar cell. In contrast, the lower ε_r' at higher scan rate results in the build-up of space-charge, such that in part of the solar cell the electric field is screened (flat energy band). Due to the absence of driving force for extraction of the charge carriers in this part of the device the photocurrent is lowered, as also observed experimentally.

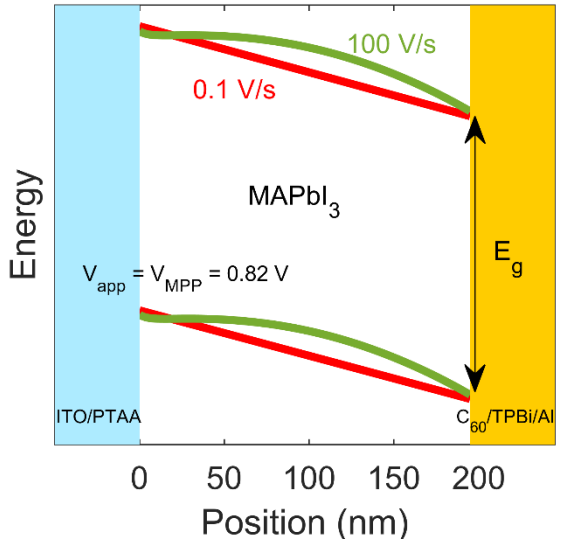

Figure 8.6. Energy band diagram of $MAPbI_3$ based solar cell. Energy band diagram of a ITO/PTAA/$MAPbI_3$/C60/TPBi/Al solar cell at the maximum power point under 1 sun illumination for different voltage scan rates.

8.3. Conclusion

Summarizing, an ionic-electronic device model is presented that describes the photocurrent of $MAPbI_3$ solar cells and its dependence on voltage scan-rate and temperature using only experimentally validated parameters. An essential ingredient is the incorporation of an enhanced permittivity under illumination, caused by the generation of a negative mobile ion with a response time in the ~ms regime. The voltage scan-rate and temperature dependence of the photocurrent of $MAPbI_3$ solar cells is governed by the frequency and temperature dependence of the permittivity. The enhanced permittivity not only weakens the build-up of space-charge, but also strongly reduces charge carrier recombination due to a reduced Coulomb interaction between electron and holes, independent of whether the carriers are free or being trapped. Realization of the essential role of the permittivity in mixed ionic-electronic device models is an important step forward towards a quantitative description of the operation of a perovskite solar cell.

8.4. References

1. Koster, L. J. A., Smits, E. C. P., Mihailetchi, V. D., & Blom, P. W. M. Device model for the operation of polymer/fullerene bulk heterojunction solar cells. *Phys. Rev. B*, **72**, 085205 (2005).

2. Sze, S.M., & Ng, K.K. *Physics of semiconductor devices*. John wiley & sons, 2006.

3. van Reenen, S., Kemerink, M., & Snaith, H. Modeling anomalous hysteresis in perovskite solar cells. *J. Phys. Chem. Lett.* **6,** 3808-3814 (2015).

4. Richardson, G., *et al.* Can slow-moving ions explain hysteresis in the current–voltage curves of perovskite solar cells? *Energy Environ. Sci.* **9,** 1476-1485 (2016).

5. Sherkar, T.S. & Koster, L.J.A. Can ferroelectric polarization explain the high performance of hybrid halide perovskite solar cells? *Phys. Chem. Chem. Phys.* **18**, 331-338 (2016).

6. Zhou, Y., & Gray-Weale, A. A numerical model for charge transport and energy conversion of perovskite solar cells. *Phys. Chem. Chem. Phys.* **18**, 4476-4486 (2016).

7. Sherkar, T.S.*, et al.* Recombination in perovskite solar cells: significance of grain boundaries, interface traps, and defect ions. *ACS Energy Lett.* **2**, 1214-1222 (2017).

8. Sherkar, T.S., Momblona, C., Gil-Escrig, L., Bolink, H.J., & Koster, L.J.A. Improving perovskite solar cells: Insights from a validated device model. *Adv. Energy Mater.* **7**, 1602432 (2017).

9. Courtier, N.E., Richardson, G., & Foster, J.M. A fast and robust numerical scheme for solving models of charge carrier transport and ion vacancy motion in perovskite solar cells. *Appl. Math. Model.* **63**, 329-348 (2018).

10. Neukom, M., *et al.* Consistent Device Simulation Model Describing Perovskite Solar Cells in Steady-State, Transient and Frequency Domain. *ACS Appl. Mater. Interfaces* **11,** 23320-23328 (2019).

11. Sajedi Alvar, M., Blom, P. W. M., & Wetzelaer, G.-J. A. H. Device Model for Methylammonium Lead Iodide Perovskite With Experimentally Validated Ion Dynamics. *Adv. Electron. Mater.* 1900935 (2020).

12. Sajedi Alvar, M., Blom. P.W.M., & Wetzelaer, G-J.A.H. Space-charge-limited electron and hole currents in hybrid organic-inorganic perovskites. *Nature Commun* **11**, 4023 (2020).

13. Courtier, N., Cave, J., Foster, J., Walker, A., & Richardson, G. How transport layer properties affect perovskite solar cell performance: insights from a coupled charge transport/ion migration model. *Energy Environ. Sci.* **12,** 396-409 (2019).

14. O'Kane, S., *et al.* Measurement and modelling of dark current decay transients in perovskite solar cells. *J. Mater. Chem. C* **5,** 452-462 (2017).

15. Chen, B., Yang, M., Priya, S., & Zhu, K. Origin of J–V hysteresis in perovskite solar cells. *J. Phys. Chem. Lett.* **7,** 905-917 (2016).

16. Tress, W., *et al*. Understanding the rate-dependent J–V hysteresis, slow time component, and aging in $CH_3NH_3PbI_3$ perovskite solar cells: the role of a compensated electric field. *Energy Environ. Sci.* **8,** 995-1004 (2015).

17. Chen, B.*, et al.* Impact of capacitive effect and ion migration on the hysteretic behavior of perovskite solar cells. *J. Phys. Chem. Lett.* **6**, 4693-4700 (2015).

18. Haruyama, J., Sodeyama, K., Han, L. & Tateyama, Y. First-principles study of ion diffusion in perovskite solar cell sensitizers. *J. Am. Chem. Soc.* **137**, 10048-10051 (2015).

19. Weber, S., *et al.* How the formation of interfacial charge causes hysteresis in perovskite solar cells. *Energy Environ. Sci.* **11,** 2404-2413 (2018).

20. Snaith, H., *et al.* Anomalous hysteresis in perovskite solar cells. *J. Phys. Chem. Lett.* **5,** 1511-1515 (2014).

21. Yang, T.Y., Gregori, G., Pellet, N., Grätzel, M., & Maier, J. The Significance of Ion Conduction in a Hybrid Organic–Inorganic Lead-Iodide-Based Perovskite Photosensitizer. *Angew. Chem.* **127**, 8016-8021 (2015).

22. Senocrate, A.*, et al.* The nature of ion conduction in methylammonium lead iodide: a multimethod approach. *Angew. Chem. Int. Ed.* **56**, 7755-7759 (2017).

23. Eames, C., *et al*. Ionic transport in hybrid lead iodide perovskite solar cells. *Nat Commun* **6,** 7497 (2015).

24. Lampert, M.A., & Mark P. Current injection in solids. 1970.

25. Calado, P., *et al.* Evidence for ion migration in hybrid perovskite solar cells with minimal hysteresis. *Nat Commun* **7,** 13831 (2016).

26. Belisle, R., *et al.* Interpretation of inverted photocurrent transients in organic lead halide perovskite solar cells: proof of the field screening by mobile ions and determination of the space charge layer widths. *Energy Environ. Sci.* **10,** 192-204 (2017).

27. Duijnstee, E.A., *et al*. Towards Understanding Space-charge Limited Current Measurements on Metal Halide Perovskites. *ACS Energy Lett.* **5,** 376-384 (2020).

28. Liu, Y.*, et al.* 20-mm-Large Single-Crystalline Formamidinium-Perovskite Wafer for Mass Production of Integrated Photodetectors. *Adv. Opt. Mater.* **4,** 1829-1837 (2016).

29. Shi, D., *et al.* Low trap-state density and long carrier diffusion in organolead trihalide perovskite single crystals. *Science* **347,** 519-522 (2015).

30. Riquelme, A., *et al.* Identification of recombination losses and charge collection efficiency in a perovskite solar cell by comparing impedance response to a drift-diffusion model. *Nanoscale*, **12,** 17385-17398 (2020).

31. Chen, T., Sun, Z., Liang, M., & Xue, S. Correlating hysteresis phenomena with interfacial charge accumulation in perovskite solar cells. *Phys. Chem. Chem. Phys.* **22**, 245-251 (2020).

32. Pospisil, J., *et al*. Density of bulk trap states of hybrid lead halide perovskite single crystals: temperature modulated space-charge-limited-currents. *Sci Rep* **9,** 3332 (2019).

33. Lin, Y.*, et al.* Unveiling the operation mechanism of layered perovskite solar cells. *Nat Commun* **10,** 1008 (2019).

34. Gu, Z., Huang, Z., Li, C., Li, M., & Song, Y. A general printing approach for scalable growth of perovskite single-crystal films. *Sci. Adv.* **4,** eaat2390 (2018).

35. Ju, D., *et al.* Tunable Band Gap and Long Carrier Recombination Lifetime of Stable Mixed $CH_3NH_3Pb_xSn_{1-x}Br_3$ Single Crystals. *Chem. Mater.* **30,** 1556-1565 (2018).

36. Wu, X., Li, H., Wang, K., Sun, X., & Wang, L. $CH_3NH_3Pb_{1-x}Eu_xI_3$ mixed halide perovskite for hybrid solar cells: the impact of divalent europium doping on efficiency and stability. *RSC Adv.* **8,** 11095-11101 (2018).

37. Zheng, G., *et al.* Manipulation of facet orientation in hybrid perovskite polycrystalline films by cation cascade. *Nat Commun* **9,** 2793 (2018).

38. Huang, Y., *et al.* The intrinsic properties of $FA_{(1-x)}MA_xPbI_3$ perovskite single crystals. *J. Mater. Chem. A* **5,** 8537-8544 (2017).

39. Murali, B., *et al.* The surface of hybrid perovskite crystals: a boon or bane. *ACS Energy Lett.* **2,** 846-856 (2017).

40. Zhumekenov, A., *et al.* Formamidinium lead halide perovskite crystals with unprecedented long carrier dynamics and diffusion length. *ACS Energy Lett*. **1,** 32-37 (2016).

41. Han, Q., *et al.* Single crystal formamidinium lead iodide ($FAPbI_3$): insight into the structural, optical, and electrical properties. *Adv. Mater.* **28,** 2253-2258, (2016).

42. Liu, Y., *et al.* Thinness-and shape-controlled growth for ultrathin single-crystalline perovskite wafers for mass production of superior photoelectronic devices. *Adv. Mater.* **28,** 9204-9209 (2016).

43. Saidaminov, M., *et al.* High-quality bulk hybrid perovskite single crystals within minutes by inverse temperature crystallization. *Nat Commun* **6,** 7586 (2015).

44. Saidaminov, M., *et al.* Planar-integrated single-crystalline perovskite photodetectors. *Nat Commun* **6,** 8724 (2015).

45. Yang, D.*, et al.* High efficiency planar-type perovskite solar cells with negligible hysteresis using EDTA-complexed SnO_2. *Nat Commun* **9,** 3239 (2018).

46. Lian, Z., *et al.* Perovskite $CH_3NH_3PbI_3$ (Cl) single crystals: rapid solution growth, unparalleled crystalline quality, and low trap density toward 108 cm^{-3}. *J. Am. Chem. Soc*. **138,** 9409-9412 (2016).

47. Hoque, M.N.F.*, et al.* Polarization and Dielectric Study of Methylammonium Lead Iodide Thin Film to Reveal its Nonferroelectric Nature under Solar Cell Operating Conditions. *ACS Energy Lett.* **1**, 142-149 (2016).

48. Onoda-Yamamuro, N., Matsuo, T., & Suga, H. Dielectric study of $CH_3NH_3PbX_3$ (X= Cl, Br, I). *J. Phys. Chem. Solids* **53,** 935-939 (1992).

49. Sajedi Alvar, M., Kumar, M., Blom, P., Wetzelaer, G., & Asadi, K. Absence of ferroelectricity in methylammonium lead iodide perovskite. *AIP Adv.* **7,** 095110 (2017).

50. Juarez-Perez, E.J.*, et al.* Photoinduced giant dielectric constant in lead halide perovskite solar cells. *J. Phys. Chem. Lett.* **5**, 2390-2394 (2014).

51. Jacobs, D.A.*, et al.* The two faces of capacitance: new interpretations for electrical impedance measurements of perovskite solar cells and their relation to hysteresis. *J. Appl. Phys.* **124,** 225702 (2018).

52. Moia, D.*, et al.* Ionic-to-electronic current amplification in hybrid perovskite solar cells: ionically gated transistor-interface circuit model explains hysteresis and impedance of mixed conducting devices. *Energy Environ. Sci.* **12**, 1296-1308 (2019).

53. Futscher, M. H., et al. Quantification of ion migration in $CH_3NH_3PbI_3$ perovskite solar cells by transient capacitance measurements. *Mater. Horiz.*, **6**, 1497-1503 (2019).

54. Senocrate, A.*, et al.* Slow $CH_3NH_3^+$ Diffusion in $CH_3NH_3PbI_3$ under Light Measured by Solid-State NMR and Tracer Diffusion. *J. Phys. Chem. C,* **122**, 21803-21806 (2018).

55. Walsh, A., Scanlon, D.O., Chen, S., Gong, X.G. & Wei, S.-H., Self-Regulation Mechanism for Charged Point Defects in Hybrid Halide Perovskites. Angew. Chem. Int. Ed., **54,** 1791-1794 (2015).

56. Dexter, D. Varley mechanism for defect formation in alkali halides. *Phys. Rev.* **118**, 934 (1960).

57. Oberschemidt, J., & Lazarus, D. Ionic conductivity and activation volumes in the lead halides $PbCl_2$, $PbBr_2$, and PbI_2. *Phys. Rev. B*, **21**, 5813 (1980).

58. Mosconi, E., Meggiolaro, D., Snaith, H.J., Stranks, S.D., & De Angelis, F. Light-induced annihilation of Frenkel defects in organo-lead halide perovskites. *Energy Environ. Sci.* **9**, 3180-3187 (2016).

59. Kim, G.Y., *et al*. Large tunable photoeffect on ion conduction in halide perovskites and implications for photodecomposition. *Nature Mater* **17**, 445–449 (2018).

60. Bandara, T., & Mellander, B. Evaluation of mobility, diffusion coefficient and density of charge carriers in ionic liquids and novel electrolytes based on a new model for dielectric response. *Ionic liquids: theory, properties, new approaches*, 383-406 (2011).

61. Jonscher, A. Analysis of the alternating current properties of ionic conductors. *J. Mater. Sci.* **13**, 553-562 (1978).

62. Paulke, A.*, et al.* Charge carrier recombination dynamics in perovskite and polymer solar cells. *Appl. Phys. Lett.* **108,** 113505 (2016).

63. Zhang, X., Shen, J-X., Wang, W., & Van de Walle, C.G. First-principles analysis of radiative recombination in lead-halide perovskites. *ACS Energy Lett.* **3,** 2329-2334 (2018).

64. Herz, L. Charge-carrier mobilities in metal halide perovskites: fundamental mechanisms and limits. *ACS Energy Lett.* **2,** 1539-1548 (2017)

65. Srimath Kandada, A.R. & Petrozza, A. Research update: luminescence in lead halide perovskites. *APL Mater.* **4**, 091506 (2016).

66. Wehrenfennig, C., Eperon, G.E., Johnston, M.B., Snaith, H.J. & Herz, L.M. High Charge Carrier Mobilities and Lifetimes in Organolead Trihalide Perovskites. *Adv. Mater. Adv. Mater.* **26**, 1584-1589 (2014).

67. Correa-Baena, J-P., *et al.* Identifying and suppressing interfacial recombination to achieve high open-circuit voltage in perovskite solar cells. *Energy Environ. Sci.* **10,** 1207-1212 (2017).

68. Caprioglio, P., *et al.* On the Origin of the Ideality Factor in Perovskite Solar Cells. *Adv. Energy Mater.* **10**, 2000502 (2020).

69. Wetzelaer, G.-J.A.H., *et al*. Trap-assisted non-radiative recombination in organic–inorganic perovskite solar cells. *Adv. Mater.* **27**, 1837-1841 (2015).

70. Shockley, W. & Read, Jr. W. Statistics of the recombinations of holes and electrons. *Phys. Rev.* **87,** 835 (1952).

71. Hall, R.N. Electron-hole recombination in germanium. *Phys. Rev.* **87,** 387 (1952).

72. Kuik, M., Koster, L., Wetzelaer, G.-J.A.H. & Blom, P. Trap-assisted recombination in disordered organic semiconductors. *Phys. Rev. Lett.* **107,** 256805 (2011).

List of Publications

1- Sajedi Alvar, M., Kumar, M., Blom, P., Wetzelaer, G., & Asadi, K. Absence of ferroelectricity in methylammonium lead iodide perovskite. *AIP Adv.* **7,** 095110 (2017).

2- Sajedi Alvar, M., Blom, P. W. M., & Wetzelaer, G.-J. A. H. Device Model for Methylammonium Lead Iodide Perovskite With Experimentally Validated Ion Dynamics. *Adv. Electron. Mater.* 1900935 (2020).

3- Sajedi Alvar, M., Blom. P.W.M., & Wetzelaer, G-J.A.H. Space-charge-limited electron and hole currents in hybrid organic-inorganic perovskites. Nature Commun 11, 4023 (2020).

4- Sajedi Alvar, M., Wetzelaer, G-J.A.H., & Blom. P.W.M. Scan-rate and temperature dependence of the photocurrent in methylammonium lead iodide based solar cells. (Submitted)